Aus dem Institut für Neuroanatomie
der Medizinischen Fakultät Mannheim, Mannheim Center for Translational Neuroscience
(Direktor: Prof. Dr. med. Christian Schultz)

Identifying novel peroxisome-associated proteins in mouse liver and pig heart by implementing different quantitative proteomics approaches.

Inauguraldissertation
zur Erlangung des Doctor scientiarum humanarum (Dr. sc. hum.)
der
Medizinischen Fakultät Mannheim
der Ruprecht-Karls-Universität
zu
Heidelberg

vorgelegt von
Öznur Singin

Aus
Nigde (Türkei)
2024

Dekan: Prof. Dr. med. Sergij Goerdt
Referent: Prof. Dr. med. Christian Schultz

TABLE OF CONTENTS

ABBREVIATIONS

ALDH3A2: Aldehyde Dehydrogenase 3 Family Member A2
ATAD1: ATPase Family AAA Domain Containing 1
ABCD1: ATP Binding Cassette Subfamily D Member 1
ABHEB: Abhydrolase Domain Containing 14B
ACAD11: Acyl-CoA Dehydrogenase Family Member 11
ACBD5: Acyl-CoA Binding Domain Containing 5
ACNT1: Actinin Alpha 1
ACOX: acyl-coenzyme A oxidase
ACSL: Acyl-CoA Synthetase Long Chain Family Member
ACTG1: Actin Gamma 1
ADE2: Phosphoribosyl aminoimidazole carboxylase
ADHAP: alkyl dihydroxyacetone phosphate
AGPS: Alkylglycerone Phosphate Synthase
Alg-2: Apoptosis-linked gene
APOB: Apolipoprotein B
ARFs: Adenosine diphosphate-Ribosylation Factor
ATAP5F1: ATP synthase F1 subunit
ATP: Adenosine triphosphate
ATPA: ATP synthase alpha
ATPB: ATP synthase beta
BioID: Proximity-dependent biotin identification
BSA: Bovine Serum Albumin
BU: Beaufay Unit
CH60: Chaperonin 60
cm: centimeter
COPI: coat protein complex I
COX5A: Cytochrome C Oxidase Subunit 5A
CPT1: Carnitine palmitoyltransferase 1
CRSIPR: Clustered Regularly Interspaced Short Palindromic R
CYB5R3: cytochrome b5 reductase 3
CYT: Cytosol
Da: Dalton
DBP: D-Bifunctional Protein
DDA: Data-dependent acquisition
ddH$_2$O: Double-distilled water
DHAPAT: Dihydroxyacetone phosphate acyltransferase
DHCA: Dihydrocaffeic acid
DHRS7b: Dehydrogenase/ Reductase 7B
DMEM: Dulbecco's Modified Eagle Medium
DNA: Deoxyribonucleic acid
DTT: Dithiothreitol
DZHK: Deutschen Zentrum für Herz-Kreislauf-Forschung
EARS2: Glutamyl-TRNA Synthetase 2
ECH1: Enoyl-CoA Hydratase 1
ECI2: Enoyl-CoA Delta Isomerase 2
ECL: Enhanced chemiluminescence
EDTA: Ethylenediaminetetraacetic acid
EMMA: European Mouse Mutant Archive
ER: Endoplasmic reticulum
ERES
ERP29: Endoplasmic reticulum protein 29
ESCRT: Endosomal sorting complex required for transport
FABP1: Fatty acid binding proteins
FAR1: Fatty Acyl-CoA Reductase 1
FBS: Fetal bovine serum
FCS: Fetal Calf Serum
FDR: False Discovery Rate
FFAT: Two phenylalanines in an acidic tract
FIS1: Mitochondrial fission 1 protein
FLM: Fluffy layer of the **LM**

GB: Gradient buffer
GEFs: Guanine nucleotide exchange factors
GmbH: Gesellschaft mit beschränkter Haftung
GNPAT: Glyceronephosphate O-Acyltransferase
GRP78: Glucose-regulated protein 78
GSTK1: Glutathione S-transferase kappa 1
GTP: Guanosine-5'-triphosphate
HB: Homogenization buffer
HCL: Hydrochloric acid
HM: Heavy mitochondrial fraction
HMCS2: Mitochondrial 3-hydroxy-3-methylglutaryl CoA synthase
HMGCL: 3-Hydroxy-3-Methylglutaryl-CoA Lyase
HPPD: 4-Hydroxyphenylpyruvate dioxygenase
hPSCs: Human pluripotent stem cells
HRP: Horse radish peroxidase
HSD3B3: Hydroxy-Delta-5-Steroid Dehydrogenase, 3 Beta- And Steroid Delta-Isomerase 1
HTATIP2: HIV-1 TAT-Interactive Protein 2
ICAT: Isotope-coded affinity tag
IDHP: Isopropyl 3-(3,4-dihydroxyphenyl)-2-hydroxypropanoate
IF: Immunofluorescence
IMMT: MICOS complex subunit MIC60
Inp1: Inheritance of peroxisomes protein 1
IRD: Infantile Refsum Disease
iRT: indexed Retention Time
iTRAQ: Isobaric tags for relative and absolute quantitation
JACoP: Just another co-localization method
JPH2: Junctophilin-2
KLHL41: Kelch like protein family 41
KO: Knock out
KOH: Potassium hydroxide
LACTB2: Lactamase Beta 2
LM: Light mitochondrial fraction
hyperLOPIT: Hyperplexed Localization of Organelle Proteins by Isotope Tagging
mA: Miliamper
mAb: Monoclonal antibody
MARC1: Mitochondrial Amidoxime Reducing Component 1
MAVS: Mitochondrial antiviral-signaling protein
MCT1/2: Monocarboxylate transporter 1/2
MDH2: Mitochondrial malate dehydrogenase
MEF: Mouse embryonic fibroblasts
MFN1: Mitofusin 1
MFP1: Multifunctional protein 1
MGST1: Microsomal Glutathione S-Transferase 1
MIC: Microsomal
MiNA: Mitochondrial Network Analysis
MIRO1: Mitochondrial Rho GTPase1
Mm:milimeter
MOPs: 3-(N-morpholino) propanesulfonic acid
MRG: Mitochondrial RNA granule
MRPL18: Mitochondrial Ribosomal Protein L18
MRPS28: Mitochondrial Ribosomal Protein S28
MS: Mass Sprectrometry
MSP: Major sperm protein
MTG2: Mitochondrial Ribosome Associated GTPase 2
MudPIT: Multi-dimensional protein identification technology
MW: Molecular weight
NA: Numerical aperture
NaCl: Sodium chloride
NALD: Neonatal Adrenoleukodystrophy
NB5R3: NADH- cytochrome b5 reductase
NEB: New England Biolabs

NTR: Nuclear transport receptor
OCIAD1: OCIA domain-containing protein 1
OCTN3: Organic Cation Transporter 3
OPA1: Optic atrophy type 1
OPT2: Oligopeptide transporter 2
ORF: Open reading frame
OXPHOS: Oxidative phosphorylation
pAb: Polyclonal antibody
PAFAH2: Platelet Activating Factor Acetylhydrolase 2
PBDs: Peroxisome Biogenesis Disorders
PBS: Phosphate-buffered saline
PBST: Phosphate-buffered saline with Tween 20
PC1: Principal component-1
PCR: Polymerase chain reaction
PDCD6: Programmed cell death 6
PDI: Protein disulfide isomerase
PDL: Poly-D-Lysine
PEG: Polyethyleneglycol
PEX: Peroxin
PFA: Paraformaldehyde
PHYH: Phytanoyl-CoA 2-Hydroxylase
PMP70: Peroxisomal membrane protein 70
PMSF: Phenylmethylsulfonyl fluoride
PMVK: Phosphomevalonate Kinase
PNPLA8: Patatin Like Phospholipase Domain Containing 8
PNS: Post-nuclear supernatant
PPARα: Peroxisome proliferator-activated receptor α
PRDX4: Peroxiredoxin 4
PTS: Peroxisome targeting signal
PVDF: Polyvinylidene fluoride
RAB: Ras-associated binding
RHOA: Ras homolog family member A
ROS: Reactive oxygen species
Rpm: Rounds Per Minute
RT: Room temperature
SAR1b: Secretion Associated Ras Related GTPase 1B
Scp2: Sterol carrier protein 2
SDS: Sodium dodecyl sulfate
SEC: Secretory
SERHL2: Serine Hydrolase Like 2
SGPL1: Sphingosine-1-Phosphate Lyase 1
SLC25A17: Solute carrier family 25 member 17
SNARE: Soluble N-ethylmaleimide-sensitive-factor
attachment protein receptor
SODM: Superoxide dismutase
SRM: Selected reaction monitoring
SSBP1: Single-stranded DNA-binding protein
SWATH-MS: Sequential Window Acquisition of all Theoretical Mass Spectra
TACO1: Translational Activator of Cytochrome C Oxidase I
TAPVC: Total anomalous pulmonary venous connection
TBS: Tris-buffered saline
THCA: Tetrahydrocannabinolic acid
THIL: Thiamine phosphate kinase
Tm: Melting temperature
Tmem: Transmembrane Protein
TOMM20: The outer mitochondrial membrane complex subunit 20
TVBE: Tris Borate EDTA
UGT1A1: Uridine diphosphate glucuronosyltransferase 1A1 gene
V: volt
VAPB: Vesicle-associated membrane protein B
VDAC1: Voltage dependent anion channel protein
VLCFA: Very long chain fatty acid
W: watt
WB: Western Blot
X-ALD: X-linked Adrenoleukodystrophy
ZS: Zellweger Syndrome

1 INTRODUCTION

1.1 Peroxisomes-an overview

In 1954, Johannes Rhodin introduced the term "microbody" to describe a particular class of cytoplasmic, vesicular bodies found in the convoluted tubule cells of the mouse kidney, which are distinguished by a single membrane and a homogenous, granular matrix. Two years later, Rouiller et al. (1956) suggested that these microbodies might be the precursors of mitochondria, but somewhat later, the identification of oxidoreductases like urate oxidase, D-amino acid oxidase, and catalase in microbodies sparked the hypothesis that they are a distinct organelle, which plays an essential role in hydrogen peroxide metabolism. Since the microbodies' functions also differed significantly from those of mitochondria, lysosomes, or the endoplasmic reticulum, Christian De Duve introduced the term peroxisome for this apparently novel organelle (De Duve and Baudhuin, 1966).

1.1.1 Metabolic functions of peroxisomes

Peroxisomes are key or essential cellular organelles performing various metabolic functions. Their main functions are the oxidative breakdown of fatty acids and amino acids, but they also detoxify harmful substances, such as alcohol, by converting them into less toxic derivatives. Additionally, they are involved in the synthesis of distinct lipid species and the breakdown of hydrogen peroxide, a toxic byproduct produced by their oxidases (Islinger et al., 2018).

The most noted key function of peroxisomes is the β-oxidation of fatty acids, a process that differs from its mitochondrial counterpart mainly by the use of acyl-CoA oxidases instead of dehydrogenases in the first step of the pathway and the inability to break down fatty acids to completeness. While mitochondria can fully degrade fatty acids into acetyl-CoA units, which then enter the Krebs cycle to be converted into CO2, H2O, and ATP, peroxisomes lack a comparable cycle and cannot pass the FADH2 produced during β-oxidation to OXPHOS complexes. As a consequence, peroxisomes only shorten fatty acid chains to octanoic acid and then pass their β-oxidation byproducts to mitochondria for full degradation, in order to maximize ATP generation (Wanders et al., 2001). In contrast to mitochondria, peroxisomes are able to metabolize very long-chain fatty acids (VLCFAs) like hexacosanoic acid (C26), methyl-branched fatty acids

like phytanic acid, and bile acid intermediates such as DHCA and THCA. Peroxisomal β-oxidation also plays a role in producing omega-3 polyunsaturated fatty acids, like docosahexaenoic acid from linolenic acid, in cooperation with the ER (Wanders 2004). The machinery for fatty acid β-oxidation in peroxisomes consists of three distinct acyl-CoA oxidases (ACOX1, -2, and -3), two multifunctional enzymes that facilitate the second and third steps of β-oxidation, and two 3-ketothiolases (Wanders et al., 2023).

Ether lipids constitute a unique group of phospholipids distinguished by an ether bond at the sn-1 location of the glycerol backbone. A specific subset with an unsaturated fatty acid at the sn-2 position is termed plasmalogens and those are essential component of various human tissues, such as brain myelin, heart muscle, skeletal muscle, and kidneys (Wanders et al., 2023). The enzymes responsible for the initial steps of the synthesis pathway, an alkyl dihydroxyacetone phosphate (ADHAP) synthase and an alkylglycerone phosphate (AGP) synthase, are uniquely situated within peroxisomes, making these cellular compartments indispensable for ether lipid synthesis (Singh et al., 1993). The synthesis of etherphospholipids involves a collaborative process between peroxisomes and the ER. The product of the AGPS reaction, alkyl-DHAP, is either reduced directly at peroxisomes to 1-O-alkyl-glycerol-3-phophate or transferred to the ER, where the correspondent acyl/alkyl DHAP reductase is located as well (Dean and Lodhi, 2017). All subsequent processes for synthesizing plasmanyl- and plasmenyl-(phospho)lipids take place at the membrane of the ER. The long-chain alcohol, which is exchanged with the acyl-group of acyl-DHAP by AGPS is also supplied by specific enzymes located at the peroxisome – the two distinct acyl-CoA reductases FAR1 or FAR2, which are rate-limiting for the pathway (Honsho and Fujiki, 2023).

Peroxisomes play a dual role in managing reactive oxygen species (ROS) homeostasis, highly unstable molecules that can oxidize and thus harm cellular structures like DNA, proteins, and fats. While ROS are generated as side-products during peroxisomal oxidase activities such as the beta-oxidation of fatty acids, peroxisomes also house an array of enzymes with antioxidant properties – such as catalase, superoxide dismutase, and peroxiredoxins – to neutralize these harmful molecules (Lismont et al., 2019). While excess ROS concentrations are a threat to the cellular environment, less reactive ROS like H_2O_2 can also act as signaling molecules,

e.g. by inducing disulfide bridge formation in proteins (Lismont et al., 2019). Hence, maintaining a balance between ROS generation and neutralization is crucial for cellular stability, and any imbalance can lead to various health issues like neurodegenerative diseases, cancer, and the aging process. As such, the control of ROS metabolism within peroxisomes might be a key aspect of their biological function (Wanders et al., 2023).

In addition to their contribution to lipid and ROS homeostasis, peroxisomes house enzymes that participate in the metabolic processing of several further substances, such as purines, polyamines, and bile acids. As a result, peroxisomes feature a broad range of enzymes essential for their biological roles (Kamoshita et al., 2022).

1.2 Peroxisome biogenesis

Peroxisome biogenesis is a complex and tightly regulated cellular process that involves the formation and maintenance of peroxisomes in order to tightly control their cellular number (Novikoff and Shin, 1964). After the initial biological and biochemical characterization of peroxisomes, two distinct models of peroxisomal biogenesis were proposed (De Duve and Baudhin, 1966).

1. *De novo* biogenesis: In this model, peroxisomes are formed anew from the ER. Lipid bilayers and specific proteins bud off from specialized regions of the ER to form a pre-peroxisomal vesicle, which then matures into a fully functional peroxisome (Tabak et al., 2003). This model became more evident when Hoepfner et al. (2005) presented convincing findings in yeast, supporting the idea of a peroxisome maturation pathway that originates from the ER.
2. Biogenesis by growth and division: Existing peroxisomes can also divide to create new peroxisomes, a process known as fission. A mature peroxisome elongates by membrane expansion and then divides into two (or more) daughter peroxisomes (Lazarow and Fujiki, 1985).

Regardless of the model, several steps are common to both peroxisome biogenesis pathways:

- Protein import: Peroxisomal matrix proteins are synthesized in the cytoplasm and transported into the peroxisome. These proteins usually have specific

targeting signals, known as peroxisomal targeting signal 1 (PTS1) or peroxisomal targeting signal 2 (PTS2), which are recognized by receptors that facilitate their transport.

- Membrane protein insertion: Peroxisomal membrane proteins are incorporated into the membrane either post-translationally or co-translationally. Some of these proteins may traffic via the ER, especially in the *de novo* biogenesis model.
- Functional maturation: After the initial formation, peroxisomes need to mature to become functional. This involves the import of additional matrix and membrane proteins, as well as lipids that are required for the organelle to carry out its metabolic functions.
- Quality control: Damaged or dysfunctional peroxisomes are typically targeted for degradation via a specific autophagy pathway known as pexophagy.
- Regulation of abundance: Peroxisome numbers and activity are tightly regulated according to the cell's metabolic needs, usually through a combination of transcriptional control and post-translational modifications (Wanders et al., 2023).

Unlike mitochondria and chloroplasts, peroxisomes lack DNA, and their matrix proteins are synthesized in the cytoplasm by ribosomes before being imported post-translationally as fully folded proteins (Walton et al., 1995). After reaching the membrane, these proteins are either imported into the peroxisome matrix or integrated into the lipid bilayer and organized into functional complexes. (Lazarow and Fujiki, 1985; Wanders et al., 2023).

Peroxisome biogenesis relies on peroxins, proteins found within the organelle membrane or in the cytosol. The biogenesis defects caused by the absence or malfunction of peroxins lead to peroxisome dysfunction, causing severe metabolic issues with a drastic prognosis for the patients' survival. Peroxins collaborate to support peroxisome formation, encompassing tasks like protein and lipid import into the organelle, pre-existing peroxisome division, and the regulation of peroxisome size and quantity (Farr et al., 2016). In summary, peroxisome biogenesis is a multifaceted process involving the coordinated action of numerous proteins, lipids, and cellular mechanisms.

1.3 Interaction of peroxisomes with other subcellular compartments

In order to perform their metabolic functions effectively, peroxisomes need ongoing collaboration with other cellular compartments such as lipid droplets, lysosomes, the ER, and mitochondria. Various mechanisms, such as signal transduction pathways, vesicular trafficking, and membrane contact sites, facilitate this essential interaction between peroxisomes and other subcellular structures (Wanders et al., 2023). For instance, peroxisomes cooperate with lipid droplets to break down fatty acids and synthesize ether lipids (Binns et al., 2006). They also interact with lysosomes to break down complex lipids and recycle their components (Chu et al., 2015).

A key mechanism of interaction between peroxisomes and other cellular organelles is the establishment of membrane contact sites between two organelles. These contact sites enable the transfer of lipids, metabolites, and signaling compounds such as hormones, growth factors, and cytokines between different organelles (Islinger et al., 2018). The most frequent crosstalk occurs between peroxisomes, ER, and mitochondria, although the underlying mechanisms and functional relevance are not yet fully understood. Peroxisome-ER contacts are supposed to be involved in the transport of ether phospholipid intermediates and DHA precursors; moreover, the ER was reported to assist in the transport of a subset of membrane proteins to peroxisomes, as well as in the formation of new peroxisomes by *de novo* biogenesis (Schrader et al., 2020).

The interaction of peroxisomes with other organelles via vesicular trafficking involves the transport of cargo molecules in vesicles that bud off from one organelle and fuse with another. For example, peroxisomes were shown to receive proteins and lipids from the ER via vesicular trafficking and can also transfer metabolites to lysosomes for degradation (Agrawal and Subramani, 2013).

Additionally, peroxisomes engage with mitochondria to manage the generation and neutralization of ROS as well as to partake in amino acid and fatty acid metabolism (Lismont et al., 2015). Thus, the interplay between peroxisomes and these various subcellular compartments is critical for both the effective operation of peroxisomes and overall cellular homeostasis (Islinger et al., 2018).

The research on membrane contact sites and interactions between organelles is an emerging field, with significant potential for discoveries of components, functions, and regulatory mechanisms. Current research has already identified several proteins and enzymes that facilitate contacts between peroxisomes and other organelles. For example, in yeast, proteins like Inp1, Pex3, Pex30, and Pex34 were shown to play roles in physically connecting peroxisomes with the ER and mitochondria. In mammals, ABC transporter proteins like ABCD1-3 are essential for fatty acid uptake into peroxisomes. A recent publication reported that spastin interacts with ABCD1 thereby connecting lipid droplets with peroxisomes in order to streamline fatty acid transport between both organelles (Chang et al., 2019). Additional proteins like OCTN3, MCT1/2, Opt2, PMP52 (Tmem135), and PMP24 (PxmP4) are also supposed to play roles in peroxisomal interactions with other organelles (Islinger et al., 2018). Nevertheless, it is important to note that our understanding of peroxisomal membrane contact sites is still advancing, with new proteins and functions likely to be identified in the future.

1.3.1 ACBD5 as a mediator for PO-ER tethering complex

A membrane-tethering complex is a set of particular proteins that help to bring membranes of cellular organelles in close proximity by protein-protein or protein-lipid interaction while preventing the organelles from fusing (Prinz, 2014). This enables various cellular processes such as the exchange of lipids, ions, or other molecules, as well as the initiation of membrane fusion events involving an additional molecular machinery like the SNARE proteins (Scorrano et al., 2019). In this context, the interaction between peroxisomes and the ER is essential for various cellular functions including lipid metabolism, detoxification processes, and even organelle biogenesis. This interaction is facilitated by membrane contact sites, shared enzymatic functions, and the exchange of essential lipids and proteins (Scorrano et al., 2019).

The discovery of membrane-tethering complexes has largely been a result of advances in cellular biology and microscopy (Prinz, 2014). Studies in membrane trafficking, organelle biogenesis, and intracellular communication have led to the identification of such complexes (Farré et al., 2019). Various experimental techniques such as fluorescence microscopy, electron microscopy, and co-immunoprecipitation tests were utilized to study and elucidate the roles of these complexes. Membrane-tethering

complexes have been discovered in multiple cellular locations, including the Golgi complex, ER, mitochondria, peroxisomes, and endosomes.

Peroxisomes and ER form frequent physical connections first described in early ultrastructural studies, which realized that both organelles are often in close proximity to each other (Novikoff and Shin, 1964; Reddy and Svoboda, 1972). Moreover, later a more recent study observed that the movements of adjacent peroxisome and ER tubules are coordinated. Specifically, peroxisomes appear to align with and track the movement of nearby ER tubules suggesting that both organelles are bridged by a physical connection (Barton et al., 2013). In two parallel studies, Costello et al. (2017) and Hua et al. (2017) discovered the same peroxisome-ER tethering complex in mammalian cells by conducting complementary experimental settings. Both groups reported that peroxisome-ER tethering complexes were facilitated by interactions between the ER membrane protein VAPB and the peroxisomal proteins ACBD4 and ACBD5, respectively. In detail, VAPB and as well VAPA bind via their MSP domain to a conserved FFAT (two phenylalanines in an acidic tract) motif found in ACBD4 and ACBD5 (Figure 1-1). The absence of ACBD5 has been shown to significantly diminish the number of membrane contacts between peroxisomes and the ER (Darwisch et al., 2020; Costello et al., 2023). Moreover, it leads to an accumulation of VLCFAs (Ferdinandusse et al., 2017; Darwisch et al., 2020), which highlights the crucial role that this tethering complex plays in lipid metabolism.

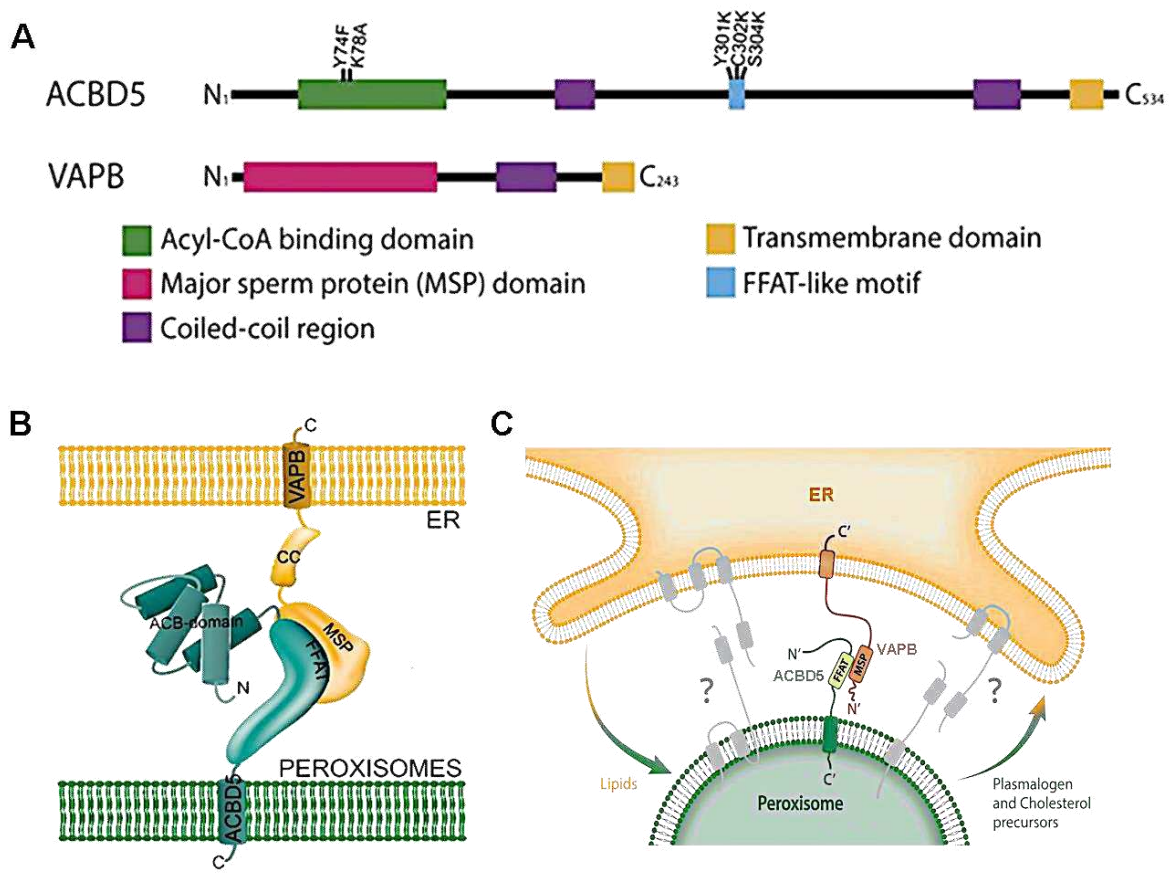

Figure 1-1: Schematic drawing of ACBD5 and VAPB

(A) Domain structures of VAPB and ACBD5. Mutations in acyl-CoA binding and FFAT-like motifs, which lead to a disruption of the domains' function, are indicated. (B) The interaction between ACBD5 and VAPB is facilitated by the FFAT motif in ACBD5 and the MSP domain in the VAPB protein. Taken from (Costello et al., 2017). (C) Both ACBD5 and VAPB proteins are anchored to the membranes of peroxisomes and the ER, respectively, via a transmembrane domain situated at their C-terminal ends, while their N-termini-bearing functional domains are exposed to the cytoplasm. This connection potentially allows for the transfer of lipids from the ER to peroxisomes, aiding in the expansion and growth of the peroxisomal membrane. It may also facilitate the transport of plasmalogens and cholesterol precursors from peroxisomes back to the ER. Likely, there are additional unidentified tethering complexes yet to be discovered (indicated by proteins drawn in gray). Modified from (Schuldiner et al., 2017).

1.4 Peroxisomal Protein Import and targeting sequences

The peroxisomal matrix enzymes are translated by polyribosomes and translocated into the peroxisomal matrix according to specific targeting signals, which are recognized by cytosolic receptors. (Lazarow and Fujiki, 1985). The import process can be divided

into four steps: (a) cargo recognition in the cytosol, (b) docking of the cargo-loaded receptor to distinct proteins at the peroxisomal membrane, (c) translocation across the peroxisomal membrane, and (d) export of the receptor back to the cytosol (Girzalsky et al. 2010).

Initially, it was suggested that the process of cargo translocation into peroxisomes is similar to pinocytosis, a process in which cells engulf fluids and particles from the extracellular environment. According to this model, the cargo-receptor complex is taken up by the peroxisome in a vesicle-like structure, similar to endocytosis. Once the vesicle is inside the peroxisome, it fuses with the peroxisomal membrane, releasing the cargo protein into the peroxisomal lumen. The import receptors are then recycled and returned to the cytosol (McNew and Goodman, 1996). In the 1990s, this model has been replaced by the “transient pore” model (Erdmann and Schliebs, 2005).

Generally, most matrix proteins are transported into peroxisomes using a C-terminal PTS1, typically featuring a C-terminal tripeptide such as SKL, along with adjacent auxiliary residues (Gould et al., 1987; Swinkels et al., 1992; Kragler et al., 1998; Lametschwandtner et al., 1998). This targeting signal was initially identified in the luciferase from the firefly Photinus pyralis, which localizes to peroxisomes and triggers bioluminescence (Gould et al., 1987; Keller et al., 1987). While the majority of peroxisomal matrix proteins carry a C-terminal PTS1 signal, a few possess an N-terminal PTS2 signal (Léon et al., 2006). The ability to predict a protein's correct subcellular location based solely on its amino acid sequence represents a significant advancement in modern biology. However, while stringent consensus sequences for PTS1 have been established, PTS2 sequences are too poorly conserved to be reliably predicted (Kunze, 2022).

In the “transient pore” model, the soluble receptors PEX5 and PEX7, which are found in the cytosol, recognize peroxisomal matrix proteins containing PTS1 and PTS2 respectively. Once PEX5/7 binds to a PTS1/2-containing protein in the cytosol, it forms a cargo-receptor complex. This complex is transported along the cytoskeleton to the peroxisomal membrane. At the peroxisomal membrane, these receptors interact with peroxisomal membrane proteins, namely PEX13 and PEX14, which serve as docking sites for the cargo-receptor complex (Erdmann and Schliebs, 2005). Subsequently, PEX5 proteins change their conformation to insert into the peroxisome membrane to

form an aqueous pore through which the nascent matrix protein is imported into the peroxisome matrix (Rudowitz and Erdmann, 2023).

In 2022, Rapoport and colleagues (Gao et al., 2022) proposed a new model based on their experimental findings that peroxisomal import occurs through a nuclear pore-like phase. The authors observed that multiple copies of a cohesive domain from the peroxisomal protein PEX13 form a dense hydrogel-like meshwork within the peroxisome membrane, which allows mobile import receptors to diffuse through this barrier and bring bound cargo along (Gao et al., 2022; Figure 1-2).

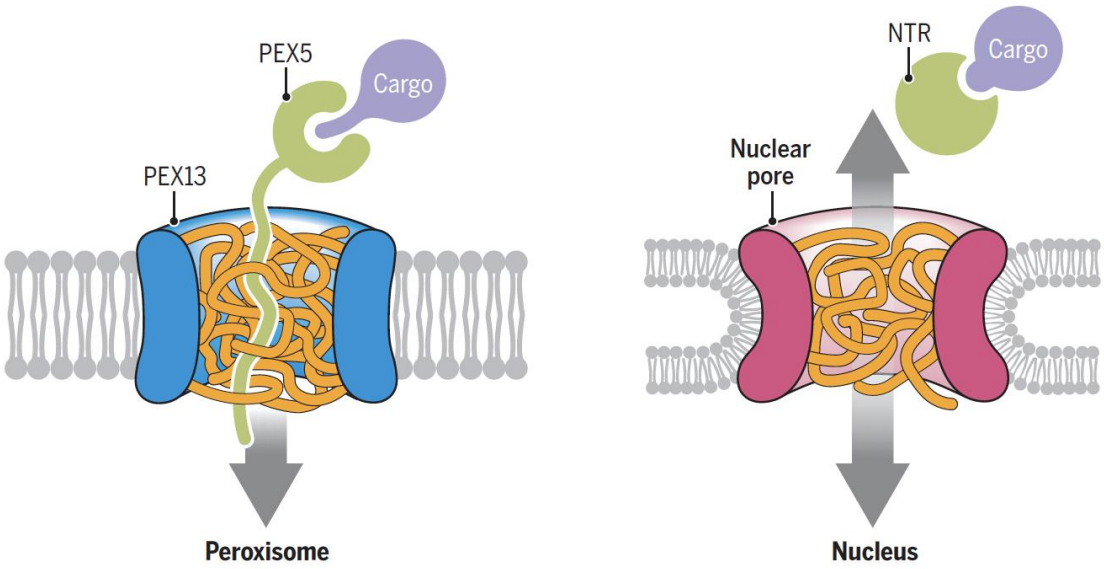

Figure 1-2: Peroxisomal protein import resembles nuclear transport.

Within the peroxisomal membrane, the YG domain of PEX13 proteins forms a dense meshwork structure. This meshwork serves as a pathway, allowing the import receptor PEX5 to move selectively and transport its cargo into the peroxisome. This mechanism resembles how a nuclear transport receptor (NTR) navigates through the FG meshwork within a nuclear pore (Taken from Gao et al., 2022).

The FG-repeat domain of nucleoporins forms a hydrogel-like meshwork that acts as a selective barrier to transport through the nuclear pore complex. The meshwork excludes large molecules while allowing small molecules and transport receptors to pass through. The authors recognized that the YG domain of PEX13 shares structural similarities with the FG-repeat domain of nucleoporins, such as the preponderance of aromatic amino acids and short linkers enriched in small residues. Thus, the YG domain of PEX13 can form a hydrogel-like meshwork similar to the FG-repeat domain

of nucleoporins. They also showed that the YG domain is necessary and sufficient for gelation (Gao et al., 2022; Figure 1-3).

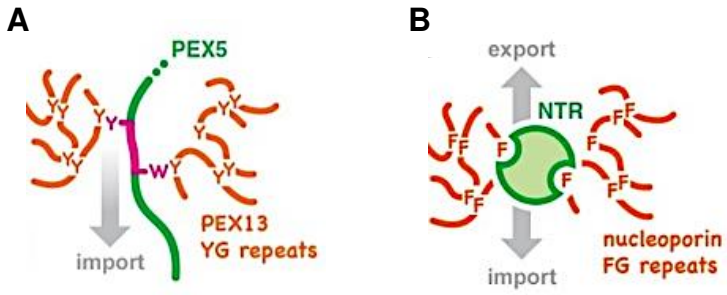

Figure 1-3: Hydrogel-like pore model of peroxisomal matrix protein import.

(A) This scheme shows the scaffold (in yellow) of the nuclear pore complex, which contains a mesh of nucleoporin FG domains (in orange). Notably, the nuclear pore complex is situated outside the lipid bilayer, unlike the peroxisomal pore, which is embedded within it. (B) NTRs utilize hydrophobic pockets and areas within their folded structures to integrate into the FG meshwork, allowing them to move through the nuclear pore by diffusion (Taken from Gao et al., 2022).

1.5 Peroxisome Disorders

Peroxisomal diseases or peroxisome disorders are a group of more than 20 different inherited disorders caused by pathogenic variants in more than 30 distinct genes that result in dysfunction or defects in peroxisomes. These disorders can manifest with a wide range of symptoms and severity, and they are often characterized by the accumulation of toxic substances in the body due to impaired peroxisomal function. The peroxisomal diseases are typically classified into two main groups: peroxisome biogenesis disorders (PBDs) and peroxisomal single enzyme deficiencies (PEDs) (Wanders et al., 2023).

PBDs are characterized by defects in genes required for the biogenesis and protein import of peroxisomes. Hence, PBDs result from mutations in genes encoding peroxins (PEX genes) involved in peroxisome assembly and function. There are major subtypes of PBDs: Zellweger Syndrome (ZS), Neonatal Adrenoleukodystrophy (NALD), and Infantile Refsum Disease (IRD). These disorders are characterized by the accumulation of toxic metabolites resulting from the impaired breakdown of fatty acids,

leading to neurological defects, liver dysfunction, and early mortality. In addition, peroxisomal dysfunction has been implicated in the pathogenesis of other diseases, such as diabetes, obesity, cancer, and age-related disorders, although the underlying mechanisms are not fully understood (Islinger et al., 2018).

In contrast to PBDs, PEDs originate from the dysfunction of specific enzymes within peroxisomes. Accordingly, PEDs are caused by mutations in genes encoding individual peroxisomal enzymes and include disorders such as X-linked adrenoleukodystrophy (X-ALD), Acyl-CoA oxidase deficiency (Pseudo-neonatal Adrenoleukodystrophy) or D-bifunctional protein deficiency (DBP Deficiency). X-ALD primarily affects the transport of very long-chain fatty acids (VLCFA) into peroxisomes and is characterized by defects in the ABCD1 gene. The rare disorder Acyl-CoA oxidase deficiency results from a deficiency in ACOX1, an enzyme involved in very long-chain fatty acid β-oxidation. DBP deficiency affects also the breakdown of VLCFA and certain amino acids and is caused by mutations in the HSD17B4 gene (Islinger et al., 2018; Wanders et al., 2023).

The symptoms of peroxisomal diseases can vary widely but often include developmental delays, intellectual disabilities, neurological abnormalities, skeletal deformities, liver dysfunction, and vision problems. Diagnosis typically involves genetic testing and biochemical analysis. Treatment options for these diseases are limited and often focus on managing symptoms and complications (Wanders et al., 2023).

It is important to note that peroxisomal disorders are extremely rare, and each subtype has its own specific genetic basis and clinical characteristics. Scientists are actively researching these disorders to gain deeper insights into their underlying mechanisms and to explore potential treatments (Wanders et al., 2023). Therefore, enhancing our understanding of genetic anomalies and uncovering the functions of proteins within peroxisomes plays a crucial role in the diagnosis and possible therapy of individual peroxisome disorders.

1.6 Peroxisomes in the liver

In mammals, the liver contains the largest number of peroxisomes, constituting approximately 2% of the liver's total volume. Peroxisomal functions have been extensively studied in the liver due to the availability of a large amount of tissue for

research (De Duve and Baudhuin,1966). Hepatocytes are not only commonly recognized for having a greater quantity of peroxisomes, but peroxisomes are also larger in size compared to those in other cell types like neural cells (Lazarow and Moser, 1995). Like in other cell types, the primary functions of peroxisomes in liver cells include α- and β-oxidation, as well as the synthesis of ether lipids (Van Veldhoven, 2010). In addition, hepatocyte peroxisomes contribute to the synthesis of bile acids, a pathway, which is absent in peroxisomes from other cell types (Islinger et al., 2010).

The liver phenotype of peroxisome diseases is most noticeable in patients with peroxisomal single enzyme deficiencies or in mouse models, which exhibit a deficiency in peroxisomal β-oxidation. So far, seven diseases caused by defects in peroxisomal β-oxidation enzymes or auxiliary proteins have been identified, but not all of them lead to liver disease (Baes and Van Veldhoven, 2016). However, it's important to note that liver problems resulting from defective peroxisomal β-oxidation can be life-threatening, as demonstrated by a single patient with ABCD3 deficiency (also known as PMP70), who experienced massive hepatosplenomegaly at the age of 1.5 years (Ferdinandusse et al., 2015).

Studies on liver pathology in both PBDs and single enzyme defects have been comprehensive. Roels and colleagues examined mouse models with hepatocytes lacking PEX5 or PEX2 and observed alterations in mitochondria and the ER, as well as the accumulation of lipids. Importantly, these changes occurred in parallel with the loss of functional peroxisomes, underscoring the interdependence of peroxisomes and other cellular compartments. However, similar to the limited morphological changes observed in mice deficient in single peroxisomal enzymes, few molecular and subcellular alterations were reported (Depreter and Roels, 2003). Notably, peroxisome proliferation and the induction of PPARα target genes were observed to varying degrees under normal conditions. This phenomenon is consistent with the accumulation of unmetabolized substrates of peroxisomal β-oxidation, which activate PPARα, and mirrors observations in the livers of other PBD models (Baes and Van Veldhoven, 2016).

Given the liver's central role in metabolism, detoxification, and other critical physiological processes, peroxisomes in liver cells are pivotal for maintaining overall

body homeostasis (De Duve and Baudhuin,1966). Of note, pathologic alterations are in liver-specific Pex5 knockout (KO) mice are more severe in neural tissue than in the organ itself underlining the central role of liver peroxisomes in general lipid homeostasis (Krysko et al., 2007).

1.7 Peroxisomes in the heart

Peroxisomes might have specialized functions in cardiomyocytes that contribute to the overall cardiovascular health and function of the heart. Also in cardiomyocytes, fatty acid β-oxidation occurs in two distinct locations: the mitochondrion and the peroxisome. Accumulation of fatty acids in the heart can overwhelm the mitochondrial oxidation system, leading to mitochondrial dysfunction, reduced ATP production, and excessive ROS generation (Lopaschuk et al., 2010). To date, research on heart pathologies has primarily concentrated on mitochondrial dysfunction. Even though peroxisomes are also involved in ROS metabolism and lipid degradation, they have received considerably less attention in studies exploring the biochemical and molecular processes underlying cardiac dysfunction but might hold the potential to be a novel target for regulating cardiac metabolism (Colasante et al., 2015).

Cardiac pathologies may be underestimated in severe peroxisomal disorders due to the short lifespan of the patients, who suffer primarily from neural defects. However, milder peroxisomal disorders can manifest with heart anomalies. For instance, adult Refsum's disease, caused by defects in PEX7 or PHYH genes, can lead to tachycardia, heart enlargement, and cardiac insufficiency in adults (Grings et al., 2012). In addition, the Pex5 KO mouse model showed mitochondrial dysfunction in various organs, including the heart (Baumgart et al., 2001). Another model, the Scp2 KO mouse, displayed cardiac issues when fed a phytol-rich diet, possibly linked to phytanic acid accumulation (Seedorf et al., 1998; Monnig et al., 2004). Pex7 KO and PHYH KO mice, mimic peroxisomal defects seen in adult Refsum's disease patients. These mice had reduced plasmalogen levels and accumulated phytanic acid, however, no clear cardiac defects have been reported (Brites et al., 2003; da Silva et al., 2012). In summary, peroxisomal disorders can have varying effects on the heart affecting cardiac function through mechanisms like mitochondrial dysfunction and lipid accumulation causing heart anomalies to different extents.

Due to their small size and distribution, peroxisomes in the heart were initially challenging to identify but were eventually detected in the ventricular myocardium of rats, mice, and guinea pigs using alkaline DAB staining (Fahimi and Herzog, 1974; Hicks and Fahimi, 1977). These peroxisomes are oval-shaped and often found near mitochondria, lipid droplets, and most strikingly the junctional sarcoplasmic reticulum. They appear to play, like in other organs, a role in fatty acid β-oxidation, particularly palmitoyl-CoA oxidation, although their activity in the heart is considerably lower than in the liver (Kvannes et al., 1994).

It was also suggested that peroxisomes might have a cardio-protective role. Studies in mice fed an ethanol-rich diet showed increased catalase activity and peroxisome numbers in heart tissue, suggesting that peroxisomal catalase contributes to maintaining heart function under stress. Inhibition of catalase activity resulted in heart tissue damage (Fahimi et al., 1979). In addition to catalase, peroxisomes in cardiomyocytes also contain further antioxidative enzymes that protect against oxidative stress (Karnati et al., 2013). Additionally, peroxisomes may prevent an overload of mitochondrial β-oxidation by degrading excess fatty acids that accumulate under pathological conditions, contributing to cardiac health (Liepinsh et al., 2013). Hence, while there is clear evidence that peroxisomes play an important role in cardiomyocyte physiology with respect to patients and KO mouse models, our knowledge of their specific role and metabolic functions in the heart is still scarcely explored.

1.8 Isolation of peroxisome fractions enriched in ER contact sites from mouse liver

A three-step isolation procedure is commonly used for isolating peroxisomes from soft tissues. The process involves mild tissue homogenization, a series of differential centrifugations, and a final step using a density gradient. Although peroxisomes from the liver and kidney have been extensively studied and characterized, the isolation of peroxisomes from these tissues is still relevant in current methods compilations. Peroxisome fractions from these tissues maintain higher purity levels compared to those from other tissues and cell cultures, making them essential as a gold standard for localizing newly identified, ubiquitously expressed peroxisomal proteins (Manders and Islinger, 2017).

A variety of different protocols has been used so far to obtain well-preserved peroxisomes in the highest possible purity. Several earlier purification protocols rely on the use of metrizamide, a tri-iodinated benzamido-derivative of glucose that has a low osmolality and low viscosity. By using metrizamide, peroxisomes have been isolated from the liver and kidney of mammals with purities >90% (Rickwood, 1975; Völkl and Fahimi 1985; Zaar et al., 1986). In the purification protocol used in this thesis, metrizamide was replaced by the non-sugar-based benzamido-derivative iodixanol (OptiPrep), which is more stable, less toxic, and exhibits significantly less interference with biological compounds. Based on previous publications from the work group (Manner and Islinger, 2017), the optimal density of the Optiprep step gradient ranges from 1.09 g/ml to 1.23 g/ml. In this purification protocol, a density gradient of sigmoidal shape is used in contrast to the more common linear density gradients. Such a gradient with a sigmoidal profile leads to a steep density incline in the central part of the gradient but shallow profiles in the top and bottom regions. To this end, the gradient guarantees a maximum separation distance between the highly dense peroxisomes and the lighter mitochondria and microsomes, which are held back in the upper part of the gradient thus facilitating the isolation of peroxisomes with a purity above 90 % from the so-called light mitochondrial fraction (LM) (Völkl and Fahimi, 1985). Of note, peroxisomes assemble in two distinct layers (LM1=1.20g/ml and LM2=1.18 g/ml) which differ slightly in their degree of mitochondrial contamination (Islinger et al., 2006; Figure 1-4). In this work, this purification protocol was modified to isolate peroxisomes from different prefractions from the differential centrifugation in order to unravel if specific protein sets localized at mitochondria and the ER might consistently co-purify with peroxisomes.

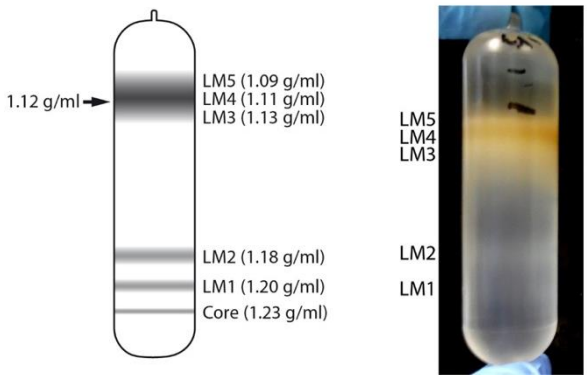

Figure 1-4: Isolation of highly pure peroxisomes from mouse liver.

Scheme and photograph of a typical post-centrifugation sigmoid Optiprep gradient. At the density of 1.12 g/mL (indicated by the arrow), fraction LM from the differential centrifugation

series is layered onto the gradient; after centrifugation, different organelles enrich in clearly distinguishable bands (Islinger et al., 2006).

1.9 Proteomics of Peroxisomes

The identification and thorough characterization of the complete proteome of human peroxisomes is crucial in order to understand the complex and varying phenotypes, which are associated with peroxisomal disorders. In this context, it can build an important fundament for revealing new insights into the functions and control mechanisms associated with peroxisomes, which may lead to new tools for diagnosing and treating individuals affected by peroxisomal disorders.

Nevertheless, comprehensively characterizing the proteome of mammalian peroxisomes involves challenges. Peroxisomes are small organelles with low abundance in cells, and they often have physical interactions with other organelles, which can lead to the contamination of peroxisomal fractions with proteins from other cell compartments. Additionally, some proteins can be localized in both peroxisomes and other organelles, making it difficult to definitively discriminate true peroxisomal proteins from contaminations (Oeljeklaus et al., 2014; Shai et al., 2016).

To address these challenges, various methods have been employed to date. An initial proteomic study enriched peroxisomes from rat liver using density gradient centrifugation and affinity purification with antibodies targeting the peroxisomal membrane protein PMP70 (ABCD3) (Kikuchi et al., 2004). Later studies utilized quantitative mass spectrometry techniques, including label-free and stable isotope labeling approaches (Gronemeyer et al., 2013; Islinger et al., 2007; Jadot et al., 2017; Kikuchi et al., 2004; Wiese et al., 2007). These methods helped distinguish true peroxisomal proteins from contaminants originating from other cell compartments by quantifying the enrichment of individual proteins across the gradient (Yifrach et al., 2018).

Despite these efforts, while these strategies were effective in identifying new peroxisomal proteins, they provide still an incomplete compilation of the peroxisomal proteome. To create a more complete map of protein subcellular localizations in mammalian cells, increasingly advanced proteomic profiling approaches have been

applied to annotate thousands of individual proteins across different density gradient fractions and allocate them to various subcellular compartments. However, a unified and comprehensive list of all peroxisomal proteins has not yet been established, drawing attention to the ongoing research in this area (Yifrach et al., 2018).

The number of newly discovered peroxisomal proteins in proteome studies may be underestimated due to potential categorization errors. Some genuine peroxisomal proteins might have been misclassified as contaminants because they lack a recognized PTS1 or PTS2, have known non-peroxisomal functions, are constituents of other cellular compartments, or were not confirmed by fluorescence microscopy due to stability issues or conditional peroxisomal targeting (Pan and Hu, 2018).

Challenges in peroxisome proteome studies include detecting membrane proteins, identifying post-translational modifications, capturing proteins with very low abundance, and temporarily targeting peroxisomes under specific conditions. To this end, peroxisome isolation protocols should be improved for higher efficiency and adaptability to different tissues including the heart.

Quantitative isotope-tagging mass spectrometry (MS) methods like LOPIT, ICAT, and iTRAQ have been applied to expand the coverage of peroxisomal proteins and offer accurate quantification of individual peptides between different samples (Reumann, 2011). However, classical shotgun methods with isotopic or chemical labeling are limited in data completeness and reproducibility when analyzing a large number of samples. Hyperplexed Localization of Organelle Proteins by Isotope Tagging (HyperLOPIT) is an advanced proteomics method used to determine the subcellular localization of proteins within a cell or tissue sample. It provides highly detailed information about the organelles or cellular compartments in which proteins are located (Christoforou et al., 2016). However, it is highly cost and labor-intensive. Targeted label-free proteomics strategies like “selected reaction monitoring” (SRM) offer precise quantification but are suitable for a limited number of proteins per measurement. An emerging technology called Sequential Window Acquisition of all Theoretical Mass Spectra (SWATH-MS) relies as well on label-free peptide quantification and promises to be a method that enables the rapid and consistent quantification of thousands of proteins across large sample cohorts without the need for isotopic or chemical labeling

(Wu et al., 2017). SWATH-MS is a variant of data-independent acquisition methods for peptide quantification, in which all ionized peptides in a given M/Z range are fragmented in an unbiased fashion using large M/Z windows. In this respect, DIA methods have the significant advantage of reproducibly identifying and quantifying low-abundant peptides in different samples, which would otherwise be often missed in data-dependent acquisition technologies (Ludwig et al., 2018).

1.10 Objectives of this work

Organelle proteomics studies are essential in order to identify and assign proteins to specific subcellular compartments, thereby providing first insights into their potential functional roles within these compartments (Islinger et al., 2012). In recent years, proteomics technologies have led to the discovery of new proteins associated with peroxisomes, enhancing our understanding of these organelles' functions and biology.

The organelle-focused proteomics benefits from the compatibility of the organelle-enriched samples with current MS-based methods. This compatibility allows for the identification of proteins, including those with low abundance, within organelles (Yifrach et al., 2018). However, the success of organelle proteomics experiments hinges on sample purity and/or accurate protein quantification between distinct samples, as both is critical to accurately distinguish genuine organelle-associated proteins from contaminants. This is especially important because there is increasing evidence that many proteins are present in multiple subcellular compartments (Thul et al., 2017).

To address these issues in peroxisome proteomics and identify new potential peroxisome-associated candidate proteins in the liver and heart, two different quantitative MS-based proteomics approaches in two different tissues were conducted in this thesis. Liver tissue offers relatively easy access to peroxisomes of highest purity (Islinger et al., 2018; Völkl and Fahimi, 1985). This makes it an ideal choice for studying peroxisomes because the presence of contaminants can be minimized, ensuring more accurate results. Since one of the research objectives of this study was to detect low-abundance proteins from peroxisomes, the liver, being a well-characterized organ, provides a controlled environment to focus on the identification of such low-abundant proteins. The SWATH-MS method provides possibility to reproducibly and accurately

quantify low abundant peptides in different samples and was thus used for mouse liver experiments to detect proteins that are typically present in low abundance. In this respect, the SWATH-MS was applied to compare two distinct, highly pure peroxisome fractions with the respective bulk organelle material retained at the upper border of the gradient. Unlike the liver, the peroxisomes in the heart are only poorly characterized and to date were not analyzed by proteomics. In concordance, there is limited knowledge about the functions of peroxisomes in the heart. This presents an opportunity to explore the relatively uncharted territory of so-called micro-peroxisomes, which are found in most cell types, potentially uncovering novel insights into their functions. Moreover, the heart may also contain tissue-specific peroxisome proteins, which may fulfill specialized functions of peroxisomes in cardiac tissue. While several methods for the purification liver peroxisomes have been developed in the past, existing protocols for the purification of heart peroxisome do not fulfill the requirements for a subsequent quantitative MS analysis. Hence, a purification protocol suitable for subsequent proteomics experiments had to be developed in this work. In contrast to the mouse liver experiments, linear density gradients were employed for organelle separation to associate individual proteins to distinct organelle species by a so-called organelle profiling approach. To this end, a Trapped Ion Mobility Spectrometry Time of Flight MS technique (TIMS-TOF) was combined with the data-independent acquisition (DIA) method for protein quantification in order to compare the distribution of all identified proteins across six serial fraction eluted from the gradient.

According to these main objectives, this study provides (1) a comprehensive overview of the peroxisomal proteome of mammalian liver peroxisomes and reveals previously unidentified peroxisomal and peroxisome-related proteins. (2) For the micro-peroxisomes from heart a method for the purification and subsequent proteome analysis was developed and validated by an initial proteomics analysis. The results from this pilot studies provide the basis for a subsequent in-depth bioinformatics data analysis in order to create a valuable reference map for the peroxisomal proteome from this tissue.

2 MATERIAL AND METHODS

For a complete list of all equipment, chemical and biological compounds, buffer recipes, and supplier details please refer to the appendix, under section 9.

2.1 Experimental animals

All mice used for research were sacrificed in accordance with the German Government Commission of Animal Care in compliance with the Heidelberg University, Medical Faculty Mannheim Animal Research Board's guidelines on the care of laboratory animals. The ACBD5-deficient C57BL/6N-A^{tm1Brd} ACBD5$^{tm1a(EUCOMM)\ Wtsi/WtsiCnbc}$ mouse strain (abbreviated with ACBD5 KO) was received as sperm from the European Mouse Mutant Archive (EMMA). To establish the strain in Mannheim, correspondent C57BL/6N female founders were fertilized with the sperms. The heterozygous Acbd5$^{+/-}$ offspring were subsequently crossed and bred to produce homozygous ACBD5 KO and ACBD5 WT (control) strains, respectively. To avoid genetic drifting, the ACBD5 KO and Acbd5 WT strains were crossbred with each other at regular intervals. All animals were fed a standard laboratory diet (food and water were provided ad libitum) and housed under an inverted 12-hour light/dark cycle (light from 8 pm – 8 am) at a temperature of 22±2 °C and a relative humidity of 45 – 65%. Animals were sacrificed by cervical dislocation for the extraction of tissue for biochemical analyses. Every effort was made to keep the number of animals and their suffering to a minimum.

2.2 Peroxisome isolation from mouse liver

Buffer solutions used for peroxisome isolation from mice livers are:

1. Homogenization buffer (HB): 250 mM sucrose, 5 mM MOPS, 1 mM EDTA, 2 mM PMSF, 1 mM DTT, 1 mM ε-aminocaproic acid, pH 7.4 adjusted with KOH.
2. Gradient buffer (GB): 5 mM MOPS, 1 mM EDTA, 2 mM PMSF, 1 mM DTT, 1 mM ε-aminocaproic acid, pH 7.4 adjusted with KOH.

A variety of alternative purification protocols have been used in the past to isolate peroxisomes from liver tissue (Islinger et al., 2018). Highly pure (>90%) and well-preserved peroxisome fractions have been initially obtained by applying metrizamide, a tri-iodinated benzamido-derivative of glucose, as a gradient medium because of its low osmolality and low medium viscosity (Rickwood and Birnie, 1975; Völkl and Fahimi,

1985). In the method used for this thesis, metrizamide was replaced by the non-glucose-based benzamido-derivative iodixanol (Optiprep), which is more stable, less toxic, and exhibits significantly less interference with biological compounds (Graham et al., 1994).

For the density gradients used for the peroxisome isolation from mouse liver in this thesis, Optiprep solutions of 1.09, 1.11, 1.13, 1.18, 1.20, and 1.23 g/mL, were prepared by diluting the 60% Optiprep stock solution (1.32 g/L) with GB. The correct density was finally adjusted by using a refractometer and the formula:

$\rho = 3.350 \times \text{refractive index} - 3.462.$

Subsequently, 4, 3, 6, 7, and 10 mL of the Optiprep solutions were in decreasing order of concentration (1.26-1.12 g/mL) layered on top of each other into 38.5 mL Quick-Seal polypropylene tubes (Beckman Coulter). To convert the step gradient into a sigmoid-shaped density gradient, the tubes were rapidly frozen in liquid nitrogen and kept at 80 °C until further use. By thawing the frozen gradient in a metallic stand on the day of the isolation experiment, a floating ice nucleus produced during the melting process leads to reproducible partial mixing of the step gradient thereby yielding a continuous, sigmoid-shaped gradient profile.

After sacrificing the mice by cervical dislocation, the animals' abdominal cavities were opened, and the liver was carefully removed and rinsed in an ice-cold 0.9% NaCl (w/v) solution. The complete subsequent purification process was carried out on ice using precooled solutions and vessels.

After weight determination, the livers were cut into small pieces and washed with HB. Thereafter, the liver pieces were homogenized in ice-cold HB (ratio of 3 mL buffer/g tissue) using a Potter-Elvehjem tissue grinder at 1000 rpm for 2 minutes performing just one single stroke. To pellet remaining cellular debris and nuclei, the homogenate was centrifuged at 600 g_{av} for 10 min, 4 °C. While keeping the supernatant on ice, the pellet was resuspended in HB and re-homogenized at 1000 rpm by one stroke for 1 min. The 600 g_{av} centrifugation step was repeated and the supernatants from both homogenization steps combined to yield the PNS. Subsequently, HM, which predominantly consists of large mitochondria, was pelleted by centrifuging the PNS at 2700 g_{max} for 10 min, 4 °C. After gentle removal of the supernatant, the HM pellet was

carefully suspended in HB using a glass rod. To increase the peroxisome yield, the HM pellet was resuspended in HB and centrifuged for a second time using the same conditions. In order to gain the peroxisome-enriched LM, the supernatants from both runs were combined and centrifuged at 37,000 g_{max} for 20 min, 4 °C. The LM consists of a mixture of mitochondria, lysosomes, and microsomes but is enriched 3–4 times enriched in peroxisomes, if compared with the PNS. After the 37,000 g_{max} centrifugation, a gel-like, reddish, loosely connected "fluffy" layer can be found at the top of the LM pellet, which will be subsequently abbreviated as FLM (**F**luffy layer of the **LM**). In classic peroxisome isolation protocols, the FLM, which is primarily enriched in microsomes, is normally removed and discarded before the final density gradient separation of the LM (Völkl and Fahimi, 1985). Since the FLM, however, as well contains considerable concentrations of apparently less dense peroxisomes, it was for this work carefully collected and separately purified on an equally shaped density gradient as used for the LM. A second 37,000 g centrifugation step was used to wash the LM pellet and to remove and collect the remaining FLM. For density gradient purification the combined FLM suspension was pelleted by centrifugation at 37,000 g_{max}, 15 minutes, 4 °C. For the final purification on the density gradient, both the LM and FLM pellets were suspended in 5 mL of HB. To obtain the microsomal (MIC) and cytosolic (CYT) fractions shown on immunoblots in this study, the supernatant of the light mitochondrial fraction was centrifuged at 100,000 g_{max} for 30 min, 4 °C. After aspiration of the supernatant CYT fraction, the MIC pellet was resuspended with a glass rod in HB. Subsequently, the LM and FLM fractions were layered on separate 1.12–1.26 g/mL Optiprep gradients and overlaid with GB. A vertical angle rotor (e.g., VTi50, Beckman) was used for centrifugation with an integrated force of $1256 \times 10^6 \times g \times \text{min}$ (g_{max} = 33,000) and gradual acceleration/deceleration at 4 °C. After the centrifugation, three distinct bands can be observed close to the tube's bottom (Figure 2-1). Crystalloid cores from peroxisomes that have been set free from ruptured organelles constitute the lowermost layer. A little above two bands, of intact peroxisomes, can be found. The purest fraction of the gradient, which constitutes more than 95% peroxisomes, is located in the lower band a density of 1.20 g/mL (Islinger et al., 2006). The band above, at 1.18 g/mL, exhibits a slightly higher level of mitochondrial contamination but still contains typically more than 90% of peroxisomes. A syringe with a needle was used to puncture the tubes and to elute each band in order to collect the individual fractions. To concentrate and remove the Optiprep, the

samples from the LM and FLM gradients were diluted at least 3:1 in HB and centrifuged at 37,000 g_{max}, 30 min, 4°C to pellet the organelles. Finally, the organelles were resuspended in a proper volume of HB with a small glass rod in order to obtain a protein concentration above 1 mg/mL. All fractions were maintained frozen until further usage. Protein concentrations of the individual fraction were measured using the Bradford assay.

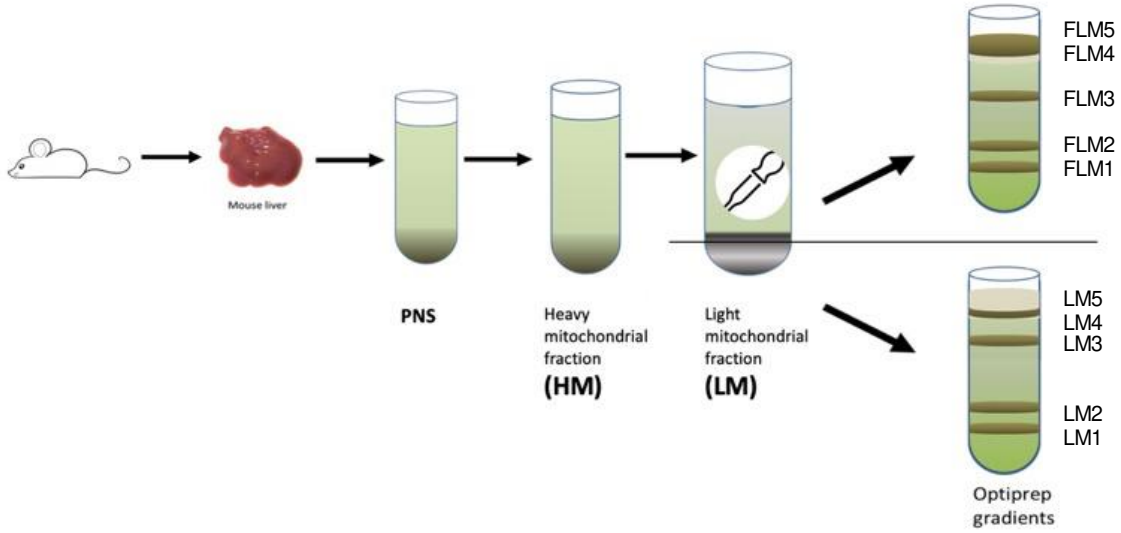

Figure 2-1: Organelles from C57BL6 mice livers were fractionated by a combination of differential and density gradient centrifugation.

A post-nuclear supernatant was produced by 600 × g_{av} centrifugation (PNS). HM was removed by centrifugation at 2,700 × g_{max}. Subsequently, the light mitochondria fraction was separated into a denser LM and a lighter FLM fraction. The supernatant from light mitochondrial fraction was separated into the cytosol and microsomes by centrifugation at 100,000 × g_{max}.

2.2.1 Electrophoresis and in-gel digestion for MS

All samples were heated to 95°C for 5 min and cooled on ice before loading onto NuPAGE 4-12% Bis-Tris Gels (Thermo Fisher Scientific, Waltham, Massachusetts). SDS polyacrylamide gel electrophoresis (SDS-PAGE) was performed according to the manufacturer's specifications. Proteins were fixed within the polyacrylamide matrix by incubating the entire gel in 5% acetic acid in 1:1 (vol/vol) water: methanol for 30 min. After Coomassie staining (60 min) the gel slab was rinsed with water (60 min) and each lane was excised and cut into small pieces.

Subsequently, the proteins were in-gel destained (100mM ammonium bicarbonate/acetonitrile 1:1 (vol/vol)), reduced (10mM DTT), alkylated (50mm Iodoacetamide), and finally Trypsin digested by overnight incubation at 37°C. The generated peptides were collected from the gel pieces, which were further subjected to a peptide extraction step with an acidic (1.5% formic acid) acetonitrile (66%) solution. Both peptides containing samples are combined and dried down in a vacuum centrifuge.

2.2.2 SWATH-MS Method

Dried peptides were redissolved in 0.1 % trifluoroacetic acid and loaded on a C18 column (Kinetex XB-C18, 150 x 0.3 mm; Phenomenex; Torrance, CA, USA) by direct injection using an Eksigent Ekspert NanoLC 425 system (AB Sciex, Framingham, MA, USA). Peptides were then eluted with an aqueous-organic gradient (4%-48% acetonitrile in 0.1% formic acid, in 125 minutes), at a flow rate of 5µl/min and electrosprayed into a TripleTOF 6600+ mass spectrometer (AB Sciex, Framingham, MA, USA). Each scan cycle consisted of one TOF-MS full scan and up to 30 product ion-dependent (IDA) MS/MS scans of the most intense ions. The mass spectrometer was run in the high sensitivity mode and the dynamic exclusion was set to 15 seconds. All analyses were performed in positive ion mode.

To generate the ion library, extracted MS/MS spectra were searched against the reviewed Uniprot mouse database using the ProteinPilot search engine (AB Sciex, Framingham, MA, USA) accepting Cysteine alkylation and common biological modifications. All protein identification experiments were carried out using the corresponding decoy database and a false discovery rate (FDR) of 1%.

The SWATH acquisition was performed for an m/z range 275-1250 Da using looped variable windows isolation. The acquired data were processed with the SWATH Acquisition MicroApp 2.0 in PeakView Software (AB Sciex, Framingham, MA, USA) using a spectral ion library generated from prior data-dependent acquisitions. Protein identification in SWATH was based on the following parameters: 1-4 peptides per protein, 3 transitions per peptide, 99% peptide confidence, 1% FDR, fragment ion extraction window of 5 min, and mass tolerance of 50 ppm.

Protein ion intensity data were imported into MarkerView (AB Sciex, Framingham, MA, USA) to perform normalization. Quantitative MS data was normalized according to the ratios gained from total Coomassie-staining intensities of the individual group samples run on SDS-PAGE and the summarized total MS signals. Group differences were examined using standard t-test.

2.3 Peroxisome isolation from pig heart

Peroxisomes in cardiomyocytes are considerably less abundant than in hepatocytes, are of significantly smaller size, and were therefore historically named microbodies (Herzog and Fahimi 1974, 1976). Hence, for the isolation of peroxisomes from pig hearts, the purification method for mouse liver (described in Section 1.2) had to be modified according to the tissue-specific requirements. To this end, conditions for the homogenization of heart tissue, differential centrifugation steps, and gradient density and slope had to be optimized (see Table 2-2). Initially, for one isolation, 50 (adaptation experiments) or 150 g (proteomics experiments) of fresh pig heart tissue, which was provided from local slaughterhouses, was cut and minced into small pieces. After optimizing the homogenization and isolation procedure (see Tables 2-1 and 2-2 for experimental details), the following protocol was used to obtain the organelle fractions which were characterized by MS-based proteomics. Firstly, 150 g of pig heart tissue was cut into pieces to approximately 12 grams and minced individually. The minced pieces were washed shortly with 1xADS buffer (see Section 9). Since the homogenization of cardiac tissue requires considerably high mechanical forces which can lead to significant disruption of peroxisomes, an enzymatic digestion step was applied prior to homogenization. Therefore, the tissue pieces were incubated for 1 hour at 4°C in a 440 mg collagenase/100 mg Pancreatin (Sigma-Aldrich) solution with 30 rpm rotation to digest the extracellular matrix in order to soften the heart tissue. The supernatant was removed by centrifugation at 300 × g_{max} for 7 min at 4°C. To remove the remaining proteases, this step was repeated after adding 360 mL fresh HB to the tissue pellet. Subsequently, the pellet from the washing centrifugation step was resuspended in 300 mL HB and the heart pieces were homogenized using a Potter-Elvehjem tissue grinder at 1000 rpm for 5 min using 5 strokes. After production of the PNS by centrifugation at 600 x g_{av}, due to the high mitochondrial content of cardiac tissue, the differential centrifugation procedure was adapted for the enrichment of microperoxisomes (optimized centrifugation speeds of 6750 × g_{max} for HM for 10 min

and 48,000 × g_{max} for LM for 20 min, respectively), FLM was not discernible from the LM pellet of heart tissue. The LM fraction was subsequently separated in a comparatively flat, linear 10 - 19% Optiprep density gradient, which was cast into 13.5 mL Quick-Seal polypropylene tubes (Beckman Coulter GmbH). Centrifugation was performed at an integrated force of $1.256 \times 10^6 \times g \times min$ (g_{max} = 33,000) for 1 hour in VTI50 vertical angle rotor using appropriate adapters for the 13.5 mL Quick-Seal tubes. Since the gradient did not produce a separation of specific optically visible bands, the gradient was eluted into 6 equal-sized fractions of 5 mL. For organelle concentration, the eluted fractions were diluted 1:3 in HB and pelleted by centrifugation at 50,000 g_{max}, for 30 min. After centrifugation, the organelle pellets were resuspended in a proper volume of HB with a small glass rod in order to obtain a protein concentration above 1 mg/mL. Comparable to the liver organelle separation procedure, the supernatant of the LM pellet was centrifuged at 100,000 g_{max} for 30 min, 4 °C to obtain MIC and cytosolic CYT fractions. After aspiration of the supernatant CYT fraction, the MIC pellet was resuspended with a glass rod in HB. Protein concentrations of each individual fraction were measured using the Bradford assay. All fractions were maintained at -80 °C until further analysis. In the proteomics analysis, 3 individual isolation experiments were performed.

Table 2-1: Adaptation of tissue preparation

Pre-grinding	Digestion	Homogenization
Tissue cut into small pieces	Not applied	Potter homogenization in HB at 1000 rpm, 5 min, 10 strokes; re-homogenization at 1000 rpm, 2 min, 2 strokes
Tissue minced with meat grinder	Not applied	Potter homogenization in HB at 1000 rpm, 5 min, 10 strokes; re-homogenization at 1000 rpm, 2 min, 2 strokes
Tissue minced with hand blender	Not applied	Potter homogenization in HB at 1000 rpm, 5 min, 5 strokes; re-homogenization at 1000 rpm, 2 min, 2 strokes
Tissue cut into small pieces	440 mg Collagenase/100 mg pancreatin/L ADS buffer, 20 min, 37°C	Potter homogenization in HB at 1000 rpm, 5 min, 5 strokes; re-homogenization at 1000 rpm, 2 min, 2 strokes

Tissue cut into small pieces	440 mg Collagenase/100 mg pancreatin/L ADS buffer, 60 min, RT	Potter homogenization in HB at 1000 rpm, 5 min, 5 strokes; re-homogenization at 1000 rpm, 2 min, 2 strokes
Tissue cut into small pieces	440 mg Collagenase/100 mg pancreatin/L ADS buffer, 60 min, 4°C	Potter homogenization in HB at 1000 rpm, 5 min, 5 strokes; re-homogenization at 1000 rpm, 2 min, 2 strokes
Tissue cut into small pieces	440 mg Collagenase/100 mg pancreatin/L ADS buffer, 60 min, 4°C	Potter homogenization in modified HB (160 mM sucrose, 12% PEG 1500) at 1000 rpm, 5 min, 5 strokes; re-homogenization at 1000 rpm, 2 min, 2 strokes
Tissue cut into small pieces	440 mg Collagenase/100 mg pancreatin/L ADS buffer, 60 min, 4°C	Potter homogenization in modified HB (227 mM sucrose, 4% PEG 6000) at 1000 rpm, 5 min, 5 strokes; re-homogenization at 1000 rpm, 2 min, 2 strokes
Tissue cut into small pieces	440 mg Collagenase/100 mg pancreatin/L ADS buffer, 60 min, 4°C	Potter homogenization in modified HB (240 mM sucrose, 2% PEG 6000) at 1000 rpm, 5 min, 5 strokes; re-homogenization at 1000 rpm, 2 min, 2 strokes

Table 2-2: Adaptation of centrifugation conditions

Differential centrifugation	**Density gradient properties**	**Gradient centrifugation conditions**
600 × g_{max}, 2700 × g_{max}, 37000 × g_{max}	Optiprep in GB 1.12/1.15/1.19/1.22/1.26 g/ml	1.256 × 10^6 g × min (32,900xg_{max}, 37 min, 4°C)
600 × g_{max}, 6750 × g_{max}, 48000 × g_{max}	Optiprep in GB 1.12/1.15/1.19/1.22/1.26 g/ml	1.256 × 10^6 g × min (32,900 × g_{max}, 37 min, 4°C)
600 × g_{max}, 6750 × g_{max}, 48000 × g_{max}	Optiprep in GB 40/36/32/28/24/20/16 % 3 mL cushion/ 4.5 mL steps Incubation overnight at 4°C	32,900 × g_{max}, 60 min, 4°C
600 × g_{max}, 6750 × g_{max}, 48000 × g_{max}	Optiprep in GB 28/25/22/19/16/13/10 % 3 mL cushion/ 4.5 mL steps Incubation overnight at 4°C	32,900 × g_{max}, 60 min, 4°C
600 × g_{max}, 6750 × g_{max},	Optiprep in GB 27/24/21.5/19/16.5/14/11.5 %	32,900 × g_{max}, 60 min, 4°C

48000 × g_{max}	3 mL cushion/ 4.5 mL steps Incubation overnight at 4°C	
600 × g_{max}, 6750 × g_{max}, 48000 × g_{max}	Optiprep in GB 28/20/18/16/14/12/10 % 3 mL cushion/ 4.5 mL steps Incubation overnight at 4°C	32,900 × g_{max}, 60 min, 4°C
600 × g_{max}, 6750 × g_{max}, 48000 × g_{max}	Optiprep in GB 28/19/17/15.5/14/12.5/10 % 3 mL cushion/ 4.5 mL steps Incubation overnight at 4°C	32,900 × g_{max}, 60 min, 4°C

2.3.1 Hyper LOPIT Method

Samples from heart peroxisomal fractions were prepared by SDS-PAGE 'short-gel' cleanup and in-gel tryptic digestion. iRT peptide standards were added for retention time normalization and sample prefractionation was pooled into 12 fractions by neutral pH RP-C18 chromatography with staggered pooling for the generation of an annotated spectral library. Then mass spectrometric analysis was performed by following the steps:

- Quantification by DIA on Bruker timsTOF Pro (400 ng equivalent loaded, 90 min gradient, 32 windows DIA-MS, 4 technical replicates)
- Spectral library generation by additional data-dependent acquisition (DDA) on Orbitrap Exploris (400 ng equivalent loaded, 90 min gradient, 2 technical replicates per fraction)

Afterwards, data processing in Biognosys Spectronaut v15.6.211220.50606 was performed as:

- Hybrid spectral library generation from all DDA and DIA files using the Pulsar search engine against UniProtKB *Sus scrofa* reference proteome v09.2021 (49.865 entries) augmented with 51 lab contaminants at 1% False Discovery Rate (FDR)
- DIA quantification using up to 6 fragments per peptide, up to 10 peptides per protein, dynamic retention time alignment, dynamic mass recalibration, and quartile normalization at 1% FDR, full data set imputation scheme

2.4 Acyl-CoA oxidase (ACOX) Assay

The spectrophotometric assay of acyl-CoA oxidase was based on the determination of H202 production, which was coupled to the oxidation of leuco-DCF in a reaction catalysed by exogenous peroxidase. For the latter the method of Kochli and Von Wartburg (1978) for measuring monoamine oxidase was adapted. The reaction was carried out in a semi-micro cuvette at 30°C in a final volume of 1 ml. The assay mixture contained 0.05 mM-leuco-DCF (prepared daily at 2.6 mM in 1 vol. of NN-dimethylformamide and 9 vol. of 0.01M-NaOH, stored in a light-tight container under N2 gas), 0.08 mg of horseradish peroxidase, 40 mM-aminotriazole, 0.02% Triton X-100, 11 mM-potassium phosphate buffer, pH 7.4, and an appropriate volume of tissue homogenate or subcellular fraction and SI medium. This mixture was preincubated in the dark for 5 min, as some impurities in the peroxidase cause a small amount of oxidation of leuco-DCF (Kochli and Von Wartburg, 1978). After this time there is a slow rate of autoxidation of the dye, which was determined by measuring the change in A502 in a Unicam split-beam recording spectrophotometer for approx. 2min. The reaction was then started with the addition of 30 pM-palmitoyl-CoA, and the enzymic reaction rate was determined. Rates were then corrected for substrate blank.

2.5 Catalase Assay

Measurement of catalase activities was performed according to the method described by Baudhuin et al. 1964 which was adapted for the measurement in 96-well plates. Each well received the following components in triplicate: 5µl of 2% Triton X 100 in water, 5µl of the sample (either undiluted or appropriately diluted in TVBE in order to avoid complete substrate depletion), and 5 µl of TVBE as a blank. The plate was then placed on ice for 5 minutes. Subsequently, 100 µl of Catalase substrate was added to each well, and the plate was incubated on ice in the dark for exactly 15 minutes. Following this, 100µl of TiOSO4 was introduced to each well and left to incubate at room temperature for 10 minutes. Finally, the well was gently shaken for 5 seconds just before measuring the absorbance at 410 nm.

Calculation:

[Incubationvolume/(samplevolume*Incubationtime*50)]*dilution*[log(ODblan/ODsample)]

Incubation volume all except TiOSO4

Incubation time 15 min
Beaufay Unit: [B.U./ml]

Catalase-substrate:
10ml 0.2M Imidazolbuffer pH:7
100mg BSA
Fill to 100 ml with milliQ water
35µl 30% H_2O_2 solution

$TiOSO_4$: 6.8g $TiOSO_4$ (50% $TiOSO_4$) was solved in 1000 ml 1M H_2SO_4 and boiled. After cooling, it was filtrated through two filers. Then it was diluted to the 1.5-fold of the volume with 1M H_2SO_4. The boiled $TiOSO_4$ stays white/ turbid.

2.6 Plasmids and antibodies

KLHL41 (RC200295), SAR1B (MR201981), PDCD6 (MR222510), OCIAD1 (MR219053), HTATIP2 (MC200905) and PAFAH2 (MC201744) constructs were purchased from OriGene (Rockville, USA) and SERHL2 (HG15830-NM) was purchased from Sino Biological (Eschborn, Germany). All cDNAs from these expression plasmids were recloned into pCMV3A vectors containing an N-terminal myc-epitope in the ORF and amplified using NEB 5-alpha Competent *E. coli* Cells (New England Biolabs, Cat. No. C2987I) with the provided protocols of the products (see paragraph 1.5). The pCMV3A vector, used for recloning was a kind gift from Joe Costello, University of Exeter, UK.

Sources and dilutions of all primary and secondary antibodies used for the Western blotting and immunofluorescence experiments shown in this thesis are listed in Table 2-3 and Table 2-4, respectively.

Table 2-3: Complete list of primary antibodies

Target	Source	Immunogen	Dilution	Host Species	Use
ABCD3	Sigma-Aldrich, (SAB4200181) Schnelldorf, Germany	ATP-binding cassette (ABC) transporter	1:1200	Mouse mAb	WB

ACAD11	Gift from G. Vockley, Pittsburg University, USA	Acyl-CoA dehydrogenase 11	1:2000	Rabbit pAb	WB
ACBD5	Abcam (ab100910) Cambridge, UK	Acyl-CoA-binding domain-containing protein 5 recombinant protein	1:1000	Rabbit pAb	WB
ACBD5	Sigma-Aldrich (sab2100022) Schnelldorf, Germany	Acyl-CoA-binding domain-containing protein 5 recombinant protein	1:1000	Rabbit pAb	WB
ACOX1	Gift from T. Hashimoto, Shinshu University School of Medicine, Nagano, JP	Peroxisomal acyl-coenzyme A oxidase 1	1:10.000	Rabbit	WB
ACSL1	Proteintech 13989-1-AP Rosemont IL, USA	Long chain fatty acid CoA ligase 1	1:1000	Rabbit pAb	WB
ACSL3	Invitrogen Life Technologies 20710-1-AP Eugene, USA	Fatty acid CoA ligase 3	1:1000	Rabbit pAb	WB
ACSL4	Santa Cruz Biotechnology sc-365230 Santa Cruz, USA	Long chain fatty acid CoA ligase 4	1:1000	Mouse mAb	WB
ATP Synthase alpha	BD Transduction Laboratories 612517 San Diego, USA	ATP synthase subunit alpha, mitochondrial	1:10.000	Mouse mAb	WB
ATPB5	Proteintech (66600) Rosemont IL, USA	The beta subunit of ATP synthase	1:5000	Mouse mAb	WB
BiP/GRP78	BD Transduction Laboratories 610978 San Diego USA	Endoplasmic Reticulum chaperone BiP	1:1000	Mouse mAb	WB
Catalase	Gift from A. Völkl, University of Heidelberg, Germany	Catalase	10 ug/ml	Rabbit	WB
c-myc tag (9B11)	Cell Signaling #2276 Danvers, Massachusetts USA	myc epitope tag	1:500	Mouse mAb	IF
ELOVL1	Biorbyt orb224117 Cambridge, UK	Elongation of very long chain fatty acids protein 1	1:1000	Rabbit pAb	WB

ERP29 (LY1C6)	Abcam ab11420-50 Cambridge, UK	Endoplasmic reticulum resident protein 29	1:5000	Rabbit pAb	WB
FATP4	Abcam 200353 Cambridge, UK	Fatty acid protein 4	1:1000	Rabbit mAb	WB
KLHL41/KBTBD10	Finetest FNab04474 Wuhan, Hubei, China	Kelch repeat and BTB (POZ) domain containing 10	1:200	Rabbit pAb	IF
LAMP1	Santa Cruz Biotechnologysc-17768 Santa Cruz, USA	Lysosome-associated membrane proteins	1:500	Mouse mAb	IF
OCIAD1	Novus biotechne NBP1-76242 Abingdon UK	OCIA-domain containing protein 1	1:100	Rabbit pAb	IF
PEX3	Gift from G. Dodt, University of Tübingen, Germany	Peroxisomal Biogenesis Factor 3	1:1000	Rabbit	WB
PEX14	Proteogenix, selfmade (7790-03107-A02) Oberhausbergen, France	Peroxisomal Biogenesis Factor 14	1:2000	Guinea pig	IF
PMP22	Gift from A. Völkl, University of Heidelberg, Germany	Peroxisomal membrane protein 22	1:500	Rabbit	WB
PMP70	Gift from A. Völkl, University of Heidelberg, Germany	Peroxisomal membrane protein 70	1:100	Rabbit	WB
PRDX3	Invitrogen / Thermo Fisher PA-5-91918 Eugene/USA	Peroxiredoxin 3	1:1000	Rabbit pAb	WB
RAB5A	Proteintech 11974-1-AP Rosemont IL, USA	The small GTPase Rab	1:1000	Rabbit pAb	IF
SAR1b	Proteintech/ptglab 22292-1-AP Rosemont IL, USA	Secretion Associated Ras Related GTPase 1B	1:200	Rabbit pAb	IF
SCP-X	MyBio Source MBS 1495100 San Diego, USA	Serol Carrier Protein	1:500	Rabbit pAb	WB
SERCA2	Novus biotechne NB300-581 Abingdon, UK	Sarco/Endoplasmic Reticulum Ca^{+2} ATPase	1:2000	Mouse mAb	WB

PO-ketothiolase	Gift from A. Völkl, University of Heidelberg, Germany	Thiolase	1:1000	Rabbit	WB
TOMM20	BD Transduction Laboratories 612278 San Diego, USA	Translocase of the Outer Membrane of the mitochondria	1:1000	Mouse mAb	WB, IF
Urate-oxidase		Urateoxidase	1:1000	Rabbit	WB
VAPB	Sigma-Aldrich HPA013144 Schnelldorf, Germany	Vesicle associated membrane protein-associated protein B	1:2000	Rabbit pAb	WB, IF
VDAC1	Abcam (ab14734) Cambridge, UK	Voltage Dependent Anion Channel 1	1:500	Mouse mAb	WB

Table 2-4: Complete list of secondary antibodies

Conjugated Molecule	Source	Dilution	Reactiviy	Use
Alexa Fluor® 488	Invitrogen A32723	1:1000	Goat anti mouse IgG	IF
Alexa Fluor® 488	Invitrogen A32723	1:1000	Goat anti mouse IgG	IF
Alexa Fluor® 568	Invitrogen A11041	1:1000	Goat anti chicken IgG	IF
Alexa Fluor® 568	Invitrogen A11011	1:1000	Goat anti rabbit IgG	IF
Alexa Fluor® 568	Invitrogen A11036	1:1000	Goat anti rat IgG	IF
Alexa Fluor® 647	Invitrogen A21450	1:500	Goat anti guinea pig IgG	IF
Alexa Fluor® 647	Invitrogen A32733	1:500	Goat anti rabbit IgG	IF
HRP IgG	DAKO (P0447), Glostrup, Denmark	1:5000	Goat anti mouse	WB
HRP IgG	DAKO (P0448), Glostrup, Denmark	1:5000	Goat anti rabbit	WB

2.7 Molecular cloning

Primers with corresponding restriction sites, which were used for amplification of the KLHL41, PDCD6, OCIAD1, PAFAH2, and HTATIP2 cDNAs in the cloning experiments were purchased from Eurofins Genomics. To produce myc-tagged plasmid constructs for IF localization studies, PDCD6 was amplified by PCR from pCMV6-Entry-PDCD6 (Origene) with BamHI/HindIII linker ends, OCIAD1 was amplified by PCR from pCMV6-Entry-OCIAD1 (Origene) with EcoRI/XhoI linker ends, PAFAH2 was amplified by PCR from pCMV6-Kan/Neo-PAFAH2 (Origene) with EcoRI/HindIII linker ends. HTATIP2 was amplified by PCR from pCMV6-Kan/Neo-HTATIP2 (Origene) with EcoRI/XhoI linker ends and KLHL41 was amplified with EcoRI/XhoI (Table 2-5). The amplification was performed with a thermal cycler with adequate Tm for each primer pair (Table 2-5) and the supplier protocol for the PRECISOR High-Fidelity DNA Polymerase. PCR products were purified using the QIAquick Gel Extraction Kit. 3 volumes of Buffer QG of the kit and 1 volume of isopropanol to 1 volume of the PCR product were added. Spin columns provided with the kit were placed on 2 mL collection tubes and the PCR Product mix was applied to spin columns. The PCR product was collected by 1 min centrifugation at 10000 × g. 0.75 mL buffer PE provided by the kit was added to the column for washing and centrifuged again at the same conditions. The DNA concentration and yield were assessed by measurement of the 260/280 absorbance using a NanoDrop spectrophotometer. Absorbance values ranging from 1.80 to 2.00 were accepted as good purities. The correct sizes of the purified amplicons were confirmed by agarose gel electrophoresis. To this end, 6 µl of the purified amplicons were mixed with 6X DNA Gel Loading Dye and loaded to 1% agarose gel.

Subsequently, the amplicons were ligated into the pCMV3A mammalian expression vector using the Quick Ligation™ kit according to the protocol provided by the manufacturer (New England BioLabs, M2200). In brief, ligation was performed using a molar ratio of 1:5 vector (pCMV 3A vector is 4214 base pair) to insert ratio for the indicated DNA sizes. 100 ng vector was used, and the required insert DNA mass was calculated via NEBioCalculator (https://nebiocalculator.neb.com/#!/ligation)

The preservation of the correct cDNA sequences in the constructs was confirmed by sequencing at Eurofins Genomics (Ebersberg, Germany).

Table 2-5: The list of primers used for cloning.

Gene	Forward	Reverse	Product Size	Tm
KLHL41	CTTGAATTCGATGGATT CCCAGCGGGAACT	CCCCTCGAGTTACAGTT TAGACAGTTTGAAG	1818 base pair	66 °C
PDCD6	CTTGGATCCCATGGCT GCCTACTCCTACCG	GGGAAGCTTTTATACAA TGCTGAAGACC	573 base pair	66 °C
OCIAD1	CTTGAATTCGATGAATG GGAGGGCTG	CCTCTCGAGTTACTCAT CCCAAGTATC	1529 base pair	64 °C
PAFAH2	CTTGAATTCGATGGGG GCCGGCCAGT	GGGAAGCTTCTATAGAC TAGACAGATAGTGCGG	1173 base pair	66 °C
HTATIP2	CTTGAATTCGATGGCG GACAAGGAAGC	CCTCTCGAGTTATCACA GTTTGGGC	729 base pair	66 °C

2.8 Cell culture and transfection

HepG2 (European Collection of Authenticated Cell Cultures (ECACC), Ref 85011430), HeLa, and HepG2 Crispr ACBD5 KO (provided by Prof. Dr. Hans Waterham, Amsterdam UMC) cell lines, mouse embryonic fibroblasts (MEF) and isolated primary neonatal rat cardiomyocytes (NRCM, provided by Dr. Rhys Wardman, Heidelberg

University UMM) were cultured in Dulbecco's modified Eagle's medium (DMEM) supplemented with 10% FBS, 1% penicillin/streptomycin and 25 mM glucose. HepG2 and ACBD5 KO HepG2 cells were split into Poly-D-Lysine (PDL; Gibco, A3890401)-coated coverslips in 24-well plates. NRCMs were seeded on an x-well cell culture chamber (94.6140.402 Sarstedt, Nümbrecht Germany) and transfected by using Lipofectamine™3000 reagent (Invitrogen, L3000001) with 0.5 µg plasmid DNA amounts. For the transfection of 70-80% confluent cells in 24 well plates, firstly 0,75 µL/well Lipofectamine 3000 (Thermo-Fisher) was diluted with 25µl/well Opti-MEM medium (Gibco, 11058021). In another tube master mix of DNA was prepared by diluting 0.5 µg DNA in 25 µL Opti-MEM and adding 1µl P3000 reagent provided by the kit. After mixing well, diluted DNA was added to diluted Lipofectamine 3000 reagent by a ratio of 1:1. This DNA-lipid complex was incubated for 15 minutes at room temperature and added to cells at 50 µL/well.

2.9 Microscopic Techniques

2.9.1 Preparation of coverslips

A required number of 12mm # 1.5 glass coverslips were immersed in an appropriate volume of 37% HCl in Erlenmeyer flasks while working under a fume hood. The flask size was chosen so that the bottom area was large enough that all the coverslips were spread out evenly to ensure contact with the HCl. After a minimum of two hours at RT on a shaker, the HCl was removed, and the coverslips were first washed with tap water for three minutes. Afterwards, coverslips were rinsed by 5 min incubations in milliQ water, 70% ethanol (diluted from 99% ethanol with milliQ water), and 99% ethanol in the given order. The cleaned coverslips were stored for a long term immersed in 99% ethanol in a sealed, sterilized glass bottle. For the experiments, the coverslips were placed into 24 well plates leaning against the walls of each well and dried completely. The plate without a lid was shaken slightly while it was still covered in the cell culture hood for roughly an hour, which allowed the coverslips to fall to the bottom of the plate and cover it horizontally. Coverslip-containing 24-well plates were placed back into their packaging and kept sealed at 4 °C until further usage.

2.9.2 Coating of coverslips

To ensure an optimum attachment of the cells to the coverslips, a coating solution containing 0.1 % PDL was prepared and sterilized by passing it through a 0.22 µm

filter. 0.1% PDL was applied to each well or dish to completely submerge the bottom surface of the vessels the day before culture preparation. After two hours of incubation inside the cell culture hood, the PDL solution was removed. Plates were then washed three times with milliQ water before being finally refilled with sterile PBS. For the following day's culture preparation, coated plates with PBS were maintained in an incubator at 37 °C. On the cell-seeding day, PBS was replaced with 500 µL/well (for 24 well plates) of culture medium. The medium-filled 24 well plates were maintained for at least an hour at 37°C in a cell culture incubator before cell seeding.

2.9.3 Immunofluorescence staining and microscopy

For the microscopy analyses of the protein overexpression and protein co-localization experiments, cells were fixed 24 hours after plasmid transfection using pre-warmed 4% paraformaldehyde (PFA) in PBS (pH 7.4) for 20 minutes. After fixation, the cells were incubated in a combined blocking and permeabilization solution (1% BSA, 0.2% fish skin gelatin, 0.1% Triton X-100) for one hour, RT. All primary and secondary antibodies were diluted in blocking buffer (1% BSA, 0.2% fish skin gelatin, 0.1% Triton X-100 in TBS) according to Table 2.3. Primary antibody incubation was performed overnight at 4 °C. Incubation of the secondary dye-labeled Alexa antibody was performed for another 1.5 hours at RT (see Tab 2-4 for dilutions). In between each antibody incubation step, the cells were rinsed 3 times for 5 minutes with PBS at RT. Before mounting onto glass microscopy slides, the coverslips were shortly rinsed one more time with ddH_2O. Afterwards, they were mounted upside down onto the glass slides using Roti, FluorCare immersion medium (Carl Roth GmbH, Karlsruhe, Germany).

Confocal images were acquired using a C2 Nikon confocal microscope equipped with 488 nm, 561 nm, and 647 nm laser lines and either an ApoPlan 60x (oil immersion, 1.4 NA) or an ApoPlan 100× (oil immersion, 1.45 NA) objective. The thickness of single optical sections was 1 µm for imaging whole cells and 0.5 µm for subcellular structures (mitochondria, peroxisomes) in stacks of 10–20 µm total depth. Image resolution was 1024*1024 pixels, with a fixed 0.08 µm pixel size. The open-source software Fijii ImageJ was used for all post-imaging analysis. For the quantification of cell numbers, stacks of images were merged into a maximum-intensity projection. For the quantification of peroxisome densities, single planes from the center of the cell were

used. Counting, size, relative area, and circularity determination of fluorescent signals in HepG2 WT and HepG2 ACBD5 KO cells were performed with Fiji ImageJ using automated thresholding and the “analyze particles” command (size: 2 pixels-infinity, circularity: 0.0–1.0) The mitochondrial network analysis was performed with ImageJ MiNA plug-in. For visual presentation, image tif-files were processed in Adobe Photoshop CC (Adobe Systems).

2.10 Determination of protein concentrations

Protein concentrations in subcellular fractions were determined with the Bradford assay (Bradford, 1976). In the assay, 1X working reagent was prepared by diluting 5X Roti Nanoquant Bradford reagent (Carl Roth GmbH, Karlsruhe, Germany) with TVBE buffer. 5 dilutions of the protein standard containing from 10 µg/µL to 100 µg/µL were prepared. 50 µl of standards and samples into a clean dry 96 well plate were pipetted and then 200 µl of diluted Bradford reagent was added into each well. The plate was incubated at room temperature for 5 minutes. After the incubation, the plate was placed in the reader and let mix for 5 seconds. The absorbances were determined at 595 nm and 450 nm via a microplate reader (TECAN).

2.11 Immunoblotting

Equal protein sample amounts (10 µg for organelle fractions) were separated on 12% or 10% SDS gels. To this end, sample volumes were first adjusted to equal volumes with TVBE buffer to avoid uneven running of the individual lanes. The even volumed samples were subsequently diluted with 5× Lämmli loading buffer (Lämmli, 1970). Meanwhile, two 0.85 mm Whatman filter papers were prepared for each Buffer (Cathode buffer, Anode buffer 1, Anode buffer 2, see Table 2-6) and soaked in these buffers for 2 to 3 minutes (Khyse-Anderson, 1984). The PVDF membrane was activated with methanol, rinsed twice with milliQ water, and stored in Anode buffer 1 until further use SDS gel was washed with Cathode buffer for a maximum of 5 minutes. After protein separation, the SDS-PAGE gel was taken out of the separation chamber and placed on PVDF membrane. The stacks were placed on the blotting machine with the membrane side facing the anode as described below.

Arrangement of the Blotting-Sandwich
(Assemble from bottom to top)

- 2 Cathode Buffer-soaked Whatman papers
- SDS gel
- Immobilon PVDF-membrane (hydrophobic surface towards the gel)
- 2 Anode Buffer 1-soaked Whatman papers
- 2 Anode Buffer 2-soaked Whatman papers

4.5 x 6 cm membranes each received a 45 mA current, which has a limit of 5V and 30W. Proteins were transferred to the membrane by the Peqlab (Erlangen, Germany) semidry-electroblotter.

Table 2-6: The list of solutions used for Kyhse Anderson buffer system.

Anode Buffer 1	-3.63g Tris (Mr. 121.14g/mol) - 800ml Deionized water - 200ml Methanol	End concentration Tris: 30mM
Anode Buffer 2	- 36.43g Tris (Mr. 121.14g/mol) - 800ml Deionized water - 200ml Methanol	End concentration Tris: 300mM
Cathode Buffer	- 3.03g Tris (Mr. 121.14g/mol) - 5.24g Aminocaproic acid (Mr.) - 800ml Deionized water - 200ml Methanol	End concentration Tris: 25mM End concentration Aminocaproic acid: 40mM

After protein transfer, the membranes were blocked in 5% fat-free milk powder in PBST for 60 minutes. All antibodies were diluted in PBST containing 1% FCS. A system of horse radish peroxidase (HRP)-coupled species-specific secondary antibodies that bind the species-specific Fc-domains was used to detect the antigen-specific primary antibodies. Primary antibodies were incubated in dilutions according to Tab 2.3 overnight at 4 °C., secondary HRP-conjugated antibodies were incubated for 1.5 h at room temperature (see Tab 2.4 for dilutions). Before addition and after removal of each antibody, the blots were washed for 3 times in PBST for 5 min each.

Chemiluminescent signals were produced with WesternBright ECL HRP substrate (Advantsa). After 1 minute incubation of the membrane with ECL, the membrane was placed between two transparent films. Image acquisition of the immunoblots was performed with a Fusion Solo S Western blot imaging system (Vilber-Lourmat, Marne-la-Vallée, France) which is operated by the Fusion software from the same provider. All images were taken without gamma correction. The "good laboratory practice"

function built into the software examined the processing of the captured photos and preserved each processing step in the meta-data of the corresponding image. Oversaturation of signals in images was avoided with the help of the software.

2.12 Exploratory data analysis

The datasets, comprising protein data for LM-Log2 Fold Change and FLM-Log2 Fold Change, as well as associated UniProt organelle localizations, were loaded into a Python environment and normalized using Min-Max Scaling (Python packages Pandas (McKinney et al., 2010), NumPy (Harris et al., 2020)). The dataset was subsequently divided into training and testing sets, with 60% of the data allocated for training and 40% for testing (Python package Scikit-Learn (Pedregosa et al., 2011)). Model Logistic Regression and Random Forest Classifier models were selected to train the model with the dataset. The dataset was further enhanced by the addition of manually curated organelle localizations, based on the information in original publications, to improve the model's learning capability. Both models were used to predict the 'Organelle cluster affiliation' on the test dataset.

2.13 Statistical analysis

For statistical analysis of the organelle morphology changes in the protein overexpression experiments, a one-tailed, unpaired t-test was applied (*P < 0.05; **P < 0.01; ***P < 0.005; ****P < 0.001; ns: not significant) using the GraphPad Prism software (Dotmatics Software Inc.). Sample sizes used for data analysis are indicated under the corresponding figures. All quantitative data were collected from at least three independent experiments and presented as mean ± SEM.

3 RESULTS

3.1 The characterization of peroxisomes in WT and ACBD5 KO mice

ACBD5 deficiency is a newly discovered disorder affecting peroxisomal function, and its underlying pathologic mechanisms and effects are not yet well understood. ACBD5 was recently identified as a component of a tethering complex with VAP proteins that facilitates communication between peroxisomes and the ER (Costello et al., 2017; Hua et al., 2017). These membrane contact sites between organelles are recognized as critical sites for the exchange of metabolites and regulation of signaling networks within cells (Scorrano et al., 2019). Although the close proximity between peroxisomes and the ER has been observed for many years, its functional significance remains poorly understood (Costello et al., 2017).

Previous studies conducted by our research team examined an ACBD5 KO in order to explore the relationship between ACBD5's tethering functions and the disease phenotype. The ACBD5 KO mice displayed increased levels of VLCFA suggesting hepatocyte-specific induction of peroxisome proliferation by activation of the nuclear receptor PPARα (Darwisch et al., 2020). Therefore, the initial focus of this thesis was to characterize peroxisomes in both wild-type and ACBD5 KO to unravel if the loss of ER-peroxisome membrane contacts specific compensatory reactions at the organelle level. To achieve this, liver samples from ACBD5 KO and ACBD5 WT control mice were isolated by a combination of differential and density gradient centrifugation techniques. In brief, following the homogenization step, the resulting PNS was subjected to consecutive differential centrifugation, resulting in the isolation of HM, LM, and microsomal fractions. Afterwards, peroxisomes were purified from the LM fraction by density centrifugation (see Material and Methods section 2.2).

As shown by immunoblotting, levels of peroxisomal proteins involved in fatty acid degradation such as ACOX1, MFP1, and PMP70 increased in the PNS from the livers of ACBD5 KO mice, while they remained largely unchanged at the level of isolated peroxisomes (Figure 3-1A, B). Likewise, the ACOX activity in peroxisome fractions from ACBD5 KO and ACBD5 WT mice was comparable, whereas they were approximately doubled in the PNS of ACBD5 KO mice (Figure 3-1C, D). The activity of the predominant peroxisomal H_2O_2 degrading enzyme catalase exhibited a

comparable elevation in the PNS of ACBD5 KO mice but was even reduced at the peroxisome level if compared to ACBD5 WT mice. Taken together, these results indicate a moderate PPARα-induced increase in peroxisome abundance (Islinger et al., 2007), likely in order to compensate the reduced VLCFA import capacities of ACBD5-deficient peroxisomes (Yagita et al., 2017). These observations were further corroborated by determination of hepatocellular peroxisome numbers by immunofluorescence and electron microscopy (Darwisch et al., 2020). Remarkably, a calculation of the total liver enzymatic catalase and ACOX capacities (Σ U) revealed a discrepancy between ACBD5 KO and WT animals, when the results were compared either between the PNS or peroxisome fractions (Figure 3-1D, G). While the total enzymatic capacities for catalase and ACOX were elevated approximately by the factor of 2 in the PNS of ACBD5 KO liver, a much higher increase by the factor of 4.2 and 16 for catalase and ACOX was calculated at the level of isolated peroxisomes, respectively. In addition, catalase activity was examined since it is the most predominant enzyme in peroxisomes, (Figure 3-1F, G). A comparison of the recovery of peroxisomes isolated from ACBD5 KO and ACBD5 WT mouse liver explains the paradoxical results (Figure 3-1E): the protein yield for peroxisomes isolated from ACBD5 KO mouse liver (factor 17 if compared to ACBD5 WT) exceeds by far the increase of peroxisomes determined at the whole organ level by either measurement of enzyme activities or calculation of peroxisome abundance by EM and immunofluorescence microscopy (factor 2 – 3)(Darwisch et al., 2020).

Interestingly, the abundance of the ER-resident VAPB, which interacts with ACBD5 thereby facilitating membrane contacts with peroxisomes, was found to be higher in peroxisome fractions of ACBD5 WT mice compared to ACBD5 KO mouse liver (Figure 3-1A). This suggests that the content of ER membranes, which could still be attached to isolated peroxisomes, appears to be less in peroxisome fractions from ACBD5 KO mice. Accordingly, the interaction with low-density ER particles appears to prevent the bulk of peroxisomes from migrating into the higher-density fraction during differential and density gradient separation. Moreover, FLM, which is normally situated above the LM pellet, was consistently observed in peroxisome purifications from ACBD5 KO mice (Figure 3-1A). Hence, we questioned whether these FLM peroxisomes could potentially contain ER membranes associated with tethering complexes. Therefore, we speculated that the isolation of peroxisomes from the FLM fraction might reveal novel

proteins involved in the formation of tethering complex between the ER and peroxisomes.

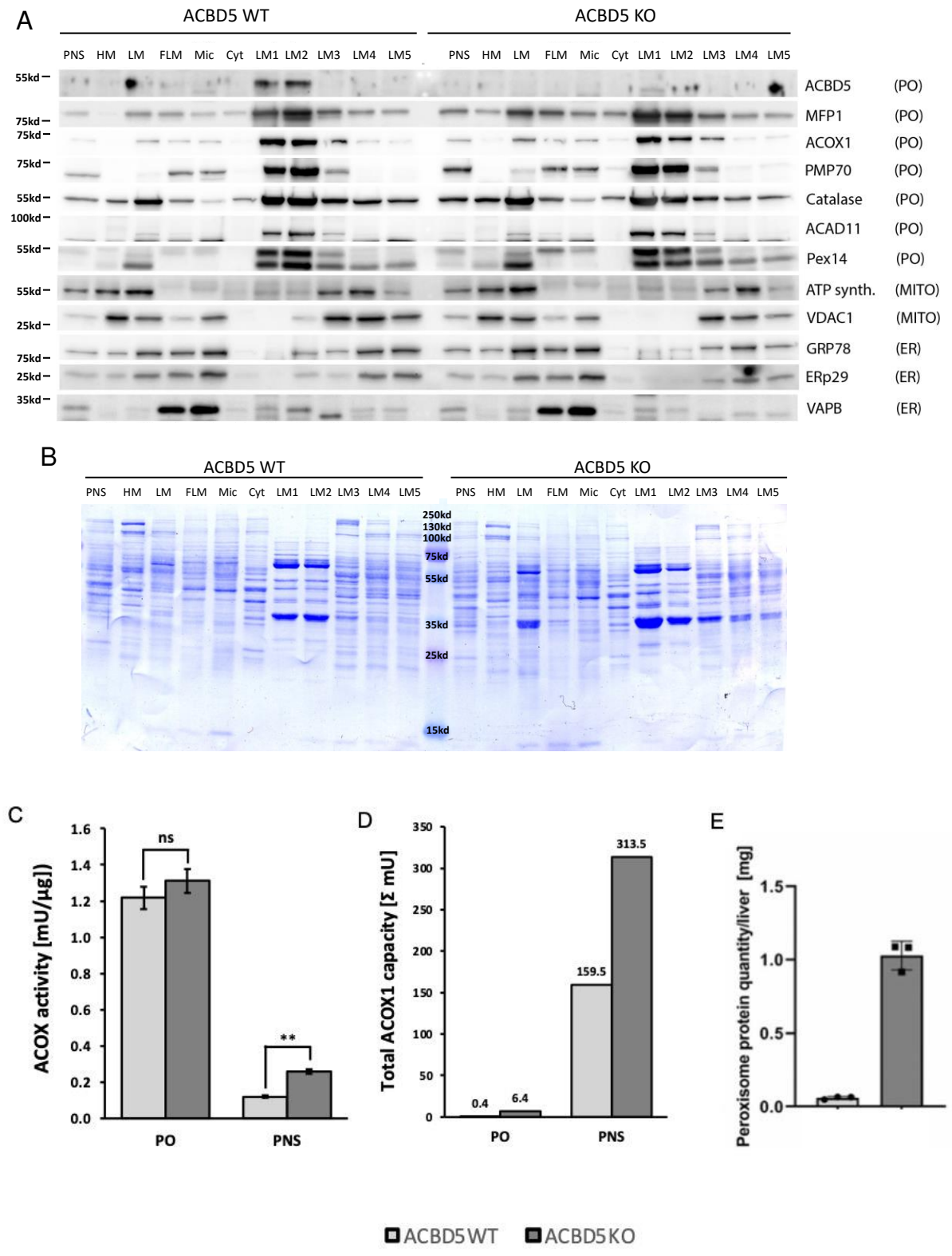

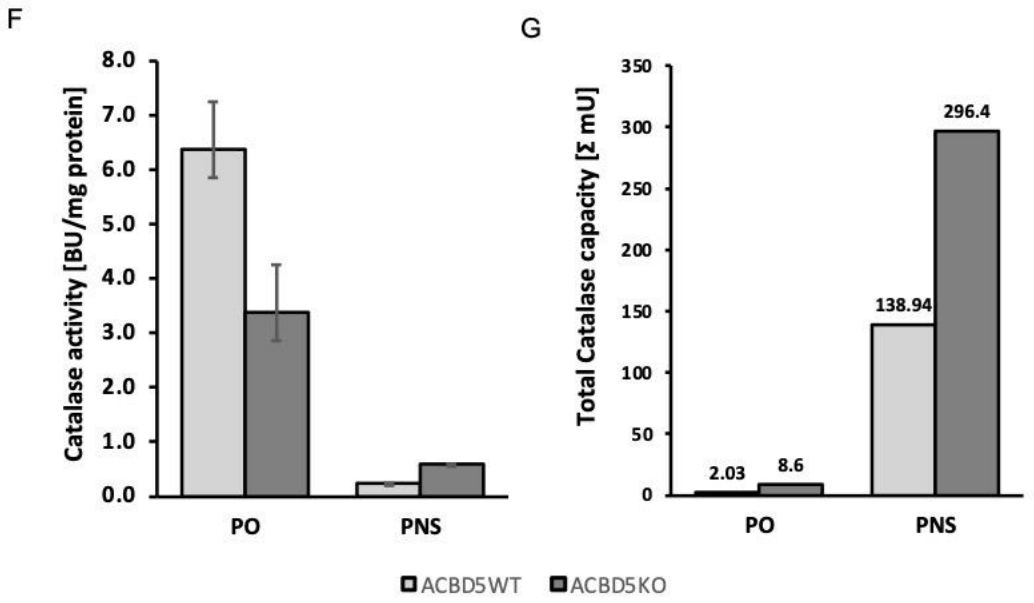

Figure 3-1: Characterization of peroxisomes from ACBD5 WT and ACBD5 KO mice liver.

(A) Immunoblots of prefractions and density gradient fractions from of ACBD5 WT and ACBD5 KO mouse liver. LM1 to LM5 represent fractions that were prepared from the LM prefraction and separated by density centrifugation. Immunoblots were performed using antibodies against peroxisome (PO), mitochondria (MITO), and ER marker proteins. ACBD5: Acyl-CoA binding domain containing 5, MFP1: peroxisomal Multifunctional protein 1, ACOX1: Acyl-CoA oxidase 1, PMP70: Peroxisomal membrane protein 70, ACAD11: Acyl-CoA dehydrogenase family member 11, Pex14: Peroxin-14, VDAC1: Voltage-dependent anion channel 1, GRP78: Glucose-regulated protein 78, ERP29: Endoplasmic reticulum protein 29, VAPB: Vesicle-associated membrane protein B. (B) Coomassie staining of a Western blot for the validation of protein loading. (C) Acyl-CoA oxidase activities in PNS and isolated peroxisome fractions (pooled LM1 and LM2 from A). (D) total ACOX capacity in PNS and peroxisomal fraction. (E) Total protein yield from ACBD5 WT and ACBD5 KO peroxisomal fractions (LM1+LM2, average from five isolations). (F) Catalase activity in PNS and isolated peroxisome fractions (measured as described in Islinger et al, 2012). BU: Beaufay Unit. (G) For confirmation, catalase enzyme capacity was calculated in total protein yielded from PNS and peroxisomal fractions and since PNS has much higher protein content, it shows a higher catalase enzyme amount.

3.2 Identification of novel candidate peroxisome-associated proteins from mice livers

3.2.1 Principal characterization of the main and gradient fractions of peroxisome purification protocol from mouse liver

In order to discover novel peroxisome-associated proteins and potential constituents of peroxisome-ER contact zones by MS-based proteomics, mice livers were homogenized for peroxisome isolation and further separated by a combination of differential and density gradient centrifugation. For peroxisome isolation, density gradient fractions are usually prepared from the peroxisome-enriched light mitochondria fraction (LM, see Section 2.2, Figure 2-1) (Islinger et al., 2018). In this work, FLM, layered on top of the LM and usually discarded, was separately applied to Optiprep density gradients. In order to evaluate the reproducibility of the preparation of the main fractions, the distribution of characteristic organelle marker proteins was validated in 4 independent experiments, which were subsequently characterized by MS (Figure 3-2). According to the immunoblot analysis, peroxisomal proteins were consistently enriched in both the LM and FLM fractions if compared to the PNS. Mitochondrial proteins like ATPA or ATPB5 continuously decrease from the HM fraction to the microsomal fraction (Mic), while ER proteins like GRP78 and FATP4 increase towards the “lighter” fractions of the differential centrifugation procedure. Remarkably, the FLM fraction contains the most intense signal of the ER-localized tethering protein VAPB, which was recently identified as an interaction partner to the peroxisomal membrane protein ACBD5 thereby facilitating membrane contacts between both organelles (Costello et al., 2017). Hence, we hypothesized that the lighter density of peroxisomes found in the FLM might be associated with the ER membranes, thus shifting to a lower density. A similar phenomenon has been observed for mitochondria-associated ER membranes, which also decreases the density of isolated mitochondria (Vance, 1990).

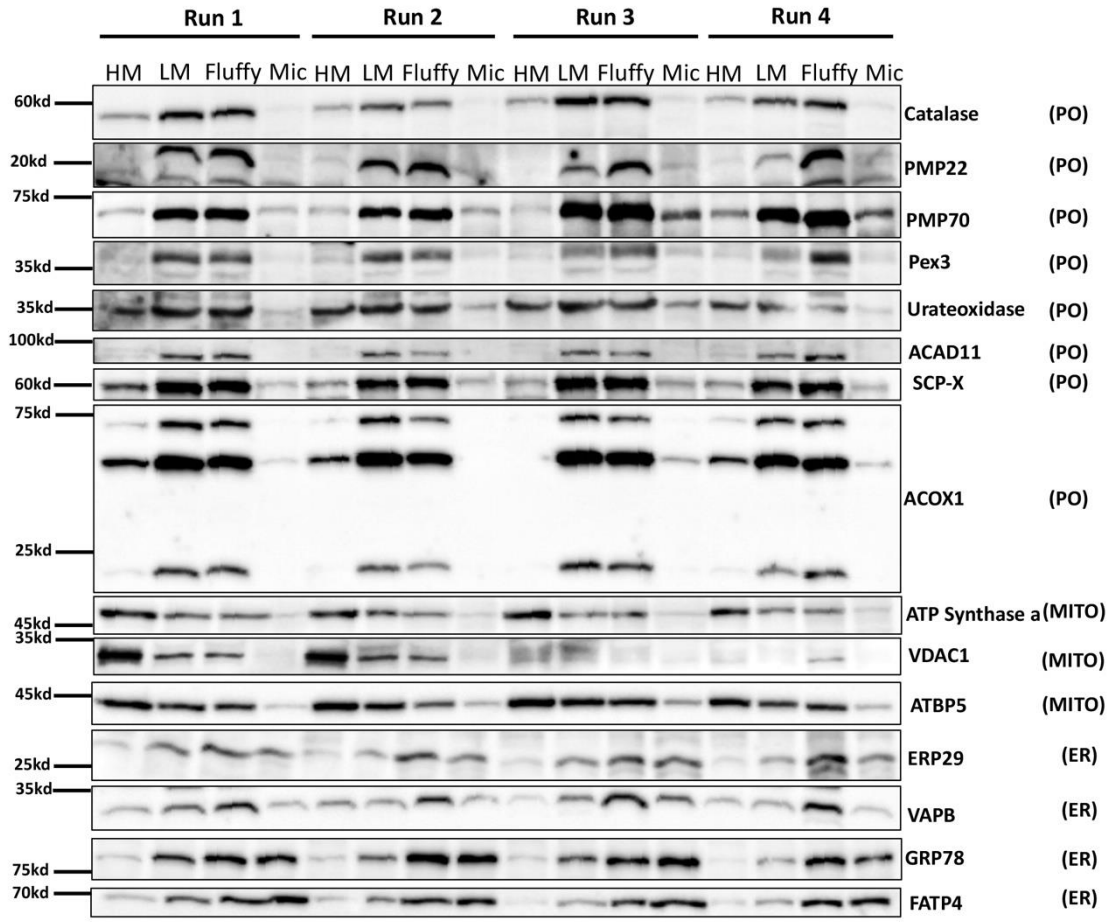

Figure 3-2: Immunoblots of liver prefractions from 4 independent peroxisome isolations.

Each run represents a sample group used for consecutive MS. LM and FLM lanes in each run show elevated peroxisomal protein abundance while mitochondrial proteins are more abundant in the HM lane. ER marker proteins show an increase from the HM lane to the microsomal lane. PMP22: Peroxisomal membrane protein 22, PMP70: Peroxisomal membrane protein 70, Pex3: Peroxin-3, ACAD11: Acyl-CoA dehydrogenase family member 11, SCP-X: Sterol carrier protein X, ACOX1: Acyl-CoA oxidase 1, VDAC1: Voltage-dependent anion channel 1, ATPB5: ATP synthase subunit beta, ERP29: Endoplasmic reticulum protein 29, VAPB: Vesicle-associated membrane protein B, GRP78: Glucose-regulated protein 78, FATP4: Fatty acid transport protein 4, MITO: Mitochondria, PO: Peroxisomes

To compare peroxisomes isolated from the LM and FLM prefractions, the density gradients were eluted into 5 fractions and compared by immunoblotting (Figure 3-3). Peroxisomal proteins are significantly enriched in the high-density fractions from both the LM and the FLM Opti prep gradient, while bands for mitochondrial, and ER marker proteins are only faintly visible. These highly pure peroxisomal fractions contain

comparable levels of the tethering protein ACBD5 (LM1, LM2, FLM1, FLM2). Remarkably, the isolated peroxisomes from the FLM fraction (FLM1, FLM2) showed a considerably higher level of its ER interaction partner VAPB, suggesting that these peroxisomes are enriched in VAPB/ACBD5-mediated ER-PO membrane contacts sites. Young et al. 2017 observed an interaction between ACSL1 and ACBD5 as well as VAPB by co-immunoprecipitation experiments. Hence ACSL1 should be enriched in parallel with ACBD5 and VAPB. In general, the intracellular localization of acyl-CoA synthetases, which are required for fatty acid activation prior to import into peroxisomes, is still not completely resolved (Watkins and Ellis, 2012). According to previous publications, ACSL1 is localized at mitochondria, plasma membrane, ER, PO, and cytosol, and ACSL4 at PO and ER (Soupene and Kuypers, 2008; Watkins and Ellis, 2012). Our findings confirm that the amount of ACLS4 is nearly identical across all fractions, supporting the multiple intracellular localization of this protein (Figure 3-3). In contrast, ACSL1 is like VAPB particularly abundant in isolated FLM-PO fractions (FLM1, FLM2) if compared to LM-PO, which supports the hypothesis that PO fractions isolated from the FLM layer fraction (FLM1/FLM2) might be enriched with peroxisome-associated ER membranes. Therefore, we concluded that an MS-based proteome comparison of FLM-PO and LM-PO might have the potential to discover further distinct ER proteins that co-purify with the FLM-PO tethering complex.

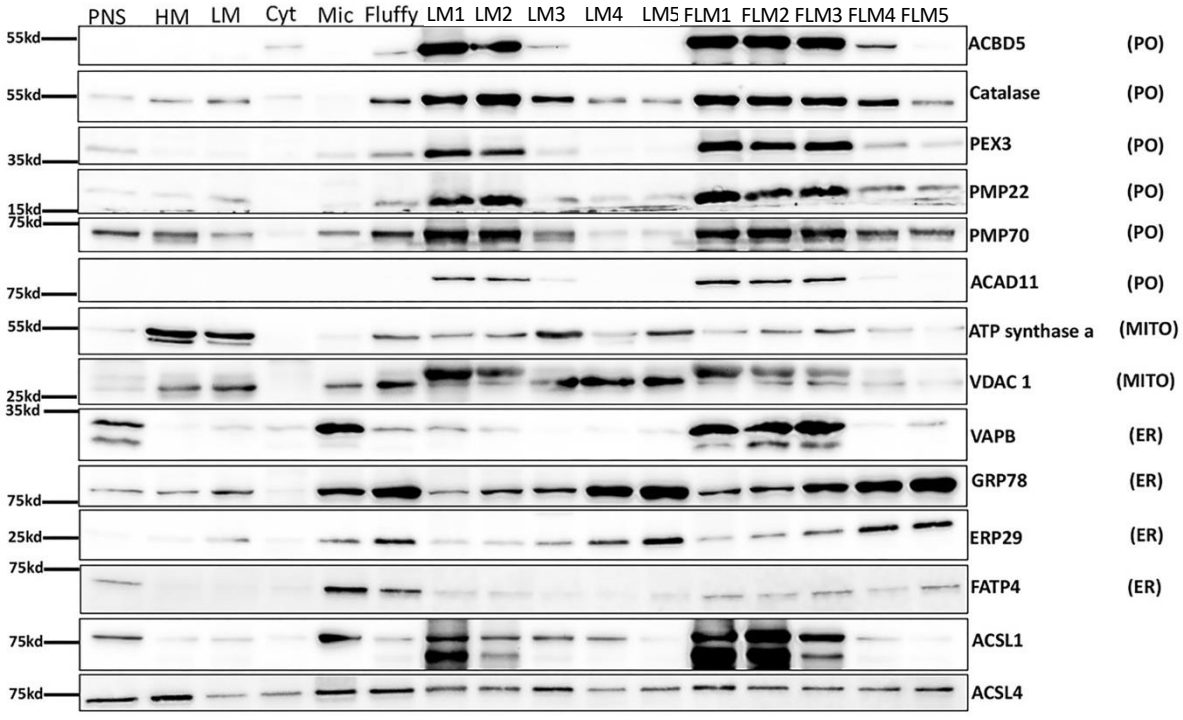

Figure 3-3: Immunoblots of prefractions and density gradient fractions from mouse liver peroxisome isolations.

LM1 to LM5 and FLM1 to FLM5 represent gradient fractions gained from the density gradient separation of LM and FLM prefractions, respectively. According to marker proteins for PO, MITO, and ER, peroxisomes are mainly contained in LM1, LM2, FLM1, FLM2, and FLM3. Mitochondrial proteins accumulate prevalently in LM and in LM3 and FLM3 fractions of the gradients. ER marker proteins except VAPB show a gradual increase from FLM1 to FLM5. VAPB shows significant enrichment on FLM1, FLM2 and FLM3 lanes. Blots from Acyl-CoA synthetases show different distributions from each other. ACSL4 indicates a similar distribution throughout the LM and FLM gradients while ACSL1 shows a VAPB-like enrichment pattern. ACBD5: Acyl-CoA binding domain containing 5, ACSL: Acyl-CoA synthetase long-chain family member.

3.2.2 Identification of peroxisome-enriched proteins in LM and FLM peroxisomal fractions using SWATH-MS quantification

In order to identify novel, less abundant peroxisomal or peroxisome-associated proteins, a quantitative SWATH-MS strategy was applied to characterize the protein composition of purified mouse liver peroxisomes. To this end, the mitochondria-enriched higher density light mitochondrial fraction (LM1-6) and the microsome-enriched lower density fluffy layer fraction (FLM1-6) from 4 independent experiments were in parallel separated on 1.21 – 1.26 g/mL Optiprep density gradients. From each gradient, the upmost low-density fraction (LM-TOP, FLM-TOP), as well as the high-density peroxisome fractions (LM-PO, FLM-PO) were eluted and analyzed by MS. MS proteome analysis continues to advance technically, making it possible to identify less common proteins and quantify the abundance of peptides with increasing accuracy. In this regard, SWATH-MS approaches were shown to provide up to more than 90 percent reproducibility allowing for the acquisition of more accurate and consistent quantitative data (Ludwig et al., 2018), and were therefore applied for the proteomic characterization of the gradient fractions.

As described in section 1.6 in sigmoidal density gradients peroxisomes separate into two adjacent bands (see FLM1+FLM2 and LM1+LM2 fractions in Figure 3-4). Since these two peroxisome fractions contain >90% peroxisomes, show no significant differences in the known peroxisome proteome and only differ insignificantly in the

degree of contaminating mitochondria (Islinger et al., 2006), both fractions were pooled to increase the protein amount subjected to the MS analyses. Initially, MS/MS experiments were run to establish a peptide-centric scoring with peptides identified in the LM and FLM fractions. As a result of this scoring study, a peptide library from the analysis of the 4 individual gradient fractions was established to reliably associate distinct peptides with their corresponding proteins in the quantitative SWATH-MS runs. Afterwards, the samples were rerun in SWATH-MS mode to compare the abundance of individual peptides and ultimately proteins in the gradient fractions.

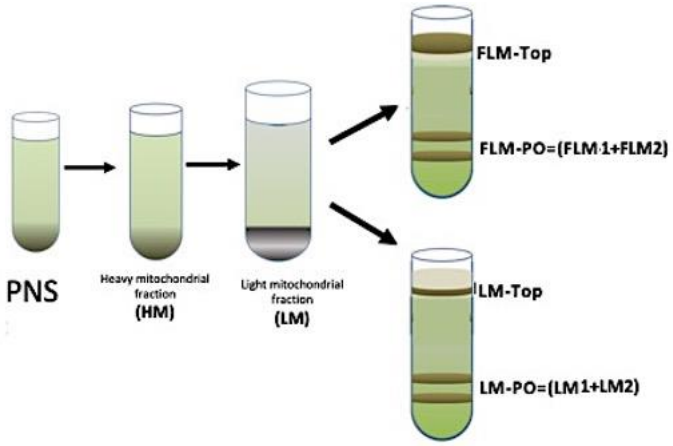

Figure 3-4: Schematic diagram of the sample preparation for SWATH-MS.

After loading the prefractions LM and FLM onto separate OptiPrep gradients., Low-density LM-TOP and FLM-TOP fractions and high-density LM-PO and FLM-PO were subjected to MS. LM-PO represents the pooled LM1 and LM2 high-density peroxisome fractions and FLM-PO the two corresponding pooled FLM1 and FLM2 gradient fractions, which were subjected to MS. The MS analyses were performed for 4 independent purification experiments.

3.2.2.1 Validation of the organelle-specific protein distribution in the subcellular fractions analyzed by SWATH-MS

The data gained from the SWATH-MS analysis was subsequently used to compare the abundance of the identified proteins in the analyzed gradient fractions. In total, 1071 proteins exhibited quantifiable peptide peak intensities across all analyzed fractions and hence were subjected to a comparative quantitative data analysis. In detail, FLM-TOP and LM-TOP fractions, FLM-PO and LM-PO fractions, FLM-TOP and FLM-PO, as well as LM-TOP and LM-PO fractions, were compared to each other in order to evaluate how different organelles distributed in the 4 analyzed fractions. Only

protein identification that exhibited significantly different protein quantities between the samples ($p < 0.05$) was considered for this analysis. To assess the distribution of peroxisomes, mitochondria, microsomes, lysosomes, and ribosomes among the enrichment of identified proteins with a known subcellular localization were compared between the four gradient fractions (Figure 3-5). The comparison of the SWATH-MS protein quantification between LM-TOP and FLM-TOP fractions reveals that 83% of the proteins enriched in the LM-TOP fraction are annotated as mitochondrial proteins. Inversely, 68% of the proteins found to be enriched in FLM-TOP are of microsomal or ribosomal origin. Thus, the SWATH-MS analysis confirms the assumption that mitochondria are the dominant organelles in the LM fraction, while the ER and ER-associated ribosomes dominate the FLM fraction.

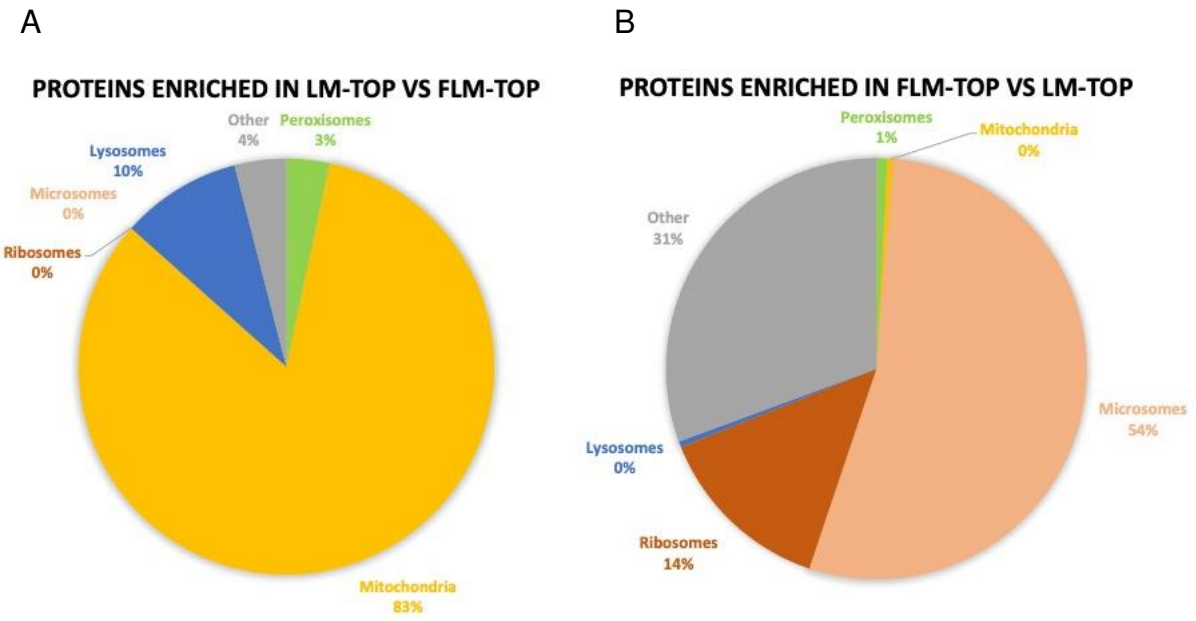

Figure 3-5: Comparison of organelle-specific protein enrichment between LM-TOP and FLM-TOP fractions according to the SWATH-MS analysis.

(A) Organelle annotations of the proteins significantly enriched in the LM-TOP fraction. The pie chart shows that 83% of enriched LM-TOP proteins are mitochondrial proteins if compared to FLM-TOP, 10% are of lysosomal/endosomal origin and peroxisomal proteins are 3%. (B) Organelle annotations of the proteins enriched in the FLM-TOP fraction. Microsomal proteins with 54% constitute the largest fraction of proteins enriched in FLM-TOP, followed by 14% ribosomal proteins when compared with LM-TOP. Of note, no lysosomal/endosomal proteins or mitochondrial proteins were found enriched in FLM-PO, while no microsomal proteins were enriched in LM-PO. Only the proteins that have significance $p<0.05$ were classified.

A quantitative comparison of the 1071 proteins between the LM-TOP and FLM-TOP fractions and the LM-PO and FLM-PO fractions, respectively, reveals that 35% and 33% of the enriched proteins in both top fractions are of mitochondrial origin whereas 34% of them are of ER origin (Figure 3-6), which might be expectable judged from the similar band intensities of ER and mitochondrial markers in LM and FLM fractions (Figure 3-3). In summary, the LM and FLM fractions contain a similar protein background in which mitochondria and ER proteins are contained in different amounts. Most importantly, known peroxisomal proteins constituted only 1% (UGT1A1, ACTG1, SOD2, SLC27A2, MGST1, CYB5A, FABP1, CYB5R3) and 2% (UGT1A1, RHOA, CYB5A, ACTG1, SLC27A2, MGST1, HSD3B3, CYB5R3, FABP1, RAB10, SOD2, RAB14, ALDH3A2) of the proteins, which were identified as enriched in LM-TOP FLM-TOP fractions, respectively, demonstrating that peroxisomes were isolated with high purity (Figure 3-6).

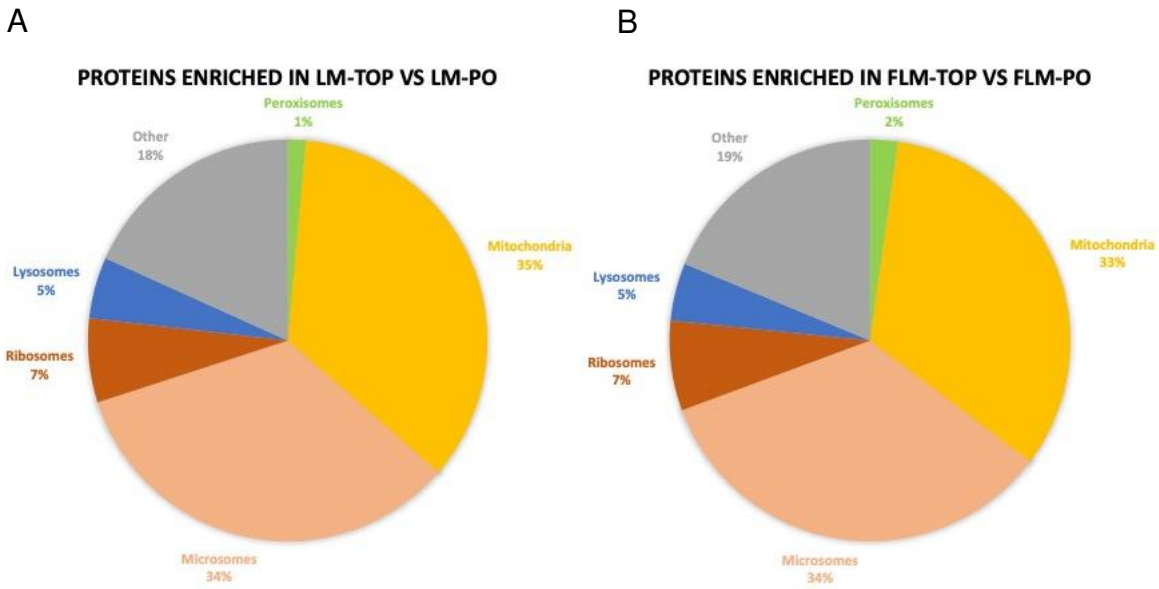

Figure 3-6: Comparison of organelle-specific protein enrichment between Gradient-TOP and PO-fractions according to the SWATH-MS analysis.

(A) Subcellular organelle distribution of proteins enriched in LM-TOP vs. LM-PO. The subcellular localization of the majority of proteins is either mitochondrial at 35% or microsomal at 34%. Only 1% of enriched proteins have been previously localized to peroxisomes. (B) Subcellular organelle distribution of proteins enriched in FLM-TOP vs. FLM-PO. The localization of the majority of proteins is either mitochondrial 33% or microsomal 34%. As for LM-TOP, only 2% of the proteins with enrichment in the FLM-TOP fraction have a previous peroxisomal annotation. Only proteins that have an enrichment with a significance $p<0.05$ were considered in the pie charts.

A reciprocal comparison of the LM- and FLM-TOP fractions with the peroxisomal fractions from the correspondent density gradients reveals that nearly all known peroxisomal proteins are highly enriched in both LM-PO and FLM-PO fractions (Figure 3-7). Moreover, LM- and FLM-PO fractions exhibit a highly similar distribution of organelle-specific proteins. In total, 52% and 61% of the proteins identified as enriched in the LM-PO and FLM-PO fraction consist of well-characterized peroxisomal proteins (average ratio LM-PO: 3.7; FLM-PO: 4.3), respectively and only 7% of mitochondrial, 13%/7% of microsomal, and 3%/4% of lysosomal proteins. Thus, despite their isolation from prefractions with a differing organelle composition, a highly similar set of proteins was enriched in both PO fractions, thereby validating the reproducibility of the SWATH-MS approach (Figure 3-7A, B).

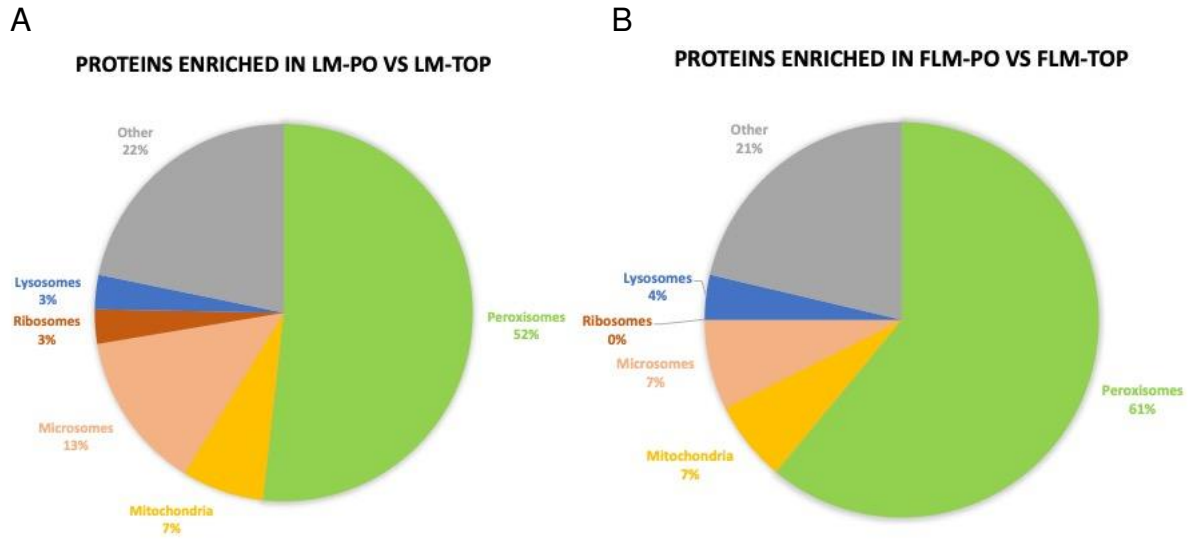

Figure 3-7: The comparison of organelle distribution of peroxisomal fractions with top fractions.

(A) shows the subcellular localizations of proteins enriched in LM-PO vs. LM-TOP. Peroxisomal proteins are 52%, mitochondrial proteins are 7% and microsomal proteins are 13% of the enriched proteins when LM-PO was compared to LM-TOP. (B) is the organelle distribution of FLM-PO. Peroxisomal proteins are 61% of this fraction whereas mitochondrial proteins and microsomal proteins are 7% compared to FLM-TOP. The other subcellular localizations are labeled on the pie chart. Only the proteins that have significance $p<0.05$ were classified.

Because of the high consistency in the composition of the LM-PO and FLM-PO-enriched proteins in comparison with top fractions, proteins found in both enrichment lists were used to annotate novel candidates for the peroxisomal mouse proteome. To

this end, LM-T/LM-PO and FLM-TOP/FLM-PO ratios were plotted on the x- and y-axis of a log2-scaled chart (Figure 3-8A). As a result, *bona fide* peroxisomal proteins align in a linear regression (R^2 = 0.8) in the “negative” quadrant of the graph. Of note, a considerable number of proteins, which were previously proposed as peroxisomal can be associated with the same quadrant implying that they are as well true peroxisomal constituents (Figure 3-8A, yellow spheres with red circles). Moreover, established microsomal and mitochondrial proteins dominate the quadrant of “positive” enrichment but can be visually discriminated by their different average enrichment factors in either FLM-TOP or LM-TOP fractions (Figure 3-8A). In this context it should be realized that some proteins previously suggested to be of partial peroxisomal localization like the mitochondrial THIL, CH60, SODM, and HMCS2 or the ER proteins UD11 and CYB5 assemble among these clusters of typical mitochondrial and ER proteins indicating that they are rather not associated with peroxisomes. A considerable number of proteins, which are known to be shared by mitochondria and peroxisomes, were found to be either enriched in both, FLM-PO and LM-PO fractions (e.g., FIS1, ATAD1) or to assemble closely to the intersection of the y- and x-axis (e.g., MAVS, MIRO1). This result indicates that they are neither increased in the peroxisome nor in the mitochondria-enriched fractions, which would be expected for proteins that are found in comparable concentrations in both organelles. Accordingly, the considerable number of orange spheres localizing to this central protein cluster might suggest that the proteome shared by both organelles might include several further proteins previously allocated to mitochondria (see orange labels in Figure 3-8A). A considerably lower number of proteins have been reported to colocalize to peroxisomes and the ER (e.g., ACSL1, DHRS7b, AL3A2). Indeed, ACSL1, DHRS7b as well as AL3A2 are located in the cluster of proteins, which are neither enriched in TOP nor PO fractions implying a dual localization to peroxisomes and the ER. However, peroxisomes also exhibit intense physical membrane contact with the ER, which might lead to the co-purification of physically associated ER proteins with peroxisomes (Costello et al., 2017). Hence, ER proteins, which are neither clearly enriched in gradient TOP- nor PO-fractions, might be not exclusively true peroxisomal proteins but also remnants of ER membranes co-purified with peroxisomes. Indeed, the allocation of both known ER tethering proteins VAPA and VAPB close to the intersection of the x- and y-axis of the graph from Figure 3-8 points to such a possibility (see labels in Figure 3-8A). Notably, in contrast to our hypothesis that constituents of ER membrane contacts should be

more abundant in FLM-PO, the ER tethering proteins VAPA, and VAPB appear to be more clearly enriched in LM-PO than in FLM-PO. Indeed, mean protein peak quantifications of VAPA and VAPB do not significantly differ between LM-PO and FLM-PO. In this regard, the resolution of the SWATH-MS approach appears to be sufficient to determine small quantitative differences between the two sample groups.

Interestingly, several small GTPases like RAB14, RAB10, RAB5C, and RAB1A/B associate with the cluster of proteins accumulating in the center of the log2 graph (Figure 3-8A). Thus, they appear to be not exclusively located in microsomes derived from the vesicular secretory system but might be associated with peroxisome membranes, where they could be involved in regulating peroxisomal fission or membrane contact formation with other organelles.

Based on the log2 LM and FLM ratios, a machine learning-based prediction model was trained in order to associate the individual proteins with the clusters “peroxisomes”, “mitochondria”, “ER”, and “multilocalized”. The performance was evaluated based on the overall accuracy of 70% observed in the random forest with relatively high prediction on all subcellular locations (Figure 3-8B).

A

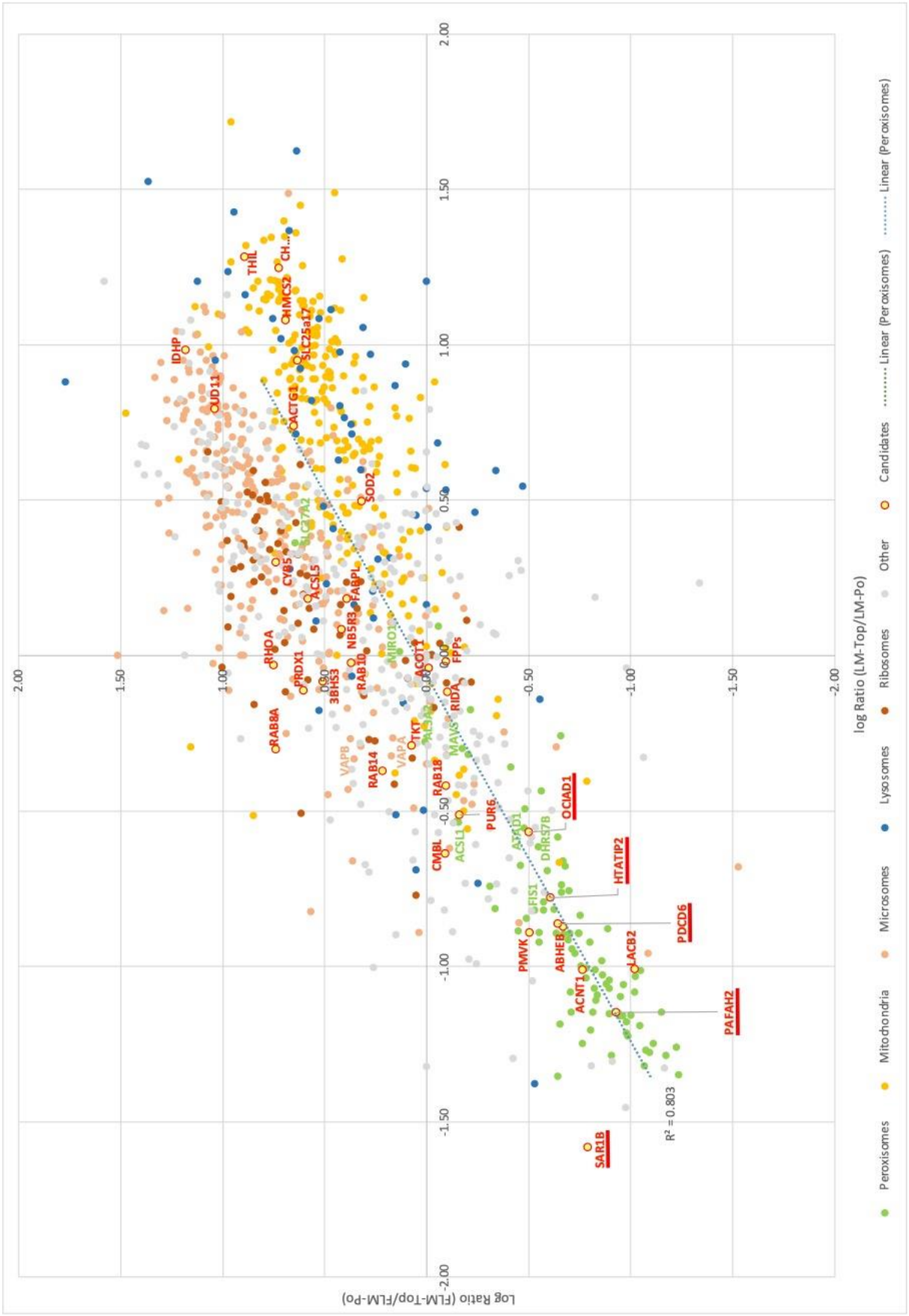
Log Ratio (FLM-Top/FLM-Po)
log Ratio (LM-Top/LM-Po)
R² = 0.803
Peroxisomes
Mitochondria
Microsomes
Lysosomes
Ribosomes
Other
Candidates
Linear (Peroxisomes)
Linear (Peroxisomes)
IDHP
CUD11
THIL
CH...
HMCS2
SLC25a17
ACTG1
SOD2
SLC7A2
CYB5
ACSL5
FABP1L
NB5R3
RHOA
PRDX1
3BHS3
RAB10
MIRO2
ACOT1
FPPS
RIDA
RAB8A
TKT
PAIS2
MAVS
VAPB
VAPA
RAB14
RAB18
PUR6
ACSL1
CMBL
ASAD1
DHRS7B
OCIAD1
HTATIP2
HS1
PDCD6
PMVK
ABHEB
LACB2
ACNT1
PAFAH2
SAR1B

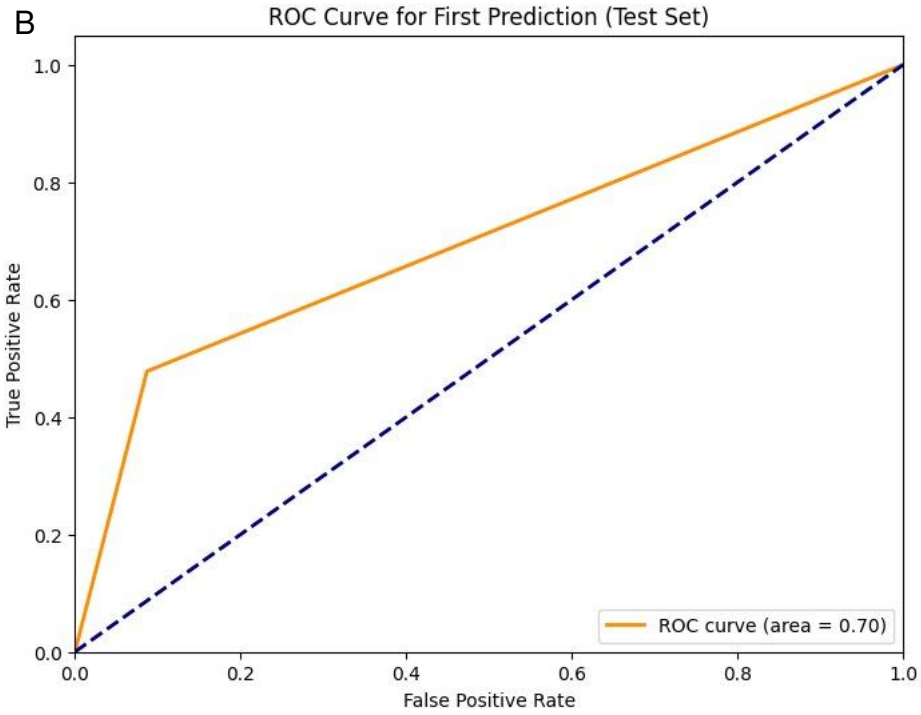

Figure 3-8: Quantitative distribution of proteins in LM-PO, FLM-PO, LM-TOP, and FLM-TOP fractions.

(A) The log2-scaled graph depicts values for FLM-TOP/FLM-PO on the y-axis and LM-TOP/LMPO ratios on the x-axis for all proteins quantified by SWATH-MS. Proteins with a peroxisome annotation are labeled in green, mitochondria in orange, microsomes in light red, ribosomes in dark red, and lysosomes in blue. FIS1, ATAD1, MAVS, and MIRO1, which are known to be shared by peroxisomes and mitochondria were labeled in green to underline their peroxisomal localization. A linear trend line was calculated from the values of all known peroxisomal proteins. Of note, the bulk of mitochondrial, microsomal, and lysosomal proteins significantly deviates from this linear regression line. Circles labeled in red with yellow filling depict potential peroxisomal candidates that have been reported in previous studies. Novel candidates are additionally labeled by red lines. (B) ROC curve shows the accuracy of 70% observed in the random forest on all subcellular locations. ROC: Receiver Operating Characteristic.

A quantitative comparison between LM-PO and FLM-PO reveals that most peroxisomal proteins are slightly more abundant in LM-PO than FLM-PO (23% of the identified peroxisomal proteins) (Figure 3-9A, C). Rather, proteins enriched in FLM-PO are 53% mitochondrial and 28% of microsomal origin (Figure 3-9B). These results imply that the FLM-PO fraction is slightly less pure than the LM-PO fraction. Indeed, the average protein enrichment for peroxisomal proteins is approximately 1.1 when

LM-PO is compared with FLM-PO fraction. Likewise, mitochondrial and microsomal proteins are on average enriched by the factor 0.92 and 0.94 respectively in FLM-PO (Figure 3-9C).

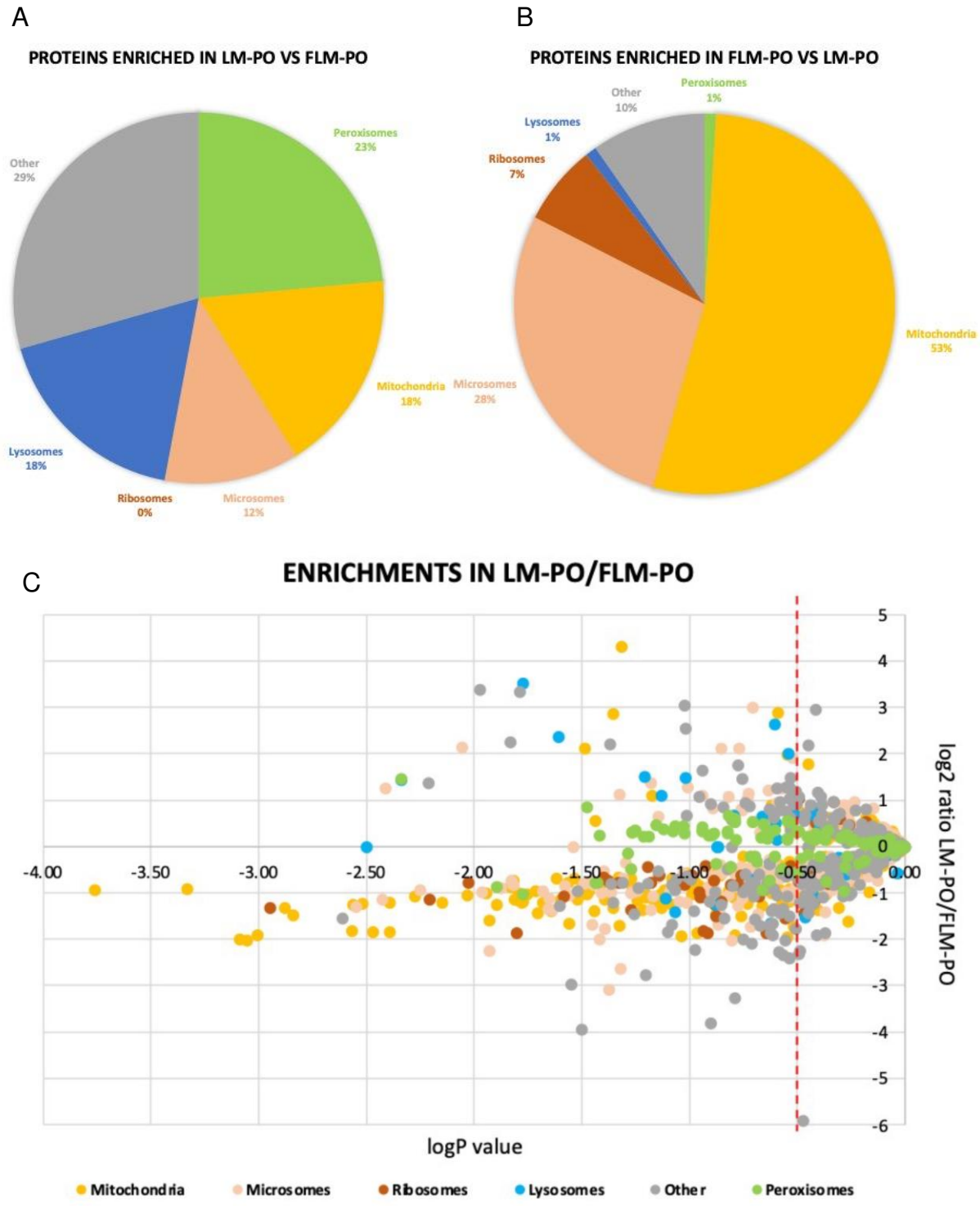

Figure 3-9: The comparison of organelle distribution of enriched protein in both peroxisomal fractions.

(A) shows the percentages of classified proteins according to their subcellular localization. The well-characterized peroxisomal proteins are 23% of peroxisomal fractions. The other subcellular localizations are labeled on the pie chart. (B) indicates the average enrichments of classified proteins. Only the proteins that have significance $p<0.05$ were classified. (C) Average LM-PO/FLM-PO ratios for proteins localized to different organelles. The red dashed line indicates the significance threshold.

In order to validate the annotation strategy, as a first step, five novel candidate proteins that were significantly enriched in both peroxisomal gradient fractions were chosen for further localization experiments (Figure 3-8A, Table 3-1). These included the oxidoreductase HTATIP2 and PAFAH2 which both possess weak predicted PTS1, PDCD6, SAR1b, and OCIAD1. For validation of the MS results, candidate protein localization was analyzed by overexpression of myc-tagged protein variants or by immunolocalization of endogenous proteins.

Table 3-1: Novel candidate proteins of mouse liver peroxisomes investigated by confocal microscopy.

Name	Gene	UniProt accession no.	Information on functional domains	PTS prediction	Localization listed by UniProt	Localization by confocal microscopy
HIV-1 Tat interactive protein 2	HTATIP2	Q9Z2G9	NAD(P)-binding Rossmann-like Domain	PTS1 Twilight zone LIQGAPHYLSSL Score: -6,512	Cytoplasm, Nucleus envelope	Peroxisomal
Platelet-activating factor (PAF) acetylhydrolase 2	PAFAH2	Q8VDG7	PAF acetylhydrolase	PTS1 Twilight zone LHLGKDRDVPKL Score: -5,831	Cytoplasm, ER membrane	Peroxisomal
Ovarian carcinoma immunoreactive antigen (OCIA) domain-containing protein 1	OCIAD1	Q9CRD0	OCIA domain	none	Endosome GO: mitochondrion	Peroxisomal and mitochondrial
Secretion-Associated Ras superfamily 1	SAR1B	Q9CQC9	GTP binding domain	none	ER membrane, Golgi apparatus	Peroxisomal and ER
Programmed cell death protein 6	PDCD6	P12825	EF-hand domain	none	ER membrane, Cytoplasm, Nucleus, Endosome	Peroxisomal and ER

3.2.1 Proteins HTATIP2 and PAFAH2 with a peroxisome-targeting sequence co-localize with peroxisomes.

The PTS1 is a tripeptide at the C-terminus of proteins that are likely to be imported into the peroxisomal matrix. Based on amino acid residue permutations previous studies established a PTS1-consensus sequence, which can be used to detect PTS1 sequences in uncharacterized proteins.

Consequently, the list of novel peroxisomal or peroxisome-associated candidate proteins from the SWATH-MS survey was mined for amino acid sequences with a C-terminal PTS1 sequence using the PTS1 predictor tool (Table 3-1). The five proteins PAFAH2, HTATIP2, LACTB2, ADE2, and HPPD showed a potential PTS1 sequence and lacked a previously confirmed peroxisomal localization. From this list, we selected HTATIP2 and PAFAH2 for further validation.

For colocalization experiments, the mouse cDNAs of HTATIP2 and PAFAH2 were fused with a myc tag on their N-termini and expressed in HepG2 cells to investigate their peroxisomal targeting. After the transfection, their potential colocalizations to peroxisomes were analyzed by confocal imaging. As shown in Figure 3-10 both HTATIP2 and PAFAH2 largely exhibit colocalizations with the Pex14 antibody signal used as a marker for peroxisomes. Thus, the results from the expression experiments validate the predicted PTS1 in both sequences and confirm the proteomics results of a bona fide peroxisomal localization.

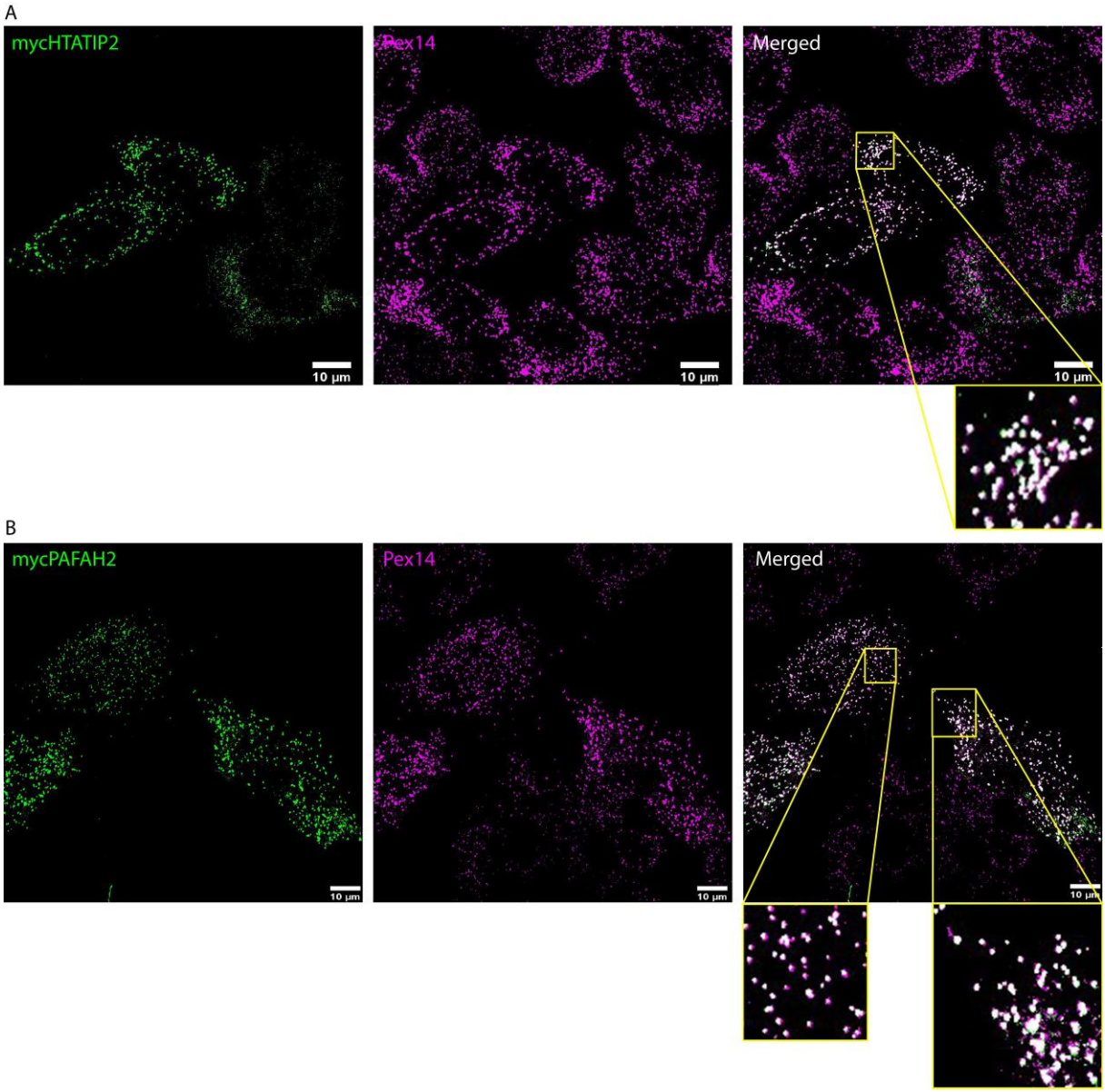

Figure 3-10: The colocalizations of HTATIP2 (A) and PAFAH2 (B) in HepG2 cells.

myc tag (green) was labeled to show the transfection of HTATIP2 and PAFAH2 constructs (green), and PEX14 (magenta) was labeled as a marker for peroxisomes. Green and magenta merged images show the colocalizations of HTATIP2 and PAFAH2 to peroxisomes. The cut-outs represent 4X magnifications from the images placed directly above.

3.2.2 Partial association of the small GTPase Sar1b with peroxisomes

The intracellular bidirectional vesicle transport between ER-Golgi-lysosome and endosome-plasma membrane is regulated by small GTPases. Peroxisomes can be as well regarded as members of the intracellular endomembrane network system, since they can be generated by *de novo* synthesis budding from the ER but might also receive phospholipids by vesicular transport for semi-self-sustaining proliferation by growth and division. This raised the question if small GTPases may play a role in

maintaining the peroxisome network. A large proteomics screen performed by Gronemeyer et al (2013) identified a few Rab GTPases localized to peroxisomes. Rab6, Rab10, Rab14, and Rab18 were detected by MS and their associations with peroxisomes by immunofluorescence analysis. In this proteomics study, we also identified Rab14 and Rab18 as candidates for a peroxisomal association. Moreover, the proteins Rab5A/C are found at similar coordinates in Fig. 3.9 and may as well play a role in peroxisomes. However, their potential association with peroxisomes requires future colocalization studies.

ARFs (e.g. ADP-ribosylation factor 1), as well belong to a subfamily of small GTPases/guanine nucleotide exchange factors (GEFs) that regulate cell behavior, organelle organization, and vesicular membrane traffic by assembling protein scaffolds to membranes. It has been suggested that the Arf family participates in COPI recruitment to the peroxisomal membrane thereby assisting in organelle fission (Just and Peränen, 2016). Since the Arf family consists of 27 members, their potential particular effect on peroxisomes still needs to be clarified. Lay et al (2006) and Just and Peränen reviewed in their papers the Arf subtypes Arf1-Arf6 and Arf1/Arf3 and reported an effect on peroxisome proliferation; moreover, for Arf6 an association with the cytoplasmic site of peroxisomes was published (Just and Peränen, 2016). In the proteomics survey from this thesis screen, however, no Arf proteins were observed to be enriched in the peroxisomal fractions. By contrast, the GEF/GTPase Sar1 (Secretion-Associated Ras superfamily 1) drew our attention since we detected the SAR1b paralog of this small GTPase with a high enrichment factor in both the fractions of purified peroxisomes. The GEF Sar1 is highly conserved among eukaryotes and involved in COPII-mediated vesicle budding required for protein trafficking from the ER to the Golgi. While Sar1a is a more general factor, Sar1b seems to act more specifically in COPII coat assembly of vesicles at ER exit sites (ERES) involved in the export of lipoproteins (e.g. ApoB) (Melville et al., 2020).To evaluate if Sar1b might also play a role in peroxisomal membrane physiology or if it may be part of co-purified membrane remnants from organelle contact sites, a myc-Sar1b construct was expressed in HepG2 cells to analyze its cellular localization.

As expected, the HepG2 cells transfected with the myc-tagged Sar1b construct show an intensive IF signal throughout the ER. Particularly the tubular ER network in the

periphery of the cells is nicely visualized. Peroxisomes, in contrast, do not directly colocalize with the myc-Sar1b signals. Despite Sar1b being found significantly enriched in both FLM and LM PO fractions (Figure 3-9), our colocalization studies revealed that its ER localization is more abundant. However, as verified by orthogonal z-plane projections of representative confocal stacks, the GTPase's ER signal pattern regularly closely encircles peroxisomes stained by antibodies against Pex14 (Figure 3-11). Of note, peroxisomal signals notably accumulate in places with a strong Sar1b signal. Hence, while the expression analysis revealed no direct localization of Sar1b at peroxisomes, the local close association between peroxisomes and surrounding Sar1b signals might visualize specific ER-PO membrane contact sites. In this context, it is interesting that so-called wrappER contacts between the rough ER and peroxisomes or mitochondria have been recently described for hepatocytes (Illaqua et al., 2022). Notably, these organelle contacts were hypothesized to coordinate the hepatocyte lipid metabolism with the export of lipoproteins into the bloodstream. Accordingly, the accumulation of Sar1b in the LM-PO and FLM-PO fractions from this work might be due to a co-purification of specialized ER membranes from such wrappER membrane contacts.

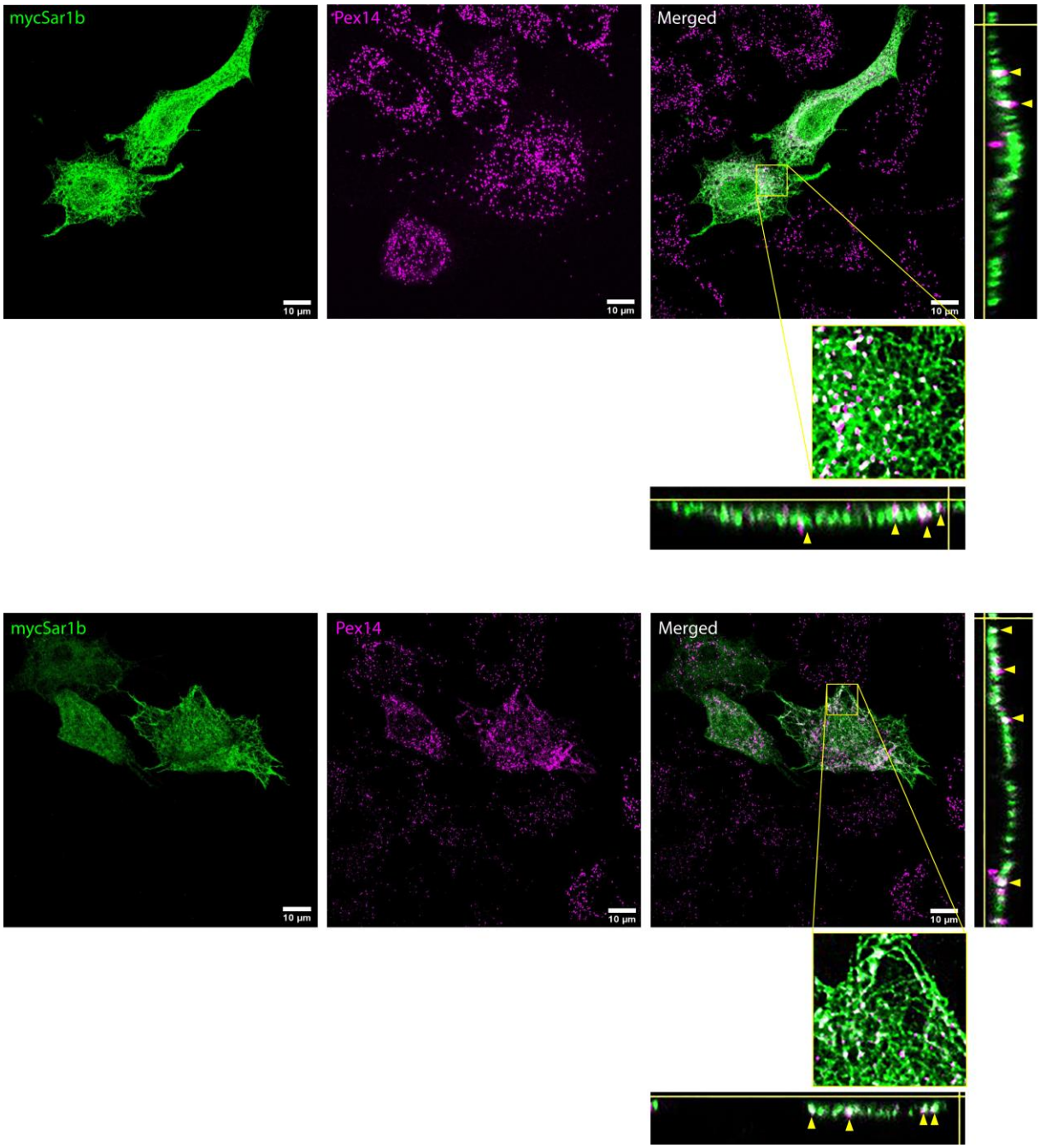

Figure 3-11: Association of Sar1b-positive ER with peroxisomes.

The association is shown by two representative images. myc-tag-staining (green) was used to show the transfection of Sar1b in HepG2 cells; PEX14-staining (magenta) was used as a marker for peroxisomes. Green and magenta merged images show a focal overlap between Sar1b and peroxisomes, especially at sites with a high Sar1b signal intensity. In the orthogonal z-plane-projections, the yellow arrowheads point out the encirclement of peroxisomes by the Sar1b signal. The cut-outs represent 4X magnifications from the images placed directly above.

3.2.3 Partial colocalization of PDCD6 with peroxisomes

Another peroxisomal candidate protein from the SWATH-MS survey is the calcium sensor and scaffolding protein “Programmed cell death protein 6” (PDCD6) also known as “Apoptosis-linked gene 2 protein” (Alg-2) (Jia et al., 2001). This protein was reported to play multiple roles in endosomal biogenesis, membrane repair, and ER-Golgi vesicular transport (Tanner et al., 2016). Since it was like Sar1b found at ERES, where it was also involved in the regulation COPII assembly, PDCD6 was selected for further analysis to evaluate if both proteins have a similar cellular localization pattern. To this end, HepG2 cells were transfected with myc-tagged PDCD6 constructs (Figure 3-12A). Generally, overexpressed PDCD6 was found in dot-like structures in the perinuclear region of the HepG2 cells. A predominant colocalization of PDCD6 with peroxisomes could not be observed but only partial colocalizations or appositions of PDCD6 to Pex14-positive peroxisomal vesicular structures were found by confocal IF microscopy. PDCD6 was also described as an endosomal resident interacting with ESCRT complexes (Okumura et al., 2013a, b). In this respect, the colocalization of PEX14 and PDCD6 may result from peroxisomes removed by autophagy. Hence, we analyzed if the dot-like PDCD6-positive structures might constitute vesicles from the endosomal/lysosomal compartment. To this end, the myc-PDCD6 transfected HepG2 cells were stained by antibodies against LAMP1 and Rab5a to mark late endosomes/lysosomes or early endosomes, respectively (Figure 3-12A). While no colocalization with Rab5a was observed some of the LAMP1-positive signals colocalize with PDCD6, however, the bulk of the PDCD6 signals did not overlap with either of the endosomal/lysosomal markers but were found in a perinuclear location suggesting a rER localization. Thus, additional PDCD6 overexpression experiments were performed and stained for Sar1b and VAPB, which were also reported to accumulate at ERES (Figure 3-12B). While Sar1b exhibited a more general ER distribution (see also Figure 3-11), especially VAPB was found to be accumulated in focal accumulations surrounding the perinuclear cell region, which might highlight the induction of large ERES by PDCD6 overexpression. Notably, both peroxisomes (Pex14) as well as PDCD6 signals were found to be accumulated in regions with a high VAPB and less obviously high Sar1b signal intensity (Figure 3-12). This might indicate that PDCD6, which was recently described as a constituent of a VAPB/CDIP1 protein complex (Inukai et al., 2021) is concentrated at ERES by interaction with VABP.

Since peroxisomes also require VABP to form contacts with ER membranes (Costello et al., 2017; Hua et al., 2017), these focal PDCD6-PEX14 colocalizations might therefore indicate peroxisome-wrappER membrane contacts, which form to regulate cellular lipid homeostasis. However, further experiments are required to substantiate this hypothesis.

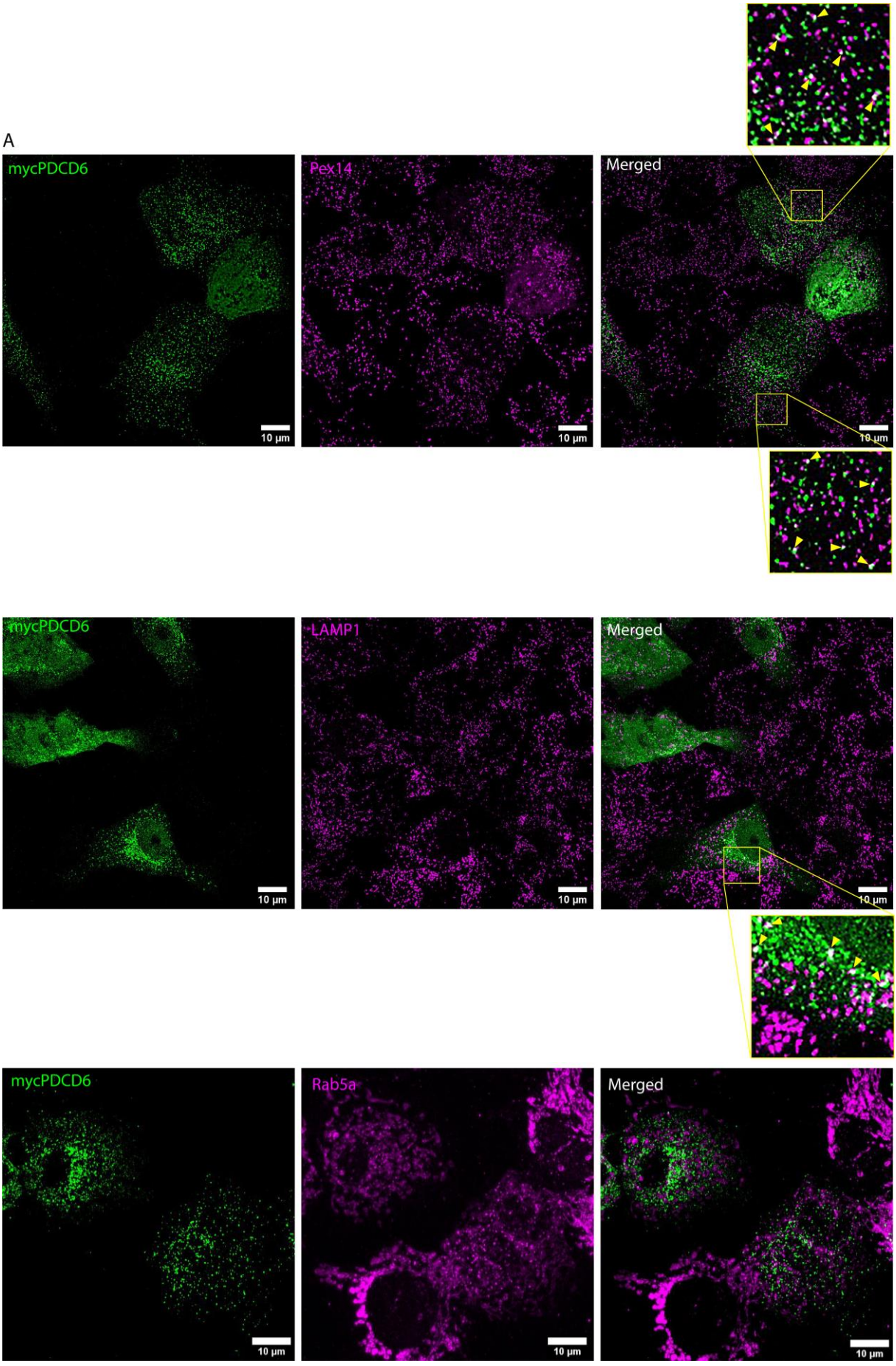
A
mycPDCD6
Pex14
Merged
10 µm
mycPDCD6
LAMP1
Merged
10 µm
mycPDCD6
Rab5a
Merged
10 µm

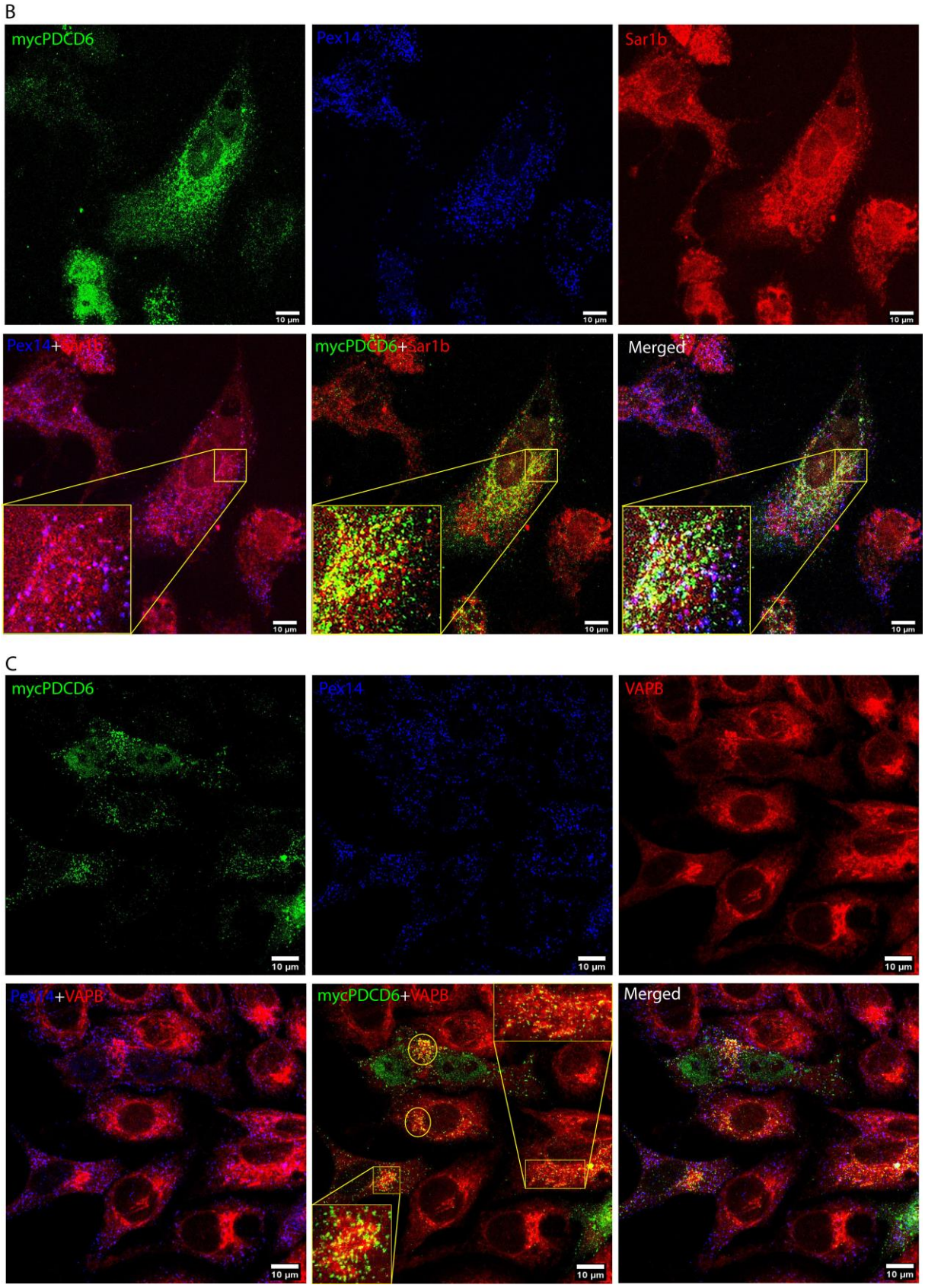

Figure 3-12: Partial colocalization of PDCD6 with peroxisomes.

(A) shows the localization of PDCD6 (green) by the co-staining of PEX14, LAMP1 and Rab5 (magenta). myc-tagged PDCD6 was accomplished by correspondent myc-antibodies (green).

The yellow arrowheads in the cut-out images show PEX14 and LAMP1 signals that partially colocalize with PDCD6. In the merged Rab5a image, no colocalization with PDCD6 was observed. (B) Costaining of PDCD6 with Sar1b (red) and PEX14 (blue). The merged images of the green and red channels show a partial overlap of PDCD6 with Sar1b but no full colocalization. Like in the overexpression experiments of Sar1b, peroxisomes can be found regularly aligned with the Sar1b-positive ER structures. The cut-outs represent 4X magnifications from the images. (C) shows the accumulation of the PDCD6-positive vesicular structures (green) in regions with high VAPB signal intensity (red). The yellow oval loops in the image of merged PDCD6 and VAPB highlight such regions. The cut-outs represent 2X magnifications from the images.

3.2.4 OCIAD1 is a protein shared by mitochondria and peroxisomes

Interestingly, another novel peroxisomal candidate from the SWATH-MS survey, the OCIA domain-containing protein 1, also known as Asrij, was described as a protein implicated in regulating mitochondrial fission/fusion (Ray et al., 2021). Moreover, in a proximity-dependent biotinylation assay (BioID), which was performed to produce a mitochondrial interaction map, an OCIAD1 bait expressed in human Flp-In T-REx 293 cells detected several peroxisomal proteins as prey (Antonicka et al., 2020). These results imply that OCIAD1 may serve as another shared component regulating peroxisomal and mitochondrial dynamics.

In order to confirm the peroxisomal localization of OCIAD1, a corresponding myc-tagged construct of the mouse cDNA was expressed in HepG2 cells. Obviously, the OCIAD1 signals adopt a typically mitochondrial network morphology (Figure 3-13A). Indeed, the Manders correlation of OCIAD1 with mitochondrial TOMM20 revealed a 95% colocalization of both signals (Figure 3-13F). However, in addition to the mitochondrial staining pattern, OCIAD1 can be also co-localized to the dot-like signals of peroxisomes with high confidence. To further verify the peroxisomal localization of OCIAD1, the cellular distribution of endogenous OCIAD1 was analyzed by immunofluorescence microscopy analysis in HepG2WT, HepG2 KO cells and MEFs. Confirming the results from the overexpression analysis, also endogenous OCIAD1 was found on peroxisomes marked by Pex14 antibodies (Figure 3-13A). Interestingly, the highest OCIAD1 signal intensities were observed in cells with a fragmented mitochondrial morphology, thus confirming publications reporting that increased

OCIAD1 expression blocks mitochondrial fusion and supports mitochondrial fission (Shetty et al., 2018; Ray et al., 2021).

OCIAD1 overexpression not only targeted the protein to mitochondria and peroxisomes but also had a significant impact on the morphology of both organelles (Figure 3-13B, D). In HepG2 WT cells, a mitochondrial network analysis was conducted, revealing that OCIAD1 overexpressing cells had a higher proportion of shorter mitochondria compared to the control based on mean and median branch lengths (Figure 3-13D). Moreover, the area occupied by mitochondrial structures within the HepG2 WT cells (mitochondrial footprint) showed an inverse correlation with OCIAD1 expression (Figure 3-13D). Peroxisomes unlike mitochondria do not fuse to form network-like structures (Carmichael et al., 2022) but multiply by growth and division in order to adjust their number dynamically to the cellular requirements. Interestingly, peroxisomes appear to be decreased in number (Figure 3-13B). In both cell lines, a quantitative assessment of the PEX14 signals confirmed the decrease in peroxisome number and total peroxisome area/cell (Figure 3-13B). Peroxisome elongation is a hallmark of intense peroxisome proliferation by growth and division (Schrader et al., 2012). Thus, the organelle circularity index (1.0 = perfectly round) gives a measure for the cellular peroxisomal proliferation activity. Interestingly, the circularity index of peroxisomes in OCIAD1 transfected HepG2 cells was significantly higher than in untransfected HepG2 cells indicating lesser tubular peroxisomes, which are in an elongation stage prior to organelle fission (Figure 3-13B). ACBD5-deficient cells generally have a reduced capacity for membrane expansion (Costello et al., 2017; Darwisch et al., 2020) and thus exhibit generally a more circular morphology. No significant change in the circularity index was observed in ACBD5-KO HepG2 cells (Figure 3-13B), which were transfected in parallel to ACBD5 WT HepG2 cells. Moreover, the decrease in peroxisome number was as well observed in the ACBD5-deficient HepG2 cells (Figure 3-13B). Remarkably, in cells with the highest OCIAD1 signal intensities, the Pex14 signals adapted a network-like mitochondrial morphology and nearly completely colocalized with mitochondrial TOMM20 (Figure 3-13C). In order to exclude bleeding of the strong 488 nm excited OCIAD1 signal into the 647 nm excited Pex14 channel, control transfections without Pex14 staining were analyzed and did not produce any signal when analyzed with the 647 nm laser (Figure 3-13E). Since in cells lacking peroxisomes Pex14 was reported to be mistargeted to

mitochondria, peroxisomes appear to be completely diminished in cells with extremely high OCIAD1 expression levels.

Judged by the optical impression, peroxisomes are less evenly distributed throughout OCIAD1 overexpressing cells but accumulate centrally at locations with a strong mitochondrial OCIAD1 signal (the yellow circle in Figure 3-13A). In order to assess these phenomena quantitatively, peroxisomes and mitochondria were analyzed via the ImageJ particle analysis tool based on their respective PEX14 and TOMM20 antibody signals. A Manders correlation analysis verified that the colocalization of the peroxisomal PEX14 and mitochondrial TOMM20 signal significantly increased to nearly 80% in response to the OCIAD1 overexpression while the colocalization is only around 60% in wild-type cells (Figure 3-13F). Hence, OCIAD1 may induce a closer apposition of both organelles potentially in order to coordinate peroxisomal with β-oxidation activity mitochondrial and OXPHOS. Since a BioID approach using the peroxisomal tethering protein ACBD5 as prey identified OCIAD1 as an interaction partner (personal communication with P. Kim, University of Toronto, Canada), ACBD5-CRISPR KO HepG2 cells (HepG2 ACBD5 KO) were transfected in addition to HepG2 wild-type (WT) to evaluate if a potential direct interaction between both proteins might induce the formation of mitochondria-PO membrane contact sites. However, peroxisomes were also frequently observed as apposed to mitochondria after OCIAD1 expression in ACBD5-KO cells. Likewise, the localization of OCIAD1 to peroxisomes in HepG2 ACBD5-KO cells confirms that OCIAD1 is directly targeted to peroxisomes (Figure 3-13A) and is not a result of apposition to mitochondria via membrane contact sites.

In summary, the colocalization experiments, confirm that HTATIP2, PAFAH2 and OCIAD1 are *bona fide* peroxisomal proteins. PDCD6 and SAR1b, in contrast, are according to the targeting experiments no endogenous constituents of peroxisomes but appear to be with respect to PEX14 signal overlaps frequently associated with the organelle, probably at membrane contacts sites between peroxisomes and specialized ER subcompartments. In this respect, the protein localization experiments, confirm the predictive value of the quantitative liver proteomics approach. However, further post proteomics analyses are required to assess if the novel candidates are true peroxisomal proteins or associated to the peroxisomes as part of an intracellular interorganellar network.

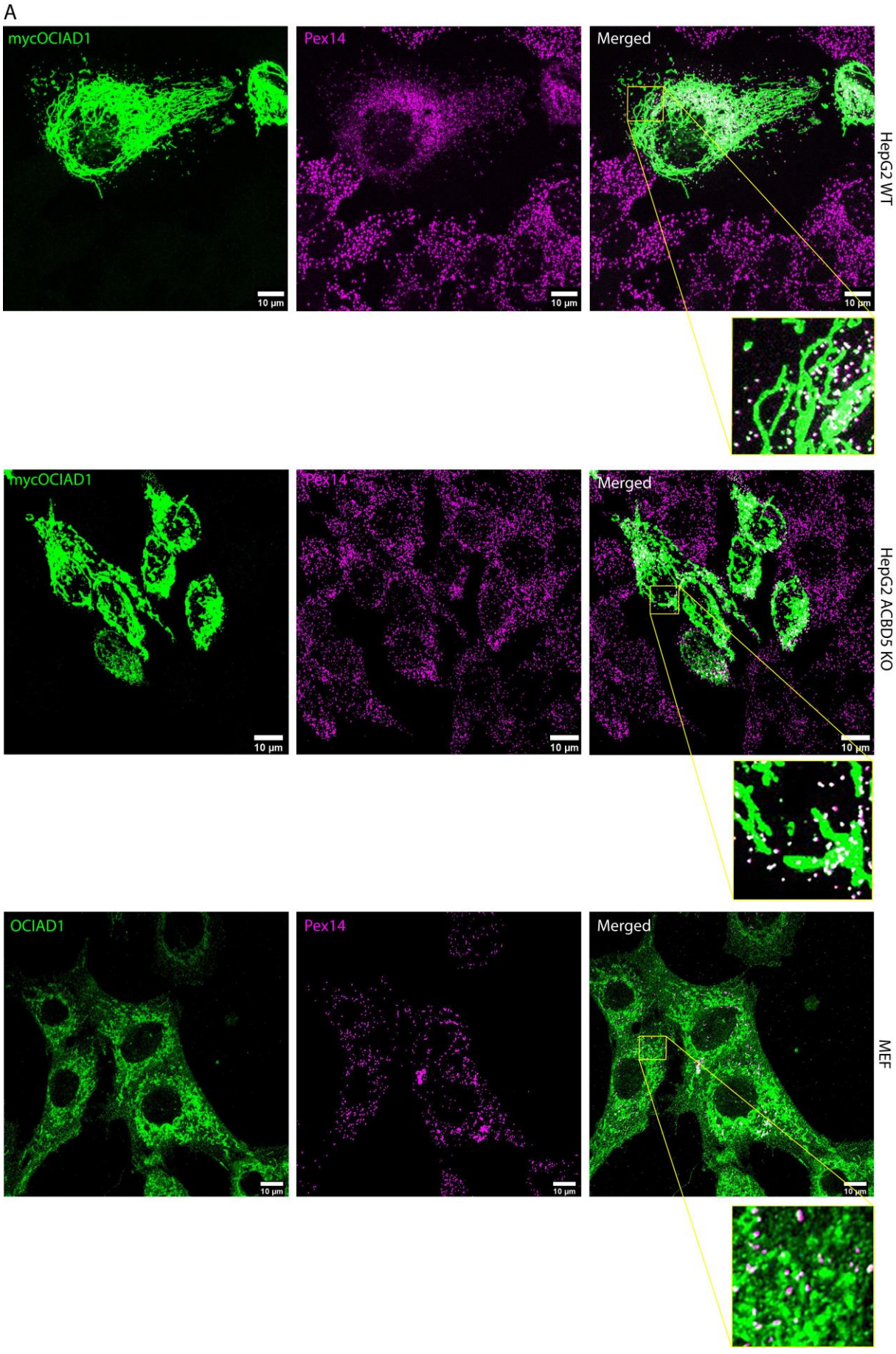
A
mycOCIAD1
Pex14
Merged
HepG2 WT
mycOCIAD1
Pex14
Merged
HepG2 ACBD5 KO
OCIAD1
Pex14
Merged
MEF
10 µm

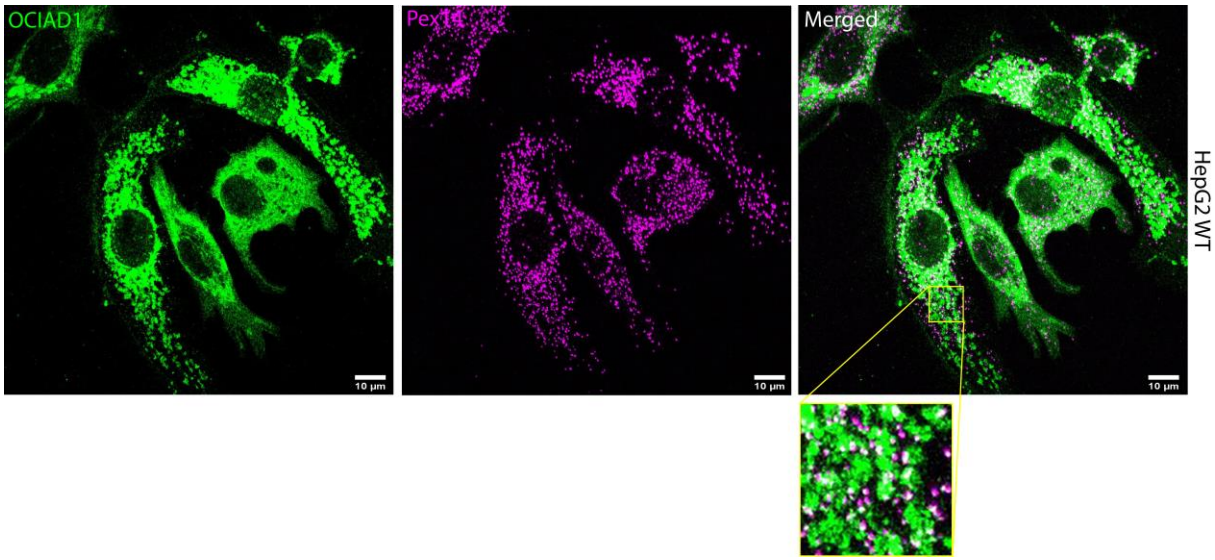
OCIAD1
Pex14
Merged
HepG2 WT
10 µm

B

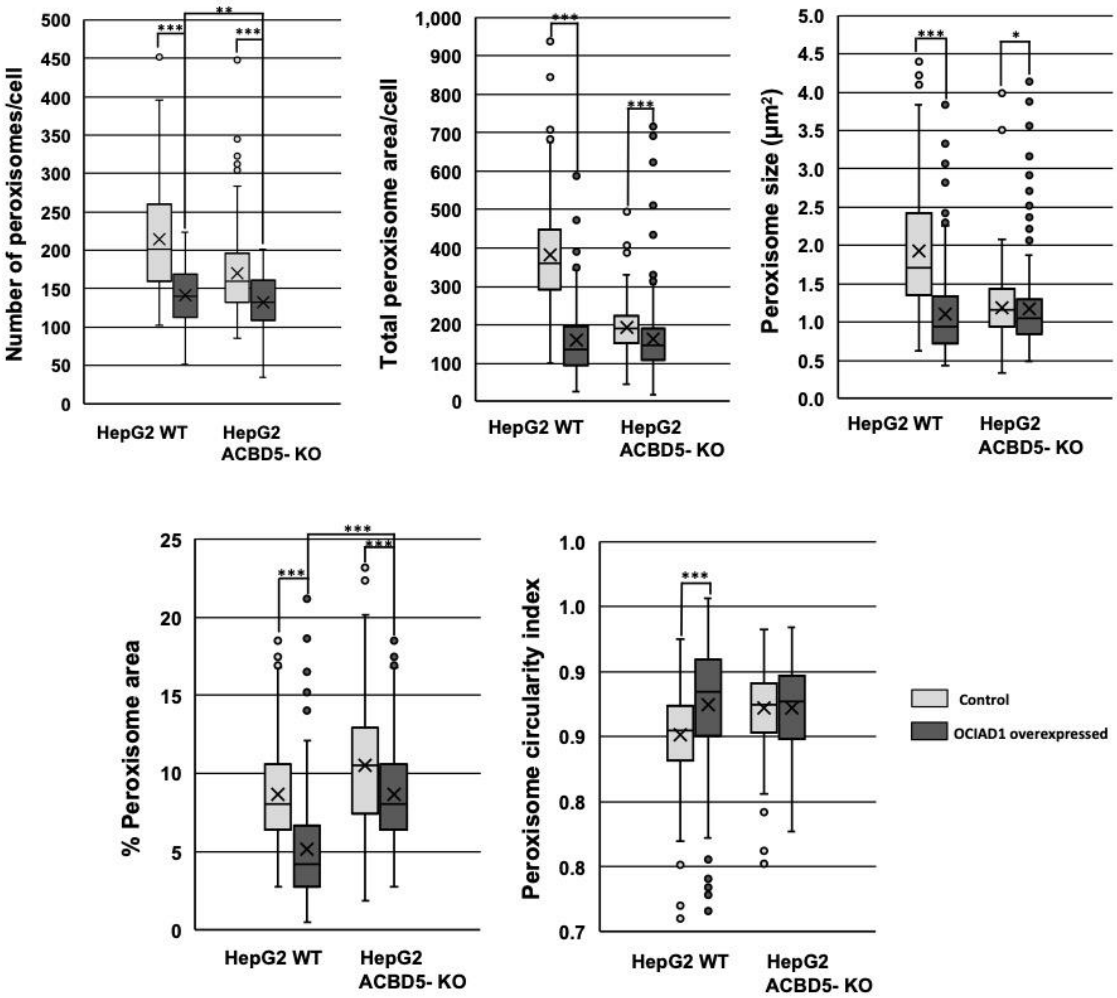
Number of peroxisomes/cell
Total peroxisome area/cell
Peroxisome size (µm²)
% Peroxisome area
Peroxisome circularity index
HepG2 WT
HepG2 ACBD5- KO
Control
OCIAD1 overexpressed

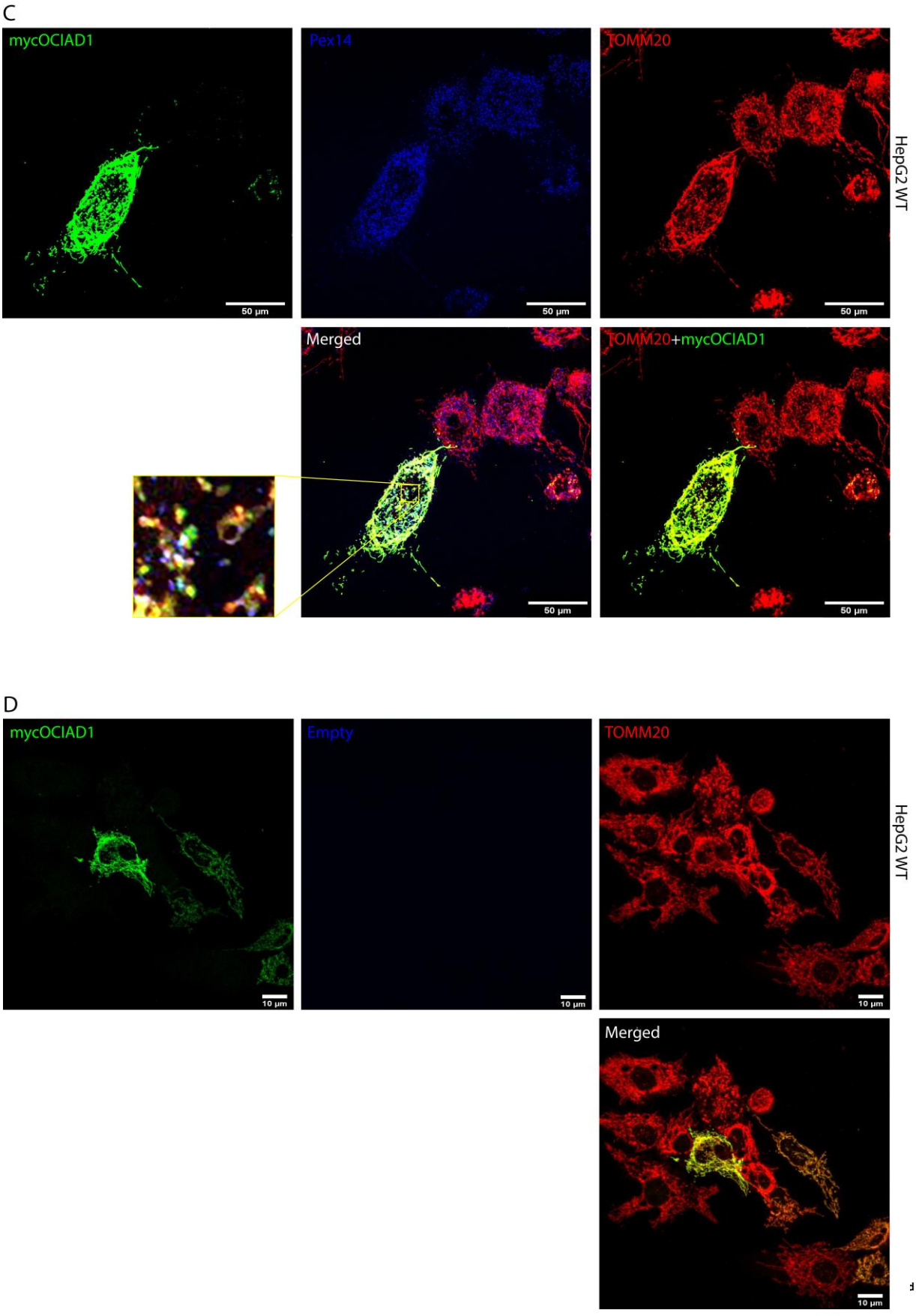
C
mycOCIAD1
Pex14
TOMM20
HepG2 WT
Merged
TOMM20+mycOCIAD1
50 µm
D
mycOCIAD1
Empty
TOMM20
HepG2 WT
Merged
10 µm

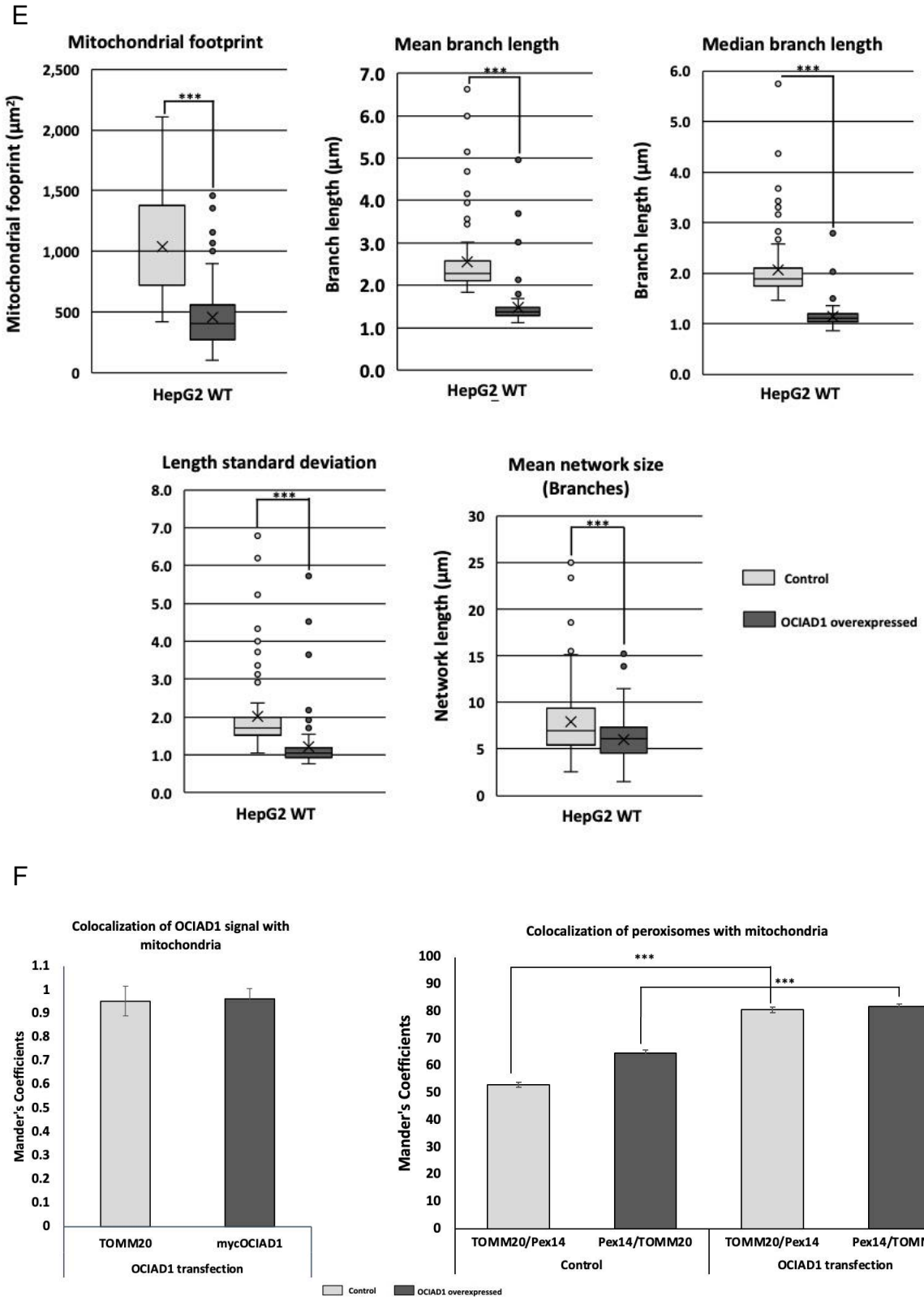

Figure 3-13: OCIAD1 colocalizes to mitochondria and peroxisomes.

(A) A myc-tagged OCIAD1 construct (green) was expressed in HepG2 WT and HepG2 ACBD5 KO cells. Peroxisomes were labeled with antibodies against PEX14 (magenta). Merged images show the colocalizations of OCIAD1 with peroxisomes (white signals). Colocalization of endogenous OCIAD1 signal with peroxisomes was further confirmed by immunofluorescence microscopy in HepG2 WT and MEF cells. Yellow circles point to areas

where peroxisomes are accumulated in areas with a strong mitochondrial OCIAD1 signal. (B) Peroxisome particle analysis was performed through ImageJ and the parameters “cellular peroxisome number”, “total peroxisome area covered per cell”, “average particle size”, “percentage of peroxisome area per cell”, and “average index of circularity” were determined in HepG2 WT and HepG2 ACBD5 KO cells. (C) The dual localization of OCIAD1 (green) to mitochondria (red) and peroxisomes (blue) was shown by adding a TOMM20 antibody as a mitochondrial marker for triple staining. The merged red and green channels show that the OCIAD1 signal nearly completely covers mitochondria. As depicted in the cut-out image from the three-channel merge the dual localization of OCIAD1 to peroxisomes in addition to mitochondria is demonstrated. The cut-outs represent 4X magnifications from the images placed directly above. Note, that the PEX14 signal colocalizes to mitochondria in cells with the highest OCIAD1 expression levels. (D) To exclude bleed-through of the OCIAD1 488 nm signal (green) to the 647 nm channel controls without PEX14 staining (blue) were performed. No signals could be observed in any OCIAD1-expressing cells at 647 nm. (E) Mitochondrial network analysis was performed with the MiNA plugin of ImageJ and the parameters were computed from 112 cells. (F) Manders correlation analysis was performed with the ImageJ JACoP plugin and the thresholded Mander’s coefficients were calculated. The co-localization of expressed OCIAD1 with TOMM20 (MITO) reveals that 95% of OCIAD1 localizes to mitochondria, whereas a minor proportion can be found at peroxisomes. The correlation of PEX14 (PO) with TOMM20 analyzed by JACoP in control and OCIAD1 transfected cells shows an increased overlap between peroxisomal and mitochondrial marker signals in response to the OCIAD1 expression. *$p < 0.05$, **$p < 0.01$, ***$p < 0.001$.

3.3 Establishment of a proteomics approach for the identification of novel candidate peroxisome-associated proteins from pig heart tissue

Cardiomyocytes preferably use fatty acid β-oxidation to produce the massive amounts of ATP required to restore continuously membrane potentials and facilitate the myosin/actin interaction required for myocardial contraction. In addition to mitochondria, fatty acid β-oxidation is performed by peroxisomes; however, there is still a considerable lack of information about the significance of these organelles for heart metabolism. Hence, a first step to generate fundamental information about peroxisome-specific pathways in cardiomyocytes can be a basic annotation of the peroxisomal proteome, which initially requires establishing a purification strategy for heart peroxisomes. In the past, peroxisomes have been efficiently isolated from soft tissues such as the liver or kidney allowing them to characterize their fundamental proteome. Since cardiomyocytes prefer fatty acids as substrates for ATP generation, peroxisomal lipid metabolic functions might have been distinctively adapted to the specialized function of this cell type. Nevertheless, peroxisomes from the heart are still poorly characterized meriting assessing their principle proteome in order to gain more information on potential heart-specific functions. However, heart tissue poses two challenges. Firstly, it exhibits considerably lower levels of catalase activity, suggesting a lower abundance of peroxisomes in this organ; second, the buoyant density of mitochondria in the heart tissue is comparable to that of peroxisomes (Fahimi et al., 1979). In conclusion, the existing protocol for isolating peroxisomes from the liver required significant revision to develop a suitable procedure for isolating peroxisomes from the heart. Since peroxisomes are significantly less abundant in heart than in liver or kidney, we decided to use hearts from pigs (*Sus scrofa domesticus*) in order to guarantee enough starting material to receive enough protein material for the proteomics experiments.

3.3.1 Optimization of the tissue disruption process

Compared to tissues with low collagen content such as the liver, kidney and brain, the homogenization process for heart tissue requires much higher mechanical forces. The conventional method of manual tissue comminution followed by direct homogenization in a Potter-Elvehjem homogenizer, commonly used for soft tissues, was hence not feasible for the rigid heart muscle. Most importantly, the considerable shearing forces applied during homogenization resulted in the disruption of relatively fragile

peroxisomes as documented by the release of the matrix enzyme catalase (see Figure 3-14B). To overcome these obstacles, an alternative approach was evaluated, inserting a tissue comminution step with a tissue blender before Potter-homogenization. While mitochondria tolerated this procedure, the more fragile membranes of peroxisomes were apparently disrupted during blending, resulting in the leakage of catalase into the cytosolic fraction (Figure 3-14), thus preventing a straightforward purification of peroxisomes with sufficient yield and purity. To make the heart tissue more accessible for homogenization, the cardiac tissue pieces were, hence, pre-digested with collagenase, at 37°C, a method typically employed to disintegrate the extracellular matrix during cardiomyocyte isolation. While this treatment reduced the leakage of catalase significantly, it led to significant degradation of peroxisomal membrane proteins like Pex14 and ABCD3 (Figure 3-14A). A reduction of the collagenase digestion temperature to 4°C, however, allowed comparable preservation of the peroxisomal catalase activities than at 37°C, while the degradation of peroxisomal membrane proteins could be avoided (Figure 3-14B, Figure 3-17B).

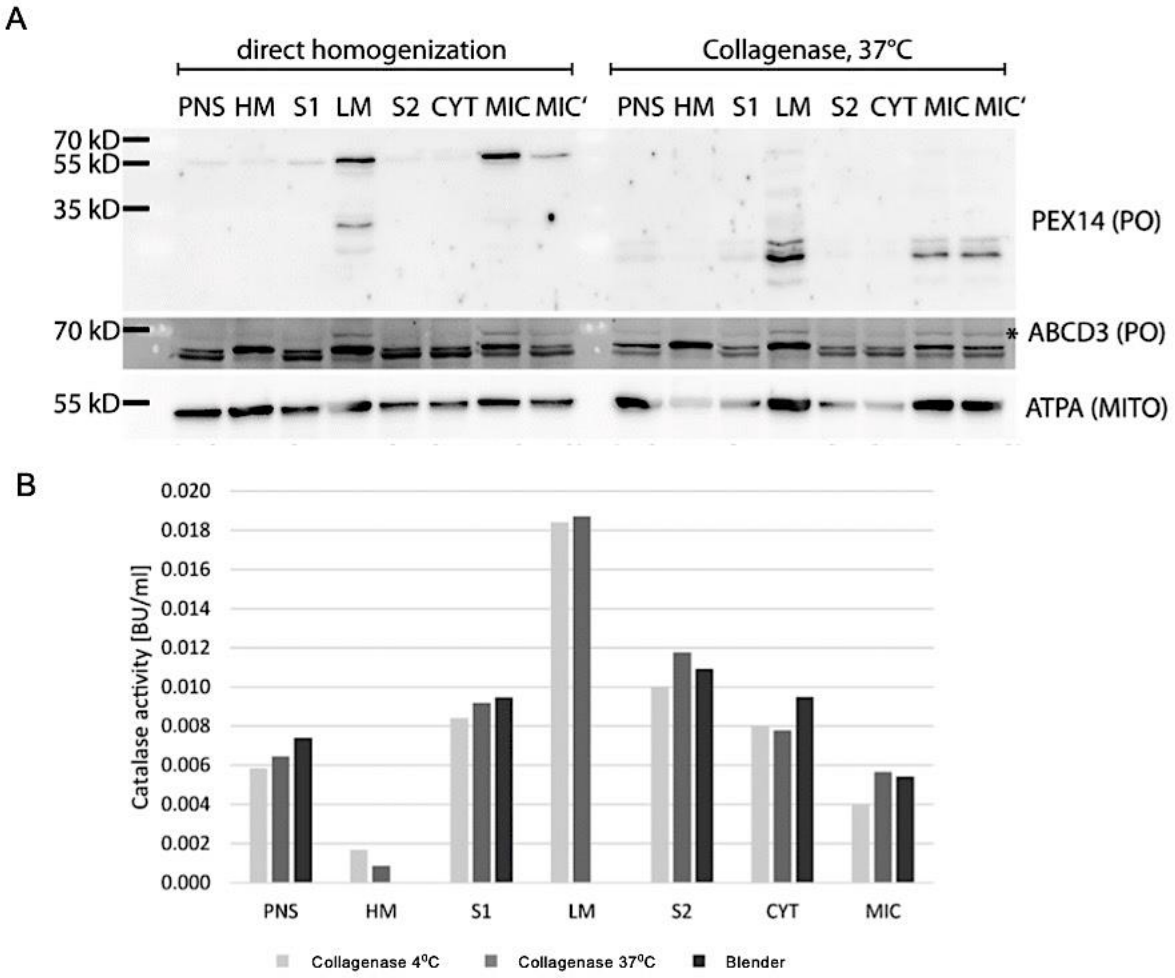

Figure 3-14: Influence of collagenase treatment of heart tissue on the yield and preservation of peroxisomes during the separation process.

(A) It was observed that collagenase digestion of the tissue at 37°C resulted in the degradation of various membrane proteins, including Pex14. This indicated that the collagenase treatment had a negative effect on the integrity of peroxisomal membranes. (B) When comparing the collagenase digestion method (optimized at 4^0C) to a rigid digestion process involving a combination of a blender and Potter homogenization, it was found that the collagenase digestion at the optimized temperature allowed for the enrichment of highly latent Catalase. The relative activity of Catalase in this fraction was at least three times higher compared to the PNS. This enriched fraction served as the starting point for subsequent density gradient centrifugation in the LM. It is worth noting that the asterisk (*) represents a band specific to ABCD3, a particular protein of interest in this study. It is worth noting that the asterisk (*) represents a band specific to ABCD3, a particular protein of interest in this study.

Despite the improvement in organelle yield achieved by the collagenase treatment, protein recovery especially in the peroxisomes, relevant high-density range remained low (approximately 0.0001 ‰ of starting material).

3.3.2 Development of a peroxisome isolation method from porcine heart tissue

In heart tissue, peroxisomes have a lower density compared to peroxisomes found in the liver, earning them the term "microbodies" (Herzog and Fahimi, 1974). To enrich peroxisomes in the prefraction subjected to density gradient centrifugation, the separation of peroxisomes from mitochondria was first optimized by adjusting the applied centrifugal forces during the differential centrifugation series. This involved optimizing the centrifugal forces used to sediment the peroxisome-enriched LM fraction and separate the bulk of mitochondria into the HM as shown by the switch of the Tom 20 signal (Figure 3-15). As a result, if compared to the protocol for liver peroxisome isolation, the centrifugal forces to produce the HM and LM pellets were raised to 6,750 × g_{max} and 48,000 × g_{max} respectively (Figure 3-15).

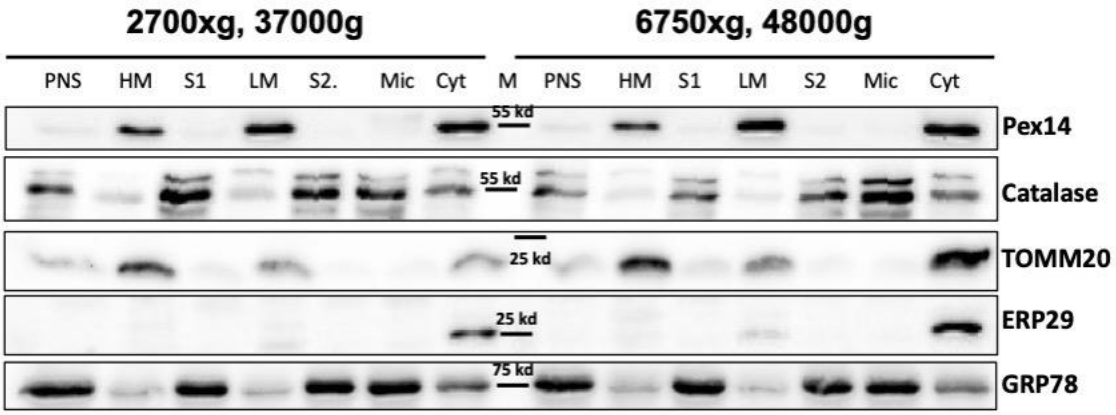

Figure 3-15: The optimization of the centrifugal force used for differential centrifugation.

Antibodies against the peroxisomal markers Pex14, Catalase; ER markers ERP29 and GRP78, and the mitochondrial marker TOMM20 were used for immunoblotting to validate the effect of centrifugal force difference. The right side of the blot represents the optimized protocol.

To achieve a maximum separation of peroxisomes from mitochondria and microsomal vesicles of the ER, tissue homogenization, density profiles, and concentrations of the gradient medium (50 - 20% Optiprep) were optimized in a series of experiments (Figure 3-14, 3-15, 3-16). The goal was to obtain an optimal separation and concentration of the peroxisome fraction while minimizing contamination by mitochondria and microsomes. Sigmoid-shaped density gradients, which are highly efficient for the isolation of peroxisome from liver and kidney, did not result in successful organelle separation when applied to tissue fractions from heart (Figure 3-16A). Hence, as an alternative, linear Optiprep gradients were gradually adapted for the isolation of peroxisomes from the heart. Unlike sigmoid-shaped density gradients, linear gradients do not provide a rapid density shift maximizing the separation of an organelle species of interest from the bulk organellar fraction but leading to partially overlapping organelle peaks across the entire gradient. To maximize the distance between peroxisomal, mitochondrial, and microsomal peaks, the density and slope of the linear gradients were gradually adjusted in a series of experiments (see Tables 2-1 and 2-2). The optimized differential centrifugation protocol resulted in HM and LM fractions with reduced mitochondrial content, as indicated by the ATPA mitochondria marker lane, while peroxisomes detected with Pex14 and Catalase showed significantly higher abundance in the LM (Figure 3-16C). However, the leakage of the highly leaky catalase (Antonenkov et al., 2004) to the LM supernatant S2 could not be entirely avoided.

The best separation by density centrifugation was achieved by using a flat density profile with a high-percentage Optiprep cushion underneath, in order to trap the lowly concentrated peroxisomes at a sharp density boundary. In order to illustrate the adaptation process, Figure 3-16 depicts results from a steep linear density gradient as previously published by Harrison & Walusimbi-Kisitu (1988) compared to a gradient with the optimized conditions used for the separations subjected to the MS analysis. While peroxisomes (Figure 3-16B, Pex14, ABCD3) partially separate from mitochondria (ATPA) and microsomes (ERp29) in a 20-50% Optiprep gradient, they only inefficiently migrate in the gradient, thereby preventing an efficiently resolved separation between the different organelle species. By comparison, peroxisomes (Pex14, Catalase) deeply migrate into the shallower 11.5%-27% gradient (maximum at LM5, LM6) and efficiently separate from microsomes. However, as well mitochondria (ATPA), which have their peak maximum at LM3, migrate into a deeper gradient fraction and are only partially separated from peroxisomes (Figure 3-16C). Nevertheless, the results from the adapted gradient provide sufficient resolution to separate the main organelle species in different peaks.

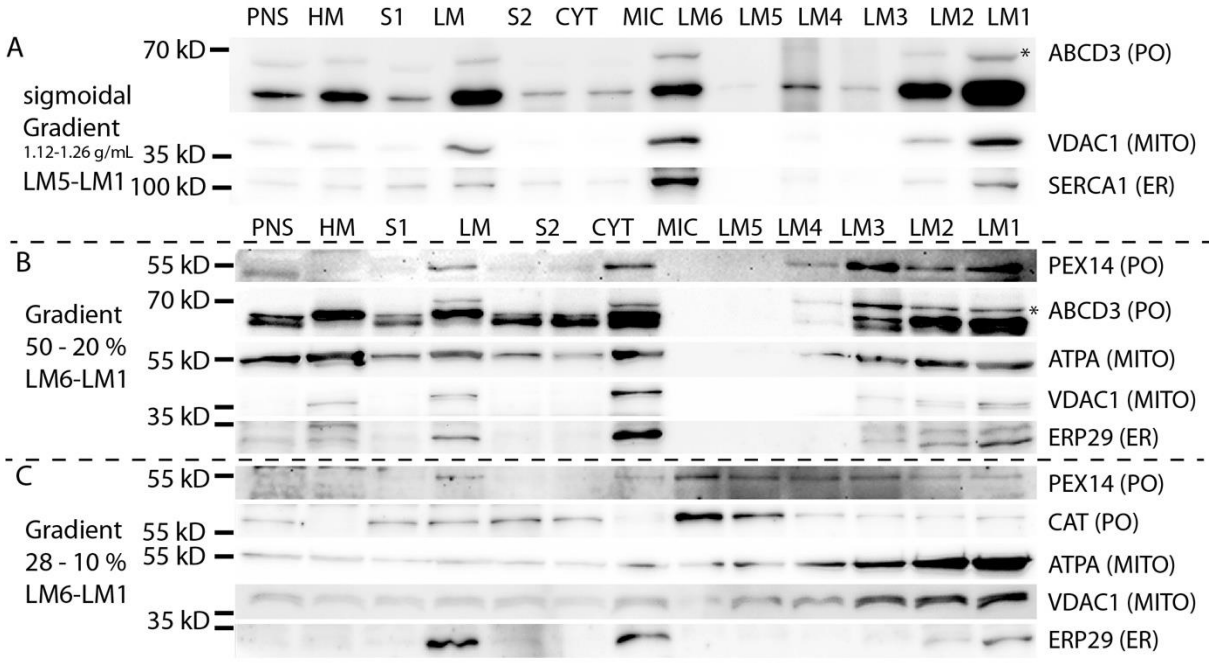

Figure 3-16: Peroxisome separation from heart tissue.

After testing a sigmoid-shaped density gradient profile (A), a linear density gradient with 20-50% Optiprep as reported by Harrison & Walusimbi-Kisitu (1988) was validated (B). (C) Optimized density gradient with a linear shallow 28-10% Optiprep gradient. Upon density gradient separation, the levels of peroxisomal proteins (Pex14, Catalase) were found to be

maximally increased in the high-density regions (A* = band for ABCD3 at approximately 70 KD, with an underlying band resulting from cross-reaction of AK with an unidentified mitochondrial protein), whereas mitochondria and the ER remain exhibit their peaks in the upper part of the gradient.

Polyethylene glycol (PEG) has been employed as a membrane stabilizer to decrease the loss of peroxisomes by membrane rupture during homogenization and purification (Antonenkov et al., 2004). The addition of PEGs of different molecular weights and concentrations to the homogenization buffer, indeed significantly increased the protein yield of the LM fraction, which was separated by density gradient centrifugation (200 mg vs. 50 mg total protein). However, the addition of 12% PEG MW1500 to the HB, as published for the isolation of liver peroxisomes (Antonenkov et al., 2004), did not yield considerable amounts of conserved peroxisomes in the LM fraction, as validated by immunoblotting against the peroxisomal marker catalase (Figure 3-17). Rather the bulk of the catalase was detected in the cytosol, indicating that most of the peroxisomes were disrupted during the isolation procedure. The addition of 4% and 2% PEG MW6000 led to a significant shift of the peroxisome density towards lighter fractions (Figure 3-17). The common phenomenon that relatively light peroxisomes shift to the high-density region in iodixanol or sucrose gradients during differential centrifugation is often attributed to the uptake of gradient medium into the organelles as a result of centrifugal forces (Islinger et al., 2018). Apparently, for microperoxisomes with their low matrix-to-membrane ratio, the insertion of PEG into the organelle membranes counteracts this effect. Hence, the bulk of peroxisomes was not satisfactorily separated from mitochondria (ATPA) or the ER (SERCA1), when PEG MW6000 was added to the HB (Figure 3-17).

Since the application of PEG did not improve yield and purity of the isolated peroxisomes, a protocol using normal HB and linear 11.5 – 27% Optiprep density gradient was finally used for the proteomics experiments. In order to gain sufficient protein for subsequent MS analysis, the protocol was upscaled from 50 to 150 g of heart tissue.

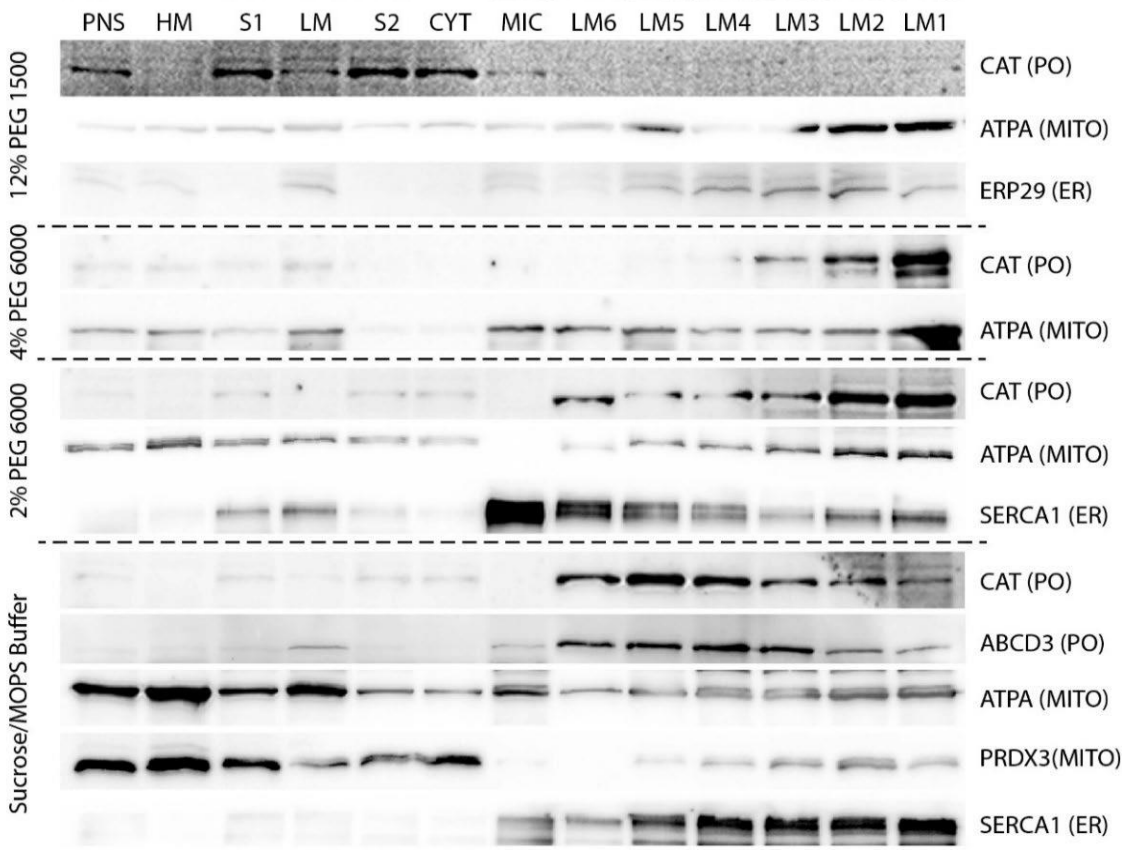

Figure 3-17: Distribution of organelle marker proteins in isolation experiments with PEG-supplemented homogenization buffer.

The respective immunoblot shows the distribution of PO, MITO and ER marker proteins in the PNS, HM, supernatant of HM (S1), LM, supernatant of LM (S2), cytosolic (CY) and microsomal (MIC) fraction of the differential centrifugation series as well as in the fractions LM1-LM6 gained by separation of the LM in 11.5 – 27 % linear Optiprep density gradients. Equal amounts of 10 µg protein/lane were subjected to SDS-PAGE. CAT: Catalase, ATPA: ATP synthase subunit alpha, ERP29: ER-resident protein 29, SERCA1: Sarcoplasmic/endoplasmic reticulum calcium ATPase 1, ABCD3: ATP-binding cassette sub-family D member 3, PRDX3: Peroxiredoxin-3 (which localizes in mitochondria and cytosol).

3.3.3 Validation of the separation procedure for the isolation of peroxisomes from the pig heart by mass spectrometric protein quantification

As observed by the immunoblotting experiments, the linear Optiprep gradients do not provide the resolution to isolate peroxisomes with the highest purity or to separate individual organelles into distinct bands. As an alternative, when organelles are not completely separated from each other, the distribution profiles of the individual organelles across the gradient fractions can be used to define organelle-specific peaks. Accordingly, identified proteins by MS can be associated with distinct organelles according to the separation profiles of known marker proteins. To validate, if the developed linear density gradient would have sufficient resolution to separate the main organelle species into different peak zones for such an organelle profiling method, a HyperLOPIT proteomics approach was employed (Christoforou et al., 2016). To this end an 11.5% - 27% linear Optiprep gradient was eluted into six equal-sized fractions, which were subsequently analyzed by MS using label-free peptide quantification in a "gradient profiling" approach (in collaboration with AG Lenz, Universitätsmedizin Göttingen, 2 technical replicates/fraction).

A more detailed analysis of the distribution of established organelle marker proteins throughout fraction LM1 – LM6 revealed organelle-specific enrichment patterns: Based on the peptide profiles the relative enrichment factors of the proteins, catalase, ACOX1, ACOX2, and GNPAT indicate that peroxisome abundance is progressively increasing from fraction LM1 towards higher density culminating in fraction LM6 (Figure 3-18A). In contrast, proteins known to localize in mitochondria, or the ER showed different enrichment profiles (Figure 3-18B, C): the mitochondrial proteins COX5A, ATAP5F1C, IMMT, MDH2 have their peak abundance in fraction LM2, while the ER residents GRP78, SGPL1, JPH2, PRDX4 have their peak in the lightest fraction of the gradient LM1. The abundance profiles of the protein representatives of both organelles continuously decline from their peak towards increasing density (Figure 3-18B, C). By contrast a protein with a bimodal localization, like GSTK1, which is present in peroxisomes and mitochondria (Figure 3-18A), exhibited a flat relative enrichment profile compared to proteins exclusively found in peroxisomes. Likewise, proteins with a partial association with peroxisomes, such as through membrane contacts (VAPA/B), did not show enrichment in the peroxisomal fractions (not shown). Principally, however,

characteristic profiles for proteins localized to peroxisomes, mitochondria, and the ER could be established according to their distinctive gradient distribution.

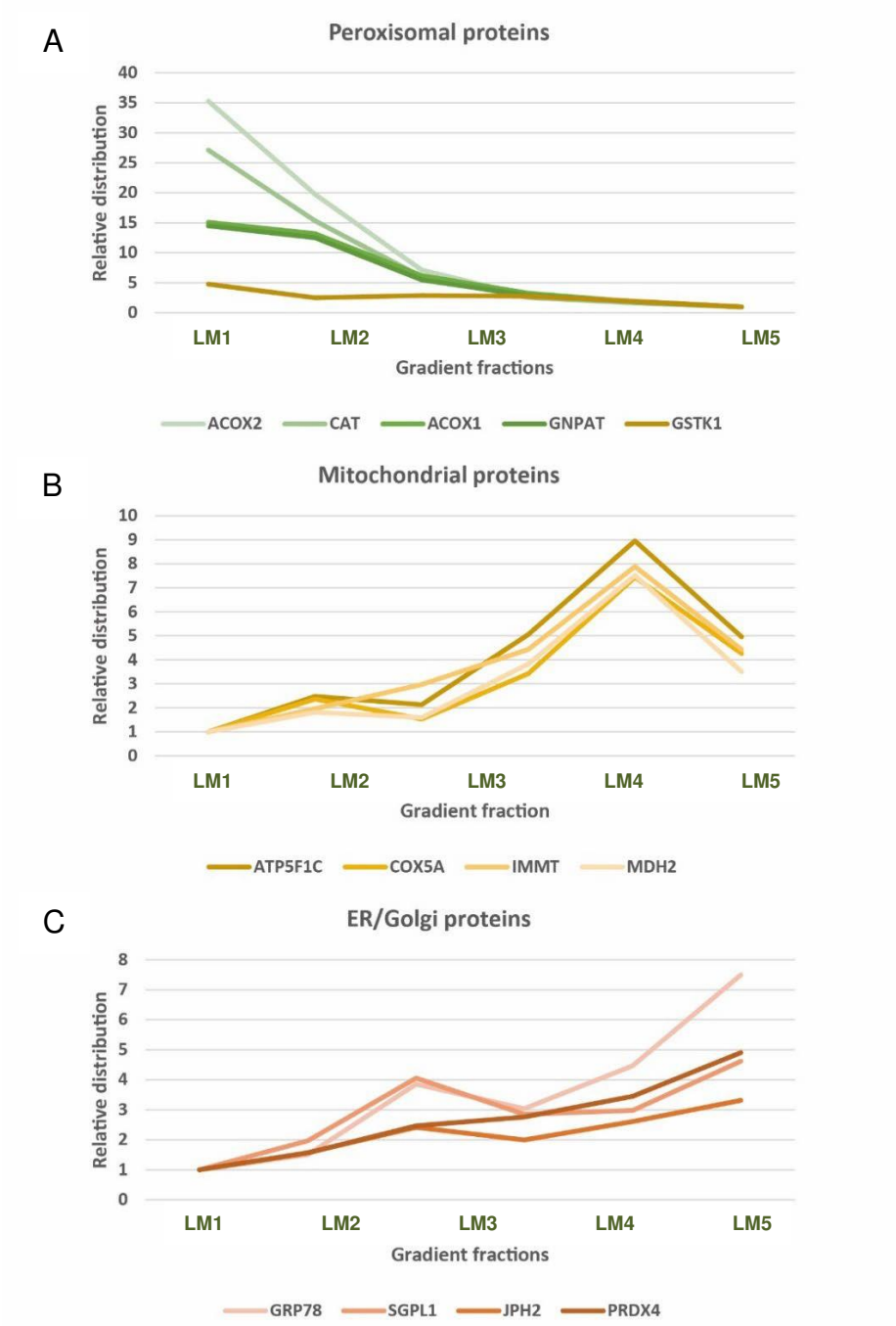

Figure 3-18: Validation of the suitability of the density gradient separation method for a subsequent organelle profiling approach.

(A) (ACOX1: Acyl-CoA oxidase 1, ACOX2: Acyl CoA oxidase 2, CAT: Catalase, GNPAT: Dihydroxyacetone phosphate acyltransferase, GSTK1: Glutathione S-transferase kappa 1), (B) In mitochondria (ATP5F1C: ATP synthase subunit gamma. COX5A: Cytochrome c oxidase subunit 5A, IMMT: MICOS complex subunit MIC60, MDH2: Mitochondrial malate

dehydrogenase and (C) in ER/Golgi Compartment (GRP78: Endoplasmic reticulum chaperone BIP SGPL1: Sphingosine-1-phosphate lyase 1, JPH2: Junctophilin-2, PRDX4: Peroxiredoxin-4)

3.3.4 Organelle distribution identified proteins from pig heart tissue

In order to annotate the proteome of pig heart peroxisomes, LM1-LM6 fractions from two independent organelle fractionation experiments were subjected to MS analysis. For each gradient fraction, 4 technical replicate MS runs were conducted per experiment. MS analysis identified peptides corresponding to 9948 genes, resulting in 4725 protein groups that included these genes. However, several protein groups containing uncharacterized and keratinocyte proteins were excluded from the analysis. As a result, a total of 4543 proteins were selected for quantification and further investigation of their gradient profiles.

PCA (Principal Component Analysis) validation revealed that the peroxisome-enriched fractions, LM1 and LM2, partially overlap but are distinctly separated from LM4, LM5, and LM6. The variation in principal component-1 (PC1) explains most of the variability of the data (38,76%) which makes the x-axis direction the main direction of the difference between the sample groups (Figure 3-19A). A comparison of LM1 and LM6 by a Volcano plot confirms that these two fractions contain largely distinct sets of proteins, as would be anticipated (Figure 3-19B).

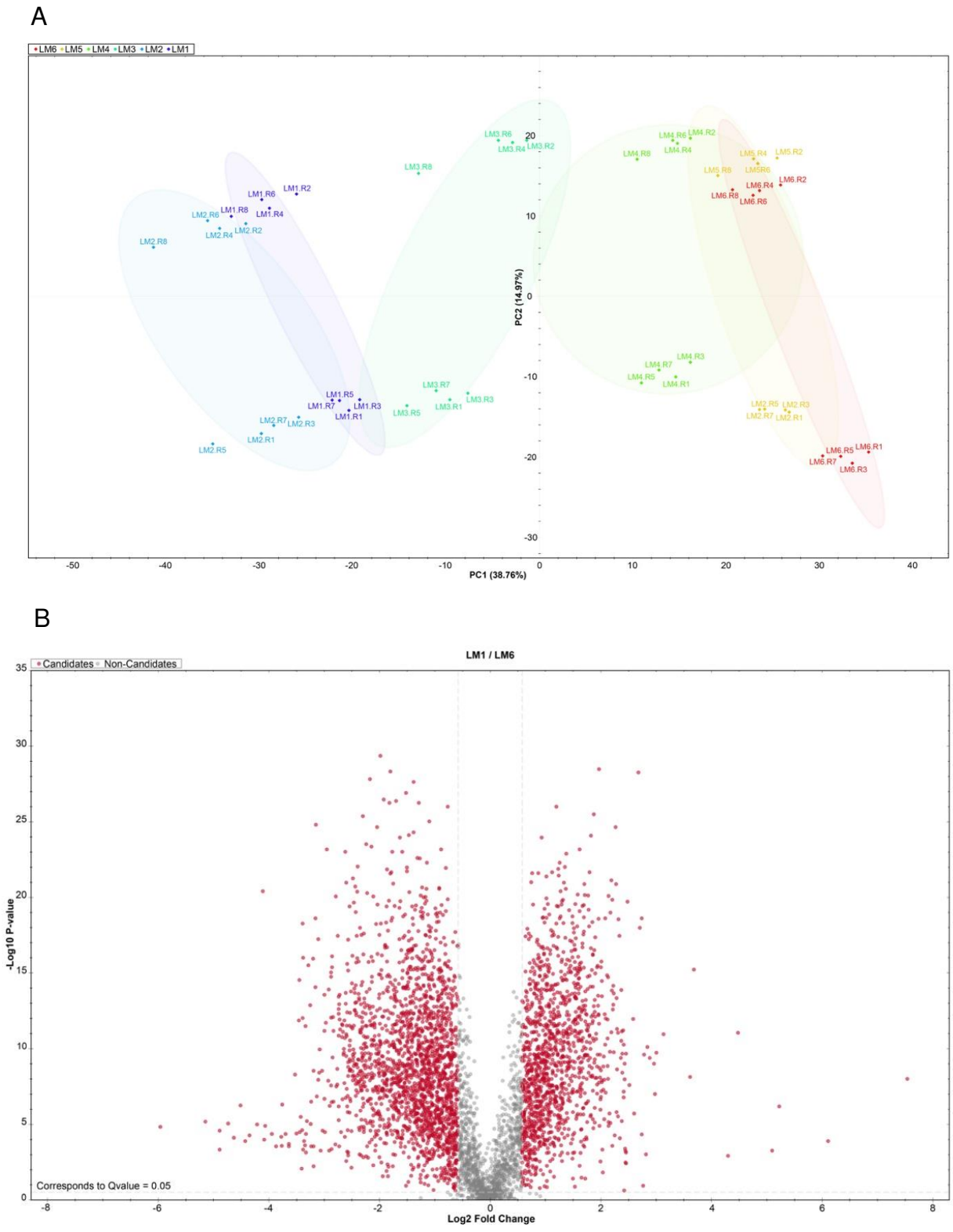

Figure 3-19: PCA analysis of LM fractions from pig heart and comparison of LM1 and LM6 fractions

(A) Principle Component Analysis according to the proteins quantified in the LM density gradient fractions. The colors denote individual LM fractions. Red: LM1, yellow: LM2, light green: LM3, dark green: LM4, blue: LM5, purple: LM6. The square of corresponding colors represents the six experimental replicates. Principal component-1 (PC1) with 38.76%

variability (B) Volcano plot comparison of the protein quantifications from fraction LM1 and LM6. The multitude of proteins, which are significantly enriched in either LM1 or LM6 indicates the substantially different protein composition of the two fractions. Grey dots symbolize protein identification, which is not significantly enriched in either fraction (threshold 1.5) between LM1 and LM6. The red dots are significant and above the 1.5-fold threshold values. Multiple testing correction Q value=0.05.

According to the subcellular localization information available in UniProt, from the proteins identified in the MS runs across the fraction LM1-LM6, 843 proteins (17%) were previously associated with mitochondria. The majority of proteins, 2411 (50%), were primarily located in the cytoplasm, nucleus, or other small compartments within the cell. Microsomes accounted for 549 proteins (11%), followed by 430 export proteins (9%), and 296 proteins (6%) associated with lysosomes or endosomes. Additionally, 243 proteins (5%) were related to the Golgi apparatus. A small subset of 81 proteins (2%) were assigned to either the peroxisome or the peroxisomal membrane (Figure 3-20).

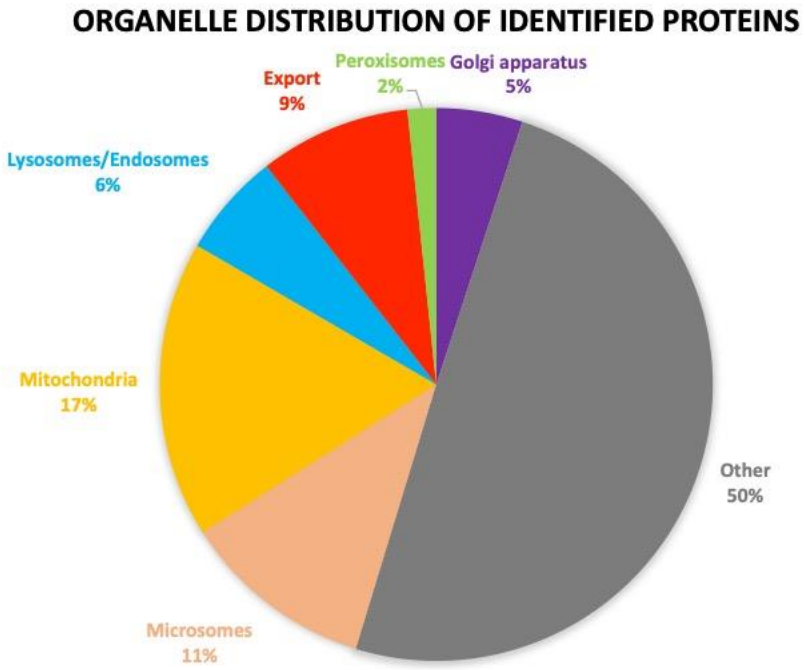

Figure 3-20: Organelle distribution of peroxisomal proteins.

(A) shows the percentages of proteins classified according to their subcellular localization. The well-characterized peroxisomal proteins constitute 2% (81 proteins, green) of LM fractions. The other subcellular localizations are labeled on the pie chart.

To identify new peroxisomal protein localizations, the frequency distribution of 25 known peroxisomal proteins was analyzed across the gradient. The relative abundances of these proteins were averaged per fraction to create a master profile (Figure 3-21). In this way, the calculated master profile for peroxisomal proteins showed declines with a linear regression from LM1 to LM6 (Figure 3-21A). Likewise, master profiles for mitochondria, the ER (microsomes), and lysosomes were created to average the different abundances of 25 proteins per organelle in six fractions (Figure 3-21 B, C, D). The master profiles of each organelle through the fractions were summed to indicate that organellar proteins show different enrichments among fractions (Figure 3-21F).

A closer examination of individual mitochondrial separation profiles revealed that a subset of mitochondrial proteins significantly deviated from the mitochondrial master profile since they did not peak in LM2 but in higher-density fractions (Figure 3-21E). Hence, this subset of mitochondrial proteins with separation profiles, which differed from the bulk mitochondrial proteins, was further examined. Of note, all proteins of this mitochondrial sub-cluster could be functionally associated with the transcription and translation of mitochondrially inherited genes (e,g, MRPL18, MRPS28, MTG2, EARS2, SSBP1, TACO1). Since transcription in mitochondria is not performed in a nuclear compartment but in the mitochondrial matrix, newly synthesized RNA, RNA processing proteins, and mitoribosome assembly factors assemble in a punctate subcompartment termed the mitochondrial RNA granule (MRG) (Rey et al. 2020). Obviously, MRGs released from mitochondria, which were disrupted during the purification process, sediment, like peroxisomes, in the high-density range of the Optiprep gradients. An assembly of a selection of 25 MRG-associated proteins to a master profile, however, shows that these proteins indeed exhibit their maximum concentration in LM1 but possess a second peak in the for other mitochondrial proteins typical LM5 fraction. Therefore, proteins from mitochondrial RNA granules might be discriminated from peroxisomal ones, which continuously increase in concentration from LM6-LM1 (Figure 3-21E).

A

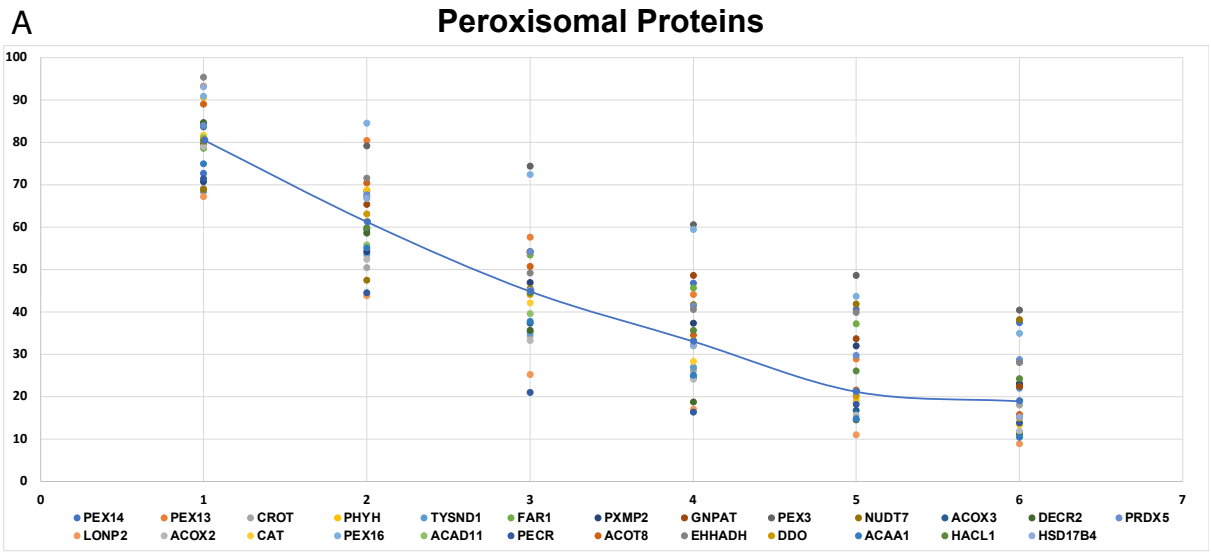
Peroxisomal Proteins
100
90
80
70
60
50
40
30
20
10
0
0
1
2
3
4
5
6
7
PEX14
PEX13
CROT
PHYH
TYSND1
FAR1
PXMP2
GNPAT
PEX3
NUDT7
ACOX3
DECR2
PRDX5
LONP2
ACOX2
CAT
PEX16
ACAD11
PECR
ACOT8
EHHADH
DDO
ACAA1
HACL1
HSD17B4

B

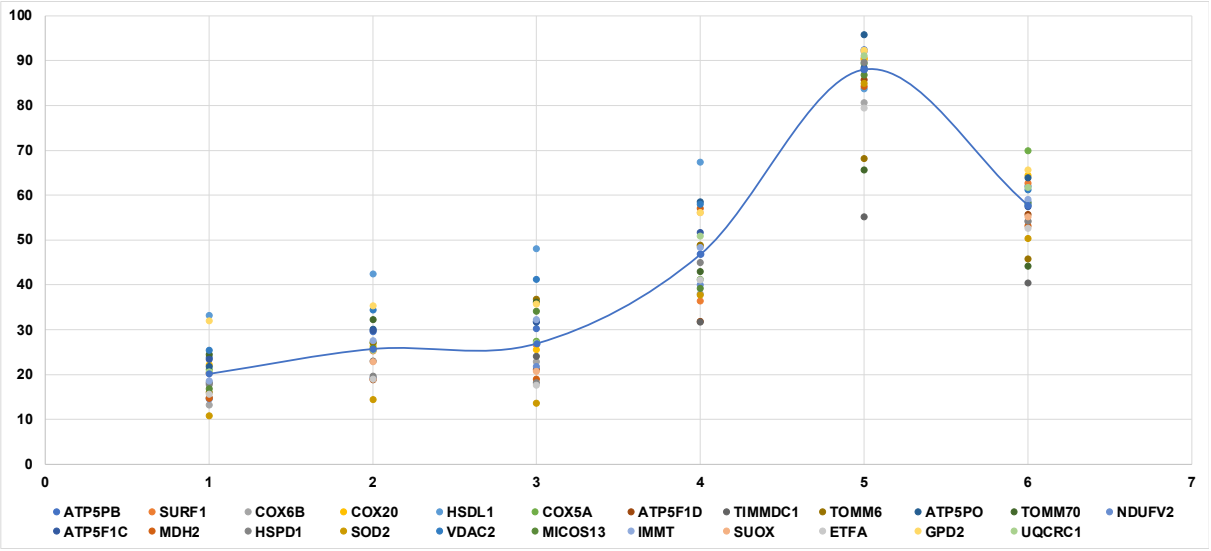
Mitochondrial Proteins
100
90
80
70
60
50
40
30
20
10
0
0
1
2
3
4
5
6
7
ATP5PB
SURF1
COX6B
COX20
HSDL1
COX5A
ATP5F1D
TIMMDC1
TOMM6
ATP5PO
TOMM70
NDUFV2
ATP5F1C
MDH2
HSPD1
SOD2
VDAC2
MICOS13
IMMT
SUOX
ETFA
GPD2
UQCRC1

C

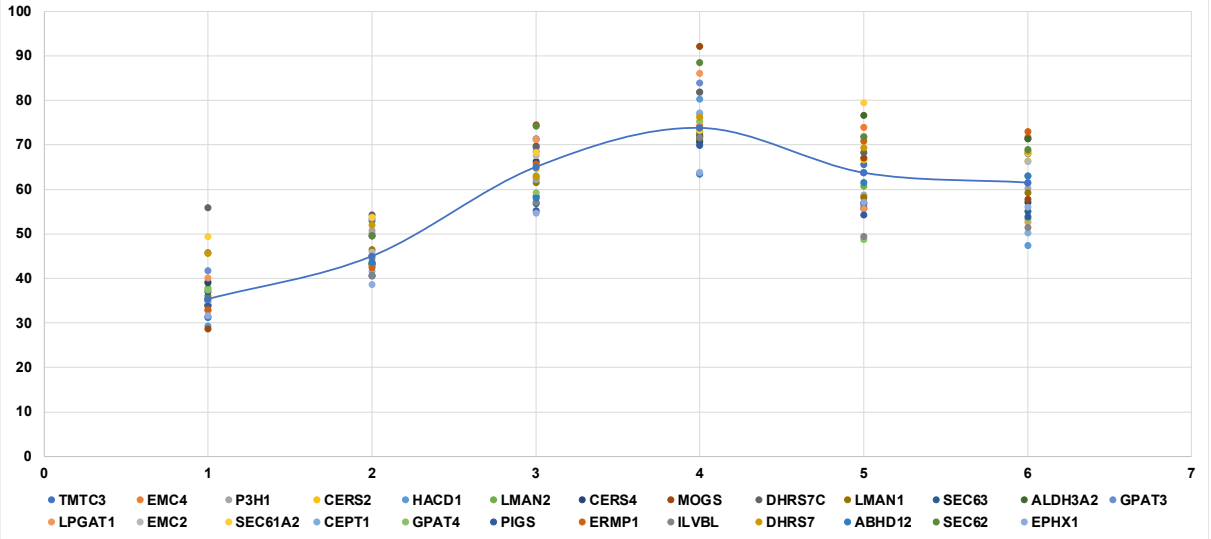
ER Proteins
100
90
80
70
60
50
40
30
20
10
0
0
1
2
3
4
5
6
7
TMTC3
EMC4
P3H1
CERS2
HACD1
LMAN2
CERS4
MOGS
DHRS7C
LMAN1
SEC63
ALDH3A2
GPAT3
LPGAT1
EMC2
SEC61A2
CEPT1
GPAT4
PIGS
ERMP1
ILVBL
DHRS7
ABHD12
SEC62
EPHX1

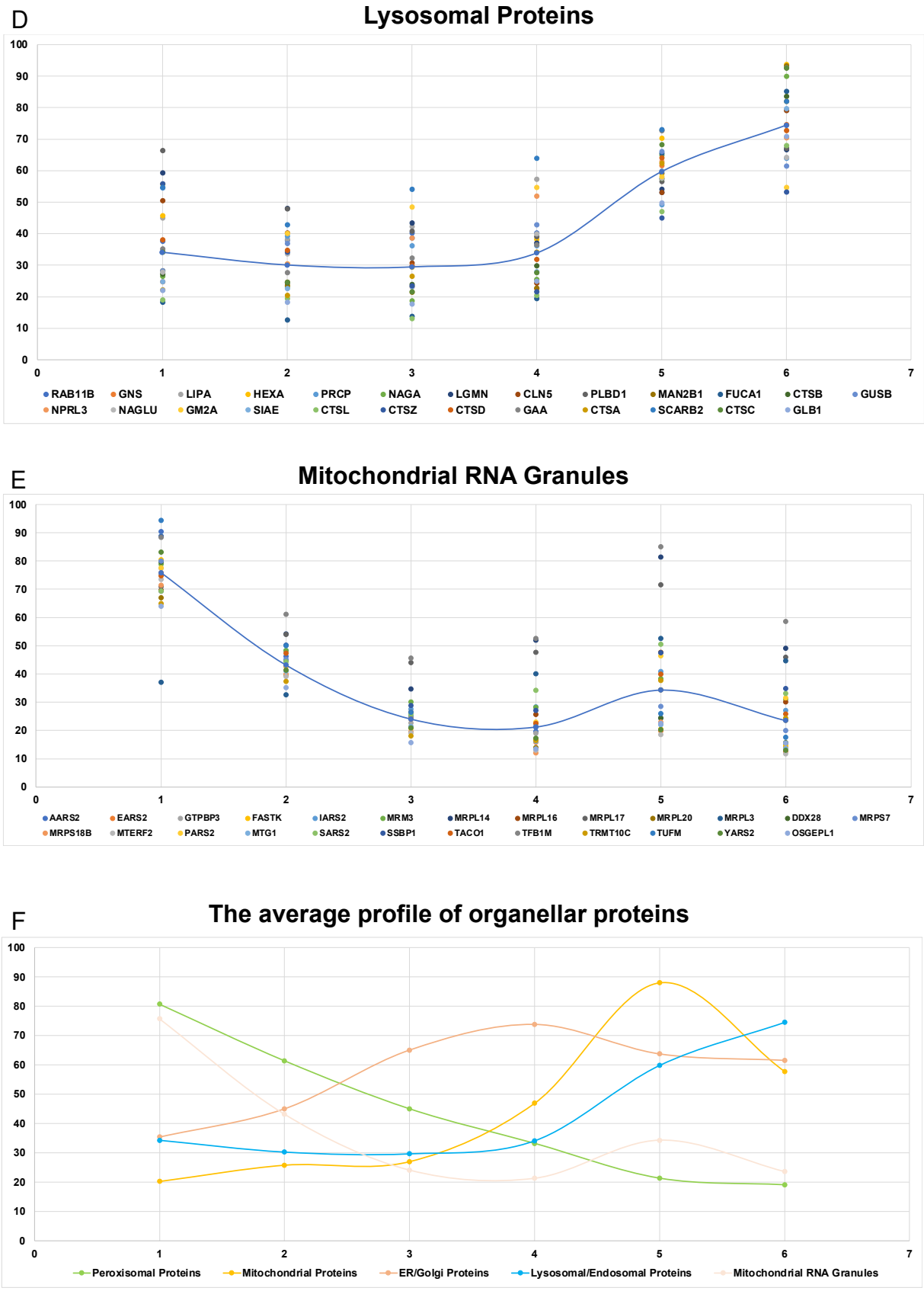

Figure 3-21: The master profiles of organelles.

Profiles A, B, C, D, and E were generated using 25 specifically chosen proteins with known localizations. Each protein was designated a unique color, and a trendline was plotted to

represent the median of these 25 proteins in each specific fraction, thereby illustrating the master profile. In figure F, all these master profiles are combined into a single graph.

To further corroborate the effectiveness of the profiling technique, two proteins – SERHL2 and KLHL41 – were selected for examination, as outlined in Table 3.2. Both proteins have a predicted PTS1 sequence, yet they display distinctly different separation profiles in the density gradient (Figure 3-22). KLHL41's separation behavior aligns partially with the master profile for peroxisomes continuously decreasing from LM1 to a plateau at LM4/LM5, but protein concertation rises again in fraction LM6 (Figure 3-22A). On the other hand, SERHL2 not only shows a peroxisomal profile but exhibits a small side peak like the mitochondrial RNA granule proteins. In addition to SERLH2 several proteins with enzymatic functions untypical for mitochondrial RNA granules. To this group belong the enzymes ECH1, GSTK1, and ECI2 as well as LACBT2. It should be noted that ECH1 (Zhang et al., 2001), GSTK1 (Kohr et al., 2011), ECI2 (Geisbrecht et al., 1999), and LACTB2 (Camões et al., 2015) also possess verified or predicted, conserved PTS1 sequences, and their mitochondrial localizations have been demonstrated in prior research. While LACTB2 was indeed described as an RNA-binding endoribonuclease (Levy et al., 2016), ECH1, GSTK1, and ECI2 are proteins proven to be dually localized to peroxisomes and mitochondria (Filppula, 1998; Geisbrecht et al., 1999; Morel et al., 2004). Thus, proteins with a dominant peroxisomal and a less prominent mitochondrial localization might adapt separation profiles, which are similar to those of mitochondrial RNA granules (Figure 3-22B, C) requiring further experimental validation.

Table 3-2: Novel candidate proteins of pig heart peroxisomes investigated by confocal microscopy.

Name	Gene	UniProt accession no.	Information on functional domains	PTS prediction	in homo sapiens listed by UniProt	Localization by confocal microscopy
Serine hydrolase-like protein 2	SERHL2	A0A287AJ52; A0A5G2QSQ3	Alpha/beta hydrolase 1 domain	PTS1 Twilight zone SFLQSKAIPAQL Score: -1,491	Cytoplasm, Peroxisome	Peroxisomal, cytoplasm
Kelch-like protein 41	KLHL41	A0A287AIE4	BTB domain	PTS1 Targeted ATRLNLFKLSKL Score:2,052	Cytoplasm, ER membrane	Cytoplasm

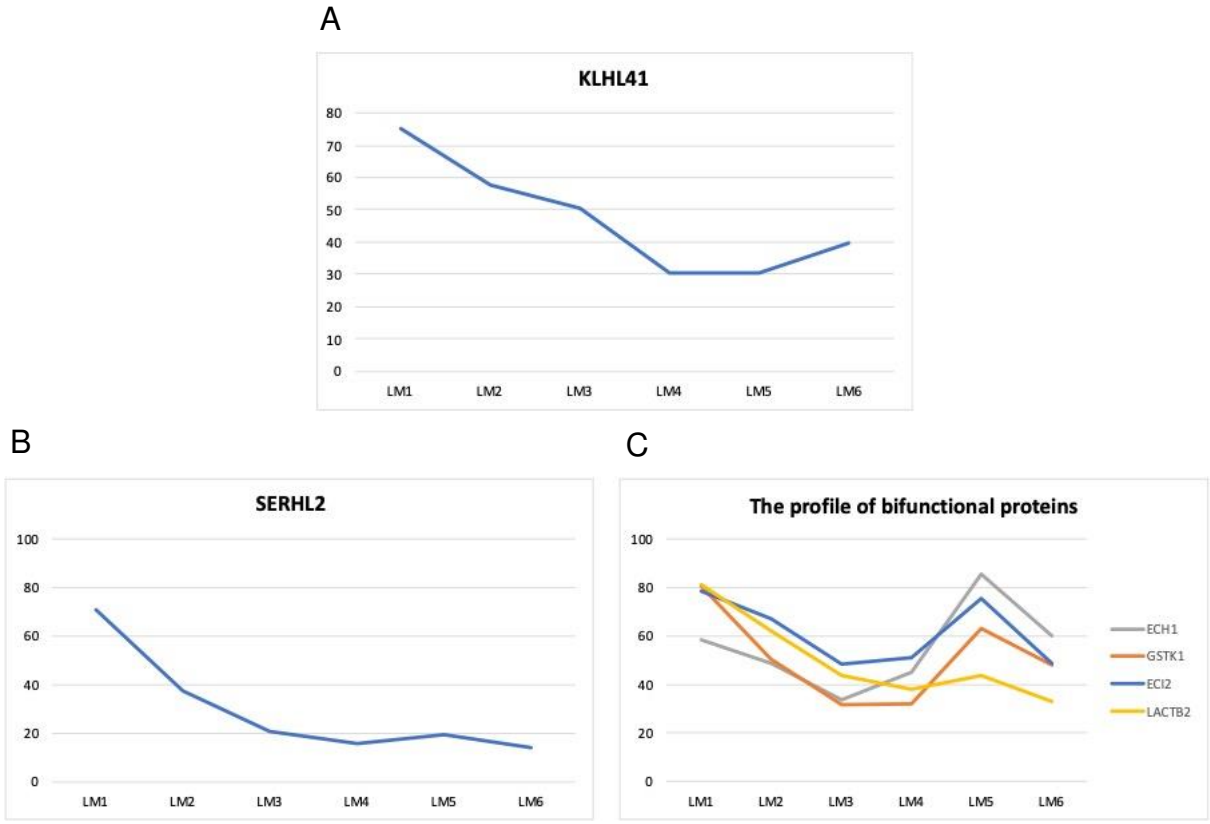

Figure 3-22: The gradient separation profiles of KLHL41 and SERHL2.

(A) The abundance profile of KLHL41 through 6 fractions. (B) is the abundance profile of SERHL2. (C) The profiles of proteins are known to be localized to peroxisomes and mitochondria. ECH1: Delta(3,5)-Delta(2,4)-dienoyl-CoA isomerase, GSTK1: Glutathione S-transferase kappa 1, ECI2: Enoyl-CoA delta isomerase 2, LACTB2: β-Lactamase-like protein 2.

3.3.5 Validation of the peroxisomal localization of novel candidate peroxisome-associated proteins

To evaluate the intracellular localization of SERHL2 and KLHL41 experimentally, both proteins were analyzed by overexpression experiments.

Serine hydrolase-like protein 2 (SERHL2), exhibits significant sequence similarity with SERLH, which was found to be concentrated in perinuclear vesicles and based on its PTS1 was also suggested as a potential peroxisomal protein in skeletal muscle (Sadusky et al., 2001). To experimentally validate the peroxisomal localization of SERHL2, N-terminally myc-tagged constructs of the human SERHL2 open reading frame were transfected into HeLa cells and primary cardiomyocyte cultures (NRCM).

Targeting of the myc-tagged SERHL2 was examined by immunofluorescence staining, along with counterstaining using a PEX14-directed antibody as a peroxisomal marker. According to the confocal immunofluorescence analysis, myc-SERHL2 and Pex14 signals show a significant colocalization in HeLa cells (Figure 3-23A). These results confirm the presence of the predicted PTS1 in the SERHL2 sequence and imply that SERLH2 is a bona fide peroxisomal protein. The expression pattern in cardiomyocytes is less obvious. In cardiomyocytes cells with a higher myc-SERLH2 show considerable mistargeting to the cytosol (Figure 3-23A arrowhead). However, in cells with a low expression level, a significant colocalization between PEX14 and myc-SERLH2 could be observed (Figure 3-23A arrow). Therefore, we conclude that under natural expression levels, SERHL2 is likely a peroxisomal protein in cardiomyocytes as well. Since it has also the same profile as proven bimodal localized proteins (Figure 3-22B), its mitochondrial localization should be considered and needs further localization experiments.

KLHL41 was identified by MS in the peroxisomal LM1 fractions of the pig heart tissue and showed an enrichment profile that might suggest a peroxisomal localization. As described above KLHL41 exhibits a predicted PTS1 at its C-terminus and was therefore chosen for further localization experiments in order to validate the suitability of the MS profiling approach. HeLa cells transfected with a human myc-tagged KLHL41 construct exhibited a strong immunofluorescence signal resembling an ER-like localization pattern (Figure 3-23B). A similar ER-like distribution of KLHL41 was also observed in cardiomyocytes. Peroxisomes, however, did not obviously colocalize with the KLHL41 signals. Orthogonal z-plane projections of representative confocal stacks show that KLHL41 signals are frequently in close proximity to peroxisomes stained by antibodies against PEX14. Of note, overlapping signals for PEX14 and myc-KLHL41 are not in the center of dot-like peroxisomes but in their periphery. According to these results, KLHL41 is despite its potential PTS1 according to the results from the overexpression experiments not imported into the peroxisome matrix but shows a distribution pattern of ER proteins (Figure 3-23B). Rather, signal overlap between PEX14 and KLHL41 likely highlights the frequent membrane contacts between peroxisomes and the ER.

The result of the overexpression experiments of myc-SERLH2 reaffirms the reliability of the mass spectrometric profiling approach as the protein displayed a gradient profile commonly seen in proteins localized to both mitochondria and peroxisomes but as well shows the limits of the heart profiling approach. With respect to their gradient profiles, Mitochondrial RNA granule proteins cannot be discriminated with high confidence from proteins that are dually localized to peroxisomes and mitochondria. KLHL41 showed a profile similar to those of known peroxisomal proteins. However, its gradient profile reaches a plateau already at LM4 with a minor increase in abundance from the LM5 to the LM6 fraction. Hence, the results from the overexpression experiments, which did not confirm a localization to peroxisomes are in line with the prediction according to the gradient profile of KLHL41, which is slightly but significantly different from the peroxisomal master profile. In summary, the results show that the profiling approach is able to identify novel, potentially cardiomyocyte-specific peroxisomal candidate proteins. However, additional information, like domain family information or interaction databases should be considered to curtail the number of candidate proteins. Ultimately, results from targeting experiments or immunofluorescence microscopy are required to validate their localization. This could indicate that overexpression led to misdirection, a phenomenon previously noted with certain potential peroxisomal proteins like LACTB2. LACTB2 and its orthologs exhibit a PTS1, which is preserved consistently among animal and fungal species (Camões et al. 2015, Kamoshita et al. 2022). However, in overexpression experiments, LACTB2 was observed to target mitochondria (Camoes et al. 2015, Kamoshita et al. 2022) confirming its previously published localization (Levy et al. 2016). Nevertheless, the protein is regularly enriched in peroxisomal fractions (Wiese et al. 2007, Islinger et al. 2007, see also the mouse liver data from this work). Prior research suggested that the peroxisomal targeting of LACTB2 may be influenced by specific environmental cellular conditions (Kamoshita et al., 2022). Hence, overexpression experiments may infrequently lead to conflicting data, when e.g. peroxisomal targeting machinery is overwhelmed by the mass of newly synthesized proteins - a situation that might also apply to the overexpression of KLHL41.

A

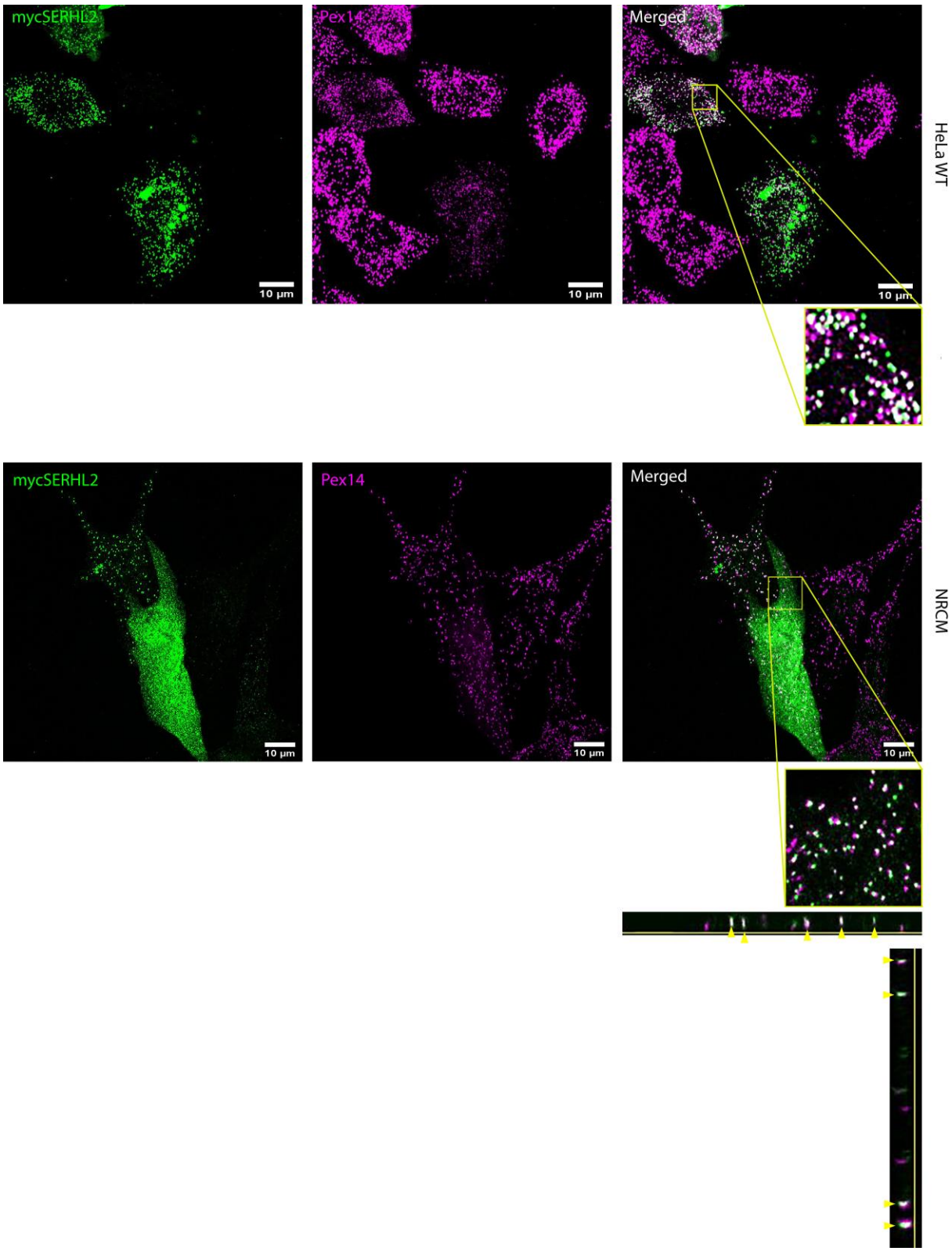

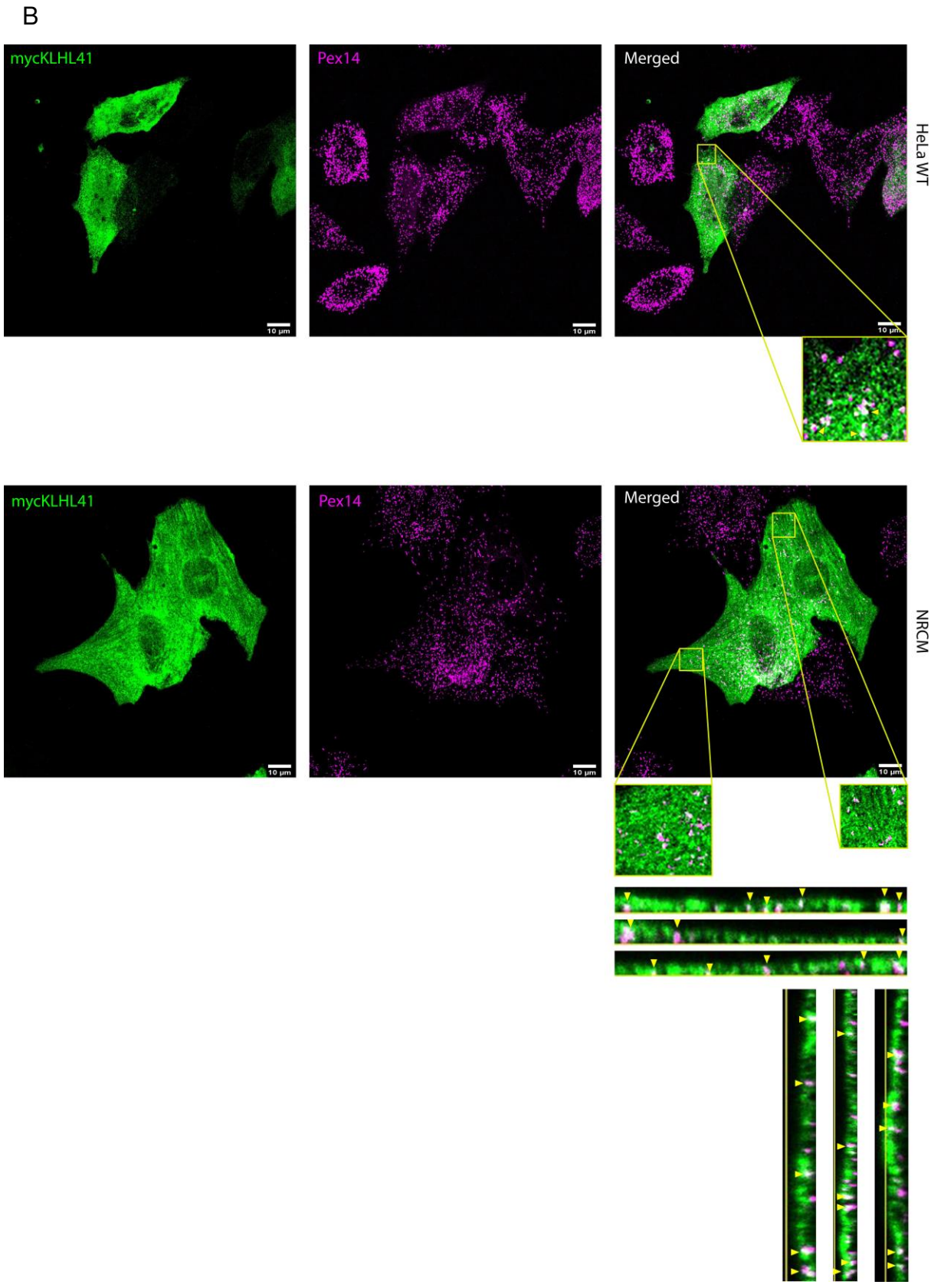

Figure 3-23: Analysis of the peroxisomal localizations of SERHL2 and KLHL41 by overexpression of correspondent myc-tagged variants.

(A) Colocalization of N-myc-SERHL2 to peroxisomes. The antibody signals for the myc-tag (green) show the localization of myc-SERHL2 in HeLa and NRCM cells. PEX14 antibodies (magenta) were used as a marker to label peroxisomes. In the orthogonal z-plane-projections, the yellow arrowheads point to SERHL2 signals, which completely merge with the signal of peroxisomal PEX14. The cut-outs represent 4X magnifications from the images above. (B) Overexpression of N-myc-KLHL41 in HeLa and NRCM cells. Signals for KLHL41 are shown in green, and peroxisomal PEX14 antibody staining is shown in magenta. In the orthogonal z-plane-projections, the yellow arrowheads point out encirclements of peroxisomes by KLHL41 signals. Of note, unlike SERH2, KLHL41 was not observed to merge with the center of peroxisomes. The cut-outs represent 4X magnifications from the images placed directly above.

4 DISCUSSION

Peroxisomes are integrated into a complex network of interconnected cellular compartments, where they play crucial roles in lipid and ROS metabolism, signaling, and the fine-tuning of cellular processes. To this end, peroxisomes interact with other subcellular organelles, including the ER, mitochondria, lysosomes, and lipid droplets in order to perform their function in metabolism and intracellular signaling. In recent years, it has become obvious that tethering proteins actively interconnect peroxisomes with other organelles to participate in metabolic pathways facilitating the effective transfer of metabolites or signaling molecules (Kors et al., 2022). Peroxisome-ER contacts were shown to play an important role in lipid transfer and influence peroxisome motility, membrane expansion, and biogenesis (Islinger et al., 2018; Costello et al., 2017; Hua et al., 2017).

Notably, around 50 % of the proteins from the human proteome were found to localize to more than one subcellular compartment (Thul et al., 2017), which implies that individual proteins perform organelle-specific functions at distinct subcellular compartments. Hence, in organelle proteomics experiments, multi-localized peroxisomal proteins have to be distinguished from mere contaminations in order to annotate a bona fide peroxisomal proteome in order to discover potential novel organelle-specific functions and to decipher the molecular background of hitherto unknown peroxisome-associated disorders. Hence, this study applied a quantitative proteomics approach to compare the protein distribution of distinct subcellular fractions isolated from mouse liver in order to discover novel peroxisomal protein constituents or co-purified, associated proteins from membrane contact sites.

4.1 A combination of organelle fractionation via sigmoidal density gradients with the SWATH-MS technology allowed the identification of low-abundant peroxisome-associated proteins from mouse liver

In order to complement the annotation of the peroxisome proteome, organelle purification via sigmoid-shaped density gradients was combined with a SWATH-MS-based proteomics approach. Density gradient centrifugation remains a timeless and essential technique for the isolation and analysis of organelles and a variety of

protocols for the isolation of peroxisomes have been published to date (Islinger et al., 2018). Mammalian cells contain only 0.1-5% peroxisomes depending on cell/tissue type or the cellular metabolic state (Islinger et al., 2010). Therefore, a serious obstacle to the detection of low abundance peroxisomal proteins is the much larger percentage of mitochondria and ER-derived vesicles present in cellular homogenates, thus requiring high enrichment rates to obtain peroxisome fractions with a low degree of contamination. Moreover, only 10% of peroxisomal proteins are membrane constituents (PMPs). Additionally, the two peroxisomal membrane proteins ABCD3 and PXMP2 represent 50% of the quantity of peroxisomal membrane proteins. As a consequence, e.g., peroxins constitute only 0.1% of the peroxisome proteome (Gouveia et al., 1999; Reguenga et al., 2001), thus illustrating the extraordinary dynamic range of individual proteins in the context of the organelle's proteome. In this context, it was pointed out that the purity of peroxisomes as low abundant and highly dynamic organelles limits the resolution of MS-based proteome studies (Gronemeyer et al., 2013). Commonly applied linear gradients result in overlapping peak profiles of gradually separated organelle species. To solve the obstacles of low organelle abundance and incomplete separation, label-free or isotope-labeled peptide profiling across linear gradients has been used to classify individual proteins according to their peptide profile (Yifrach et al., 2018). However, to provide robust profiles this approach requires numerous MS runs and is, hence, time and cost-intensive. Sigmoid-shaped gradients provide a steep slope in the gradient mid-section and shoulders of flat-angle at its two ends. Compared to linear or step gradients they are therefore ideally suited to separate a low-abundant particle of interest from a bulk of contaminating particle species. Peroxisomes have been successfully purified to exceptional purities of > 95% using sigmoid-shaped metrizamide or iodixanol gradients (Völkl and Fahimi 1985; Islinger et al., 2007). Thus, such gradients promise to be well-suited to compare the fraction of isolated peroxisome fraction with the bulk organelle fraction at the top of the gradient in order to define the peroxisomal proteome by quantitative MS.

Advancements in MS sensitivity continuously increase the identification numbers of peptides thus allowing the detection of proteins of increasingly lower abundance in peroxisome fractions. During the two recent decades, technological developments have greatly expanded our understanding of the metabolic and regulatory networks associated with these crucial cellular organelles (Saleem et al., 2006; Schuldiner and

Zalckvar 2015; Islinger et al., 2007). However, organelle proteomics approaches require discriminating reliably between proteins, which are truly enriched in peroxisomes from mere contaminants. Accurate peptide quantification across different samples is therefore a hallmark for the quality of quantitative proteomic studies. Classic MS/MS instruments prioritize precursor peptide ion selection according to the abundance of individual peptides in the injected sample. Therefore, low abundant peptides exhibit poorly reproducible selection rates resulting in the quantification of the correspondent proteins with low accuracy (Ludwig et al., 2018). As a solution for this problem and to cover the need for large-scale protein identification with parallel accurate, selective, and sensitive quantification a data-independent acquisition method to a targeted data analysis strategy has been recently developed with the SWATH-MS approach (Gillet et al., 2012). Since the SWATH-MS approach does not require a step-by-step preselection of single peptide precursors ions but identifies a bulk of peptides in parallel based on a predefined peptide library, its non-selective quantitative properties allow for significantly more accurate quantification of thousands of proteins quickly and reproducibly across large-scale sample cohorts (Ludwig et al., 2018).

4.1.1 Novel peroxisome-associated proteins were identified by quantitative proteomic analysis of mouse liver fractions

In order to characterize the proteome of mouse liver peroxisomes and to potentially identify proteins enriched in ER-contact sites, the quantitative SWATH-MS approach was applied to compare 4 gradient fractions from two alternative prefractions with a differing organelle composition – the LM and FLM fraction. Whereas the LM fraction is dominated by mitochondria, the FLM fraction contains a higher degree of ER. Therefore, we hypothesized, that the latter might contain peroxisomes, which are retained at a lesser density due to their attachment to ER-derived microsomal vesicles. However, the comparison of protein identifications enriched LM-PO and FLM-PO fractions did not reveal a specific enrichment of ER-derived proteins in the latter. By contrast, both PO-fractions show comparable enrichments of a subset of proteins previously localized at mitochondria or the ER if compared to the low-density TOP-fractions from the gradient ($p < 0.05$), which mainly consist of mitochondrial and microsomal proteins. Yifrach et al. (2018) annotated the results of different quantitative

and non-quantitative proteomic studies to produce a compiled list of peroxisomal proteins (Gronemeyer et al., 2013; Islinger et al., 2007; Jadot et al., 2017; Kikuchi et al., 2004; Wiese et al., 2007). The authors listed 196 proteins, which were identified as peroxisomal in at least two quantitative proteomic studies with high or low detection frequencies. According to their significant enrichment in both peroxisome fractions analyzed in this study, the proposed peroxisomal localization of the proteins ACNT1, PMVK, ABHEB, LACB2, OCIAD1, and SERHL2 could be confirmed. With PAFAH2, HTATIP2, PDCD6, and SAR1b, we further identified several previously undescribed peroxisomal candidate proteins. In the case of HTATIP2, OCIAD1 we could verify the peroxisomal targeting of the protein by overexpression and IF experiments.

Notably, a second subset of proteins including mitochondrial and ER proteins were neither significantly enriched in the peroxisome nor in TOP-fractions of the LM or FLM gradients. Compared to the bulk of the identified microsomal proteins, the microsomal tethering proteins VAPA and VAPB belong to this protein cluster, which shows neither enrichment in TOP- nor peroxisome fractions. Both tail-anchored proteins interact with the peroxisomal membrane protein ACBD5 facilitating membrane contact sites between both organelles (Costello et al., 2017; Hua et al., 2017). Thus, ER membranes from contact sites appear to be in part firmly attached to peroxisomes and are co-purified with both FLM-PO and LM-PO. In addition, several Rab proteins, which regulate vesicular transport and membrane interactions, were found among this cluster of proteins with no significant enrichment. Likewise, mitochondrial proteins, which were previously identified as constituents of peroxisomes like MIRO1, MARC2, PNPLA8, HMGCL, or MAVS (Castro et al., 2018; Dixit et al., 2010; Yang et al., 2003) could be found among this protein cluster implying that these proteins are comparably abundant in peroxisomes and another organelle like mitochondria. Interestingly, several further mitochondrial proteins like OPA1, MARC1, CPT1, or MFN1 suggest that they are multi-localized proteins. Alternatively, these proteins might be constituents of mitochondria-derived membrane contact zones co-purified with peroxisomes.

A peroxisomal contribution to cholesterol biosynthesis has been repeatedly discussed through the decades (Charles et al., 2020). Specifically, the enzymes of the presqualene segment have been proposed for a peroxisomal localization, since this would enable peroxisomes to use acetyl-CoA generated by fatty acid β-oxidation for

cholesterol biosynthesis (Faust and Kovacs, 2014). Remarkably, enzymes of the initial reactions of the pathway (HMCS2, THIL) were found in the mitochondrial protein cluster in this work. In contrast, MVK, PMVK, and FPPS were either found enriched in peroxisomes or among the cluster of potentially multi-localized proteins. Thus, instead of housing a complete set of enzymes generating farnesylpyrophosphate, peroxisomes may have to import mevalonate generated by the ER HMG-CoA reductase in order to perform the remaining steps of the presqualene segment. While the mevalonate might be at organelle membrane contact sites efficiently transported from the ER to peroxisomes, the functional significance of such a partial peroxisomal pathway still remains to be determined but may be required to control the flux of cholesterol through mammalian cells. Such a secondary role of peroxisomes in cholesterol biosynthesis might explain the conflicting results obtained from the analysis of different KO mouse models (Hogenboom et al., 2003; Charles et al., 2020).

Quite a few other of the previously suggested peroxisome-associated candidates from the list of Yifrach et al., (2018) were found enriched in either the microsomal and mitochondrial clusters from the TOP fractions from the SWATH-MS survey. NB5R3, FABPL, ACSL5, CYB5, UD11, and IDHP proteins accumulated in the microsomal cluster of the FLM-TOP fractions. Likewise, CH60, SLC25A17, ACTG, and SOD2 were associated with the mitochondrial cluster of the TOP-fractions. With regard to the results from this SWATH-MS approach, these proteins appear not to be localized to peroxisomes. Of note, localization of SOD2 by immunofluorescence microscopy did not support localization in peroxisomes but solely to mitochondria (Karnati et al., 2013), thus supporting our proteomics results.

Unexpectedly, the very long-chain acyl-CoA synthetase (VLACS or SLC27A2) showed significant enrichment in both top fractions aligning with the cluster of microsomal rather than peroxisomal proteins, even if it was previously suggested as a peroxisome-associated protein (Yifrach et al., 2018). VLACS was reported to be localized to the microsomes and peroxisomes (Yamada et al., 2000; Falcon et al., 2010). However, the majority of VLACS has been reported to be localized at the plasma membrane (Falcon et al., 2010). In light of the results of this work, these findings should be re-evaluated, since both publications did not evaluate to which extent peroxisomal VLACS might be the result of contamination by microsomes.

In summary, the largely identical peroxisomal protein identifications obtained by the SWATH-MS approach from two alternatively generated peroxisome fractions confirmed the suitability of a sigmoid-shaped density gradient for quantitative organelle proteomics studies. Owing to peptide-centric scoring from the MS/MS run, the SWATH-MS approach provided largely accurate quantitative data also for less common proteins, which led to the identification of novel peroxisomal proteins in this study. While this work focused on the proteomic characterization of the two most extremely separated parts of the density gradients (the high-density PO and lowest density TOP-fraction), a more extensive MS analysis of more gradient fractions (e.g. from LM1 – LM5) will allow to more precisely categorize the identified proteins to specific organelles based on their quantitative enrichment in different peaks within the density gradient.

4.1.2 Identification of novel proteins with a predicted PTS1-consensus sequence

Peroxisomal matrix protein import requires one of the two peroxisomal targeting sequences – the C-terminal PTS1 or the N-terminal PTS2 (Kunze, 2018). While the majority of known matrix proteins contain a PTS1, only a few proteins with a PTS2 are known to date. Initially identified by Gould et al. 1989 as a consensus of the amino acids S-K-L, later investigations revealed that the presence of this tripeptide alone is insufficient for effective peroxisomal targeting but requires several auxiliary amino acids upstream to gain maximum import efficiency. Currently, several machine learning algorithms have been developed to predict potential PTS1 (Kunze, 2018). To analyse the dataset of peroxisomal candidates identified in this study we applied the PTS1 predictor search algorithm (Neuberger et al., 2003) to mine the list of novel candidates for a potential PTS1. In contrast to the relatively well-defined PTS1, the PTS2 consisting of a relatively variable nonapeptide, is much less well characterized, and no reliable algorithms to identify a potential PTS2 currently exist (Kunze, 2018). Hence, our data set was not mined for a potential PTS2.

According to previous publications, 61 PTS1 sequence-including proteins have been identified in mammalian tissues so far (Yifrach et al., 2018). In this study 58 of them were identified as peroxisomal in LM-PO and FLM-PO fractions. Besides these established PTS1 sequence-containing proteins, four peroxisome-enriched proteins

from the data set generated in this work – PAFAH2, HTATIP2, LACTB2, and ADE2– exhibit a potential PTS1 sequence at their C-terminus. Another potentially PTS1-containing protein identified in this work, HPPD, exhibited only low enrichment in both LM-PO and FLM-PO fractions and was thus not considered as a novel peroxisomal candidate protein. Islinger et al. 2007, identified LACTB2 in quantitative mass spectrometry approaches in rat liver peroxisome fractions utilizing the iTRAQ labeling technique. Interestingly, Camoes et al. 2015 observed a conserved PTS1 in the homologous LACTB2 protein of the basidiomycete Ustilago maydis. However, ectopic expression of human, rat, and fungal LACTB2 in corresponding cell cultures could not confirm its peroxisomal targeting but localized the protein at mitochondria. This observation demonstrates that the presence of a PTS1 analog-targeting sequence does not always guarantee effective import into peroxisomes. Peroxisomal matrix proteins are completely folded in the cytosol prior to their import (Léon et al., 2006). In this respect, the recurrent identifications of LACTB2 in peroxisomal fractions might suggest, that the C-terminal PTS1 is functional but in the folded protein only exposed to cytosol under specific cellular conditions or in a not yet identified splice variant. Alternatively, the high, non-physiological LACTB2 synthesis rates under a CMV promotor may exceed the capacities of cytosolic chaperones and thus lead to improper folding of the nascent peptide chain. As a result, the N-terminal mitochondrial targeting sequence of LACTB2 might be primarily recognized by the mitochondrial import machinery. In summary, the repeated identification of LACTB2 in peroxisomal fractions might indicate that targeting experiments based on protein overexpression can be of limited significance and have ultimately to be validated by immunofluorescence microscopy.

Considering ADE2, our results confirm the observation by Wiese et al (2007), who provided the first evidence for a peroxisomal localization of ADE2 in their proteome data of mouse kidney peroxisomes, in addition to its previous identification in the cytoplasm (Agarwal et al., 2020). Both HTATIP2 and PAFAH2 are highly and significantly enriched in LM-PO and FLM-PO and were not identified as peroxisomal in previous studies. Thus, both were chosen as novel peroxisomal candidate proteins to be validated by further localization experiments.

4.1.2.1 Ectopic expression of HTATIP2 and PAFAH2 confirms their targeting to peroxisomes

To validate the reliability of our SWATH-MS approach, we selected five candidate proteins (HATIP2, PAFAH2, SAR1b, PDCD6, OCIAD1), which were not previously identified as peroxisomal via fractionation-based organelle proteomics studies, for further localization experiments. The results of the experiments will be discussed in the following paragraphs.

HTATIP2, also known as TIP30 and CC3, was first identified as a tumor suppressor gene by Shtivelman and colleagues (1997). HTATIP2 was identified as an interaction partner of the human immunodeficiency virus-1 (HIV1) transcription protein Tat and was therefore given its current name **H**IV-1 **TAT**-**I**nteractive **P**rotein **2** (Yu et al., 2015). HTATIP2 belongs to the large oxidoreductase family but even though the amino acid sequence of this protein is evolutionarily highly conserved and expressed in many tissues including the kidney, heart, brain, lung, pancreas, and skeletal muscle, the exact cellular and enzymatic function remains currently unclear. Since we located HTATIP2 in peroxisomes via the MS approach and in targeting experiments, it is tempting to speculate which role HTATIP2 could play in peroxisomes. A genome-wide association study conducted by Cardinale et al. (2023) suggested a role for HTATIP2 as an enhancer in antiviral interferon signaling. In this context, it should be mentioned that peroxisomes have been shown to function as a crucial platform for antiviral signaling, thereby contributing to innate immunity (Dixit et al., 2010; Bender et al., 2015). However, according to its PTS1 HTATIP2 is imported into the matrix of peroxisomes, whereas the peroxisomal antiviral defense protein MAVS is a tail-anchored membrane protein with its functional domains facing the cytosol (Costello et al., 2017). In order to unravel the potential contribution of HTATIP2 in the peroxisome-facilitated innate immune response, it is necessary to conduct additional research.

Recent research indicates that peroxisomes play a significant role in maintaining energy balance and disturbances in peroxisomal functions have been linked to increased susceptibility to obesity and related metabolic conditions such as type 2 diabetes and hepatic steatosis (Kleiboeker and Lodhi, 2022). Therefore, it is crucial to identify potential pathways and proteins that could be involved in regulating lipid metabolism and insulin action. In a study investigating the metabolic dysregulation in

Type 2 diabetes, HTATIP2 was found to be enriched in the liver of PKCδ/ε KO mice fed a high-fat diet using quantitative proteomics (Liao et al., 2014). Subsequent HTATIP2 overexpression experiments in HepG2 cells revealed that HTATIP2 promoted an increase in lipid droplet formation upon palmitate treatment. Moreover, the overexpression of HTATIP2 in hepatocytes resulted in enhanced incorporation of fatty acids into triglycerides (TG) and cholesterol esters, while the knockdown of HTATIP2 showed the opposite effect (Liao et al., 2014). Additionally, Zhang et al. demonstrated that HTATIP2 forms a complex with long-chain acyl-CoA synthase 4 (ACSL4) regulating endocytic trafficking of the EGF receptor (Zhang et al., 2011). Since ACSL4 was described to reside as well on peroxisomes where it supposedly activates fatty acids for peroxisomal import and breakdown (Lewin et al., 2002), an interaction between both proteins at peroxisomes might have an impact on the regulation of fatty acid metabolism, which might explain the impact of HTATIP2 on TG homeostasis (Liao et al., 2014).

Another PTS1-containing enzyme, Platelet-activating factor acetylhydrolase PAFAH2, was identified as a candidate peroxisome-associated protein. PAFAH2 is known for its role in lipid catabolic and anabolic processes, and phospholipid binding but was previously located in the liver cytoplasm (Hattori et al., 1996). By contrast, the myc-PAFAH2 overexpressed in HepG2 cells was clearly targeted to peroxisomes, indicating that the enzymes might be found in both subcellular compartments. Since PAFAH2 is a lipid metabolic enzyme, it is tempting to speculate on its potential function inside peroxisomes. Of note, PAFAH2 was described to have a broad range of substrate specificity, not only cleaving acetyl-chains from the platelet-activating factor but also acyl-chains from other phospholipids (Hattori et al., 1996). In this context, it was initially suggested that the plasma PAF acetylhydrolase has a physiological role in the degradation of oxidized phospholipids generated within circulating lipoproteins (Stremler et al., 1991). Oxidative damage can significantly affect phospholipids, and it was subsequently proposed that PAFAH2 assists in the degradation of phospholipids carrying oxidized acyl-chains (Dong et al., 2021). Supporting this hypothesis, it has been reported that overexpression of PAFAH2 can mitigate oxidative stress-induced cell death (Kono et al., 2008). Peroxisomes earned their name due to their involvement in H_2O_2 metabolism, and their contribution to oxidative stress has been extensively investigated (Schrader and Fahimi 2004 and 2006; Bonekamp et al., 2009; Nordgen

and Fransen 2014; He et al., 2021). Peroxisomes are involved in multiple metabolic functions, such as the breakdown of VLCFA, branched-chain fatty acids, D-amino acids, and polyamines, which all produce H_2O_2 as a ROS (Lodhi et al., 2014). Consequently, a peroxisomal PAFAH2 could be necessary to remove oxidized acyl chains from the inner leaflet of the peroxisome membrane.

4.1.3 SAR1b and PDCD6 are partially associated with peroxisomes

According to the traditional model of peroxisome biogenesis, novel peroxisomes are formed by growth and division of existing ones, with peroxisomal matrix and membrane proteins being directly recruited from the cytosol. However, more recent research challenged this model proposing that pre-peroxisomal membranes with specific peroxisomal membrane proteins bud instead from the ER to reach peroxisomes (Tabak et al., 2003). Additionally, peroxisomes might also receive phospholipids by vesicular transport. The generation of vesicles responsible for the intracellular transport of lipid and protein cargoes from the ER is facilitated by a group of coat proteins in the cytoplasm termed the COPII coat (Miller and Schekman, 2013). Research on COPII-mediated vesicular transport has significantly enhanced our understanding of ER exit sites. Based on these discoveries, the present study aimed to explore the relationship of SAR1b and PDCD6 with peroxisomes. These two proteins were selected due to their involvement in facilitating vesicular trafficking and their unexpectedly high abundance in peroxisomal fractions. Previous publications proposed that ARF small GTPases are involved in recruiting COPI to the peroxisomal membrane, in order to foster peroxisomal biogenesis by fission (Just and Peränen, 2016; Lay et al., 2006). Members of this small GTPase subfamily play crucial roles in regulating membrane traffic, organelle structure, and cellular behavior (Donaldson et al., 2011). However, our proteome data did not detect any ARF protein, including ARF1-ARF6 and the 20 ARF-like proteins, as enriched in either LM-PO or FLM-PO. However, SAR1b, as another member of the ARF protein family, which was to our knowledge not before associated with peroxisomes, was significantly enriched in peroxisomal fractions analysed in this work.

SAR1 proteins are not evenly distributed through the ER but are known to be concentrated on smooth membranes in the transitional region between the ER and Golgi, comprising ER exit sites (Kuge et al., 1994). Expectably, immunofluorescence and overexpression experiments conducted in this study revealed no direct

colocalization between Sar1b signals and peroxisomes. However, peroxisomes are regularly enclosed by SAR1b-positive ER structures, implying their close association with ER export domains. This assumption was supported by examining orthogonal z-plane projections of confocal stacks, which show that peroxisomes are closely wrapped inside Sar1-positive ER. This finding is intriguing, considering recent reports on the existence of physical "wrappER contacts" between rough ER, peroxisomes, and mitochondria in hepatocytes. These organelle contacts were supposed to coordinate hepatocyte lipid metabolism with the export of lipoproteins into the bloodstream (Illaqua et al., 2022). A study conducted by Melville et al., (2020) identified slight sequence differences between Sar1a and Sar1b and proposed that Sar1a forms homodimers at the membrane to facilitate the remodeling of ER exit sites, while Sar1b exhibits a stronger affinity for SEC23, resulting in increased recruitment of the SEC23/24 heterodimer. This enhanced recruitment of Sec23/24 enables more efficient secretion of large cargo molecules, which relies on precise regulation of COPII vesicle formation kinetics. Consequently, SAR1b plays a critical role in the secretion of lipoproteins (Melville et al., 2020). According to these previous observations, the notable enrichment of SAR1b in both peroxisomal fractions might suggest that ER-exit sites are co-purified as membrane remnants of peroxisome-ER contact sites. These correspondent ER sites might be involved in the export of lipoproteins, which have before export been loaded with triglycerides. Fatty acid-degrading organelles, like peroxisomes and mitochondria, could interfere with this process in order to balance lipid export with cellular energy homeostasis. Nevertheless, since no strong colocalization but only associations between SAR1b and peroxisomes were observed by immunofluorescence microscopy, extreme enrichment of SAR1b in peroxisomal fractions might not be entirely explained by the co-purification of ER-derived membrane contact sites. Further experiments are hence required to clarify if the discrepancies between overexpression and subcellular fractionation experiments might result from tissue/cell-type differences, or a particular metabolic state of the liver tissue used in the isolation experiments.

PDCD6, also known as "Apoptosis-linked gene 2 protein" (Alg-2), is a calcium-binding protein that has been implicated in various cellular processes such as endosomal biogenesis, membrane repair, and particularly ER-Golgi vesicular transport (Jia et al., 2001; Tanner et al., 2016). Like SAR1b, PDCD6 was identified at ER exit sites (ERES),

where it assists in regulating COPII assembly (la Cour et al., 2013). As another peroxisome-enriched protein from our MS survey, which has a functional association with ER protein export, PDCD6 was chosen for further analysis in order to determine its cellular distribution pattern.

Unlike SAR1b, PDCD6 did not exhibit a typical ER network distribution but a spot-like localization pattern. Moreover, only partial colocalizations or close associations between PDCD6 and peroxisomal vesicular structures were observed. Since the endosomal/lysosomal markers RAB5A and LAMP1 did not show a significant degree of overlap with PDCD6, its localization to ERES was investigated by co-staining with SAR1b and VAPB antibodies. In contrast to the extended, network-like ER distribution of SAR1b, VAPB was found to be accumulated in focal accumulations surrounding the perinuclear region of the cells. Notably, PDCD6 positive spots were found to accumulate in regions with strong VAPB signal intensities. These observations are supported by a recent publication, which reported that PDCD6 is a component of a VAPA/B protein complex concentrated at ER exit sites (ERES) (Inukai et al., 2021). Hence, the PDCD6 signals might highlight specific sites of the ERES, where lipoproteins are loaded into COPII-coated vesicles. The partial overlap with PEX14 might indicate that peroxisomes are involved in controlling the loading of lipoprotein with specific fatty acid species.

4.1.3.1 Overexpressed OCIAD1 localizes to both mitochondria and peroxisomes dually and induces morphological changes in peroxisomes

The OCIAD1 protein was discovered by the Inamdar group and was originally named Asrij (Sanskrit for blood) due to its initial identification in blood vessels (Mukhopadhyay et al., 2003). While it has been reported that human OCIAD1 is abnormally expressed in various carcinomas (De Marchi et al., 2016), its normal expression and function remain unclear. The protein has been found to localize to endosomal compartments (Kulkarni et al., 2011) and mitochondria (Calvo et al., 2015), supposedly exerting regulatory effects on multiple signaling pathways such as JAK/STAT, Notch, and PI3K/AKT, which influence cell fate (Sinha et al., 2013). Shetty et al. (2018) demonstrated that OCIAD1 is predominantly a mitochondrial protein highly expressed in human pluripotent stem cells (hPSCs). They further revealed that OCIAD1 interacts

with the mitochondrial complex I thereby regulating its activity (Shetty et al., 2018). In a separate study utilizing genome-wide CRISPRi screening, OCIAD1 was identified as a sensitizing factor along with genes from mitochondrial OXPHOS Complex III. Depletion of OCIAD1 resulted in a specific defect in Complex III assembly (Le Vasseur et al., 2021). According to this publication, OCIAD1 is blocking a metabolic shift from glycolysis to mitochondrial oxidative phosphorylation which is necessary for the differentiation of stem cells.

In a comprehensive investigation of human mitochondrial proximity interactions, OCIAD1 was found to exhibit interactions with several peroxisomal proteins. Immunostaining experiments using OCIAD1 antibodies in human fibroblasts and HeLa cells demonstrated that OCIAD1 primarily localizes to mitochondria but suggested that a small proportion of OCIAD1 might colocalize with the peroxisomal marker ABCD3 (Antonicka et al., 2020). In our study, we confirmed the mitochondrial localizations of OCIAD1 and, importantly, its localization to peroxisomes by three alternative approaches: (1) subcellular fractionation-based proteomics using mouse liver tissue, (2) targeting studies based on the expression of myc-tagged mouse OCIAD1 and (3) identification of endogenous on peroxisomes in MEF, HepG2 WT and HepG2 KO cells using OCIAD1-directed antibodies. In parallel to our studies, OCIAD1 was identified in a BioID approach using peroxisomal ACBD5 as bait (Peter Kim, University of Toronto, Canada, personal communication).

In our work, OCIAD1 transfected cells showed an effect on peroxisomal and mitochondrial morphology. Mitochondrial dynamics involve various membrane-shaping proteins and interactions with other organelles and the cytoskeleton. These dynamic changes in mitochondrial morphology exert significant effects on cellular processes such as apoptosis, mitophagy, mitochondrial metabolism, ATP production, quality control, mtDNA inheritance, cell fate determination, cell cycle, and mitochondrial transport (Sabouny and Shutt, 2020). Similarly, peroxisomes are highly adaptable organelles that modify their shape, number, position, metabolic functions, and interactions with other organelles based on cellular requirements (Islinger et al., 2018). Peroxisomes and mitochondria share common components of their division/fission machinery, including FIS1, MFF, and DRP1 (Schrader et al., 2015). Hence, overexpression or downregulation of proteins involved in peroxisomal

and mitochondrial fission and resulting dynamics, such as FIS1, MFF, and DRP1, have been shown to affect the morphology of both organelles and a loss in one of the three proteins results in elongated mitochondria and peroxisomes (Carmichael et al., 2022). A proteomics study conducted in OCIAD1-depleted *Drosophila* lymph glands observed a decrease in DRP1 levels, which were accompanied by changes in mitochondrial morphology (Sinha et al., 2019). In line with these observations, OCIAD1 knockout in hESCs led to an increase in mitochondrial branch length and elongation, while OCIAD1 overexpression had an adverse effect (Wanet et al., 2015; Shetty et al., 2018; Ray et al., 2021). Notably, experiments performed in this work in HepG2 cells confirmed the reduction in mitochondrial branch length and reduced network formation in response to OCIAD1 overexpression. Importantly, mitochondrial elongation promotes ATP production via OXPHOS since it facilitates increased cristae formation and the assembly of electron transport chain complexes (Wanet et al., 2015; Mishra and Chan, 2016). Thus, OCIAD1 expression appears to suppress mitochondrial OXPHOS in part by remodeling mitochondrial dynamics (Ray et al., 2021). In our study, we were not only able to confirm the peroxisomal targeting and localization of OCIAD1 in different cell types, but as well observed changes not only in mitochondrial but also in peroxisomal morphology. Remarkably, we observed a decline in cellular peroxisome numbers in response to OCIAD1 expression. Peroxisomes transfer octanoyl-CoA generated by β-oxidation of VLCFA to mitochondria for complete degradation. Reduction equivalents generated during β-oxidation are subsequently transferred to OXPHOS in order to generate ATP. Hence, it would make sense to reduce peroxisome numbers and β-oxidation, when mitochondrial OXPHOS capacities are reduced. Under extremely high OCIAD1 expression levels, peroxisomes as judged by the mitochondrial PEX14 signal were even absent. Interestingly, we noticed in addition that the degree of colocalization between peroxisomal spheres and the mitochondrial network increased upon OCIAD1 transfection. This suggests that OCIAD1 expression may induce physical proximity between these two organelles, potentially in order to facilitate the coordination of peroxisomal activities, such as β-oxidation, with mitochondrial functions, including OXPHOS.

Mitochondrial maturation and activity undergo significant changes during metabolic cellular adaptation, it is crucial to discover mechanisms and targets that can regulate mitochondrial metabolism. Likewise, peroxisomes play a vital cellular role and closely

cooperate with mitochondria in various metabolic pathways (Schrader et al., 2020). Therefore, OCIAD1 promises to be a novel protein shared by mitochondria and peroxisomes, which enables to coordination of abundance and activities of these closely cooperating organelles.

4.2 Novel peroxisome-associated proteins were identified by quantitative proteomic analysis of pig heart fractions

Hypertrophic cardiomyopathy and cardiac insufficiency lead to significant metabolic remodeling, particularly affecting the lipid metabolism of cardiomyocytes (van der Velden et al., 2018; Bedi et al., 2016). The underlying molecular causes of cardiac dysfunction in most heart diseases remain largely unknown, necessitating investigations at the organelle level to understand the biochemical and physiological changes associated with cardiomyopathy. Peroxisomes are essential organelles for lipid metabolism and play a crucial role in maintaining cellular homeostasis. Their absence is associated with severe and often fatal diseases, particularly affecting children (Wanders et al., 2010). Despite their importance for lipid metabolism, peroxisomes in cardiomyocytes have been relatively overlooked compared to mitochondria, and there is consequently a lack of comprehensive studies characterizing these organelles in cardiac tissue. Existing publications provide only limited information on the role of peroxisomes in the heart. Previous studies mainly focused on their morphological characterization by immuno- and electron-microscopic approaches or targeted activity analyses of peroxisomal enzymes (Fahimi et al., 1979; Craemer et al., 1994). While the neurological and nephrological phenotypes are a hallmark of peroxisomal disorders, information on the significance of peroxisomes for heart homeostasis remains scarce. A heart-specific knockout of the mouse Pex5 gene, however, resulted in dilative cardiomyopathy causing the death of the animals at the age of approximately 6 months (personal communication with Prof. Sven Thoms, Bielefeld University). Garikapati et al. (2022) examined a Pex11α KO mouse model performing proteomic and lipidomic analyses on its heart tissue to decipher the molecular alterations caused by the peroxisomal defect. The authors observed increased amounts of saturated phosphatidylcholines as well as significant changes in the abundance of a number of lipid metabolic proteins in the hearts of Pex11α KO adult mice compared to wild-type controls (Garikapati et al., 2022), thus indicating, that peroxisomes have a significant impact on heart lipid homeostasis. Of note,

cardiomyocytes express a significant number of proteins, which are tissue-specific and may play crucial roles in ensuring proper heart muscle function, performance, and capacity (Remedios et al., 2003). Consequently, the objective of this study was to annotate the proteome of heart peroxisomes and to potentially identify novel tissue-specific peroxisomal proteins in order to provide the basis for future investigations on the specific impact of peroxisomes on heart function.

Gramolini et al. (2007) developed a fractionation protocol combined with “Liquid Chromatography–Mass Spectrometry-Based Expression Proteomics” to annotate and categorize the cardiac muscle proteome. This approach focused on associating the unidentified proteins to nuclei, cytosol, microsomes, and mitochondria, employing the MS-multidimensional protein identification technology (MudPIT), however, peroxisomes were not included as a distinct organelle in this study. In order to perform a proteomics survey on heart peroxisomes, the first focus of this study had to be set on the development of an appropriate separation procedure for isolating peroxisomes from pig heart tissue. While peroxisomes can be isolated with high purity from "soft" tissues like the liver or kidney (>95%) and have been used for peroxisome proteome characterization, the low catalase activity in heart tissue indicates a profoundly lower abundance of the significantly smaller peroxisomes from the heart if compared to liver or kidney, which necessitates to specifically adapt a purification protocol for this tissue. As observed in this work, the highly abundant mitochondria in cardiomyocytes exhibit similar densities like peroxisomes, which impeded the development of a straightforward protocol for the isolation of highly pure peroxisome fractions as used for mouse liver in this thesis. As an alternative approach, "correlation profiling" based on the differential distribution of known marker proteins across a linear density gradient was utilized to assign unknown proteins to specific subcellular localizations (Mulvey et al., 2017). To apply such a hyperLOPIT method to cardiac tissue, a separation procedure was developed in this work, which allowed the separation of low-abundance peroxisomes, microsomes, and mitochondria into distinct peaks while sufficiently preserving the organelle structure. To this end, a tissue incubation step with collagenase/pancrease was included, to reduce the rigidity of the collagen-rich muscle tissue in order to avoid deleterious shearing forces during the homogenization step. Subsequently, conditions for differential centrifugation were optimized to maximize the concentration of peroxisomes in the prefraction applied to density gradient centrifugation. Finally, the slope and density range of the linear Optiprep gradient were

adapted to yield a maximally broad distribution of individual organelle peaks inside the gradient. After establishing the separation method, the suitability of the separation for a hyperLOPIT proteomics approach was validated. The results of a first MS analysis confirmed that proteins known to localize at peroxisomes, mitochondria, and the ER could be associated with distinct, well-separated peaks. A second, more extensive proteomics survey allowed the creation of protein sets for master profiles for the organelles: peroxisomes, mitochondria, lysosomes/endosomes, and the ER. However, as a single drawback, mitochondrial RNA granules were observed to exhibit similar gradient profiles as proteins with a bimodal localization to peroxisomes and mitochondria. These profiles can now be used to train AI-based software in order to categorize hitherto uncharacterized proteins into individual compartments. This approach will enable the production of a list of hitherto unidentified and potentially heart-specific peroxisomal candidate proteins, which will serve as the basis for functional studies characterizing the significance of peroxisomes in cardiomyocytes. Proteins, which show a double peak at peroxisomal and mitochondrial maxima, have however, been manually curated for a potentially known function in mitochondrial RNA processing. For an initial validation of the hyperLOPIT approach for the characterization of the peroxisomal heart proteome, two proteins with predicted PTS1s were selected from the list of identified proteins: SERLH2 and KLHL41 analyzed by overexpression experiments in order to confirm their subcellular localization.

4.2.1 KLHL41 is not imported into the matrix of peroxisomes

KLHL41 (also known as KBTBD10, Krp1, or Sarcosin), is a member of the kelch-like protein family and was suggested to play a crucial role in the development and differentiation of skeletal and cardiac muscle (Greenberg et al., 2008; Puy et al., 2012). It achieves this function by controlling the proliferation and differentiation of myoblasts thus contributing to the assembly of myofibrils. According to this function, KLHL41 was reported to be primarily expressed in both muscle types (Greenberg et al., 2008; Puy et al., 2012). Previous bioinformatics screens for PTS1-containing proteins in the mammalian genome identified KLHL41 as a potential peroxisome-targeted protein (Kurochkin IV et al., 2005; Mizuno et al., 2008). In cultured mouse cardiomyocytes, KLHL41 displayed a punctate localization inside the cytoplasm, which might point to its presence in vesicular structures like peroxisomes (Greenberg et al., 2008). In line with its predicted PTS1, the profile of KLHL41 in the density gradients also showed a

similar but partially different profile than typical peroxisomal marker proteins. According to these conflicting data, it was chosen for the evaluation of its localization to validate the power of the profiling approach to identify peroxisomal candidate proteins.

The expression of human myc-KLHL41 in HeLa cells and cardiomyocytes did not result in localization inside the peroxisomal matrix as suggested by the predicted PTS1, thus, corroborating findings from Mizuno and colleagues (2008), who overexpressed the mouse KLHL41 in CHO cells. Rather, its fluorescence signal highlights a reticular intracellular network resembling the typical pattern of an ER-resident protein. A previous study colocalized KLHL41 with the ER marker protein disulfide isomerase (PDI) in both myofibers and skeletal muscles by immunofluorescence microscopy, implying a localization to the sarcoplasmic reticulum (Gupta et al., 2013). While KLHL41 shows mostly ER distribution when it was overexpressed, its separation profile in the pig heart density gradients is relatively shallow but shows two peaks: one in the low-density area of the gradient typical for proteins of microsomal origin and another more prominent in the highest density fraction typical for peroxisomal proteins. It remains to be determined if KLHL41 is different and not completely resolved into subcellular structures (e.g. remaining myofibrils) or if its peroxisomal targeting requires specific expression levels and a controlled intracellular environment only provided in cardiomyocytes under *in vivo* conditions. Nevertheless, according to both, its non-linear gradient separation profile as well as non-peroxisomal targeting in cell culture, there is no direct evidence that KLHL41 is a peroxisomal protein.

4.2.2 SERHL2 is a novel bona fide peroxisomal proteins

The mouse enzyme SERHL belongs to the serine hydrolase family, which commonly catalyses the cleavage of ester and peptide bonds. An mRNA was discovered that increased expression of SERHL when murine skeletal muscle tissue was passively stretched, suggesting a role in muscle growth in response to mechanical stress (Sadusky et al., 2001). According to a predicted PTS1 at its C-terminus and a perinuclear, vesicular staining pattern observed by immunofluorescence microscopy, the authors suggested that SERHL is a constituent of peroxisomes. In addition to this study, Hawkins et al. (2007) identified mouse SERHL as a new peroxisomal protein by overexpression of a myc-epitope-tagged variant in BHK-21 cells. According to the *Ensembl* database, SERHL is a pseudogene in humans and pigs and is therefore not

transcribed into mRNA. Both species, however, possess a functional SERHL2 gene, which must have functionally replaced SERHL after duplication of the precursor gene. As observed for mouse SERHL, our proteomic profiling data as well as the results from the overexpression experiments of the myc-tagged SERHL2 imply its localization to peroxisomes in both HeLa cells and NRCMs. Of note, its small second peak on the LM5 fraction in the proteomics profile matches with the profile of dually localized proteins like GSTK1, ECH1, or ECI2. Hence it is tempting to speculate about a bimodal localization and the metabolic function of a peroxisomal SERHL2. According to the protein domain structure, SERLH2 is a rather unlikely constituent of mitochondrial RNA granules, which can show a similar separation profile but may have minor second localization. Indeed, in cells with higher overexpression levels, SERHL2 was observed to target further subcellular structures, such as perinuclear and vesicular, but this was not nearer investigated.

With respect to the protein significance for the heart, promoter methylation of the human SERHL2 gene was reported to coincide with the occurrence of atherosclerotic plaques. However, the gene's role in atherosclerosis or other cardiovascular diseases remains uncertain (Kim et al., 2020). Moreover, a whole exome sequencing survey investigating a rare congenital heart defect known as “Total Anomalous Pulmonary Venous Connection” (TAPVC) also identified the SERHL2 gene as a candidate gene (Shi et al., 2018) underlining its potential significance for cardiovascular health. Unfortunately, no publications on the enzymatic activity of either SERHL or SERHL2 exist to date. According to a PSI-Blast search, the SERHL2 protein sequence shows relatively low sequence similarities to other representatives of the serine hydrolase family. Nevertheless, the hydrolases ABHD6 and ABHD11 as well as epoxide hydrolase 2 were identified as the most closely related family members. ABHD6 and ABHD11 are monoacyl-glycerol and diacyl-glycerol hydrolases and might point to the role of SERHL2 in peroxisomal membrane maintenance. Epoxide hydrolase 2 is a peroxisomal protein (Waechter et al., 1983; Hollinshead and Meijer, 1988), which converts epoxides of oxidized PUFAs into their corresponding diols (Harris and Hammock, 2013). Hence, SERHL2 might be a novel peroxisomal protein metabolizing lipid or fatty acid derivatives. However, further research is required to characterize the physiological substrates and enzymatic activity of SERHL2.

4.3 Concluding Remarks

The quantity, size, shape, protein content, and function of peroxisomes can vary significantly according to the physiological state and metabolic requirements of a specific cell type, tissue, organ, or even the entire organism (Baumgart et al., 1997). Thus, the annotation of tissue-specific peroxisomal proteome can help to assess organ- or cell-type specific functions of this still poorly characterized organelle.

In this study, two different proteomics approaches were used for two different tissues from different species in order to identify novel peroxisomal or peroxisome-associated proteins. In both proteomics approaches DIA methods have been used for peptide quantification via MS. Compared to the older DDA, in which a fixed number of precursor ions are stepwise selected for fragmentation, a whole range of precursor ions entering the MS at a given time are selected for fragmentation and subsequent daughter ion m/z determination. While requiring the establishment of peptide libraries and intense post-MS analysis, DIA methods promise superior quantification of low abundant peptides, which are less reliably selected for fragmentation in DDA-based approaches. Since the major challenge in organelle proteomics experiments is the discrimination of low-abundant true organelle residents from contaminating proteins, the DIA-dependent protein quantification approach was combined with two different organelle separation approaches to evaluate its feasibility for the annotation of organelle-specific proteomes. For mouse liver, several previous proteomics surveys have been published to date (see Section 4.1.1). Therefore, for the mouse proteomics survey from this thesis, the main focus was laid on maximum accurate, selective, and sensitive quantification, in order to identify low abundant peroxisomal proteins, which were missed in previous studies. To this end, highly pure peroxisome fractions (> 90%) were separated by a sigmoid-shaped density gradient from the remaining organelles, in order to maximize the enrichment factors for subsequent MS protein quantification. In this way, the SWATH-MS approach provided a list of a significant number of previously not identified peroxisomal candidate proteins. The total or partial association of the five selected candidates could be confirmed by overexpression experiments of immunofluorescence microscopy. By contrast, peroxisomes from cardiac tissue are poorly characterized and studies to characterize their organelle-specific proteome are entirely lacking However, the low abundance and different physical properties of cardiac micro-peroxisomes impeded a straightforward isolation to high purity.

Therefore, a gradient profiling approach, which associates individual proteins according to their gradient distribution pattern was established, since it does not require the separation of individual organelles into utmost pure fractions. This approach allowed the compilation of master profiles for the individual organelles. Evaluation of the targeting of two uncharacterized PTS1-containing proteins confirmed their localization to the ER and peroxisomes, respectively, and principally proved the feasibility of the profiling approach. Hence, the existent master profile data can now be used to train an AI-based algorithm in order to associate hitherto uncharacterized proteins to individual organelles. Since the heart peroxisome project is part of a DZHK "Shared expertise" project, further data evaluation will be performed at the collaborating institute (AG S. Thoms, Bielefeld University) and is, therefore, not part of this thesis. In conclusion, this thesis describes two alternative, successful, quantitative MS approaches to characterize the peroxisomal proteome from different tissues. Future experiments will now be required to assess the function of the novel peroxisome-associated proteins identified in this work and confirm a bona fide localization of further potentially tissue-specific candidates at peroxisomes.

5 SUMMARY

Peroxisomes are involved in a variety of metabolic functions such as the degradation of very long-chain fatty acids, D-amino acids and purins or the synthesis of ether lipids, PUFAs and bile acids. Accordingly, the absence of single peroxisomal enzymes or the whole organelle leads to severe inherited peroxisome disorders, which often lead to death during early childhood. Despite their obvious significance for human health, peroxisomes are still the least characterized subcellular compartment. To increase the knowledge on peroxisome-related functions and to complement the peroxisomal proteome, this thesis focused on identifying new potential peroxisome-associated candidate proteins in the liver and heart by conducting two different quantitative MS-based approaches in the two tissues.

The proteomic survey performed in mouse liver – the tissue, in which peroxisomes are best characterized – aimed to identify novel, low abundant peroxisome-associated proteins using a quantitative SWATH-MS approach. To this end, peroxisomes were isolated from two different prefractions with a differing organelle composition produced by step-wise differential centrifugation – the so-called light mitochondrial and fluffy layer fractions. The comparison of the protein enrichment lists from both respective peroxisome fractions generated by SWATH MS, revealed a nearly identical set of proteins, which was therefore considered to be candidates of a *bona fide* peroxisomal proteome. In order to validate the proteomics data, the peroxisomal targeting and/or localization was investigated for the five selected novel peroxisomal candidate proteins HTATIP2, PAFAH2, SAR1b, PDCD6 and OCIAD1. Confocal immunofluorescence analysis of myc-tagged HATIP2 and PAFAH2 variants confirmed their peroxisomal localization. In contrast, a direct localization of endogenous or overexpressed SAR1b at peroxisomes could not be observed. However, the reticular ER-signal pattern of SAR1b regularly enclosed peroxisomes suggesting a close membrane association between a SAR1b-positive ER subcompartment and peroxisomes. Likewise, the results of the PDCD6 overexpression analysis, suggested that the protein is not a true peroxisomal constituent, but like SAR1b localizes focally to ER exit sites, which were often found in in apposition with peroxisomes. These findings suggested a potential function for both SAR1b and PDCD6 in so-called peroxisome-wrappER membrane contacts, which were recently described to play a role in the regulation of liver

lipoprotein export. The last candidate OCIAD1 localized to mitochondria and peroxisomes Of note, OCIAD1 overexpression induced mitochondrial fractionation and reduction of peroxisome abundance, which suggests that OCIAD1 might play a role in coordinating peroxisomal and mitochondrial metabolic activities.

Cardiomyocytes primarily rely on fatty acid β-oxidation for ATP production. Despite the important role of peroxisomes in lipid metabolism, their significance in cardiomyocytes is still poorly understood. Hence, in order to provide fundamental data on the heart-specific peroxisomal proteome, an MS-based organellar profiling approach was developed in this thesis.

To this end, a linear density gradient was invented to gradually distribute distinct organelle species in different gradient zones. This density gradient technique was subsequently combined with a quantitative HyperLOPIT MS analysis of 6 consecutive gradient fractions. The distribution of known organelle marker proteins was used to generate characteristic separation profiles for peroxisomes, mitochondria, the ER and lyso-/endosomes. To validate if the gradient profiles would allow to predict a potential peroxisomal localization of hitherto unknown proteins, two potential candidates, SERHL2 and KLHL41, with a potential peroxisomal targeting sequence were selected for overexpression experiments. Matching with the shape of their gradient profiles, the localization of SERHL2 was confirmed as peroxisomal, while KLHL41 showed an ER-like distribution. These results confirm the suitability of the organelle profiling approach as a tool to identify potential peroxisomal proteins in cardiomyocytes. In this respect, the proteomics data will provide the basis for an AI-driven bioinformatics analysis, which will be used to associate further uncharacterized proteins to the peroxisomal cluster.

In summary, this thesis introduced two alternative quantitative organelle proteomics approaches for heart and liver, which both successfully allowed to expand the list of peroxisome-localized proteins. However, it also demonstrates the importance of combining proteomic analysis with supplementary subcellular localization experiments to validate organelle-specific localization of the identified protein candidates.

6 BIBLIOGRAPHY

Agarwal, S., Chakravarthi, B. V., Behring, M., Kim, H. G., Chandrashekar, D. S., Gupta, N., ... & Manne, U. (2020). PAICS, a purine nucleotide metabolic enzyme, is involved in tumor growth and the metastasis of colorectal cancer. Cancers, 12(4), 772.

Agrawal, G., & Subramani, S. (2013). Emerging role of the endoplasmic reticulum in peroxisome biogenesis. Frontiers in physiology, 4, 286.

Antonenkov, V. D., Sormunen, R. T., & Hiltunen, J. K. (2004). The behavior of peroxisomes in vitro: mammalian peroxisomes are osmotically sensitive particles. American Journal of Physiology-Cell Physiology, 287(6), C1623-C1635.

Antonicka, H., Lin, Z. Y., Janer, A., Aaltonen, M. J., Weraarpachai, W., Gingras, A. C., & Shoubridge, E. A. (2020). A high-density human mitochondrial proximity interaction network. Cell Metabolism, 32(3), 479-497.

Baes, M., & Van Veldhoven, P. P. (2016). Hepatic dysfunction in peroxisomal disorders. Biochimica et Biophysica Acta (BBA)-Molecular Cell Research, 1863(5), 956-970.

Barton, K., Mathur, N., & Mathur, J. (2013). Simultaneous live-imaging of peroxisomes and the ER in plant cells suggests contiguity but no luminal continuity between the two organelles. Frontiers in physiology, 4, 196.

Baumgart, E. (1997). Application of in situ hybridization, cytochemical and immunocytochemical techniques for the investigation of peroxisomes: A review including novel data. Histochemistry and cell biology, 108(3), 185-210.

Baumgart, E., Vanhorebeek, I., Grabenbauer, M., Borgers, M., Declercq, P. E., Fahimi, H. D., & Baes, M. (2001). Mitochondrial alterations caused by defective peroxisomal biogenesis in a mouse model for Zellweger syndrome (PEX5 knockout mouse). The American journal of pathology, 159(4), 1477-1494.

Bedi Jr, K. C., Snyder, N. W., Brandimarto, J., Aziz, M., Mesaros, C., Worth, A. J., ... & Rame, J. E. (2016). Evidence for intramyocardial disruption of lipid metabolism and increased myocardial ketone utilization in advanced human heart failure. Circulation, 133(8), 706-716.

Bender, S., Reuter, A., Eberle, F., Einhorn, E., Binder, M., & Bartenschlager, R. (2015). Activation of type I and III interferon response by mitochondrial and

peroxisomal MAVS and inhibition by hepatitis C virus. PLoS pathogens, 11(11), e1005264.

Bernhard, W., & Rouiller, C. (1956). Close topographical relationship between mitochondria and ergastoplasm of liver cells in a definite phase of cellular activity. The Journal of biophysical and biochemical cytology, 2(4), 73.

Binns, D., Januszewski, T., Chen, Y., Hill, J., Markin, V. S., Zhao, Y., ... & Goodman, J. M. (2006). An intimate collaboration between peroxisomes and lipid bodies. The Journal of cell biology, 173(5), 719-731.

Bonekamp, N. A., Völkl, A., Fahimi, H. D., & Schrader, M. (2009). Reactive oxygen species and peroxisomes: struggling for balance. Biofactors, 35(4), 346-355.

Bradford, M. M. (1976). A rapid and sensitive method for the quantitation of microgram quantities of protein utilizing the principle of protein-dye binding. Analytical biochemistry, 72(1-2), 248-254.

Brites, P., Motley, A. M., Gressens, P., Mooyer, P. A., Ploegaert, I., Everts, V., ... & Baes, M. (2003). Impaired neuronal migration and endochondral ossification in Pex7 knockout mice: a model for rhizomelic chondrodysplasia punctata. Human molecular genetics, 12(18), 2255-2267.

Calvo, S. E., Clauser, K. R., & Mootha, V. K. (2016). MitoCarta2. 0: an updated inventory of mammalian mitochondrial proteins. Nucleic acids research, 44(D1), D1251-D1257.

Camões, F., Islinger, M., Guimarães, S. C., Kilaru, S., Schuster, M., Godinho, L. F., ... & Schrader, M. (2015). New insights into the peroxisomal protein inventory: Acyl-CoA oxidases and-dehydrogenases are an ancient feature of peroxisomes. Biochimica et Biophysica Acta (BBA)-Molecular Cell Research, 1853(1), 111-125.

Cardinale, C. J., Chang, X., Wei, Z., Qu, H. Q., Bradfield, J. P., Polychronakos, C., & Hakonarson, H. (2023). Genome-wide association study of the age of onset of type 1 diabetes reveals HTATIP2 as a novel T cell regulator. Frontiers in Immunology, 14, 1101488.

Carmichael, R. E., Islinger, M., & Schrader, M. (2022). Fission Impossible (?)—New Insights into Disorders of Peroxisome Dynamics. Cells, 11(12), 1922.

Castro, I. G., Richards, D. M., Metz, J., Costello, J. L., Passmore, J. B., Schrader, T. A., ... & Schrader, M. (2018). A role for Mitochondrial Rho GTPase 1 (MIRO1) in motility and membrane dynamics of peroxisomes. Traffic, 19(3), 229-242.

Charles, K. N., Shackelford, J. E., Faust, P. L., Fliesler, S. J., Stangl, H., & Kovacs, W. J. (2020). Functional peroxisomes are essential for efficient cholesterol sensing and synthesis. Frontiers in cell and developmental biology, 8, 560266.

Christoforou, A., Mulvey, C. M., Breckels, L. M., Geladaki, A., Hurrell, T., Hayward, P. C., ... & Lilley, K. S. (2016). A draft map of the mouse pluripotent stem cell spatial proteome. Nature communications, 7(1), 9992.

Chu, B. B., Liao, Y. C., Qi, W., Xie, C., Du, X., Wang, J., ... & Song, B. L. (2015). Cholesterol transport through lysosome-peroxisome membrane contacts. Cell, 161(2), 291-306.

Colasante, C., Chen, J., Ahlemeyer, B., & Baumgart-Vogt, E. (2015). Peroxisomes in cardiomyocytes and the peroxisome/peroxisome proliferator-activated receptor-loop. Thrombosis and haemostasis, 113(03), 452-463.

Costello, J. L., Castro, I. G., Hacker, C., Schrader, T. A., Metz, J., Zeuschner, D., ... & Schrader, M. (2017). ACBD5 and VAPB mediate membrane associations between peroxisomes and the ER. Journal of Cell Biology, 216(2), 331-342.

Costello, J. L., Koster, J., Silva, B. S., Worthy, H. L., Schrader, T. A., Hacker, C., ... & Schrader, M. (2023). Differential roles for ACBD4 and ACBD5 in peroxisome–ER interactions and lipid metabolism. Journal of Biological Chemistry, 299(8).

da Silva, T. F., Sousa, V. F., Malheiro, A. R., & Brites, P. (2012). The importance of ether-phospholipids: a view from the perspective of mouse models. Biochimica et Biophysica Acta (BBA)-Molecular Basis of Disease, 1822(9), 1501-1508.

Darwisch, W., von Spangenberg, M., Lehmann, J., Singin, Ö., Deubert, G., Kühl, S., ... & Islinger, M. (2020). Cerebellar and hepatic alterations in ACBD5-deficient mice are associated with unexpected, distinct alterations in cellular lipid homeostasis. Communications Biology, 3(1), 713.

De Craemer, D., Vamecq, J., Roels, F., Vallée, L., Pauwels, M., & Van den Branden, C. (1994). Peroxisomes in liver, heart, and kidney of mice fed a commercial fish oil preparation: original data and review on peroxisomal changes induced by high-fat diets. Journal of lipid research, 35(7), 1241-1250.

De Duve, C. A. B. P., & Baudhuin, P. (1966). Peroxisomes (microbodies and related particles). Physiological reviews, 46(2), 323-357.

De Marchi, T., Liu, N. Q., Stingl, C., Timmermans, M. A., Smid, M., Look, M. P., ... & Umar, A. (2016). 4-protein signature predicting tamoxifen treatment outcome in recurrent breast cancer. Molecular oncology, 10(1), 24-39.

Depreter, M., Espeel, M., & Roels, F. (2003). Human peroxisomal disorders. Microscopy research and technique, 61(2), 203-223.

Dixit, E., Boulant, S., Zhang, Y., Lee, A. S., Odendall, C., Shum, B., ... & Kagan, J. C. (2010). Peroxisomes are signaling platforms for antiviral innate immunity. Cell, 141(4), 668-681.

Donaldson, J. G., & Jackson, C. L. (2011). ARF family G proteins and their regulators: roles in membrane transport, development and disease. Nature reviews Molecular cell biology, 12(6), 362-375.

Dong, L., Li, Y., & Wu, H. (2021). Platelet activating-factor acetylhydrolase II: A member of phospholipase A2 family that hydrolyzes oxidized phospholipids. Chemistry and Physics of Lipids, 239, 105103.

Dos Remedios, C. G., Liew, C. C., Allen, P. D., Winslow, R. L., Van Eyk, J. E., & Dunn, M. J. (2003). Genomics, proteomics and bioinformatics of human heart failure. Journal of Muscle Research & Cell Motility, 24, 251-261.

Du Puy, L., Beqqali, A., Van Tol, H. T., Monshouwer-Kloots, J., Passier, R., Haagsman, H. P., & Roelen, B. A. (2012). Sarcosin (Krp1) in skeletal muscle differentiation: gene expression profiling and knockdown experiments. International Journal of Developmental Biology, 56(4), 301-309.

Erdmann, R., & Schliebs, W. (2005). Peroxisomal matrix protein import: the transient pore model. Nature Reviews Molecular Cell Biology, 6(9), 738-742.

Fahimi, H. D., Kino, M., Hicks, L., Thorp, K. A., & Abelman, W. H. (1979). Increased myocardial catalase in rats fed ethanol. The American Journal of Pathology, 96(2), 373.

Falcon, A., Doege, H., Fluitt, A., Tsang, B., Watson, N., Kay, M. A., & Stahl, A. (2010). FATP2 is a hepatic fatty acid transporter and peroxisomal very long-chain acyl-CoA synthetase. American Journal of Physiology-Endocrinology and Metabolism, 299(3), E384-E393.

Farre, J. C., Carolino, K., Devanneaux, L., & Subramani, S. (2022). OXPHOS deficiencies affect peroxisome proliferation by downregulating genes controlled by the SNF1 signaling pathway. Elife, 11, e75143.

Farré, J. C., Mahalingam, S. S., Proietto, M., & Subramani, S. (2019). Peroxisome biogenesis, membrane contact sites, and quality control. EMBO reports, 20(1), e46864.

Faust, P. L., & Kovacs, W. J. (2014). Cholesterol biosynthesis and ER stress in peroxisome deficiency. Biochimie, 98, 75-85.

Ferdinandusse, S., Jimenez-Sanchez, G., Koster, J., Denis, S., Van Roermund, C. W., Silva-Zolezzi, I., ... & Valle, D. (2015). A novel bile acid biosynthesis defect due to a deficiency of peroxisomal ABCD3. Human molecular genetics, 24(2), 361-370.

Filppula, S. A., Yagi, A. I., Kilpelainen, S. H., Novikov, D., FitzPatrick, D. R., Vihinen, M., ... & Hiltunen, J. K. (1998). Δ3, 5-Δ2, 4-Dienoyl-CoA Isomerase from Rat Liver: MOLECULAR CHARACTERIZATION. Journal of Biological Chemistry, 273(1), 349-355.

Gao, Y., Skowyra, M. L., Feng, P., & Rapoport, T. A. (2022). Protein import into peroxisomes occurs through a nuclear pore–like phase. Science, 378(6625), eadf3971.

Garikapati, V., Colasante, C., Baumgart-Vogt, E., & Spengler, B. (2022). Sequential lipidomic, metabolomic, and proteomic analyses of serum, liver, and heart tissue specimens from peroxisomal biogenesis factor 11α knockout mice. Analytical and Bioanalytical Chemistry, 414(6), 2235-2250.

Geisbrecht, B. V., Zhang, D., Schulz, H., & Gould, S. J. (1999). Characterization of PECI, a novel monofunctional Δ3, Δ2-enoyl-CoA isomerase of mammalian peroxisomes. Journal of Biological Chemistry, 274(31), 21797-21803.

Gillet, L. C., Navarro, P., Tate, S., Röst, H., Selevsek, N., Reiter, L., ... & Aebersold, R. (2012). Targeted data extraction of the MS/MS spectra generated by data-independent acquisition: a new concept for consistent and accurate proteome analysis. Molecular & Cellular Proteomics, 11(6).

Girzalsky, W., Saffian, D., & Erdmann, R. (2010). Peroxisomal protein translocation. Biochimica et Biophysica Acta (BBA)-Molecular Cell Research, 1803(6), 724-731.

Gould, S. G., Keller, G. A., & Subramani, S. (1987). Identification of a peroxisomal targeting signal at the carboxy terminus of firefly luciferase. The Journal of cell biology, 105(6), 2923-2931.

Gouveia, A. M., Reguenga, C., Oliveira, M. E., Eckerskorn, C., Sá-Miranda, C., & Azevedo, J. E. (1999). Alkaline density gradient floatation of membranes: polypeptide composition of the mammalian peroxisomal membrane. Analytical biochemistry, 274(2), 270-277.

Graham, J., Ford, T., & Rickwood, D. (1994). The preparation of subcellular organelles from mouse liver in self-generated gradients of iodixanol. Analytical biochemistry, 220(2), 367-373.

Gramolini, A. O., Kislinger, T., Liu, P., MacLennan, D. H., & Emili, A. (2007). Analyzing the cardiac muscle proteome by liquid chromatography-mass spectrometry-based expression proteomics. Cardiovascular Proteomics: Methods and Protocols, 15-31.

Greenberg, C. C., Connelly, P. S., Daniels, M. P., & Horowits, R. (2008). Krp1 (Sarcosin) promotes lateral fusion of myofibril assembly intermediates in cultured mouse cardiomyocytes. Experimental cell research, 314(5), 1177-1191.

Grings, M., Tonin, A. M., Knebel, L. A., Zanatta, Â., Moura, A. P., Filho, C. S. D., ... & Leipnitz, G. (2012). Phytanic acid disturbs mitochondrial homeostasis in heart of young rats: a possible pathomechanism of cardiomyopathy in Refsum disease. Molecular and cellular biochemistry, 366, 335-343.

Gronemeyer, T., Wiese, S., Ofman, R., Bunse, C., Pawlas, M., Hayen, H., ... & Warscheid, B. (2013). The proteome of human liver peroxisomes: identification of five new peroxisomal constituents by a label-free quantitative proteomics survey. PloS one, 8(2), e57395.

Gupta, V. A., Ravenscroft, G., Shaheen, R., Todd, E. J., Swanson, L. C., Shiina, M., ... & Beggs, A. H. (2013). Identification of KLHL41 mutations implicates BTB-Kelch-mediated ubiquitination as an alternate pathway to myofibrillar disruption in nemaline myopathy. The American Journal of Human Genetics, 93(6), 1108-1117.

Harris, C. R., Millman, K. J., Van Der Walt, S. J., Gommers, R., Virtanen, P., Cournapeau, D., ... & Oliphant, T. E. (2020). Array programming with NumPy. *Nature*, *585*(7825), 357-362.

Harris, T. R., & Hammock, B. D. (2013). Soluble epoxide hydrolase: gene structure, expression and deletion. Gene, 526(2), 61-74.

Harrison, E. H., & Walusimbi-Kisitu, M. B. A. G. A. (1988). Properties and subcellular localization of myocardial fatty acyl-coenzyme A oxidase. American Journal of Physiology-Heart and Circulatory Physiology, 255(3), H441-H445.

Hattori, K., Adachi, H., Matsuzawa, A., Yamamoto, K., Tsujimoto, M., Aoki, J., ... & Inoue, K. (1996). cDNA cloning and expression of intracellular platelet-

activating factor (PAF) acetylhydrolase II: its homology with plasma PAF acetylhydrolase. Journal of Biological Chemistry, 271(51), 33032-33038.

Hawkins, J., Mahony, D., Maetschke, S., Wakabayashi, M., Teasdale, R. D., & Bodén, M. (2007). Identifying novel peroxisomal proteins. Proteins: Structure, Function, and Bioinformatics, 69(3), 606-616.

He, A., Dean, J. M., & Lodhi, I. J. (2021). Peroxisomes as cellular adaptors to metabolic and environmental stress. Trends in cell biology, 31(8), 656-670.

Herzog, V., & Fahimi, H. D. (1974). Microbodies (peroxisomes) containing catalase in myocardium: morphological and biochemical evidence. Science, 185(4147), 271-273.

Herzog, V., & Fahimi, H. D. (1974). The Effect of Glutaraldehyde on Catalase: Biochemical and Cytochemical Studies with Beef Liver Catalase and Rat Liver Peroxisomes. The Journal of cell biology, 60(1), 303.

Herzog, V., & Fahimi, H. D. (1976). Intracellular distinction between peroxidase and catalase in exocrine cells of rat lacrimal gland: a biochemical and cytochemical study. Histochemistry, 46(4), 273-286.

Hoepfner, D., Schildknegt, D., Braakman, I., Philippsen, P., & Tabak, H. F. (2005). Contribution of the endoplasmic reticulum to peroxisome formation. Cell, 122(1), 85-95.

Hogenboom, S., Wanders, R. J., & Waterham, H. R. (2003). Cholesterol biosynthesis is not defective in peroxisome biogenesis defective fibroblasts. Molecular genetics and metabolism, 80(3), 290-295.

Hollinshead, M., & Meijer, J. (1988). Immunocytochemical analysis of soluble epoxide hydrolase and catalase in mouse and rat hepatocytes demonstrates a peroxisomal localization before and after clofibrate treatment. European journal of cell biology, 46(3), 394-402.

Hua, R., Cheng, D., Coyaud, É., Freeman, S., Di Pietro, E., Wang, Y., ... & Kim, P. K. (2017). VAPs and ACBD5 tether peroxisomes to the ER for peroxisome maintenance and lipid homeostasis. Journal of Cell Biology, 216(2), 367-377.

Ilacqua, N., Anastasia, I., Raimondi, A., Lemieux, P., de Aguiar Vallim, T. Q., Toth, K., ... & Pellegrini, L. (2022). A three-organelle complex made by wrappER contacts with peroxisomes and mitochondria responds to liver lipid flux changes. Journal of cell science, 135(5), jcs259091.

Inukai, Ryuta, Kanako Mori, Keiko KuwatInukai, R., Mori, K., Kuwata, K., Suzuki, C., Maki, M., Takahara, T., & Shibata, H. (2021). The novel ALG-2 target protein CDIP1 promotes cell death by interacting with ESCRT-I and VAPA/B. International Journal of Molecular Sciences, 22(3), 1175.a, Chihiro Suzuki, Masatoshi Maki, Terunao Takahara, and Hideki Shibata. "The novel ALG-2 target protein CDIP1 promotes cell death by interacting with ESCRT-I and VAPA/B." International Journal of Molecular Sciences 22, no. 3 (2021): 1175.

Islinger, M., Grille, S., Fahimi, H. D., & Schrader, M. (2012). The peroxisome: an update on mysteries. Histochemistry and cell biology, 137, 547-574.

Islinger, M., Li, K. W., Loos, M., Liebler, S., Angermüller, S., Eckerskorn, C., ... & Völkl, A. (2010). Peroxisomes from the heavy mitochondrial fraction: isolation by zonal free flow electrophoresis and quantitative mass spectrometrical characterization. Journal of proteome research, 9(1), 113-124.

Islinger, M., Lüers, G. H., Zischka, H., Ueffing, M., & Völkl, A. (2006). Insights into the membrane proteome of rat liver peroxisomes: microsomal glutathione-S-transferase is shared by both subcellular compartments. Proteomics, 6(3), 804-816.

Islinger, M., Luöers, G. H., Li, K. W., Loos, M., & Voölkl, A. (2007). Rat liver peroxisomes after fibrate treatment: a survey using quantitative mass spectrometry. Journal of Biological Chemistry, 282(32), 23055-23069.

Islinger, M., Voelkl, A., Fahimi, H. D., & Schrader, M. (2018). The peroxisome: an update on mysteries 2.0. Histochemistry and cell biology, 150, 443-471.

Jadot, M., Boonen, M., Thirion, J., Wang, N., Xing, J., Zhao, C., ... & Lobel, P. (2017). Accounting for protein subcellular localization: a compartmental map of the rat liver proteome. Molecular & cellular proteomics, 16(2), 194-212.

Jia, J., Tarabykina, S., Hansen, C., Berchtold, M., & Cygler, M. (2001). Structure of apoptosis-linked protein ALG-2: insights into Ca2+-induced changes in penta-EF-hand proteins. Structure, 9(4), 267-275.

Just, W. W., & Peränen, J. (2016). Small GTPases in peroxisome dynamics. Biochimica et Biophysica Acta (BBA)-Molecular Cell Research, 1863(5), 1006-1013.

Kamoshita, M., Kumar, R., Anteghini, M., Kunze, M., Islinger, M., Martins dos Santos, V., & Schrader, M. (2022). Insights into the peroxisomal protein inventory of zebrafish. Frontiers in physiology, 322.

Karnati, S., Lüers, G., Pfreimer, S., & Baumgart-Vogt, E. (2013). Mammalian SOD2 is exclusively located in mitochondria and not present in peroxisomes. Histochemistry and cell biology, 140, 105-117.

Keller, G. A., Gould, S., Deluca, M., & Subramani, S. (1987). Firefly luciferase is targeted to peroxisomes in mammalian cells. Proceedings of the National Academy of Sciences, 84(10), 3264-3268.

Kikuchi, M., Hatano, N., Yokota, S., Shimozawa, N., Imanaka, T., & Taniguchi, H. (2004). Proteomic analysis of rat liver peroxisome: presence of peroxisome-specific isozyme of Lon protease. Journal of Biological Chemistry, 279(1), 421-428.

Kim, J. Y., Choi, B. G., Jelinek, J., Kim, D. H., Lee, S. H., Cho, K., ... & Kim, J. (2020). Promoter methylation changes in ALOX12 and AIRE1: novel epigenetic markers for atherosclerosis. Clinical Epigenetics, 12, 1-13.

Kleiboeker, B., & Lodhi, I. J. (2022). Peroxisomal regulation of energy homeostasis: Effect on obesity and related metabolic disorders. Molecular Metabolism, 101577.

Kohr, M. J., Aponte, A. M., Sun, J., Wang, G., Murphy, E., Gucek, M., & Steenbergen, C. (2011). Characterization of potential S-nitrosylation sites in the myocardium. American Journal of Physiology-Heart and Circulatory Physiology, 300(4), H1327-H1335.

Kono, N., Inoue, T., Yoshida, Y., Sato, H., Matsusue, T., Itabe, H., ... & Arai, H. (2008). Protection against oxidative stress-induced hepatic injury by intracellular type II platelet-activating factor acetylhydrolase by metabolism of oxidized phospholipids in vivo. Journal of Biological Chemistry, 283(3), 1628-1636.

Kors, S., Hacker, C., Bolton, C., Maier, R., Reimann, L., Kitchener, E. J., ... & Schrader, M. (2022). Regulating peroxisome–ER contacts via the ACBD5-VAPB tether by FFAT motif phosphorylation and GSK3β. Journal of Cell Biology, 221(3), e202003143.

Kragler, F., Lametschwandtner, G., Christmann, J., Hartig, A., & Harada, J. J. (1998). Identification and analysis of the plant peroxisomal targeting signal 1 receptor NtPEX5. Proceedings of the National Academy of Sciences, 95(22), 13336-13341.

Krysko, O., Hulshagen, L., Janssen, A., Schütz, G., Klein, R., De Bruycker, M., ... & Baes, M. (2007). Neocortical and cerebellar developmental abnormalities in

conditions of selective elimination of peroxisomes from brain or from liver. Journal of neuroscience research, 85(1), 58-72.

Kuge, O., Dascher, C., Orci, L., Rowe, T., Amherdt, M., Plutner, H., ... & Balch, W. E. (1994). Sar1 promotes vesicle budding from the endoplasmic reticulum but not Golgi compartments. The Journal of cell biology, 125(1), 51-65.

Kulkarni, V., Khadilkar, R. J., MS, S., & Inamdar, M. S. (2011). Asrij maintains the stem cell niche and controls differentiation during Drosophila lymph gland hematopoiesis. PLoS One, 6(11), e27667.

Kunze, M. (2018). Predicting peroxisomal targeting signals to elucidate the peroxisomal proteome of mammals. Proteomics of Peroxisomes: Identifying Novel Functions and Regulatory Networks, 157-199.

Kurochkin, I. V., Mizuno, Y., Konagaya, A., Sakaki, Y., Schönbach, C., & Okazaki, Y. (2007). Novel peroxisomal protease Tysnd1 processes PTS1-and PTS2-containing enzymes involved in β-oxidation of fatty acids. The EMBO Journal, 26(3), 835-845.

Kvannes, J., Eikhom, T. S., & Flatmark, T. (1994). The peroxisomal β-oxidation enzyme system of rat heart. Basal level and effect of the peroxisome proliferator clofibrate. Biochimica et Biophysica Acta (BBA)-General Subjects, 1201(2), 203-216.

Kyhse-Andersen, J. (1984). Electroblotting of multiple gels: a simple apparatus without buffer tank for rapid transfer of proteins from polycrylamide to nitrocellulose. Journal of biochemical and biophysical methods, 10(3-4), 203-209.

la Cour, J. M., Schindler, A. J., Berchtold, M. W., & Schekman, R. (2013). ALG-2 attenuates COPII budding in vitro and stabilizes the Sec23/Sec31A complex. PloS one, 8(9), e75309.

Laemmli, U. K. (1970). Cleavage of structural proteins during the assembly of the head of bacteriophage T4. nature, 227(5259), 680-685.

Lametschwandtner, G., Brocard, C., Fransen, M., Van Veldhoven, P., Berger, J., & Hartig, A. (1998). The difference in recognition of terminal tripeptides as peroxisomal targeting signal 1 between yeast and human is due to different affinities of their receptor Pex5p to the cognate signal and to residues adjacent to it. Journal of Biological Chemistry, 273(50), 33635-33643.

Lay, D., Gorgas, K., & Just, W. W. (2006). Peroxisome biogenesis: where Arf and coatomer might be involved. Biochimica et Biophysica Acta (BBA)-Molecular Cell Research, 1763(12), 1678-1687.

Lazarow, P. B. (1995). Disorders of peroxisome biogenesis. The Metabolic and Molecular Bases of Inherited Disease, 7th edition, 2287-2324.

Lazarow, P. B., & Fujiki, Y. (1985). Biogenesis of peroxisomes. Annual review of cell biology, 1(1), 489-530.

Le Vasseur, M., Friedman, J., Jost, M., Xu, J., Yamada, J., Kampmann, M., ... & Nunnari, J. (2021). Genome-wide CRISPRi screening identifies OCIAD1 as a prohibitin client and regulatory determinant of mitochondrial Complex III assembly in human cells. Elife, 10, e67624.

Léon, S., Goodman, J. M., & Subramani, S. (2006). Uniqueness of the mechanism of protein import into the peroxisome matrix: transport of folded, co-factor-bound and oligomeric proteins by shuttling receptors. Biochimica et Biophysica Acta (BBA)-Molecular Cell Research, 1763(12), 1552-1564.

Levy, S., Allerston, C. K., Liveanu, V., Habib, M. R., Gileadi, O., & Schuster, G. (2016). Identification of LACTB2, a metallo-β-lactamase protein, as a human mitochondrial endoribonuclease. Nucleic Acids Research, 44(4), 1813-1832.

Lewin, T. M., Van Horn, C. G., Krisans, S. K., & Coleman, R. A. (2002). Rat liver acyl-CoA synthetase 4 is a peripheral-membrane protein located in two distinct subcellular organelles, peroxisomes, and mitochondrial-associated membrane. Archives of biochemistry and biophysics, 404(2), 263-270.

Liao, B. M., Raddatz, K., Zhong, L., Parker, B. L., Raftery, M. J., & Schmitz-Peiffer, C. (2014). Proteomic analysis of livers from fat-fed mice deficient in either PKCδ or PKCε identifies Htatip2 as a regulator of lipid metabolism. Proteomics, 14(21-22), 2578-2587.

Liepinsh, E., Skapare, E., Kuka, J., Makrecka, M., Cirule, H., Vavers, E., ... & Dambrova, M. (2013). Activated peroxisomal fatty acid metabolism improves cardiac recovery in ischemia-reperfusion. Naunyn-Schmiedeberg's archives of pharmacology, 386, 541-550.

Lismont, C., Nordgren, M., Van Veldhoven, P. P., & Fransen, M. (2015). Redox interplay between mitochondria and peroxisomes. Frontiers in cell and developmental biology, 3, 35.

Lismont, C., Revenco, I., & Fransen, M. (2019). Peroxisomal hydrogen peroxide metabolism and signaling in health and disease. International Journal of Molecular Sciences, 20(15), 3673.

Lodhi, I. J., & Semenkovich, C. F. (2014). Peroxisomes: a nexus for lipid metabolism and cellular signaling. Cell metabolism, 19(3), 380-392.

Lopaschuk, G. D., Ussher, J. R., Folmes, C. D., Jaswal, J. S., & Stanley, W. C. (2010). Myocardial fatty acid metabolism in health and disease. Physiological reviews, 90(1), 207-258.

Ludwig, C., Gillet, L., Rosenberger, G., Amon, S., Collins, B. C., & Aebersold, R. (2018). Data-independent acquisition-based SWATH-MS for quantitative proteomics: a tutorial. Molecular systems biology, 14(8), e8126.

Manner, A., & Islinger, M. (2017). Isolation of peroxisomes from rat liver and cultured hepatoma cells by density gradient centrifugation. Peroxisomes: Methods and Protocols, 1-11.

McKinney, W. (2010, June). Data structures for statistical computing in python. In *Proceedings of the 9th Python in Science Conference* (Vol. 445, No. 1, pp. 51-56).

McNew, J. A., & Goodman, J. M. (1996). The targeting and assembly of peroxisomal proteins: some old rules do not apply. Trends in biochemical sciences, 21(2), 54-58.

Melville, D. B., Studer, S., & Schekman, R. (2020). SAR1 paralogs differ biochemically in assembly of the COPII coat. bioRxiv, 2020-02.

Miller, E. A., & Schekman, R. (2013). COPII—a flexible vesicle formation system. Current opinion in cell biology, 25(4), 420-427.

Mishra, P., & Chan, D. C. (2016). Metabolic regulation of mitochondrial dynamics. Journal of Cell Biology, 212(4), 379-387.

Mizuno, Y., Kurochkin, I. V., Herberth, M., Okazaki, Y., & Schönbach, C. (2008). Predicted mouse peroxisome-targeted proteins and their actual subcellular locations. Bmc Bioinformatics, 9, 1-11.

Mönnig, G., Wiekowski, J., Kirchhof, P., Stypmann, J., Plenz, G., Fabritz, L., ... & Seedorf, U. (2004). Phytanic acid accumulation is associated with conduction delay and sudden cardiac death in sterol carrier protein-2/sterol carrier protein-x deficient mice. Journal of cardiovascular electrophysiology, 15(11), 1310-1316.

Morel, F., Rauch, C., Petit, E., Piton, A., Theret, N., Coles, B., & Guillouzo, A. (2004). Gene and protein characterization of the human glutathione S-transferase kappa and evidence for a peroxisomal localization. Journal of biological chemistry, 279(16), 16246-16253.

Mukhopadhyay, A., Das, D., & Inamdar, M. S. (2003). Embryonic stem cell and tissue-specific expression of a novel conserved gene, asrij. Developmental Dynamics: An Official Publication of the American Association of Anatomists, 227(4), 578-586.

Mulvey, C. M., Breckels, L. M., Geladaki, A., Britovšek, N. K., Nightingale, D. J., Christoforou, A., ... & Lilley, K. S. (2017). Using hyperLOPIT to perform high-resolution mapping of the spatial proteome. Nature protocols, 12(6), 1110-1135.

Neuberger, G., Maurer-Stroh, S., Eisenhaber, B., Hartig, A., & Eisenhaber, F. (2003). Prediction of peroxisomal targeting signal 1 containing proteins from amino acid sequence. Journal of molecular biology, 328(3), 581-592.

Nordgren, M., & Fransen, M. (2014). Peroxisomal metabolism and oxidative stress. Biochimie, 98, 56-62.

Novikoff, A. B., & Shin, W. Y. (1978). Endoplasmic reticulum and autophagy in rat hepatocytes. Proceedings of the National Academy of Sciences, 75(10), 5039-5042.

Oeljeklaus, S., Schummer, A., & Warscheid, B. (2014). The proteomics toolbox applied to peroxisomes. Molecular machines involved in peroxisome biogenesis and maintenance, 275-301.

Okumura, M., Katsuyama, A. M., Shibata, H., & Maki, M. (2013). VPS37 isoforms differentially modulate the ternary complex formation of ALIX, ALG-2, and ESCRT-I. Bioscience, biotechnology, and biochemistry, 77(8), 1715-1721.

Okumura, M., Takahashi, T., Shibata, H., & Maki, M. (2013). Mammalian ESCRT-III-related protein IST1 has a distinctive met-pro repeat sequence that is essential for interaction with ALG-2 in the presence of Ca2+. Bioscience, biotechnology, and biochemistry, 77(5), 1049-1054.

Pan, R., & Hu, J. (2018). Proteome of plant peroxisomes. Proteomics of Peroxisomes: Identifying Novel Functions and Regulatory Networks, 3-45.

Pedregosa, F., Varoquaux, G., Gramfort, A., Michel, V., Thirion, B., Grisel, O., ... & Duchesnay, É. (2011). Scikit-learn: Machine learning in Python. *the Journal of machine Learning research*, *12*, 2825-2830.

Phillips, M. J., & Voeltz, G. K. (2016). Structure and function of ER membrane contact sites with other organelles. Nature reviews Molecular cell biology, 17(2), 69-82.

Prinz, W. A. (2014). Bridging the gap: membrane contact sites in signaling, metabolism, and organelle dynamics. Journal of Cell Biology, 205(6), 759-769.

Ray, A., Kamat, K., & Inamdar, M. S. (2021). A conserved role for Asrij/OCIAD1 in progenitor differentiation and lineage specification through functional interaction with the regulators of mitochondrial dynamics. Frontiers in Cell and Developmental Biology, 9, 643444.

Reguenga, C., Oliveira, M. E., Gouveia, A. M., Sá-Miranda, C., & Azevedo, J. E. (2001). Characterization of the mammalian peroxisomal import machinery: Pex2p, Pex5p, Pex12p, and Pex14p are subunits of the same protein assembly. Journal of Biological Chemistry, 276(32), 29935-29942.

Reumann, S. (2011). Toward a definition of the complete proteome of plant peroxisomes: where experimental proteomics must be complemented by bioinformatics. Proteomics, 11(9), 1764-1779.

Rey, T., Zaganelli, S., Cuillery, E., Vartholomaiou, E., Croisier, M., Martinou, J. C., & Manley, S. (2020). Mitochondrial RNA granules are fluid condensates positioned by membrane dynamics. Nature cell biology, 22(10), 1180-1186.

Rickwood, D., & Birnie, G. D. (1975). Metrizamide, a new density-gradient medium. FEBS letters, 50(2), 102-110.

Sabouny, R., & Shutt, T. E. (2020). Reciprocal regulation of mitochondrial fission and fusion. Trends in biochemical sciences, 45(7), 564-577.

Sadusky, T. J., Kemp, T. J., Simon, M., Carey, N., & Coulton, G. R. (2001). Identification of Serhl, a new member of the serine hydrolase family induced by passive stretch of skeletal muscle in vivo. Genomics, 73(1), 38-49.

Saleem, R. A., Smith, J. J., & Aitchison, J. D. (2006). Proteomics of the peroxisome. Biochimica et Biophysica Acta (BBA)-Molecular Cell Research, 1763(12), 1541-1551.

Schrader, M., & Fahimi, H. D. (2004). Mammalian peroxisomes and reactive oxygen species. Histochemistry and cell biology, 122, 383-393.

Schrader, M., & Fahimi, H. D. (2006). Peroxisomes and oxidative stress. Biochimica et Biophysica Acta (BBA)-Molecular Cell Research, 1763(12), 1755-1766.

Schrader, M., Bonekamp, N. A., & Islinger, M. (2012). Fission and proliferation of peroxisomes. Biochimica et Biophysica Acta (BBA)-Molecular Basis of Disease, 1822(9), 1343-1357.

Schrader, M., Costello, J., Godinho, L. F., & Islinger, M. (2015). Peroxisome-mitochondria interplay and disease. Journal of inherited metabolic disease, 38, 681-702.

Schrader, M., Kamoshita, M., & Islinger, M. (2020). Organelle interplay—peroxisome interactions in health and disease. Journal of Inherited Metabolic Disease, 43(1), 71-89.

Schuldiner, M., & Zalckvar, E. (2015). Peroxisystem: Harnessing systems cell biology to study peroxisomes. Biology of the Cell, 107(4), 89-97.

Schuldiner, M., & Zalckvar, E. (2017). Incredibly close—A newly identified peroxisome–ER contact site in humans. Journal of Cell Biology, 216(2), 287-289.

Scorrano, L., De Matteis, M. A., Emr, S., Giordano, F., Hajnóczky, G., Kornmann, B., ... & Schuldiner, M. (2019). Coming together to define membrane contact sites. Nature communications, 10(1), 1287.

Seedorf, U., Raabe, M., Ellinghaus, P., Kannenberg, F., Fobker, M., Engel, T., ... & Assmann, G. (1998). Defective peroxisomal catabolism of branched fatty acyl coenzyme A in mice lacking the sterol carrier protein-2/sterol carrier protein-x gene function. Genes & development, 12(8), 1189.

Shai, N., Schuldiner, M., & Zalckvar, E. (2016). No peroxisome is an island—peroxisome contact sites. Biochimica et Biophysica Acta (BBA)-Molecular Cell Research, 1863(5), 1061-1069.

Shetty, D. K., Kalamkar, K. P., & Inamdar, M. S. (2018). OCIAD1 controls electron transport chain complex I activity to regulate energy metabolism in human pluripotent stem cells. Stem Cell Reports, 11(1), 128-141.

Shi, X., Cheng, L., Jiao, X., Chen, B., Li, Z., Liang, Y., ... & Chen, S. (2018). Rare copy number variants identify novel genes in sporadic total anomalous pulmonary vein connection. Frontiers in Genetics, 9, 559.

Shtivelman, E. (1997). A link between metastasis and resistance to apoptosis of variant small cell lung carcinoma. Oncogene, 14(18), 2167-2173.

Singh, H., Beckman, K., & Poulos, A. (1993). Exclusive localization in peroxisomes of dihydroxyacetone phosphate acyltransferase and alkyl-dihydroxyacetone phosphate synthase in rat liver. Journal of lipid research, 34(3), 467-477.

Sinha, A., Khadilkar, R. J., Vinay, K. S., Sinha, A. R., & Inamdar, M. S. (2013). Conserved regulation of the Jak/STAT pathway by the endosomal protein asrij maintains stem cell potency. Cell Reports, 4(4), 649-658.

Sinha, S., Ray, A., Abhilash, L., Kumar, M., Sreenivasamurthy, S. K., Prasad, T. K., & Inamdar, M. S. (2019). Proteomics of Asrij Perturbation in Drosophila Lymph Glands for Identification of New Regulators of Hematopoiesis*[S]. Molecular & Cellular Proteomics, 18(6), 1171-1182.

Soupene, E., & Kuypers, F. A. (2008). Mammalian long-chain acyl-CoA synthetases. Experimental biology and medicine, 233(5), 507-521.

Stremler, K. E., Stafforini, D. M., Prescott, S. M., & McIntyre, T. M. (1991). Human plasma platelet-activating factor acetylhydrolase. Oxidatively fragmented phospholipids as substrates. Journal of Biological Chemistry, 266(17), 11095-11103.

Swinkels, B. W., Gould, S. J., & Subramani, S. (1992). Targeting efficiencies of various permutations of the consensus C-terminal tripeptide peroxisomal targeting signal. FEBS letters, 305(2), 133-136.

Tabak, H. F., Murk, J. L., Braakman, I., & Geuze, H. J. (2003). Peroxisomes start their life in the endoplasmic reticulum. Traffic, 4(8), 512-518.

Tanner, J. J., Frey, B. B., Pemberton, T., & Henzl, M. T. (2016). EF5 is the high-affinity Mg2+ site in ALG-2. Biochemistry, 55(36), 5128-5141.

Thul, P. J., & Lindskog, C. (2018). The human protein atlas: a spatial map of the human proteome. Protein Science, 27(1), 233-244.

Thul, P. J., Åkesson, L., Wiking, M., Mahdessian, D., Geladaki, A., Ait Blal, H., ... & Lundberg, E. (2017). A subcellular map of the human proteome. Science, 356(6340), eaal3321.

van der Velden, J., Tocchetti, C. G., Varricchi, G., Bianco, A., Sequeira, V., Hilfiker-Kleiner, D., ... & Heymans, S. (2018). Metabolic changes in hypertrophic cardiomyopathies: scientific update from the Working Group of Myocardial Function of the European Society of Cardiology. Cardiovascular research, 114(10), 1273-1280.

Van Veldhoven, P. P. (2010). Biochemistry and genetics of inherited disorders of peroxisomal fatty acid metabolism [S]. Journal of lipid research, 51(10), 2863-2895.

Vance, J. E. (1990). Phospholipid synthesis in a membrane fraction associated with mitochondria. Journal of Biological Chemistry, 265(13), 7248-7256.

Völkl, A., & Fahimi, H. D. (1985). Isolation and characterization of peroxisomes from the liver of normal untreated rats. European journal of biochemistry, 149(2), 257-265.

Waechter, F., Philip, B., Françoise, B., Willy, S., Alfred, V., & Fahimi, H. D. (1983). Epoxide hydrolase activity in isolated peroxisomes of mouse liver. FEBS letters, 158(2), 225-228.

Wanders, R. J. (2004). Metabolic and molecular basis of peroxisomal disorders: a review. American Journal of Medical Genetics Part A, 126(4), 355-375.

Wanders, R. J. A., Ferdinandusse, S., Brites, P., & Kemp, S. (2010). Peroxisomes, lipid metabolism and lipotoxicity. Biochimica et Biophysica Acta (BBA)-Molecular and Cell Biology of Lipids, 1801(3), 272-280.

Wanders, R. J., Baes, M., Ribeiro, D., Ferdinandusse, S., & Waterham, H. R. (2023). The Physiological Functions of Human Peroxisomes. Physiological Reviews(103), 957–1024.

Wanders, R. J., Jansen, G. A., & Skjeldal, O. H. (2001). Refsum disease, peroxisomes and phytanic acid oxidation: a review. Journal of Neuropathology & Experimental Neurology, 60(11), 1021-1031.

Wanet, A., Arnould, T., Najimi, M., & Renard, P. (2015). Connecting mitochondria, metabolism, and stem cell fate. Stem cells and development, 24(17), 1957-1971.

Watkins, P. A., & Ellis, J. M. (2012). Peroxisomal acyl-CoA synthetases. Biochimica et Biophysica Acta (BBA)-Molecular Basis of Disease, 1822(9), 1411-1420.

Wiese, S., Gronemeyer, T., Ofman, R., Kunze, M., Grou, C. P., Almeida, J. A., ... & Warscheid, B. (2007). Proteomics characterization of mouse kidney peroxisomes by tandem mass spectrometry and protein correlation profiling. Molecular & cellular proteomics, 6(12), 2045-2057.

Wu, Y., Williams, E. G., & Aebersold, R. (2017). Application of SWATH proteomics to mouse biology. Current protocols in mouse biology, 7(2), 130-143.

Yamada, T., Shinnoh, N., Kondo, A., Uchiyama, A., Shimozawa, N., Kira, J. I., & Kobayashi, T. (2000). Very-long-chain fatty acid metabolism in adrenoleukodystrophy protein-deficient mice. Cell Biochemistry and Biophysics, 32, 239-246.

Yang, Y., Song, Y., & Loscalzo, J. (2007). Regulation of the protein disulfide proteome by mitochondria in mammalian cells. Proceedings of the National Academy of Sciences, 104(26), 10813-10817.

Yifrach, E., Fischer, S., Oeljeklaus, S., Schuldiner, M., Zalckvar, E., & Warscheid, B. (2018). Defining the mammalian peroxisomal proteome. Proteomics of Peroxisomes: Identifying Novel Functions and Regulatory Networks, 47-66.

Yu, X., Li, Z., & Wu, W. K. (2015). TIP30: a novel tumor-suppressor gene. Oncology Research Featuring Preclinical and Clinical Cancer Therapeutics, 22(5-6), 339-348.

Zhang, C., Li, A., Zhang, X., & Xiao, H. (2011). A novel TIP30 protein complex regulates EGF receptor signaling and endocytic degradation. Journal of Biological Chemistry, 286(11), 9373-9381.

Zhang, D., Liang, X., He, X. Y., Alipui, O. D., Yang, S. Y., & Schulz, H. (2001). Δ3, 5, Δ2, 4-dienoyl-CoA Isomerase is a multifunctional isomerase: a structural and mechanistic study. Journal of Biological Chemistry, 276(17), 13622-13627.

7 THE LIST OF FIGURES

8 THE LIST OF TABLES

9 APPENDIX

9.1 Equipment

Fume hood (EN14175, LABORA GmbH)
Water bath (SMB20, Medingen)
Thermo Mixer (comfort, 50 ml, Eppendorf)
pH meter (PB-11, Sartorius)
Cell culture hood (KS12, Thermo Electron Corp.)
Centrifugation (centrigue 5804, Eppendorf)
Vortexer (Vortex GENIE, Scientific Industries)
Cell culture Incubator (HERA Cell150, Thermo Scientific)
Sterilizer (Rotilabo®-Syringe filter, CME, Sterile, pore size 0.22µm, Ø outer 33mm, Roth)
Dissection equipment sets (FST by Dumont, Switzerland)
Cryostat (HM550, Microm)
Dissecting microscope (OPTICA)
Phase contrast microscope amounted with fluorescence lamp (Nikon Eclipse TS100)
Nikon C1plus (Nikon Instruments Europe, Düsseldorf, Germany)
Laser lines: 488 nm, 548 nm, 642 nm
Objectives: Nikon Plan Apo VC 20×/0.75 NA, Nikon Plan Apo VC 60×/1.4 NA oil; Nikon Plan Apo VC 100×/1.45 NA oil
Leica SP5 MP (Leica Microsystems CMS GmhH, Mannheim, Germany)
Laser lines: Ar-Laser; DPSS; HeNe
Objectives: 5x/0.15 NA; 10x/0.30 NA; 20x/0.7 NA; 25x/0.95 NA water; 40x/1,3 NA oil; 63x/1,1 NA glycerol
Digital-Refraktometer DR 301-95 (A.Krüss Optronic, Hamburg, Germany)
Rotina 420R centrifuge (Hettich Zentrifugen, Tuttlingen, Germany)
Sorvall WX Ultra 100 centrifuge (Thermo Fisher Scientific, Waltham, USA)
Sorvall Surespin 360 swinging bucket ultracentrifuge rotor (Thermo Fisher Scientific, Waltham, USA)
Beckman VTI50 fixed angle rotor (Beckman Coulter, Brea, USA)
Refractometer (Digital Refractometer DR 301-95, A. Krüss Optronic Hamburg Germany)

Ultracentrifuge and a fixed angle rotor (Rotina 420R centrifuge, Hettich Zentrifugen, Tuttlingen, Germany; Sorvall RC6 plus centrifuge, Sorvall Surespin 360 swinging bucket ultracentrifuge rotor and Sorwall WX Ultra 100 centrifuge Thermo Fisher Scientific, Wattham, USA; VTi 50, VTi 65.1 type vertical rotor, Beckman Coulter, Brea, USA)

Quick-seal polyallomer tubes 25 Å~ 89 mm (39 mL, Beckman Coulter)

Motor-driven Potter-Elvehjem tissue grinder (Schuett-Biotech, Göttingen, Germany) with loose fitting pestle (clearance 0.1–0.15 mm, vol. 30 mL)

9.2 Chemicals and other consumables

0.9% (w/v) NaCl solution

1.5 # coverslips (CS-12R15, Warner Instruments, LLC)

24-well plate (REF 83.3920, SARSTEDT)

40 µm cell strainer (REF352340, BD Falcon)

100 bp DNA Ladder (306017, Bioron)

6X DNA Gel Loading Dye (R0611)

Agarose NEEO Ultra-Quality (2267.4, Carl Roth GmbH)

Biozym Red HS Taq Master Mix (331126L, Biozym)

BSA (P06-1395500, PANTM BIOTECH)

$CaCl_2$ (A3652.0500, Applichem)

Cell Culture Flasks 75 cm^2, 650 ml, 20-85 ml (CNC3.1, Carl Roth GmbH)

Dimethylsulfoxid (5179.1, Carl Roth GmbH)

Embedding media for Immunofluorescence staining (Roti®-Mount FluorCare, Roth)

Ethanol (≥99.5%, Art-Nr. 5054.3, Roth)

Fetal Bovine Serum, qualified (A31608, Gibco™)

Glucose (G8270-100g, Sigma)

Glutamax (GlutaMax™ Supplement, 350500038, Glibo)

HCl (37%, Art-Nr. 7476.2, Carl Roth GmbH)

HEPES (A1069.0500, Applichem)

Horse serum (16050122, Gibco™)

Isoflurane (CDS019936, Aldrich)

KCl (67811, Merck)

LB Agar Lennox (X965.1, Carl Roth GmbH)

Methanol, 2.5 l, Kunst. ROTIPURAN® ≥99,9% (4627.5, Carl Roth GmbH)

Milk powder (T145.2, Carl Roth GmbH)

NaCl (278, Baker Analyzed)

Ø35mm image chamber (µ-Dish 35 mm Grid-500, ibidi®)

Optiprep: 60% (w/v) iodixanol solution in water (Axis Shield, Rodel.kka, Sweden)

PageRuler™ Plus Prestained Protein Ladder, 10 to 250 kDa (26619X4, Thermo Fisher Scientific)

PCR Grade Water (351900301, Biozym)

PCR SingleCap 8er-SoftStrips 0.2 ml (710980X, Biozym)

PEI (Polyethyleniminie, branched, 408727, Sigma)

Pen/Strep (P0781, Sigma)

PRECISOR High-Fidelity DNA Polymerase (1706-250-BL)

PVDF Transfer Membrane 0.45 µm, 26.5 cmx3.75 m (88518, Thermo Fisher Scientific)

QIAGEN Plasmid Midi Kit (25) (12143, QIAGEN)

QIAquick Gel Extraction Kit (28706X4, QIAGEN)

Quick Ligation™ Kit (M2200S, New England Biolabs Inc.)

ROTI®Cell DPBS (9124.1, Carl Roth GmbH)

TAE Buffer (50X) (A4686, ITW Reagents, S.R.L.)

Triton® ×100 (3051.4, Roth)

Trypan blue (T8154, Sigma)

Trypsin-EDTA (T4299, Sigma)

VELOCITY DNA Polymerase (BIO-21098, Meridian Bioscience)

x-well cell culture chamber, 4-well, on PCA slide, removable frame (94.6140.402, Sarsted)

9.3 Buffers

10X PBS: For 5 L 89 g Na2HPO4x2H2O (#4984.1 Roth MW 177,99) (17.8 g/1L)

10 g KH2PO4 (MW 136.09 Merck #4873.1000 or 3904.1 Roth) (2 g/1 L)

400 g NaCl (#3957.1 Roth MW58,44) (80 g/1 L)

10 g KCl (Roth # 6781.1 MW 74.56) (2 g/1 L)

After everything is solved add to the final volume with Milli-Q water water

For use dilute 1:10 with water.

For PBST use 1 ml Tween 20 for 1 L 1x PBS

10X Running Buffer: 30.25 g TRIS (Pufferan), 144g Glycin, 100 ml 10% SDS up to 1L with Milli-Q water

2X Laemmlli buffer: 40 ml 10% SDS, 20 ml 0.5% Tris, 20 ml Glycerol, 10 ml Mercaptoethanol, 2.2 mg Bromophenolblue

RIPA buffer: 10 mM Tris–HCl pH 7.5, 150 mM NaCl, 1% Triton X-100, 0.1% SDS, 1% sodium deoxycholate)

TVBE buffer

4% para-formaldehyde (pFA) in 1x PBS

Fish block: 1% BSA, 0.2% Fish skin gelatin, 0.1% Triton –x 100

BSA Block: 20 ml PBS, 0.2 g BSA 60 µl Triton X 100

BSA dilution solution: 20 ml PBS, 40 µl Triton X 100

Substance Staining solution	**%**	**For 1L**
Comassie Brilliant Blue R 250	0.1	1 g
Acetic acid	10	100 ml
Methanol	40	400 ml
Water	50	500 ml
Substance Destain Solution		
Acetic acid	10	100 ml
Methanol	40	400 ml
Water	50	500 ml
Substance Storgae solution		
Ethanol	20	200 ml
Glycerol	2	20 ml
Water		780 ml

High Glucose DMEM Medium: 3.8 ml Glucose solution Sigma (G8769-100ML =45% = 45 g/100 ml = 0.45 g/ml) per 500 ml bottle of medium DMEM (D6046=1000 mg/L) to reach high glucose Medium with 4500 mg/L

Ponceau staining: 0.1% w/w Ponceau S dye – 0.5 g**,** 1% v/v acetic acid – 5 mL**,** ad to 500 mL with Milli-Q water

Separation gel buffer=1.5 M Tris/HCl pH 8.8: (MW) 121.14 Tris Buffer 181.71 g final Volume 1 L adjust pH with HCl at pH 8.8 ad water to final volume of 1L

Stacking gel buffer=0.5 M Tris /HCl pH 6.8: 60.57 g of Tris Pufferan for final volume of 1 L adjust pH with HCL at 6.8 ad water to final volume of 1 L

TVBE Buffer: for 1000 ml

84 mg $NaHCO_3$ (Mr. 84.01) Final concentration: 1 mM

372.24 mg EDTA (Mr. 372.24)	Final concentration: 1 mM
or 10 ml 100mM EDTA	
1 ml Ethanol	Final concentration: 0.1%
5 ml 2% Triton x-100	Final concentration: 0.01%

5x SDS-Sample buffer according to Laemmli (50 ml): 5 g SDS; 12.5 ml 1 M Tris pH 6.8; 12.5 ml ß-Mercaptoethanol; 25 ml Glycerin; Bromphenolblue

250 mM Sucrose in MOPS **500 ml**

Substant	Concentration	
20 mM MOPS	5 mM	125 ml
10 mM EDTA/1% Ethanol		50 ml
Benzamidin/HCl 0.5 M		5 ml
Aminocaproic acid 1 M		500 µl
Milli-Q water		319.5 ml
Sucrose		42.8 g

Gradient Buffer in MOPS **500 ml**

Substant	Concentration	
20 mM MOPS	5mM	125 ml
10 mM EDTA/1% Ethanol		50 ml
Benzamidin/HCl 0.5 M		5 ml
Aminocaproic acid 1 M		500 µl
MilliQ water		319.5 ml

900 mM Sucrose in MOPS **200 ml**

Substant	Concentration	
20 mM MOPS	5 mM	50 ml
10 mM EDTA/1% Ethanol		20 ml

Benzamidin/HCl 0.5 M	2 ml
Aminocaproic acid 1 M	200 µl
Milli-Q water	127.8 ml
Sucrose	61.6133 g

500 mM Sucrose in MOPS **50 ml**

Substant	**Concentration**	
20 mM MOPS	5 mM	12.5 ml
10 mM EDTA/1% Ethanol		5 ml
Benzamidin/HCl 0.5 M		0.5 ml
Aminocaproic acid 1 M		50 µl
Milli-Q water		31.95 ml
Sucrose		8.557 g

0.95 M Sucrose in MOPS

Substant	**Concentration**	
Sucrose		16.26 g
Gradient Buffer		Ad 50 ml

1.1 M Sucrose in MOPS

Substant	**Concentration**	
Sucrose		18.82 g
Gradient Buffer		Ad 50 ml

1.0 M Sucrose in MOPS

Substant	**Concentration**	
Sucrose		17.12 g
Gradient Buffer		Ad 50 ml

9.4 Softwares

Fiji ImageJ, written by J. Rietdorf and A. Seitz; v2.0.0-rc-61/1.51n/Java1.8.0_66, 64-bit

Adobe Photoshop CS4, Adobe System, Adobe Inc.

GraphPad Prism, Dotmatics

9.5 Proteomics Data of Mouse Liver from LM-TOP vs LM-PO and FLM-TOP vs FLM-PO

Peak Name	p-value	LM-PO/LM-Top	LM-Top/LM-Po-Fold Change	L-Log (Fold Change)	p-value	FLM-Po/FLMTop	FFLM-Top/FLM-PO	FL-Log (Fold Change)
P35762|CD81_MOUSE	0,03	#DIV/0!	0,00	0,00	0,01	0,03	32,54	1,51
Q8BM55|TM214_MOUSE	0,04	#DIV/0!	0,00	0,00	0,01	0,12	8,14	0,91
P00397|COX1_MOUSE	0,04	#DIV/0!	0,00	0,00	0,47	0,36	2,74	0,44
Q7TMF3|NDUAC_MOUSE	0,08	#DIV/0!	0,00	0,00	0,14	#DIV/0!	0,00	0,00
Q8K2M0|RM38_MOUSE	0,15	#DIV/0!	0,00	0,00	0,36	#DIV/0!	0,00	0,00
Q9ESB3|HRG_MOUSE	0,15	#DIV/0!	0,00	0,00	0,03	0,07	15,33	1,19
Q80WW9|DDRGK_MOUSE	0,17	#DIV/0!	0,00	0,00	0,22	0,13	7,86	0,90
P15535|B4GT1_MOUSE	0,36	#DIV/0!	0,00	0,00	0,05	#DIV/0!	0,00	0,00
P10518|HEM2_MOUSE	1,00	#DIV/0!	0,00	0,00	0,36	#DIV/0!	0,00	0,00
Q8R429|AT2A1_MOUSE	1,00	#DIV/0!	0,00	0,00	0,36	#DIV/0!	0,00	0,00
Q9CQC9|SAR1B_MOUSE	0,00	38,21	0,03	-1,58	0,05	6,15	0,16	-0,79
Q9WUB3|PYGM_MOUSE	0,07	28,55	0,04	-1,46	0,09	9,45	0,11	-0,98
Q571E4|GALNS_MOUSE	0,00	23,83	0,04	-1,38	0,08	3,40	0,29	-0,53
P48410|ABCD1_MOUSE	0,01	22,55	0,04	-1,35	0,08	4,41	0,23	-0,64
Q91X34|BAAT_MOUSE	0,00	22,30	0,04	-1,35	0,00	17,18	0,06	-1,23
Q8C767|PPR3B_MOUSE	0,02	21,25	0,05	-1,33	0,06	14,68	0,07	-1,17
Q3ULJ0|GPD1L_MOUSE	0,00	21,00	0,05	-1,32	0,03	#DIV/0!	0,00	0,00
Q9D826|SOX_MOUSE	0,00	20,94	0,05	-1,32	0,01	11,72	0,09	-1,07
P00688|AMYP_MOUSE	0,03	20,92	0,05	-1,32	0,13	6,44	0,16	-0,81
Q9ET01|PYGL_MOUSE	0,10	20,23	0,05	-1,31	0,21	8,15	0,12	-0,91

P00687|AMY1_MOUSE	0,08	19,76	0,05	-1,30	0,08	2,65	0,38	-0,42
P32020|SCP2_MOUSE	0,00	19,39	0,05	-1,29	0,00	8,10	0,12	-0,91
Q99P30|NUDT7_MOUSE	0,00	19,33	0,05	-1,29	0,01	14,89	0,07	-1,17
Q9CRB3|HIUH_MOUSE	0,00	18,91	0,05	-1,28	0,00	12,39	0,08	-1,09
Q9DC50|OCTC_MOUSE	0,00	18,66	0,05	-1,27	0,00	11,91	0,08	-1,08
P13707|GPDA_MOUSE	0,00	18,23	0,05	-1,26	0,00	16,78	0,06	-1,22
P11930|NUD19_MOUSE	0,00	17,78	0,06	-1,25	0,04	12,95	0,08	-1,11
Q8BGG9|ACNT2_MOUSE	0,00	17,70	0,06	-1,25	0,01	5,80	0,17	-0,76
P24270|CATA_MOUSE	0,00	16,80	0,06	-1,23	0,01	9,71	0,10	-0,99
Q99LC9|PEX6_MOUSE	0,00	16,38	0,06	-1,21	0,01	9,58	0,10	-0,98
Q91XC9|PEX16_MOUSE	0,00	16,06	0,06	-1,21	0,01	6,38	0,16	-0,80
O35386|PAHX_MOUSE	0,00	15,50	0,06	-1,19	0,00	11,12	0,09	-1,05
Q9EPL9|ACOX3_MOUSE	0,00	15,36	0,07	-1,19	0,03	4,52	0,22	-0,65
Q9DBM2|ECHP_MOUSE	0,00	15,08	0,07	-1,18	0,00	9,54	0,10	-0,98
Q9WU19|HAOX1_MOUSE	0,00	14,47	0,07	-1,16	0,00	8,88	0,11	-0,95
P51660|DHB4_MOUSE	0,00	14,46	0,07	-1,16	0,01	9,19	0,11	-0,96
Q921H8|THIKA_MOUSE	0,00	14,41	0,07	-1,16	0,00	10,04	0,10	-1,00
Q9QXE0|HACL1_MOUSE	0,00	14,21	0,07	-1,15	0,02	7,88	0,13	-0,90
P34914|HYES_MOUSE	0,00	14,16	0,07	-1,15	0,01	8,67	0,12	-0,94
Q9QXY9|PEX3_MOUSE	0,02	14,09	0,07	-1,15	0,03	5,12	0,20	-0,71
Q9R0A0|PEX14_MOUSE	0,00	14,08	0,07	-1,15	0,02	6,54	0,15	-0,82
Q8VDG7|PAFA2_MOUSE	0,00	14,04	0,07	-1,15	0,01	8,49	0,12	-0,93
Q9R0H0|ACOX1_MOUSE	0,00	14,03	0,07	-1,15	0,00	14,24	0,07	-1,15
Q8VCH0|THIKB_MOUSE	0,00	12,90	0,08	-1,11	0,00	6,78	0,15	-0,83
Q9DCN1|NUD12_MOUSE	0,00	12,55	0,08	-1,10	0,05	8,95	0,11	-0,95
Q80XL6|ACD11_MOUSE	0,00	12,39	0,08	-1,09	0,00	6,88	0,15	-0,84
Q9DBK0|ACO12_MOUSE	0,00	12,13	0,08	-1,08	0,01	10,45	0,10	-1,02
Q2TPA8|HSDL2_MOUSE	0,00	12,13	0,08	-1,08	0,00	5,10	0,20	-0,71
Q99MZ7|PECR_MOUSE	0,00	11,80	0,08	-1,07	0,00	7,88	0,13	-0,90
Q5BL07|PEX1_MOUSE	0,00	11,79	0,08	-1,07	0,00	6,67	0,15	-0,82
O09174|AMACR_MOUSE	0,00	11,47	0,09	-1,06	0,00	9,23	0,11	-0,97

Q8BWN8|ACOT4_MOUSE	0,00	11,39	0,09	-1,06	0,00	7,61	0,13	-0,88
Q8R1M2|H2AJ_MOUSE	0,21	11,16	0,09	-1,05	0,24	3,31	0,30	-0,52
Q9CYV5|TM135_MOUSE	0,00	11,10	0,09	-1,05	0,01	7,85	0,13	-0,89
Q9QXD1|ACOX2_MOUSE	0,00	10,89	0,09	-1,04	0,01	6,07	0,16	-0,78
Q9DBA6|TYSD1_MOUSE	0,00	10,82	0,09	-1,03	0,01	10,56	0,09	-1,02
Q9WV68|DECR2_MOUSE	0,00	10,66	0,09	-1,03	0,00	7,30	0,14	-0,86
O35423|SPYA_MOUSE	0,00	10,32	0,10	-1,01	0,01	11,19	0,09	-1,05
O09012|PEX5_MOUSE	0,00	10,29	0,10	-1,01	0,01	6,71	0,15	-0,83
A2AKK5|ACNT1_MOUSE	0,00	10,27	0,10	-1,01	0,04	5,83	0,17	-0,77
Q99KR3|LACB2_MOUSE	0,00	10,22	0,10	-1,01	0,01	10,50	0,10	-1,02
Q9DBN5|LONP2_MOUSE	0,00	10,14	0,10	-1,01	0,01	6,06	0,16	-0,78
P50431|GLYC_MOUSE	0,37	10,07	0,10	-1,00	0,34	0,55	1,82	0,26
P55096|ABCD3_MOUSE	0,00	9,97	0,10	-1,00	0,02	5,70	0,18	-0,76
O35678|MGLL_MOUSE	0,07	9,83	0,10	-0,99	0,46	1,75	0,57	-0,24
Q99LB2|DHRS4_MOUSE	0,00	9,59	0,10	-0,98	0,00	7,23	0,14	-0,86
P07146|TRY2_MOUSE	0,04	9,52	0,11	-0,98	0,41	1,62	0,62	-0,21
Q8C7E7|STBD1_MOUSE	0,05	9,10	0,11	-0,96	0,05	12,19	0,08	-1,09
Q9QYR7|ACOT3_MOUSE	0,00	9,10	0,11	-0,96	0,00	5,34	0,19	-0,73
O88844|IDHC_MOUSE	0,00	8,79	0,11	-0,94	0,03	5,18	0,19	-0,71
O70579|PM34_MOUSE	0,00	8,38	0,12	-0,92	0,09	3,55	0,28	-0,55
P42925|PXMP2_MOUSE	0,00	8,37	0,12	-0,92	0,00	6,31	0,16	-0,80
Q9DCM2|GSTK1_MOUSE	0,00	8,25	0,12	-0,92	0,01	4,96	0,20	-0,70
P05208|CEL2A_MOUSE	0,01	7,90	0,13	-0,90	0,52	0,71	1,41	0,15
P98192|GNPAT_MOUSE	0,00	7,87	0,13	-0,90	0,08	4,69	0,21	-0,67
Q8BGC4|PTGR3_MOUSE	0,00	7,85	0,13	-0,89	0,00	5,58	0,18	-0,75
Q61285|ABCD2_MOUSE	0,00	7,84	0,13	-0,89	0,01	5,03	0,20	-0,70
P25688|URIC_MOUSE	0,00	7,82	0,13	-0,89	0,00	5,57	0,18	-0,75
Q6P6M5|PX11C_MOUSE	0,00	7,82	0,13	-0,89	0,03	4,35	0,23	-0,64
Q8CHK3|MBOA7_MOUSE	0,16	7,80	0,13	-0,89	0,95	0,92	1,09	0,04
Q9D1G2|PMVK_MOUSE	0,10	7,79	0,13	-0,89	0,33	3,18	0,31	-0,50
Q9Z211|PX11A_MOUSE	0,08	7,78	0,13	-0,89	0,06	3,55	0,28	-0,55

Q61878|PRG2_MOUSE	0,01	7,75	0,13	-0,89	0,62	1,35	0,74	-0,13
Q9Z210|PX11B_MOUSE	0,00	7,72	0,13	-0,89	0,04	2,81	0,36	-0,45
P58137|ACOT8_MOUSE	0,00	7,59	0,13	-0,88	0,03	7,73	0,13	-0,89
Q8VCR7|ABHEB_MOUSE	0,00	7,45	0,13	-0,87	0,05	4,68	0,21	-0,67
P12815|PDCD6_MOUSE	0,01	7,29	0,14	-0,86	0,00	4,39	0,23	-0,64
Q99MD6|TRXR3_MOUSE	0,02	7,26	0,14	-0,86	0,09	2,85	0,35	-0,46
P14152|MDHC_MOUSE	0,00	7,04	0,14	-0,85	0,04	3,08	0,32	-0,49
Q8BGI5|PEX26_MOUSE	0,00	6,85	0,15	-0,84	0,00	5,68	0,18	-0,75
P15116|CADH2_MOUSE	0,08	6,68	0,15	-0,82	0,14	0,27	3,70	0,57
P09405|NUCL_MOUSE	0,00	6,63	0,15	-0,82	0,09	3,28	0,30	-0,52
Q8VC48|PEX12_MOUSE	0,02	6,62	0,15	-0,82	0,00	3,75	0,27	-0,57
P49290|PERE_MOUSE	0,02	6,61	0,15	-0,82	0,52	1,23	0,81	-0,09
Q9CQ92|FIS1_MOUSE	0,00	6,60	0,15	-0,82	0,08	3,40	0,29	-0,53
Q9JJW0|PXMP4_MOUSE	0,00	6,57	0,15	-0,82	0,02	4,21	0,24	-0,62
Q8C0I1|ADAS_MOUSE	0,00	6,54	0,15	-0,82	0,22	2,18	0,46	-0,34
P11679|K2C8_MOUSE	0,01	6,54	0,15	-0,82	0,29	1,51	0,66	-0,18
Q6NXH9|K2C73_MOUSE	0,04	6,26	0,16	-0,80	0,08	9,85	0,10	-0,99
B1AUE5|PEX10_MOUSE	0,01	6,22	0,16	-0,79	0,05	3,76	0,27	-0,58
P53657|KPYR_MOUSE	0,37	6,16	0,16	-0,79	0,93	1,05	0,95	-0,02
Q8CI51|PDLI5_MOUSE	0,01	6,07	0,16	-0,78	0,06	2,02	0,50	-0,30
Q9Z2G9|HTAI2_MOUSE	0,01	6,02	0,17	-0,78	0,02	4,04	0,25	-0,61
P62702|RS4X_MOUSE	0,03	5,90	0,17	-0,77	0,91	0,89	1,12	0,05
Q9WUR2|ECI2_MOUSE	0,00	5,80	0,17	-0,76	0,03	4,59	0,22	-0,66
O35381|AN32A_MOUSE	0,09	5,80	0,17	-0,76	0,17	3,79	0,26	-0,58
Q8BWP5|TTPA_MOUSE	0,01	5,73	0,17	-0,76	0,13	2,71	0,37	-0,43
Q9NYQ2|HAOX2_MOUSE	0,00	5,71	0,18	-0,76	0,00	4,99	0,20	-0,70
Q5XG73|ACBD5_MOUSE	0,00	5,54	0,18	-0,74	0,03	2,05	0,49	-0,31
Q8K1N1|PLPL8_MOUSE	0,00	5,47	0,18	-0,74	0,01	4,61	0,22	-0,66
P62137|PP1A_MOUSE	0,08	5,46	0,18	-0,74	0,31	2,21	0,45	-0,34
Q9CQD1|RAB5A_MOUSE	0,00	5,41	0,18	-0,73	0,44	1,78	0,56	-0,25
P97364|SPS2_MOUSE	0,01	5,40	0,19	-0,73	0,19	1,55	0,65	-0,19

Q9R0P3|ESTD_MOUSE	0,12	4,98	0,20	-0,70	0,41	0,52	1,91	0,28
P06151|LDHA_MOUSE	0,00	4,93	0,20	-0,69	0,05	3,92	0,25	-0,59
O08917|FLOT1_MOUSE	0,21	4,91	0,20	-0,69	0,85	0,89	1,13	0,05
P97425|ECP2_MOUSE	0,38	4,79	0,21	-0,68	0,13	33,85	0,03	-1,53
Q91V64|ISOC1_MOUSE	0,01	4,78	0,21	-0,68	0,05	4,81	0,21	-0,68
P47934|CACP_MOUSE	0,00	4,74	0,21	-0,68	0,07	2,88	0,35	-0,46
Q07076|ANXA7_MOUSE	0,20	4,72	0,21	-0,67	0,23	0,50	1,99	0,30
Q99KB8|GLO2_MOUSE	0,00	4,64	0,22	-0,67	0,01	4,49	0,22	-0,65
Q8CC88|VWA8_MOUSE	0,00	4,59	0,22	-0,66	0,01	4,68	0,21	-0,67
Q8JZS0|LIN7A_MOUSE	0,06	4,59	0,22	-0,66	0,14	0,44	2,29	0,36
Q8VBT2|SDHL_MOUSE	0,04	4,57	0,22	-0,66	0,52	1,13	0,89	-0,05
Q9CR35|CTRB1_MOUSE	0,05	4,56	0,22	-0,66	0,74	0,86	1,16	0,07
Q61792|LASP1_MOUSE	0,03	4,48	0,22	-0,65	0,15	2,55	0,39	-0,41
Q8R1G2|CMBL_MOUSE	0,06	4,34	0,23	-0,64	0,78	1,24	0,81	-0,09
P09411|PGK1_MOUSE	0,06	4,22	0,24	-0,62	0,80	1,15	0,87	-0,06
Q8BI84|TGO1_MOUSE	0,05	4,18	0,24	-0,62	0,74	1,30	0,77	-0,11
Q99J47|DRS7B_MOUSE	0,00	4,12	0,24	-0,61	0,02	3,55	0,28	-0,55
Q9WUA5|EPM2A_MOUSE	0,20	4,06	0,25	-0,61	0,44	1,74	0,58	-0,24
Q9EST5|AN32B_MOUSE	0,00	4,01	0,25	-0,60	0,02	3,23	0,31	-0,51
Q64339|ISG15_MOUSE	0,11	3,84	0,26	-0,58	0,09	3,29	0,30	-0,52
Q9D0K1|PEX13_MOUSE	0,26	3,83	0,26	-0,58	0,12	4,40	0,23	-0,64
P63037|DNJA1_MOUSE	0,02	3,72	0,27	-0,57	0,63	1,14	0,87	-0,06
Q9CRD0|OCAD1_MOUSE	0,00	3,71	0,27	-0,57	0,01	3,16	0,32	-0,50
P47757|CAPZB_MOUSE	0,00	3,70	0,27	-0,57	0,77	0,88	1,13	0,05
Q811U4|MFN1_MOUSE	0,10	3,61	0,28	-0,56	0,63	1,59	0,63	-0,20
Q9D5T0|ATAD1_MOUSE	0,00	3,60	0,28	-0,56	0,05	3,02	0,33	-0,48
Q3UZZ6|ST1D1_MOUSE	0,13	3,59	0,28	-0,56	0,29	2,05	0,49	-0,31
Q62093|SRSF2_MOUSE	0,05	3,59	0,28	-0,55	0,05	3,41	0,29	-0,53
P52840|ST1A1_MOUSE	0,03	3,46	0,29	-0,54	0,50	1,35	0,74	-0,13
Q922Z0|OXDD_MOUSE	0,00	3,44	0,29	-0,54	0,42	1,43	0,70	-0,16
P41216|ACSL1_MOUSE	0,00	3,43	0,29	-0,53	0,22	1,40	0,71	-0,15

Q61147|CERU_MOUSE	0,09	3,38	0,30	-0,53	0,16	0,34	2,96	0,47
P29788|VTNC_MOUSE	0,21	3,37	0,30	-0,53	0,10	2,57	0,39	-0,41
Q9D1N9|RM21_MOUSE	0,32	3,27	0,31	-0,51	0,09	0,14	7,05	0,85
Q9DCL9|PUR6_MOUSE	0,02	3,26	0,31	-0,51	0,34	1,45	0,69	-0,16
P60335|PCBP1_MOUSE	0,01	3,26	0,31	-0,51	0,88	1,09	0,91	-0,04
O70400|PDLI1_MOUSE	0,00	3,25	0,31	-0,51	0,66	0,71	1,41	0,15
P51410|RL9_MOUSE	0,04	3,22	0,31	-0,51	0,05	0,24	4,10	0,61
Q99L20|GSTT3_MOUSE	0,29	3,18	0,31	-0,50	0,32	0,66	1,52	0,18
P59017|B2L13_MOUSE	0,48	3,18	0,31	-0,50	0,52	1,52	0,66	-0,18
P35762|CD81_MOUSE	0,06	3,52	0,28	-0,62	0,33	3,59	0,28	-0,24
Q8BM55|TM214_MOUSE	0,06	3,50	0,29	-0,62	0,34	3,70	0,27	-0,24
P00397|COX1_MOUSE	0,06	3,48	0,29	-0,62	0,34	3,81	0,26	-0,24
Q7TMF3|NDUAC_MOUSE	0,06	3,45	0,29	-0,61	0,34	3,93	0,25	-0,23
Q8K2M0|RM38_MOUSE	0,06	3,43	0,29	-0,61	0,34	4,07	0,25	-0,23
Q9ESB3|HRG_MOUSE	0,06	3,41	0,29	-0,61	0,35	4,21	0,24	-0,23
Q80WW9|DDRGK_MOUSE	0,06	3,39	0,30	-0,61	0,35	4,36	0,23	-0,22
P15535|B4GT1_MOUSE	0,06	3,37	0,30	-0,60	0,35	4,52	0,22	-0,22
P10518|HEM2_MOUSE	0,06	3,34	0,30	-0,60	0,35	4,69	0,21	-0,22
Q8R429|AT2A1_MOUSE	0,06	3,32	0,30	-0,60	0,35	4,88	0,21	-0,21
Q9CQC9|SAR1B_MOUSE	0,06	3,30	0,30	-0,59	0,36	5,08	0,20	-0,21
Q9WUB3|PYGM_MOUSE	0,06	3,28	0,30	-0,59	0,36	5,30	0,19	-0,21
Q571E4|GALNS_MOUSE	0,06	3,26	0,31	-0,59	0,36	5,54	0,18	-0,21
P48410|ABCD1_MOUSE	0,06	3,24	0,31	-0,59	0,36	5,80	0,17	-0,20
Q91X34|BAAT_MOUSE	0,06	3,22	0,31	-0,58	0,36	6,09	0,16	-0,20
Q8C767|PPR3B_MOUSE	0,06	3,20	0,31	-0,58	0,37	6,41	0,16	-0,20
Q3ULJ0|GPD1L_MOUSE	0,06	3,18	0,31	-0,58	0,37	6,76	0,15	-0,19
Q9D826|SOX_MOUSE	0,06	3,16	0,32	-0,57	0,37	7,16	0,14	-0,19
P00688|AMYP_MOUSE	0,06	3,14	0,32	-0,57	0,37	7,60	0,13	-0,19
Q9ET01|PYGL_MOUSE	0,06	3,13	0,32	-0,57	0,38	8,11	0,12	-0,18
P00687|AMY1_MOUSE	0,06	3,11	0,32	-0,57	0,38	8,68	0,12	-0,18
P32020|SCP2_MOUSE	0,06	3,09	0,32	-0,56	0,38	9,35	0,11	-0,18

Q99P30|NUDT7_MOUSE	0,06	3,07	0,33	-0,56	0,38	10,12	0,10	-0,18
Q9CRB3|HIUH_MOUSE	0,06	3,05	0,33	-0,56	0,38	11,03	0,09	-0,17
Q9DC50|OCTC_MOUSE	0,06	3,04	0,33	-0,55	0,39	12,13	0,08	-0,17
P13707|GPDA_MOUSE	0,06	3,02	0,33	-0,55	0,39	13,46	0,07	-0,17
P11930|NUD19_MOUSE	0,06	3,00	0,33	-0,55	0,39	15,13	0,07	-0,16
Q8BGG9|ACNT2_MOUSE	0,06	2,98	0,34	-0,55	0,39	17,26	0,06	-0,16
P24270|CATA_MOUSE	0,06	2,97	0,34	-0,54	0,40	20,10	0,05	-0,16
Q99LC9|PEX6_MOUSE	0,06	2,95	0,34	-0,54	0,40	24,05	0,04	-0,15
Q91XC9|PEX16_MOUSE	0,06	2,93	0,34	-0,54	0,40	29,94	0,03	-0,15
O35386|PAHX_MOUSE	0,06	2,92	0,34	-0,54	0,40	39,65	0,03	-0,15
Q9EPL9|ACOX3_MOUSE	0,06	2,90	0,34	-0,53	0,40	58,66	0,02	-0,14
Q9DBM2|ECHP_MOUSE	0,06	2,89	0,35	-0,53	0,41	112,72	0,01	-0,14
Q9WU19|HAOX1_MOUSE	0,06	2,87	0,35	-0,53	0,41	#######	0,00	-0,14
P51660|DHB4_MOUSE	0,06	2,85	0,35	-0,52	0,41	-133,69	-0,01	-0,14
Q921H8|THIKA_MOUSE	0,06	2,84	0,35	-0,52	0,41	-63,87	-0,02	-0,13
Q9QXE0|HACL1_MOUSE	0,06	2,82	0,35	-0,52	0,42	-41,96	-0,02	-0,13
P34914|HYES_MOUSE	0,06	2,81	0,36	-0,52	0,42	-31,24	-0,03	-0,13
Q9QXY9|PEX3_MOUSE	0,06	2,79	0,36	-0,51	0,42	-24,89	-0,04	-0,12
Q9R0A0|PEX14_MOUSE	0,06	2,78	0,36	-0,51	0,42	-20,68	-0,05	-0,12
Q8VDG7|PAFA2_MOUSE	0,06	2,77	0,36	-0,51	0,42	-17,69	-0,06	-0,12
Q9R0H0|ACOX1_MOUSE	0,06	2,75	0,36	-0,50	0,43	-15,45	-0,06	-0,11
Q8VCH0|THIKB_MOUSE	0,06	2,74	0,37	-0,50	0,43	-13,72	-0,07	-0,11
Q9DCN1|NUD12_MOUSE	0,06	2,72	0,37	-0,50	0,43	-12,34	-0,08	-0,11
Q80XL6|ACD11_MOUSE	0,06	2,71	0,37	-0,50	0,43	-11,21	-0,09	-0,11
Q9DBK0|ACO12_MOUSE	0,06	2,69	0,37	-0,49	0,43	-10,27	-0,10	-0,10
Q2TPA8|HSDL2_MOUSE	0,06	2,68	0,37	-0,49	0,44	-9,47	-0,11	-0,10
Q99MZ7|PECR_MOUSE	0,06	2,67	0,37	-0,49	0,44	-8,79	-0,11	-0,10
Q5BL07|PEX1_MOUSE	0,06	2,65	0,38	-0,48	0,44	-8,20	-0,12	-0,09
O09174|AMACR_MOUSE	0,06	2,64	0,38	-0,48	0,44	-7,69	-0,13	-0,09
Q8BWN8|ACOT4_MOUSE	0,06	2,63	0,38	-0,48	0,45	-7,23	-0,14	-0,09
Q8R1M2|H2AJ_MOUSE	0,06	2,61	0,38	-0,48	0,45	-6,83	-0,15	-0,08

Q9CYV5|TM135_MOUSE	0,06	2,60	0,38	-0,47	0,45	-6,47	-0,15	-0,08
Q9QXD1|ACOX2_MOUSE	0,06	2,59	0,39	-0,47	0,45	-6,14	-0,16	-0,08
Q9DBA6|TYSD1_MOUSE	0,06	2,58	0,39	-0,47	0,45	-5,85	-0,17	-0,07
Q9WV68|DECR2_MOUSE	0,06	2,56	0,39	-0,46	0,46	-5,58	-0,18	-0,07
O35423|SPYA_MOUSE	0,06	2,55	0,39	-0,46	0,46	-5,34	-0,19	-0,07
O09012|PEX5_MOUSE	0,06	2,54	0,39	-0,46	0,46	-5,11	-0,20	-0,07
A2AKK5|ACNT1_MOUSE	0,06	2,53	0,40	-0,46	0,46	-4,91	-0,20	-0,06
Q99KR3|LACB2_MOUSE	0,06	2,51	0,40	-0,45	0,47	-4,72	-0,21	-0,06
Q9DBN5|LONP2_MOUSE	0,06	2,50	0,40	-0,45	0,47	-4,54	-0,22	-0,06
P50431|GLYC_MOUSE	0,06	2,49	0,40	-0,45	0,47	-4,38	-0,23	-0,05
P55096|ABCD3_MOUSE	0,06	2,48	0,40	-0,44	0,47	-4,23	-0,24	-0,05
O35678|MGLL_MOUSE	0,06	2,47	0,41	-0,44	0,47	-4,09	-0,24	-0,05
Q99LB2|DHRS4_MOUSE	0,06	2,46	0,41	-0,44	0,48	-3,96	-0,25	-0,04
P07146|TRY2_MOUSE	0,06	2,44	0,41	-0,44	0,48	-3,83	-0,26	-0,04
Q8C7E7|STBD1_MOUSE	0,06	2,43	0,41	-0,43	0,48	-3,72	-0,27	-0,04
Q9QYR7|ACOT3_MOUSE	0,06	2,42	0,41	-0,43	0,48	-3,61	-0,28	-0,03
O88844|IDHC_MOUSE	0,06	2,41	0,41	-0,43	0,48	-3,50	-0,29	-0,03
O70579|PM34_MOUSE	0,06	2,40	0,42	-0,42	0,49	-3,41	-0,29	-0,03
P42925|PXMP2_MOUSE	0,06	2,39	0,42	-0,42	0,49	-3,31	-0,30	-0,03
Q9DCM2|GSTK1_MOUSE	0,06	2,38	0,42	-0,42	0,49	-3,23	-0,31	-0,02
P05208|CEL2A_MOUSE	0,06	2,37	0,42	-0,42	0,49	-3,14	-0,32	-0,02
P98192|GNPAT_MOUSE	0,06	2,36	0,42	-0,41	0,50	-3,06	-0,33	-0,02
Q8BGC4|PTGR3_MOUSE	0,06	2,35	0,43	-0,41	0,50	-2,99	-0,33	-0,01
Q61285|ABCD2_MOUSE	0,06	2,34	0,43	-0,41	0,50	-2,92	-0,34	-0,01
P25688|URIC_MOUSE	0,06	2,33	0,43	-0,40	0,50	-2,85	-0,35	-0,01
Q6P6M5|PX11C_MOUSE	0,06	2,32	0,43	-0,40	0,50	-2,79	-0,36	0,00
Q8CHK3|MBOA7_MOUSE	0,06	2,31	0,43	-0,40	0,51	-2,72	-0,37	0,00
Q9D1G2|PMVK_MOUSE	0,06	2,30	0,44	-0,40	0,51	-2,66	-0,38	0,00
Q9Z211|PX11A_MOUSE	0,06	2,29	0,44	-0,39	0,51	-2,61	-0,38	0,00
Q61878|PRG2_MOUSE	0,06	2,28	0,44	-0,39	0,51	-2,55	-0,39	0,01
Q9Z210|PX11B_MOUSE	0,06	2,27	0,44	-0,39	0,52	-2,50	-0,40	0,01

P58137|ACOT8_MOUSE	0,06	2,26	0,44	-0,38	0,52	-2,45	-0,41	0,01
Q8VCR7|ABHEB_MOUSE	0,06	2,25	0,45	-0,38	0,52	-2,40	-0,42	0,02
P12815|PDCD6_MOUSE	0,06	2,24	0,45	-0,38	0,52	-2,36	-0,42	0,02
Q99MD6|TRXR3_MOUSE	0,06	2,23	0,45	-0,38	0,52	-2,31	-0,43	0,02
P14152|MDHC_MOUSE	0,06	2,22	0,45	-0,37	0,53	-2,27	-0,44	0,03
Q8BGI5|PEX26_MOUSE	0,06	2,21	0,45	-0,37	0,53	-2,23	-0,45	0,03
P15116|CADH2_MOUSE	0,06	2,20	0,45	-0,37	0,53	-2,19	-0,46	0,03
P09405|NUCL_MOUSE	0,06	2,19	0,46	-0,36	0,53	-2,15	-0,47	0,04
Q8VC48|PEX12_MOUSE	0,06	2,18	0,46	-0,36	0,54	-2,11	-0,47	0,04
P49290|PERE_MOUSE	0,06	2,17	0,46	-0,36	0,54	-2,08	-0,48	0,04
Q9CQ92|FIS1_MOUSE	0,06	2,16	0,46	-0,36	0,54	-2,04	-0,49	0,04
Q9JJW0|PXMP4_MOUSE	0,06	2,15	0,46	-0,35	0,54	-2,01	-0,50	0,05
Q8C0I1|ADAS_MOUSE	0,06	2,15	0,47	-0,35	0,54	-1,98	-0,51	0,05
P11679|K2C8_MOUSE	0,06	2,14	0,47	-0,35	0,55	-1,94	-0,51	0,05
Q6NXH9|K2C73_MOUSE	0,06	2,13	0,47	-0,34	0,55	-1,91	-0,52	0,06
B1AUE5|PEX10_MOUSE	0,06	2,12	0,47	-0,34	0,55	-1,88	-0,53	0,06
P53657|KPYR_MOUSE	0,06	2,11	0,47	-0,34	0,55	-1,86	-0,54	0,06
Q8CI51|PDLI5_MOUSE	0,06	2,10	0,48	-0,34	0,55	-1,83	-0,55	0,07
Q9Z2G9|HTAI2_MOUSE	0,06	2,09	0,48	-0,33	0,56	-1,80	-0,56	0,07
P62702|RS4X_MOUSE	0,06	2,09	0,48	-0,33	0,56	-1,77	-0,56	0,07
Q9WUR2|ECI2_MOUSE	0,06	2,08	0,48	-0,33	0,56	-1,75	-0,57	0,07
O35381|AN32A_MOUSE	0,06	2,07	0,48	-0,32	0,56	-1,72	-0,58	0,08
Q8BWP5|TTPA_MOUSE	0,06	2,06	0,48	-0,32	0,57	-1,70	-0,59	0,08
Q9NYQ2|HAOX2_MOUSE	0,06	2,05	0,49	-0,32	0,57	-1,68	-0,60	0,08
Q5XG73|ACBD5_MOUSE	0,06	2,05	0,49	-0,32	0,57	-1,65	-0,60	0,09
Q8K1N1|PLPL8_MOUSE	0,06	2,04	0,49	-0,31	0,57	-1,63	-0,61	0,09
P62137|PP1A_MOUSE	0,06	2,03	0,49	-0,31	0,57	-1,61	-0,62	0,09
Q9CQD1|RAB5A_MOUSE	0,06	2,02	0,49	-0,31	0,58	-1,59	-0,63	0,10
P97364|SPS2_MOUSE	0,06	2,01	0,50	-0,31	0,58	-1,57	-0,64	0,10
Q9R0P3|ESTD_MOUSE	0,06	2,01	0,50	-0,30	0,58	-1,55	-0,65	0,10
P06151|LDHA_MOUSE	0,06	2,00	0,50	-0,30	0,58	-1,53	-0,65	0,11

O08917|FLOT1_MOUSE	0,06	1,99	0,50	-0,30	0,59	-1,51	-0,66	0,11
P97425|ECP2_MOUSE	0,06	1,98	0,50	-0,29	0,59	-1,49	-0,67	0,11
Q91V64|ISOC1_MOUSE	0,06	1,98	0,51	-0,29	0,59	-1,48	-0,68	0,11
P47934|CACP_MOUSE	0,06	1,97	0,51	-0,29	0,59	-1,46	-0,69	0,12
Q07076|ANXA7_MOUSE	0,06	1,96	0,51	-0,29	0,59	-1,44	-0,69	0,12
Q99KB8|GLO2_MOUSE	0,06	1,96	0,51	-0,28	0,60	-1,42	-0,70	0,12
Q8CC88|VWA8_MOUSE	0,06	1,95	0,51	-0,28	0,60	-1,41	-0,71	0,13
Q8JZS0|LIN7A_MOUSE	0,06	1,94	0,52	-0,28	0,60	-1,39	-0,72	0,13
Q8VBT2|SDHL_MOUSE	0,06	1,93	0,52	-0,27	0,60	-1,38	-0,73	0,13
Q9CR35|CTRB1_MOUSE	0,06	1,93	0,52	-0,27	0,60	-1,36	-0,74	0,14
Q61792|LASP1_MOUSE	0,06	1,92	0,52	-0,27	0,61	-1,35	-0,74	0,14
Q8R1G2|CMBL_MOUSE	0,06	1,91	0,52	-0,27	0,61	-1,33	-0,75	0,14
P09411|PGK1_MOUSE	0,06	1,91	0,52	-0,26	0,61	-1,32	-0,76	0,15
Q8BI84|TGO1_MOUSE	0,06	1,90	0,53	-0,26	0,61	-1,30	-0,77	0,15
Q99J47|DRS7B_MOUSE	0,06	1,89	0,53	-0,26	0,62	-1,29	-0,78	0,15
Q9WUA5|EPM2A_MOUSE	0,06	1,89	0,53	-0,25	0,62	-1,28	-0,78	0,15
Q9EST5|AN32B_MOUSE	0,06	1,88	0,53	-0,25	0,62	-1,26	-0,79	0,16
Q64339|ISG15_MOUSE	0,06	1,87	0,53	-0,25	0,62	-1,25	-0,80	0,16
Q9D0K1|PEX13_MOUSE	0,06	1,87	0,54	-0,25	0,62	-1,24	-0,81	0,16
P63037|DNJA1_MOUSE	0,06	1,86	0,54	-0,24	0,63	-1,22	-0,82	0,17
Q9CRD0|OCAD1_MOUSE	0,06	1,85	0,54	-0,24	0,63	-1,21	-0,83	0,17
P47757|CAPZB_MOUSE	0,06	1,85	0,54	-0,24	0,63	-1,20	-0,83	0,17
Q811U4|MFN1_MOUSE	0,06	1,84	0,54	-0,23	0,63	-1,19	-0,84	0,18
Q9D5T0|ATAD1_MOUSE	0,06	1,83	0,55	-0,23	0,64	-1,18	-0,85	0,18
Q3UZZ6|ST1D1_MOUSE	0,06	1,83	0,55	-0,23	0,64	-1,17	-0,86	0,18
Q62093|SRSF2_MOUSE	0,06	1,82	0,55	-0,23	0,64	-1,15	-0,87	0,18
P52840|ST1A1_MOUSE	0,06	1,81	0,55	-0,22	0,64	-1,14	-0,87	0,19
Q922Z0|OXDD_MOUSE	0,06	1,81	0,55	-0,22	0,64	-1,13	-0,88	0,19
P41216|ACSL1_MOUSE	0,06	1,80	0,56	-0,22	0,65	-1,12	-0,89	0,19
Q61147|CERU_MOUSE	0,06	1,80	0,56	-0,21	0,65	-1,11	-0,90	0,20
P29788|VTNC_MOUSE	0,06	1,79	0,56	-0,21	0,65	-1,10	-0,91	0,20

Q9D1N9|RM21_MOUSE	0,06	1,78	0,56	-0,21	0,65	-1,09	-0,91	0,20
Q9DCL9|PUR6_MOUSE	0,06	1,78	0,56	-0,21	0,66	-1,08	-0,92	0,21
P60335|PCBP1_MOUSE	0,06	1,77	0,56	-0,20	0,66	-1,07	-0,93	0,21
O70400|PDLI1_MOUSE	0,06	1,77	0,57	-0,20	0,66	-1,06	-0,94	0,21
P51410|RL9_MOUSE	0,06	1,76	0,57	-0,20	0,66	-1,06	-0,95	0,22
Q99L20|GSTT3_MOUSE	0,06	1,75	0,57	-0,19	0,66	-1,05	-0,96	0,22
P59017|B2L13_MOUSE	0,06	1,75	0,57	-0,19	0,67	-1,04	-0,96	0,22
P35762|CD81_MOUSE	0,06	1,74	0,57	-0,19	0,67	-1,03	-0,97	0,22
Q8BM55|TM214_MOUSE	0,06	1,74	0,58	-0,19	0,67	-1,02	-0,98	0,23
P00397|COX1_MOUSE	0,06	1,73	0,58	-0,18	0,67	-1,01	-0,99	0,23
Q7TMF3|NDUAC_MOUSE	0,06	1,72	0,58	-0,18	0,67	-1,00	-1,00	0,23
Q8K2M0|RM38_MOUSE	0,06	1,72	0,58	-0,18	0,68	-1,00	-1,00	0,24
Q9ESB3|HRG_MOUSE	0,06	1,71	0,58	-0,17	0,68	-0,99	-1,01	0,24
Q80WW9|DDRGK_MOUSE	0,06	1,71	0,59	-0,17	0,68	-0,98	-1,02	0,24
P15535|B4GT1_MOUSE	0,06	1,70	0,59	-0,17	0,68	-0,97	-1,03	0,25
P10518|HEM2_MOUSE	0,06	1,70	0,59	-0,17	0,69	-0,96	-1,04	0,25
Q8R429|AT2A1_MOUSE	0,06	1,69	0,59	-0,16	0,69	-0,96	-1,05	0,25
Q9CQC9|SAR1B_MOUSE	0,06	1,69	0,59	-0,16	0,69	-0,95	-1,05	0,25
Q9WUB3|PYGM_MOUSE	0,06	1,68	0,59	-0,16	0,69	-0,94	-1,06	0,26
Q571E4|GALNS_MOUSE	0,06	1,68	0,60	-0,15	0,69	-0,93	-1,07	0,26
P48410|ABCD1_MOUSE	0,06	1,67	0,60	-0,15	0,70	-0,93	-1,08	0,26
Q91X34|BAAT_MOUSE	0,06	1,66	0,60	-0,15	0,70	-0,92	-1,09	0,27
Q8C767|PPR3B_MOUSE	0,06	1,66	0,60	-0,15	0,70	-0,91	-1,09	0,27
Q3ULJ0|GPD1L_MOUSE	0,06	1,65	0,60	-0,14	0,70	-0,91	-1,10	0,27
Q9D826|SOX_MOUSE	0,06	1,65	0,61	-0,14	0,71	-0,90	-1,11	0,28
P00688|AMYP_MOUSE	0,06	1,64	0,61	-0,14	0,71	-0,89	-1,12	0,28
Q9ET01|PYGL_MOUSE	0,06	1,64	0,61	-0,13	0,71	-0,89	-1,13	0,28
P00687|AMY1_MOUSE	0,06	1,63	0,61	-0,13	0,71	-0,88	-1,14	0,29
P32020|SCP2_MOUSE	0,06	1,63	0,61	-0,13	0,71	-0,87	-1,14	0,29
Q99P30|NUDT7_MOUSE	0,06	1,62	0,62	-0,13	0,72	-0,87	-1,15	0,29
Q9CRB3|HIUH_MOUSE	0,06	1,62	0,62	-0,12	0,72	-0,86	-1,16	0,29

Q9DC50|OCTC_MOUSE	0,06	1,61	0,62	-0,12	0,72	-0,86	-1,17	0,30
P13707|GPDA_MOUSE	0,06	1,61	0,62	-0,12	0,72	-0,85	-1,18	0,30
P11930|NUD19_MOUSE	0,06	1,60	0,62	-0,11	0,72	-0,84	-1,18	0,30
Q8BGG9|ACNT2_MOUSE	0,06	1,60	0,63	-0,11	0,73	-0,84	-1,19	0,31
P24270|CATA_MOUSE	0,06	1,59	0,63	-0,11	0,73	-0,83	-1,20	0,31
Q99LC9|PEX6_MOUSE	0,06	1,59	0,63	-0,11	0,73	-0,83	-1,21	0,31
Q91XC9|PEX16_MOUSE	0,06	1,58	0,63	-0,10	0,73	-0,82	-1,22	0,32
O35386|PAHX_MOUSE	0,06	1,58	0,63	-0,10	0,74	-0,82	-1,23	0,32
Q9EPL9|ACOX3_MOUSE	0,06	1,58	0,63	-0,10	0,74	-0,81	-1,23	0,32
Q9DBM2|ECHP_MOUSE	0,06	1,57	0,64	-0,09	0,74	-0,81	-1,24	0,33
Q9WU19|HAOX1_MOUSE	0,06	1,57	0,64	-0,09	0,74	-0,80	-1,25	0,33
P51660|DHB4_MOUSE	0,06	1,56	0,64	-0,09	0,74	-0,79	-1,26	0,33
Q921H8|THIKA_MOUSE	0,06	1,56	0,64	-0,09	0,75	-0,79	-1,27	0,33
Q9QXE0|HACL1_MOUSE	0,06	1,55	0,64	-0,08	0,75	-0,78	-1,27	0,34
P34914|HYES_MOUSE	0,06	1,55	0,65	-0,08	0,75	-0,78	-1,28	0,34
Q9QXY9|PEX3_MOUSE	0,06	1,54	0,65	-0,08	0,75	-0,77	-1,29	0,34
Q9R0A0|PEX14_MOUSE	0,06	1,54	0,65	-0,07	0,76	-0,77	-1,30	0,35
Q8VDG7|PAFA2_MOUSE	0,06	1,53	0,65	-0,07	0,76	-0,76	-1,31	0,35
Q9R0H0|ACOX1_MOUSE	0,06	1,53	0,65	-0,07	0,76	-0,76	-1,32	0,35
Q8VCH0|THIKB_MOUSE	0,06	1,53	0,66	-0,07	0,76	-0,76	-1,32	0,36
Q9DCN1|NUD12_MOUSE	0,06	1,52	0,66	-0,06	0,76	-0,75	-1,33	0,36
Q80XL6|ACD11_MOUSE	0,06	1,52	0,66	-0,06	0,77	-0,75	-1,34	0,36
Q9DBK0|ACO12_MOUSE	0,06	1,51	0,66	-0,06	0,77	-0,74	-1,35	0,36
Q2TPA8|HSDL2_MOUSE	0,06	1,51	0,66	-0,06	0,77	-0,74	-1,36	0,37
Q99MZ7|PECR_MOUSE	0,06	1,50	0,67	-0,05	0,77	-0,73	-1,36	0,37
Q5BL07|PEX1_MOUSE	0,06	1,50	0,67	-0,05	0,78	-0,73	-1,37	0,37
O09174|AMACR_MOUSE	0,06	1,50	0,67	-0,05	0,78	-0,72	-1,38	0,38
Q8BWN8|ACOT4_MOUSE	0,06	1,49	0,67	-0,04	0,78	-0,72	-1,39	0,38
Q8R1M2|H2AJ_MOUSE	0,06	1,49	0,67	-0,04	0,78	-0,72	-1,40	0,38
Q9CYV5|TM135_MOUSE	0,06	1,48	0,67	-0,04	0,78	-0,71	-1,41	0,39
Q9QXD1|ACOX2_MOUSE	0,06	1,48	0,68	-0,04	0,79	-0,71	-1,41	0,39

Q9DBA6|TYSD1_MOUSE	0,06	1,47	0,68	-0,03	0,79	-0,70	-1,42	0,39
Q9WV68|DECR2_MOUSE	0,06	1,47	0,68	-0,03	0,79	-0,70	-1,43	0,40
O35423|SPYA_MOUSE	0,06	1,47	0,68	-0,03	0,79	-0,70	-1,44	0,40
O09012|PEX5_MOUSE	0,06	1,46	0,68	-0,02	0,79	-0,69	-1,45	0,40
A2AKK5|ACNT1_MOUSE	0,06	1,46	0,69	-0,02	0,80	-0,69	-1,45	0,40
Q99KR3|LACB2_MOUSE	0,06	1,45	0,69	-0,02	0,80	-0,68	-1,46	0,41
Q9DBN5|LONP2_MOUSE	0,06	1,45	0,69	-0,02	0,80	-0,68	-1,47	0,41
P50431|GLYC_MOUSE	0,06	1,45	0,69	-0,01	0,80	-0,68	-1,48	0,41
P55096|ABCD3_MOUSE	0,06	1,44	0,69	-0,01	0,81	-0,67	-1,49	0,42
O35678|MGLL_MOUSE	0,06	1,44	0,70	-0,01	0,81	-0,67	-1,50	0,42
Q99LB2|DHRS4_MOUSE	0,06	1,43	0,70	0,00	0,81	-0,67	-1,50	0,42
P07146|TRY2_MOUSE	0,06	1,43	0,70	0,00	0,81	-0,66	-1,51	0,43
Q8C7E7|STBD1_MOUSE	0,06	1,43	0,70	0,00	0,81	-0,66	-1,52	0,43
Q9QYR7|ACOT3_MOUSE	0,06	1,42	0,70	0,00	0,82	-0,65	-1,53	0,43
O88844|IDHC_MOUSE	0,06	1,42	0,70	0,01	0,82	-0,65	-1,54	0,43
O70579|PM34_MOUSE	0,06	1,41	0,71	0,01	0,82	-0,65	-1,54	0,44
P42925|PXMP2_MOUSE	0,06	1,41	0,71	0,01	0,82	-0,64	-1,55	0,44
Q9DCM2|GSTK1_MOUSE	0,06	1,41	0,71	0,02	0,83	-0,64	-1,56	0,44
P05208|CEL2A_MOUSE	0,06	1,40	0,71	0,02	0,83	-0,64	-1,57	0,45
P98192|GNPAT_MOUSE	0,06	1,40	0,71	0,02	0,83	-0,63	-1,58	0,45
Q8BGC4|PTGR3_MOUSE	0,06	1,40	0,72	0,02	0,83	-0,63	-1,59	0,45
Q61285|ABCD2_MOUSE	0,06	1,39	0,72	0,03	0,83	-0,63	-1,59	0,46
P25688|URIC_MOUSE	0,06	1,39	0,72	0,03	0,84	-0,62	-1,60	0,46
Q6P6M5|PX11C_MOUSE	0,06	1,39	0,72	0,03	0,84	-0,62	-1,61	0,46
Q8CHK3|MBOA7_MOUSE	0,06	1,38	0,72	0,04	0,84	-0,62	-1,62	0,47
Q9D1G2|PMVK_MOUSE	0,06	1,38	0,73	0,04	0,84	-0,61	-1,63	0,47
Q9Z211|PX11A_MOUSE	0,06	1,37	0,73	0,04	0,84	-0,61	-1,63	0,47
Q61878|PRG2_MOUSE	0,06	1,37	0,73	0,04	0,85	-0,61	-1,64	0,47
Q9Z210|PX11B_MOUSE	0,06	1,37	0,73	0,05	0,85	-0,61	-1,65	0,48
P58137|ACOT8_MOUSE	0,06	1,36	0,73	0,05	0,85	-0,60	-1,66	0,48
Q8VCR7|ABHEB_MOUSE	0,06	1,36	0,74	0,05	0,85	-0,60	-1,67	0,48

P12815|PDCD6_MOUSE	0,06	1,36	0,74	0,06	0,86	-0,60	-1,68	0,49
Q99MD6|TRXR3_MOUSE	0,06	1,35	0,74	0,06	0,86	-0,59	-1,68	0,49
P14152|MDHC_MOUSE	0,06	1,35	0,74	0,06	0,86	-0,59	-1,69	0,49
Q8BGI5|PEX26_MOUSE	0,06	1,35	0,74	0,06	0,86	-0,59	-1,70	0,50
P15116|CADH2_MOUSE	0,06	1,34	0,74	0,07	0,86	-0,59	-1,71	0,50
P09405|NUCL_MOUSE	0,06	1,34	0,75	0,07	0,87	-0,58	-1,72	0,50
Q8VC48|PEX12_MOUSE	0,06	1,34	0,75	0,07	0,87	-0,58	-1,72	0,51
P49290|PERE_MOUSE	0,06	1,33	0,75	0,08	0,87	-0,58	-1,73	0,51
Q9CQ92|FIS1_MOUSE	0,06	1,33	0,75	0,08	0,87	-0,57	-1,74	0,51
Q9JJW0|PXMP4_MOUSE	0,06	1,33	0,75	0,08	0,88	-0,57	-1,75	0,51
Q8C0I1|ADAS_MOUSE	0,06	1,32	0,76	0,08	0,88	-0,57	-1,76	0,52
P11679|K2C8_MOUSE	0,06	1,32	0,76	0,09	0,88	-0,57	-1,77	0,52
Q6NXH9|K2C73_MOUSE	0,06	1,32	0,76	0,09	0,88	-0,56	-1,77	0,52
B1AUE5|PEX10_MOUSE	0,06	1,31	0,76	0,09	0,88	-0,56	-1,78	0,53
P53657|KPYR_MOUSE	0,06	1,31	0,76	0,10	0,89	-0,56	-1,79	0,53
Q8CI51|PDLI5_MOUSE	0,06	1,31	0,77	0,10	0,89	-0,56	-1,80	0,53
Q9Z2G9|HTAI2_MOUSE	0,06	1,30	0,77	0,10	0,89	-0,55	-1,81	0,54
P62702|RS4X_MOUSE	0,06	1,30	0,77	0,10	0,89	-0,55	-1,81	0,54
Q9WUR2|ECI2_MOUSE	0,06	1,30	0,77	0,11	0,90	-0,55	-1,82	0,54
O35381|AN32A_MOUSE	0,06	1,29	0,77	0,11	0,90	-0,55	-1,83	0,54
Q8BWP5|TTPA_MOUSE	0,06	1,29	0,78	0,11	0,90	-0,54	-1,84	0,55
Q9NYQ2|HAOX2_MOUSE	0,06	1,29	0,78	0,12	0,90	-0,54	-1,85	0,55
Q5XG73|ACBD5_MOUSE	0,06	1,28	0,78	0,12	0,90	-0,54	-1,86	0,55
Q8K1N1|PLPL8_MOUSE	0,06	1,28	0,78	0,12	0,91	-0,54	-1,86	0,56
P62137|PP1A_MOUSE	0,06	1,28	0,78	0,12	0,91	-0,53	-1,87	0,56
Q9CQD1|RAB5A_MOUSE	0,06	1,27	0,78	0,13	0,91	-0,53	-1,88	0,56
P97364|SPS2_MOUSE	0,06	1,27	0,79	0,13	0,91	-0,53	-1,89	0,57
Q9R0P3|ESTD_MOUSE	0,06	1,27	0,79	0,13	0,91	-0,53	-1,90	0,57
P06151|LDHA_MOUSE	0,06	1,27	0,79	0,14	0,92	-0,53	-1,90	0,57
O08917|FLOT1_MOUSE	0,06	1,26	0,79	0,14	0,92	-0,52	-1,91	0,58
P97425|ECP2_MOUSE	0,06	1,26	0,79	0,14	0,92	-0,52	-1,92	0,58

Q91V64|ISOC1_MOUSE	0,06	1,26	0,80	0,14	0,92	-0,52	-1,93	0,58
P47934|CACP_MOUSE	0,06	1,25	0,80	0,15	0,93	-0,52	-1,94	0,58
Q07076|ANXA7_MOUSE	0,06	1,25	0,80	0,15	0,93	-0,51	-1,95	0,59
Q99KB8|GLO2_MOUSE	0,06	1,25	0,80	0,15	0,93	-0,51	-1,95	0,59
Q8CC88|VWA8_MOUSE	0,06	1,24	0,80	0,16	0,93	-0,51	-1,96	0,59
Q8JZS0|LIN7A_MOUSE	0,06	1,24	0,81	0,16	0,93	-0,51	-1,97	0,60
Q8VBT2|SDHL_MOUSE	0,06	1,24	0,81	0,16	0,94	-0,51	-1,98	0,60
Q9CR35|CTRB1_MOUSE	0,06	1,24	0,81	0,16	0,94	-0,50	-1,99	0,60
Q61792|LASP1_MOUSE	0,06	1,23	0,81	0,17	0,94	-0,50	-1,99	0,61
Q8R1G2|CMBL_MOUSE	0,06	1,23	0,81	0,17	0,94	-0,50	-2,00	0,61
P09411|PGK1_MOUSE	0,06	1,23	0,81	0,17	0,95	-0,50	-2,01	0,61
Q8BI84|TGO1_MOUSE	0,06	1,22	0,82	0,17	0,95	-0,50	-2,02	0,61
Q99J47|DRS7B_MOUSE	0,06	1,22	0,82	0,18	0,95	-0,49	-2,03	0,62
Q9WUA5|EPM2A_MOUSE	0,06	1,22	0,82	0,18	0,95	-0,49	-2,04	0,62
Q9EST5|AN32B_MOUSE	0,06	1,22	0,82	0,18	0,95	-0,49	-2,04	0,62
Q64339|ISG15_MOUSE	0,06	1,21	0,82	0,19	0,96	-0,49	-2,05	0,63
Q9D0K1|PEX13_MOUSE	0,06	1,21	0,83	0,19	0,96	-0,49	-2,06	0,63
P63037|DNJA1_MOUSE	0,06	1,21	0,83	0,19	0,96	-0,48	-2,07	0,63
Q9CRD0|OCAD1_MOUSE	0,06	1,20	0,83	0,19	0,96	-0,48	-2,08	0,64
P47757|CAPZB_MOUSE	0,06	1,20	0,83	0,20	0,96	-0,48	-2,08	0,64
Q811U4|MFN1_MOUSE	0,06	1,20	0,83	0,20	0,97	-0,48	-2,09	0,64
Q9D5T0|ATAD1_MOUSE	0,06	1,20	0,84	0,20	0,97	-0,48	-2,10	0,65
Q3UZZ6|ST1D1_MOUSE	0,06	1,19	0,84	0,21	0,97	-0,47	-2,11	0,65
Q62093|SRSF2_MOUSE	0,06	1,19	0,84	0,21	0,97	-0,47	-2,12	0,65
P52840|ST1A1_MOUSE	0,06	1,19	0,84	0,21	0,98	-0,47	-2,13	0,65
Q922Z0|OXDD_MOUSE	0,06	1,19	0,84	0,21	0,98	-0,47	-2,13	0,66
P41216|ACSL1_MOUSE	0,06	1,18	0,85	0,22	0,98	-0,47	-2,14	0,66
Q61147|CERU_MOUSE	0,06	1,18	0,85	0,22	0,98	-0,47	-2,15	0,66
P29788|VTNC_MOUSE	0,06	1,18	0,85	0,22	0,98	-0,46	-2,16	0,67
Q9D1N9|RM21_MOUSE	0,06	1,18	0,85	0,23	0,99	-0,46	-2,17	0,67
Q9DCL9|PUR6_MOUSE	0,06	1,17	0,85	0,23	0,99	-0,46	-2,17	0,67

P60335|PCBP1_MOUSE	0,06	1,17	0,85	0,23	0,99	-0,46	-2,18	0,68
O70400|PDLI1_MOUSE	0,06	1,17	0,86	0,23	0,99	-0,46	-2,19	0,68
P51410|RL9_MOUSE	0,06	1,16	0,86	0,24	1,00	-0,45	-2,20	0,68
Q99L20|GSTT3_MOUSE	0,06	1,16	0,86	0,24	1,00	-0,45	-2,21	0,69
P59017|B2L13_MOUSE	0,06	1,16	0,86	0,24	1,00	-0,45	-2,21	0,69
P35762|CD81_MOUSE	0,06	1,16	0,86	0,25	1,00	-0,45	-2,22	0,69
Q8BM55|TM214_MOUSE	0,06	1,15	0,87	0,25	1,00	-0,45	-2,23	0,69
P00397|COX1_MOUSE	0,06	1,15	0,87	0,25	1,01	-0,45	-2,24	0,70
Q7TMF3|NDUAC_MOUSE	0,06	1,15	0,87	0,25	1,01	-0,44	-2,25	0,70
Q8K2M0|RM38_MOUSE	0,06	1,15	0,87	0,26	1,01	-0,44	-2,26	0,70
Q9ESB3|HRG_MOUSE	0,06	1,14	0,87	0,26	1,01	-0,44	-2,26	0,71
Q80WW9|DDRGK_MOUSE	0,06	1,14	0,88	0,26	1,02	-0,44	-2,27	0,71
P15535|B4GT1_MOUSE	0,06	1,14	0,88	0,27	1,02	-0,44	-2,28	0,71
P10518|HEM2_MOUSE	0,06	1,14	0,88	0,27	1,02	-0,44	-2,29	0,72
Q8R429|AT2A1_MOUSE	0,06	1,13	0,88	0,27	1,02	-0,44	-2,30	0,72
Q9CQC9|SAR1B_MOUSE	0,06	1,13	0,88	0,27	1,02	-0,43	-2,30	0,72
Q9WUB3|PYGM_MOUSE	0,06	1,13	0,89	0,28	1,03	-0,43	-2,31	0,72
Q571E4|GALNS_MOUSE	0,06	1,13	0,89	0,28	1,03	-0,43	-2,32	0,73
P48410|ABCD1_MOUSE	0,06	1,13	0,89	0,28	1,03	-0,43	-2,33	0,73
Q91X34|BAAT_MOUSE	0,06	1,12	0,89	0,29	1,03	-0,43	-2,34	0,73
Q8C767|PPR3B_MOUSE	0,06	1,12	0,89	0,29	1,03	-0,43	-2,35	0,74
Q3ULJ0|GPD1L_MOUSE	0,06	1,12	0,89	0,29	1,04	-0,42	-2,35	0,74
Q9D826|SOX_MOUSE	0,06	1,12	0,90	0,29	1,04	-0,42	-2,36	0,74
P00688|AMYP_MOUSE	0,06	1,11	0,90	0,30	1,04	-0,42	-2,37	0,75
Q9ET01|PYGL_MOUSE	0,06	1,11	0,90	0,30	1,04	-0,42	-2,38	0,75
P00687|AMY1_MOUSE	0,06	1,11	0,90	0,30	1,05	-0,42	-2,39	0,75
P32020|SCP2_MOUSE	0,06	1,11	0,90	0,31	1,05	-0,42	-2,39	0,76
Q99P30|NUDT7_MOUSE	0,06	1,10	0,91	0,31	1,05	-0,42	-2,40	0,76
Q9CRB3|HIUH_MOUSE	0,06	1,10	0,91	0,31	1,05	-0,41	-2,41	0,76
Q9DC50|OCTC_MOUSE	0,06	1,10	0,91	0,31	1,05	-0,41	-2,42	0,76
P13707|GPDA_MOUSE	0,06	1,10	0,91	0,32	1,06	-0,41	-2,43	0,77

P11930|NUD19_MOUSE	0,06	1,09	0,91	0,32	1,06	-0,41	-2,44	0,77
Q8BGG9|ACNT2_MOUSE	0,06	1,09	0,92	0,32	1,06	-0,41	-2,44	0,77
P24270|CATA_MOUSE	0,06	1,09	0,92	0,33	1,06	-0,41	-2,45	0,78
Q99LC9|PEX6_MOUSE	0,06	1,09	0,92	0,33	1,07	-0,41	-2,46	0,78
Q91XC9|PEX16_MOUSE	0,06	1,09	0,92	0,33	1,07	-0,41	-2,47	0,78
O35386|PAHX_MOUSE	0,06	1,08	0,92	0,33	1,07	-0,40	-2,48	0,79
Q9EPL9|ACOX3_MOUSE	0,06	1,08	0,92	0,34	1,07	-0,40	-2,48	0,79
Q9DBM2|ECHP_MOUSE	0,06	1,08	0,93	0,34	1,07	-0,40	-2,49	0,79
Q9WU19|HAOX1_MOUSE	0,06	1,08	0,93	0,34	1,08	-0,40	-2,50	0,79
P51660|DHB4_MOUSE	0,06	1,07	0,93	0,35	1,08	-0,40	-2,51	0,80
Q921H8|THIKA_MOUSE	0,06	1,07	0,93	0,35	1,08	-0,40	-2,52	0,80
Q9QXE0|HACL1_MOUSE	0,06	1,07	0,93	0,35	1,08	-0,40	-2,53	0,80
P34914|HYES_MOUSE	0,06	1,07	0,94	0,35	1,08	-0,39	-2,53	0,81
Q9QXY9|PEX3_MOUSE	0,06	1,07	0,94	0,36	1,09	-0,39	-2,54	0,81
Q9R0A0|PEX14_MOUSE	0,06	1,06	0,94	0,36	1,09	-0,39	-2,55	0,81
Q8VDG7|PAFA2_MOUSE	0,06	1,06	0,94	0,36	1,09	-0,39	-2,56	0,82
Q9R0H0|ACOX1_MOUSE	0,06	1,06	0,94	0,37	1,09	-0,39	-2,57	0,82
Q8VCH0|THIKB_MOUSE	0,06	1,06	0,95	0,37	1,10	-0,39	-2,57	0,82
Q9DCN1|NUD12_MOUSE	0,06	1,06	0,95	0,37	1,10	-0,39	-2,58	0,83
Q80XL6|ACD11_MOUSE	0,06	1,05	0,95	0,37	1,10	-0,39	-2,59	0,83
Q9DBK0|ACO12_MOUSE	0,06	1,05	0,95	0,38	1,10	-0,38	-2,60	0,83
Q2TPA8|HSDL2_MOUSE	0,06	1,05	0,95	0,38	1,10	-0,38	-2,61	0,83
Q99MZ7|PECR_MOUSE	0,06	1,05	0,96	0,38	1,11	-0,38	-2,62	0,84
Q5BL07|PEX1_MOUSE	0,06	1,04	0,96	0,39	1,11	-0,38	-2,62	0,84
O09174|AMACR_MOUSE	0,06	1,04	0,96	0,39	1,11	-0,38	-2,63	0,84
Q8BWN8|ACOT4_MOUSE	0,06	1,04	0,96	0,39	1,11	-0,38	-2,64	0,85
Q8R1M2|H2AJ_MOUSE	0,06	1,04	0,96	0,39	1,12	-0,38	-2,65	0,85
Q9CYV5|TM135_MOUSE	0,06	1,04	0,96	0,40	1,12	-0,38	-2,66	0,85
Q9QXD1|ACOX2_MOUSE	0,06	1,03	0,97	0,40	1,12	-0,38	-2,66	0,86
Q9DBA6|TYSD1_MOUSE	0,06	1,03	0,97	0,40	1,12	-0,37	-2,67	0,86
Q9WV68|DECR2_MOUSE	0,06	1,03	0,97	0,40	1,12	-0,37	-2,68	0,86

O35423|SPYA_MOUSE	0,06	1,03	0,97	0,41	1,13	-0,37	-2,69	0,87
O09012|PEX5_MOUSE	0,06	1,03	0,97	0,41	1,13	-0,37	-2,70	0,87
A2AKK5|ACNT1_MOUSE	0,06	1,02	0,98	0,41	1,13	-0,37	-2,71	0,87
Q99KR3|LACB2_MOUSE	0,06	1,02	0,98	0,42	1,13	-0,37	-2,71	0,87
Q9DBN5|LONP2_MOUSE	0,06	1,02	0,98	0,42	1,14	-0,37	-2,72	0,88
P50431|GLYC_MOUSE	0,06	1,02	0,98	0,42	1,14	-0,37	-2,73	0,88
P55096|ABCD3_MOUSE	0,06	1,02	0,98	0,42	1,14	-0,37	-2,74	0,88
O35678|MGLL_MOUSE	0,06	1,01	0,99	0,43	1,14	-0,36	-2,75	0,89
Q99LB2|DHRS4_MOUSE	0,06	1,01	0,99	0,43	1,14	-0,36	-2,75	0,89
P07146|TRY2_MOUSE	0,06	1,01	0,99	0,43	1,15	-0,36	-2,76	0,89
Q8C7E7|STBD1_MOUSE	0,06	1,01	0,99	0,44	1,15	-0,36	-2,77	0,90
Q9QYR7|ACOT3_MOUSE	0,06	1,01	0,99	0,44	1,15	-0,36	-2,78	0,90
O88844|IDHC_MOUSE	0,06	1,00	1,00	0,44	1,15	-0,36	-2,79	0,90
O70579|PM34_MOUSE	0,06	1,00	1,00	0,44	1,15	-0,36	-2,80	0,90
P42925|PXMP2_MOUSE	0,06	1,00	1,00	0,45	1,16	-0,36	-2,80	0,91
Q9DCM2|GSTK1_MOUSE	0,06	1,00	1,00	0,45	1,16	-0,36	-2,81	0,91
P05208|CEL2A_MOUSE	0,06	1,00	1,00	0,45	1,16	-0,35	-2,82	0,91
P98192|GNPAT_MOUSE	0,06	1,00	1,00	0,46	1,16	-0,35	-2,83	0,92
Q8BGC4|PTGR3_MOUSE	0,06	0,99	1,01	0,46	1,17	-0,35	-2,84	0,92
Q61285|ABCD2_MOUSE	0,06	0,99	1,01	0,46	1,17	-0,35	-2,84	0,92
P25688|URIC_MOUSE	0,06	0,99	1,01	0,46	1,17	-0,35	-2,85	0,93
Q6P6M5|PX11C_MOUSE	0,06	0,99	1,01	0,47	1,17	-0,35	-2,86	0,93
Q8CHK3|MBOA7_MOUSE	0,06	0,99	1,01	0,47	1,17	-0,35	-2,87	0,93
Q9D1G2|PMVK_MOUSE	0,06	0,98	1,02	0,47	1,18	-0,35	-2,88	0,94
Q9Z211|PX11A_MOUSE	0,06	0,98	1,02	0,48	1,18	-0,35	-2,89	0,94
Q61878|PRG2_MOUSE	0,06	0,98	1,02	0,48	1,18	-0,35	-2,89	0,94
Q9Z210|PX11B_MOUSE	0,06	0,98	1,02	0,48	1,18	-0,34	-2,90	0,94
P58137|ACOT8_MOUSE	0,06	0,98	1,02	0,48	1,19	-0,34	-2,91	0,95
Q8VCR7|ABHEB_MOUSE	0,06	0,98	1,03	0,49	1,19	-0,34	-2,92	0,95
P12815|PDCD6_MOUSE	0,06	0,97	1,03	0,49	1,19	-0,34	-2,93	0,95
Q99MD6|TRXR3_MOUSE	0,06	0,97	1,03	0,49	1,19	-0,34	-2,93	0,96

P14152|MDHC_MOUSE	0,06	0,97	1,03	0,50	1,19	-0,34	-2,94	0,96
Q8BGI5|PEX26_MOUSE	0,06	0,97	1,03	0,50	1,20	-0,34	-2,95	0,96
P15116|CADH2_MOUSE	0,06	0,97	1,03	0,50	1,20	-0,34	-2,96	0,97
P09405|NUCL_MOUSE	0,06	0,96	1,04	0,50	1,20	-0,34	-2,97	0,97
Q8VC48|PEX12_MOUSE	0,06	0,96	1,04	0,51	1,20	-0,34	-2,98	0,97
P49290|PERE_MOUSE	0,06	0,96	1,04	0,51	1,20	-0,34	-2,98	0,97
Q9CQ92|FIS1_MOUSE	0,06	0,96	1,04	0,51	1,21	-0,33	-2,99	0,98
Q9JJW0|PXMP4_MOUSE	0,06	0,96	1,04	0,52	1,21	-0,33	-3,00	0,98
Q8C0I1|ADAS_MOUSE	0,06	0,96	1,05	0,52	1,21	-0,33	-3,01	0,98
P11679|K2C8_MOUSE	0,06	0,95	1,05	0,52	1,21	-0,33	-3,02	0,99
Q6NXH9|K2C73_MOUSE	0,06	0,95	1,05	0,52	1,22	-0,33	-3,02	0,99
B1AUE5|PEX10_MOUSE	0,06	0,95	1,05	0,53	1,22	-0,33	-3,03	0,99
P53657|KPYR_MOUSE	0,06	0,95	1,05	0,53	1,22	-0,33	-3,04	1,00
Q8CI51|PDLI5_MOUSE	0,06	0,95	1,06	0,53	1,22	-0,33	-3,05	1,00
Q9Z2G9|HTAI2_MOUSE	0,06	0,95	1,06	0,54	1,22	-0,33	-3,06	1,00
P62702|RS4X_MOUSE	0,06	0,94	1,06	0,54	1,23	-0,33	-3,07	1,01
Q9WUR2|ECI2_MOUSE	0,06	0,94	1,06	0,54	1,23	-0,33	-3,07	1,01
O35381|AN32A_MOUSE	0,06	0,94	1,06	0,54	1,23	-0,32	-3,08	1,01
Q8BWP5|TTPA_MOUSE	0,06	0,94	1,07	0,55	1,23	-0,32	-3,09	1,01
Q9NYQ2|HAOX2_MOUSE	0,06	0,94	1,07	0,55	1,24	-0,32	-3,10	1,02
Q5XG73|ACBD5_MOUSE	0,05	0,94	1,07	0,55	1,24	-0,32	-3,11	1,02
Q8K1N1|PLPL8_MOUSE	0,05	0,93	1,07	0,56	1,24	-0,32	-3,11	1,02
P62137|PP1A_MOUSE	0,05	0,93	1,07	0,56	1,24	-0,32	-3,12	1,03
Q9CQD1|RAB5A_MOUSE	0,05	0,93	1,07	0,56	1,24	-0,32	-3,13	1,03
P97364|SPS2_MOUSE	0,05	0,93	1,08	0,56	1,25	-0,32	-3,14	1,03
Q9R0P3|ESTD_MOUSE	0,05	0,93	1,08	0,57	1,25	-0,32	-3,15	1,04
P06151|LDHA_MOUSE	0,05	0,93	1,08	0,57	1,25	-0,32	-3,16	1,04
O08917|FLOT1_MOUSE	0,05	0,92	1,08	0,57	1,25	-0,32	-3,16	1,04
P97425|ECP2_MOUSE	0,05	0,92	1,08	0,58	1,26	-0,32	-3,17	1,05
Q91V64|ISOC1_MOUSE	0,05	0,92	1,09	0,58	1,26	-0,31	-3,18	1,05
P47934|CACP_MOUSE	0,05	0,92	1,09	0,58	1,26	-0,31	-3,19	1,05

Q07076|ANXA7_MOUSE	0,05	0,92	1,09	0,58	1,26	-0,31	-3,20	1,05
Q99KB8|GLO2_MOUSE	0,05	0,92	1,09	0,59	1,26	-0,31	-3,20	1,06
Q8CC88|VWA8_MOUSE	0,05	0,91	1,09	0,59	1,27	-0,31	-3,21	1,06
Q8JZS0|LIN7A_MOUSE	0,05	0,91	1,10	0,59	1,27	-0,31	-3,22	1,06
Q8VBT2|SDHL_MOUSE	0,05	0,91	1,10	0,60	1,27	-0,31	-3,23	1,07
Q9CR35|CTRB1_MOUSE	0,05	0,91	1,10	0,60	1,27	-0,31	-3,24	1,07
Q61792|LASP1_MOUSE	0,05	0,91	1,10	0,60	1,27	-0,31	-3,25	1,07
Q8R1G2|CMBL_MOUSE	0,05	0,91	1,10	0,60	1,28	-0,31	-3,25	1,08
P09411|PGK1_MOUSE	0,05	0,90	1,11	0,61	1,28	-0,31	-3,26	1,08
Q8BI84|TGO1_MOUSE	0,05	0,90	1,11	0,61	1,28	-0,31	-3,27	1,08
Q99J47|DRS7B_MOUSE	0,05	0,90	1,11	0,61	1,28	-0,31	-3,28	1,08
Q9WUA5|EPM2A_MOUSE	0,05	0,90	1,11	0,62	1,29	-0,30	-3,29	1,09
Q9EST5|AN32B_MOUSE	0,05	0,90	1,11	0,62	1,29	-0,30	-3,29	1,09
Q64339|ISG15_MOUSE	0,05	0,90	1,11	0,62	1,29	-0,30	-3,30	1,09
Q9D0K1|PEX13_MOUSE	0,05	0,90	1,12	0,62	1,29	-0,30	-3,31	1,10
P63037|DNJA1_MOUSE	0,05	0,89	1,12	0,63	1,29	-0,30	-3,32	1,10
Q9CRD0|OCAD1_MOUSE	0,05	0,89	1,12	0,63	1,30	-0,30	-3,33	1,10
P47757|CAPZB_MOUSE	0,05	0,89	1,12	0,63	1,30	-0,30	-3,34	1,11
Q811U4|MFN1_MOUSE	0,05	0,89	1,12	0,63	1,30	-0,30	-3,34	1,11
Q9D5T0|ATAD1_MOUSE	0,05	0,89	1,13	0,64	1,30	-0,30	-3,35	1,11
Q3UZZ6|ST1D1_MOUSE	0,05	0,89	1,13	0,64	1,31	-0,30	-3,36	1,12
Q62093|SRSF2_MOUSE	0,05	0,89	1,13	0,64	1,31	-0,30	-3,37	1,12
P52840|ST1A1_MOUSE	0,05	0,88	1,13	0,65	1,31	-0,30	-3,38	1,12
Q922Z0|OXDD_MOUSE	0,05	0,88	1,13	0,65	1,31	-0,30	-3,38	1,12
P41216|ACSL1_MOUSE	0,05	0,88	1,14	0,65	1,31	-0,29	-3,39	1,13
Q61147|CERU_MOUSE	0,05	0,88	1,14	0,65	1,32	-0,29	-3,40	1,13
P29788|VTNC_MOUSE	0,05	0,88	1,14	0,66	1,32	-0,29	-3,41	1,13
Q9D1N9|RM21_MOUSE	0,05	0,88	1,14	0,66	1,32	-0,29	-3,42	1,14
Q9DCL9|PUR6_MOUSE	0,05	0,87	1,14	0,66	1,32	-0,29	-3,42	1,14
P60335|PCBP1_MOUSE	0,05	0,87	1,14	0,67	1,32	-0,29	-3,43	1,14
O70400|PDLI1_MOUSE	0,05	0,87	1,15	0,67	1,33	-0,29	-3,44	1,15

P51410|RL9_MOUSE	0,05	0,87	1,15	0,67	1,33	-0,29	-3,45	1,15
Q99L20|GSTT3_MOUSE	0,05	0,87	1,15	0,67	1,33	-0,29	-3,46	1,15
P59017|B2L13_MOUSE	0,05	0,87	1,15	0,68	1,33	-0,29	-3,47	1,15
P35762|CD81_MOUSE	0,05	0,87	1,15	0,68	1,34	-0,29	-3,47	1,16
Q8BM55|TM214_MOUSE	0,05	0,86	1,16	0,68	1,34	-0,29	-3,48	1,16
P00397|COX1_MOUSE	0,05	0,86	1,16	0,69	1,34	-0,29	-3,49	1,16
Q7TMF3|NDUAC_MOUSE	0,05	0,86	1,16	0,69	1,34	-0,29	-3,50	1,17
Q8K2M0|RM38_MOUSE	0,05	0,86	1,16	0,69	1,34	-0,29	-3,51	1,17
Q9ESB3|HRG_MOUSE	0,05	0,86	1,16	0,69	1,35	-0,28	-3,51	1,17
Q80WW9|DDRGK_MOUSE	0,05	0,86	1,17	0,70	1,35	-0,28	-3,52	1,18
P15535|B4GT1_MOUSE	0,05	0,86	1,17	0,70	1,35	-0,28	-3,53	1,18
P10518|HEM2_MOUSE	0,05	0,86	1,17	0,70	1,35	-0,28	-3,54	1,18
Q8R429|AT2A1_MOUSE	0,05	0,85	1,17	0,71	1,36	-0,28	-3,55	1,19
Q9CQC9|SAR1B_MOUSE	0,05	0,85	1,17	0,71	1,36	-0,28	-3,56	1,19
Q9WUB3|PYGM_MOUSE	0,05	0,85	1,18	0,71	1,36	-0,28	-3,56	1,19
Q571E4|GALNS_MOUSE	0,05	0,85	1,18	0,71	1,36	-0,28	-3,57	1,19
P48410|ABCD1_MOUSE	0,05	0,85	1,18	0,72	1,36	-0,28	-3,58	1,20
Q91X34|BAAT_MOUSE	0,05	0,85	1,18	0,72	1,37	-0,28	-3,59	1,20
Q8C767|PPR3B_MOUSE	0,05	0,85	1,18	0,72	1,37	-0,28	-3,60	1,20
Q3ULJ0|GPD1L_MOUSE	0,05	0,84	1,18	0,73	1,37	-0,28	-3,60	1,21
Q9D826|SOX_MOUSE	0,05	0,84	1,19	0,73	1,37	-0,28	-3,61	1,21
P00688|AMYP_MOUSE	0,05	0,84	1,19	0,73	1,38	-0,28	-3,62	1,21
Q9ET01|PYGL_MOUSE	0,05	0,84	1,19	0,73	1,38	-0,28	-3,63	1,22
P00687|AMY1_MOUSE	0,05	0,84	1,19	0,74	1,38	-0,27	-3,64	1,22
P32020|SCP2_MOUSE	0,05	0,84	1,19	0,74	1,38	-0,27	-3,65	1,22
Q99P30|NUDT7_MOUSE	0,05	0,84	1,20	0,74	1,38	-0,27	-3,65	1,23
Q9CRB3|HIUH_MOUSE	0,05	0,83	1,20	0,75	1,39	-0,27	-3,66	1,23
Q9DC50|OCTC_MOUSE	0,05	0,83	1,20	0,75	1,39	-0,27	-3,67	1,23
P13707|GPDA_MOUSE	0,05	0,83	1,20	0,75	1,39	-0,27	-3,68	1,23
P11930|NUD19_MOUSE	0,05	0,83	1,20	0,75	1,39	-0,27	-3,69	1,24
Q8BGG9|ACNT2_MOUSE	0,05	0,83	1,21	0,76	1,39	-0,27	-3,69	1,24

P24270|CATA_MOUSE	0,05	0,83	1,21	0,76	1,40	-0,27	-3,70	1,24
Q99LC9|PEX6_MOUSE	0,05	0,83	1,21	0,76	1,40	-0,27	-3,71	1,25
Q91XC9|PEX16_MOUSE	0,05	0,83	1,21	0,77	1,40	-0,27	-3,72	1,25
O35386|PAHX_MOUSE	0,05	0,82	1,21	0,77	1,40	-0,27	-3,73	1,25
Q9EPL9|ACOX3_MOUSE	0,05	0,82	1,22	0,77	1,41	-0,27	-3,74	1,26
Q9DBM2|ECHP_MOUSE	0,05	0,82	1,22	0,77	1,41	-0,27	-3,74	1,26
Q9WU19|HAOX1_MOUSE	0,05	0,82	1,22	0,78	1,41	-0,27	-3,75	1,26
P51660|DHB4_MOUSE	0,05	0,82	1,22	0,78	1,41	-0,27	-3,76	1,26
Q921H8|THIKA_MOUSE	0,05	0,82	1,22	0,78	1,41	-0,27	-3,77	1,27
Q9QXE0|HACL1_MOUSE	0,05	0,82	1,22	0,79	1,42	-0,26	-3,78	1,27
P34914|HYES_MOUSE	0,05	0,82	1,23	0,79	1,42	-0,26	-3,78	1,27
Q9QXY9|PEX3_MOUSE	0,05	0,81	1,23	0,79	1,42	-0,26	-3,79	1,28
Q9R0A0|PEX14_MOUSE	0,05	0,81	1,23	0,79	1,42	-0,26	-3,80	1,28
Q8VDG7|PAFA2_MOUSE	0,05	0,81	1,23	0,80	1,43	-0,26	-3,81	1,28
Q9R0H0|ACOX1_MOUSE	0,05	0,81	1,23	0,80	1,43	-0,26	-3,82	1,29
Q8VCH0|THIKB_MOUSE	0,05	0,81	1,24	0,80	1,43	-0,26	-3,83	1,29
Q9DCN1|NUD12_MOUSE	0,05	0,81	1,24	0,81	1,43	-0,26	-3,83	1,29
Q80XL6|ACD11_MOUSE	0,05	0,81	1,24	0,81	1,43	-0,26	-3,84	1,30
Q9DBK0|ACO12_MOUSE	0,05	0,81	1,24	0,81	1,44	-0,26	-3,85	1,30
Q2TPA8|HSDL2_MOUSE	0,05	0,80	1,24	0,81	1,44	-0,26	-3,86	1,30
Q99MZ7|PECR_MOUSE	0,05	0,80	1,25	0,82	1,44	-0,26	-3,87	1,30
Q5BL07|PEX1_MOUSE	0,05	0,80	1,25	0,82	1,44	-0,26	-3,87	1,31
O09174|AMACR_MOUSE	0,05	0,80	1,25	0,82	1,44	-0,26	-3,88	1,31
Q8BWN8|ACOT4_MOUSE	0,05	0,80	1,25	0,83	1,45	-0,26	-3,89	1,31
Q8R1M2|H2AJ_MOUSE	0,05	0,80	1,25	0,83	1,45	-0,26	-3,90	1,32
Q9CYV5|TM135_MOUSE	0,05	0,80	1,25	0,83	1,45	-0,26	-3,91	1,32
Q9QXD1|ACOX2_MOUSE	0,05	0,80	1,26	0,83	1,45	-0,26	-3,92	1,32
Q9DBA6|TYSD1_MOUSE	0,05	0,79	1,26	0,84	1,46	-0,25	-3,92	1,33
Q9WV68|DECR2_MOUSE	0,05	0,79	1,26	0,84	1,46	-0,25	-3,93	1,33
O35423|SPYA_MOUSE	0,05	0,79	1,26	0,84	1,46	-0,25	-3,94	1,33
O09012|PEX5_MOUSE	0,05	0,79	1,26	0,85	1,46	-0,25	-3,95	1,33

A2AKK5|ACNT1_MOUSE	0,05	0,79	1,27	0,85	1,46	-0,25	-3,96	1,34
Q99KR3|LACB2_MOUSE	0,05	0,79	1,27	0,85	1,47	-0,25	-3,96	1,34
Q9DBN5|LONP2_MOUSE	0,05	0,79	1,27	0,85	1,47	-0,25	-3,97	1,34
P50431|GLYC_MOUSE	0,05	0,79	1,27	0,86	1,47	-0,25	-3,98	1,35
P55096|ABCD3_MOUSE	0,05	0,79	1,27	0,86	1,47	-0,25	-3,99	1,35
O35678|MGLL_MOUSE	0,05	0,78	1,28	0,86	1,48	-0,25	-4,00	1,35
Q99LB2|DHRS4_MOUSE	0,05	0,78	1,28	0,86	1,48	-0,25	-4,01	1,36
P07146|TRY2_MOUSE	0,05	0,78	1,28	0,87	1,48	-0,25	-4,01	1,36
Q8C7E7|STBD1_MOUSE	0,05	0,78	1,28	0,87	1,48	-0,25	-4,02	1,36
Q9QYR7|ACOT3_MOUSE	0,05	0,78	1,28	0,87	1,48	-0,25	-4,03	1,37
O88844|IDHC_MOUSE	0,05	0,78	1,29	0,88	1,49	-0,25	-4,04	1,37
O70579|PM34_MOUSE	0,05	0,78	1,29	0,88	1,49	-0,25	-4,05	1,37
P42925|PXMP2_MOUSE	0,05	0,78	1,29	0,88	1,49	-0,25	-4,05	1,37
Q9DCM2|GSTK1_MOUSE	0,05	0,77	1,29	0,88	1,49	-0,25	-4,06	1,38
P05208|CEL2A_MOUSE	0,05	0,77	1,29	0,89	1,50	-0,25	-4,07	1,38
P98192|GNPAT_MOUSE	0,05	0,77	1,29	0,89	1,50	-0,25	-4,08	1,38
Q8BGC4|PTGR3_MOUSE	0,05	0,77	1,30	0,89	1,50	-0,24	-4,09	1,39
Q61285|ABCD2_MOUSE	0,05	0,77	1,30	0,90	1,50	-0,24	-4,10	1,39
P25688|URIC_MOUSE	0,05	0,77	1,30	0,90	1,50	-0,24	-4,10	1,39
Q6P6M5|PX11C_MOUSE	0,05	0,77	1,30	0,90	1,51	-0,24	-4,11	1,40
Q8CHK3|MBOA7_MOUSE	0,05	0,77	1,30	0,90	1,51	-0,24	-4,12	1,40
Q9D1G2|PMVK_MOUSE	0,05	0,77	1,31	0,91	1,51	-0,24	-4,13	1,40
Q9Z211|PX11A_MOUSE	0,05	0,76	1,31	0,91	1,51	-0,24	-4,14	1,41
Q61878|PRG2_MOUSE	0,05	0,76	1,31	0,91	1,51	-0,24	-4,14	1,41
Q9Z210|PX11B_MOUSE	0,05	0,76	1,31	0,92	1,52	-0,24	-4,15	1,41
P58137|ACOT8_MOUSE	0,05	0,76	1,31	0,92	1,52	-0,24	-4,16	1,41
Q8VCR7|ABHEB_MOUSE	0,05	0,76	1,32	0,92	1,52	-0,24	-4,17	1,42
P12815|PDCD6_MOUSE	0,05	0,76	1,32	0,92	1,52	-0,24	-4,18	1,42
Q99MD6|TRXR3_MOUSE	0,05	0,76	1,32	0,93	1,53	-0,24	-4,19	1,42
P14152|MDHC_MOUSE	0,05	0,76	1,32	0,93	1,53	-0,24	-4,19	1,43
Q8BGI5|PEX26_MOUSE	0,05	0,76	1,32	0,93	1,53	-0,24	-4,20	1,43

P15116|CADH2_MOUSE	0,05	0,75	1,33	0,94	1,53	-0,24	-4,21	1,43
P09405|NUCL_MOUSE	0,05	0,75	1,33	0,94	1,53	-0,24	-4,22	1,44
Q8VC48|PEX12_MOUSE	0,05	0,75	1,33	0,94	1,54	-0,24	-4,23	1,44
P49290|PERE_MOUSE	0,05	0,75	1,33	0,94	1,54	-0,24	-4,23	1,44
Q9CQ92|FIS1_MOUSE	0,05	0,75	1,33	0,95	1,54	-0,24	-4,24	1,44
Q9JJW0|PXMP4_MOUSE	0,05	0,75	1,33	0,95	1,54	-0,24	-4,25	1,45
Q8C0I1|ADAS_MOUSE	0,05	0,75	1,34	0,95	1,55	-0,23	-4,26	1,45
P11679|K2C8_MOUSE	0,05	0,75	1,34	0,96	1,55	-0,23	-4,27	1,45
Q6NXH9|K2C73_MOUSE	0,05	0,75	1,34	0,96	1,55	-0,23	-4,28	1,46
B1AUE5|PEX10_MOUSE	0,05	0,75	1,34	0,96	1,55	-0,23	-4,28	1,46
P53657|KPYR_MOUSE	0,05	0,74	1,34	0,96	1,55	-0,23	-4,29	1,46
Q8CI51|PDLI5_MOUSE	0,05	0,74	1,35	0,97	1,56	-0,23	-4,30	1,47
Q9Z2G9|HTAI2_MOUSE	0,05	0,74	1,35	0,97	1,56	-0,23	-4,31	1,47
P62702|RS4X_MOUSE	0,05	0,74	1,35	0,97	1,56	-0,23	-4,32	1,47
Q9WUR2|ECI2_MOUSE	0,05	0,74	1,35	0,98	1,56	-0,23	-4,32	1,48
O35381|AN32A_MOUSE	0,05	0,74	1,35	0,98	1,56	-0,23	-4,33	1,48
Q8BWP5|TTPA_MOUSE	0,05	0,74	1,36	0,98	1,57	-0,23	-4,34	1,48
Q9NYQ2|HAOX2_MOUSE	0,05	0,74	1,36	0,98	1,57	-0,23	-4,35	1,48
Q5XG73|ACBD5_MOUSE	0,05	0,74	1,36	0,99	1,57	-0,23	-4,36	1,49
Q8K1N1|PLPL8_MOUSE	0,05	0,73	1,36	0,99	1,57	-0,23	-4,37	1,49
P62137|PP1A_MOUSE	0,05	0,73	1,36	0,99	1,58	-0,23	-4,37	1,49
Q9CQD1|RAB5A_MOUSE	0,05	0,73	1,36	1,00	1,58	-0,23	-4,38	1,50
P97364|SPS2_MOUSE	0,05	0,73	1,37	1,00	1,58	-0,23	-4,39	1,50
Q9R0P3|ESTD_MOUSE	0,05	0,73	1,37	1,00	1,58	-0,23	-4,40	1,50
P06151|LDHA_MOUSE	0,05	0,73	1,37	1,00	1,58	-0,23	-4,41	1,51
O08917|FLOT1_MOUSE	0,05	0,73	1,37	1,01	1,59	-0,23	-4,41	1,51
P97425|ECP2_MOUSE	0,05	0,73	1,37	1,01	1,59	-0,23	-4,42	1,51
Q91V64|ISOC1_MOUSE	0,05	0,73	1,38	1,01	1,59	-0,23	-4,43	1,51
P47934|CACP_MOUSE	0,05	0,73	1,38	1,02	1,59	-0,23	-4,44	1,52
Q07076|ANXA7_MOUSE	0,05	0,72	1,38	1,02	1,60	-0,22	-4,45	1,52
Q99KB8|GLO2_MOUSE	0,05	0,72	1,38	1,02	1,60	-0,22	-4,46	1,52

Q8CC88|VWA8_MOUSE	0,05	0,72	1,38	1,02	1,60	-0,22	-4,46	1,53
Q8JZS0|LIN7A_MOUSE	0,05	0,72	1,39	1,03	1,60	-0,22	-4,47	1,53
Q8VBT2|SDHL_MOUSE	0,05	0,72	1,39	1,03	1,60	-0,22	-4,48	1,53
Q9CR35|CTRB1_MOUSE	0,05	0,72	1,39	1,03	1,61	-0,22	-4,49	1,54
Q61792|LASP1_MOUSE	0,05	0,72	1,39	1,04	1,61	-0,22	-4,50	1,54
Q8R1G2|CMBL_MOUSE	0,05	0,72	1,39	1,04	1,61	-0,22	-4,50	1,54
P09411|PGK1_MOUSE	0,05	0,72	1,40	1,04	1,61	-0,22	-4,51	1,55
Q8BI84|TGO1_MOUSE	0,05	0,72	1,40	1,04	1,62	-0,22	-4,52	1,55
Q99J47|DRS7B_MOUSE	0,05	0,71	1,40	1,05	1,62	-0,22	-4,53	1,55
Q9WUA5|EPM2A_MOUSE	0,05	0,71	1,40	1,05	1,62	-0,22	-4,54	1,55
Q9EST5|AN32B_MOUSE	0,05	0,71	1,40	1,05	1,62	-0,22	-4,55	1,56
Q64339|ISG15_MOUSE	0,05	0,71	1,40	1,06	1,62	-0,22	-4,55	1,56
Q9D0K1|PEX13_MOUSE	0,05	0,71	1,41	1,06	1,63	-0,22	-4,56	1,56
P63037|DNJA1_MOUSE	0,05	0,71	1,41	1,06	1,63	-0,22	-4,57	1,57
Q9CRD0|OCAD1_MOUSE	0,05	0,71	1,41	1,06	1,63	-0,22	-4,58	1,57
P47757|CAPZB_MOUSE	0,05	0,71	1,41	1,07	1,63	-0,22	-4,59	1,57
Q811U4|MFN1_MOUSE	0,05	0,71	1,41	1,07	1,63	-0,22	-4,59	1,58
Q9D5T0|ATAD1_MOUSE	0,05	0,71	1,42	1,07	1,64	-0,22	-4,60	1,58
Q3UZZ6|ST1D1_MOUSE	0,05	0,71	1,42	1,08	1,64	-0,22	-4,61	1,58
Q62093|SRSF2_MOUSE	0,05	0,70	1,42	1,08	1,64	-0,22	-4,62	1,59
P52840|ST1A1_MOUSE	0,05	0,70	1,42	1,08	1,64	-0,22	-4,63	1,59
Q922Z0|OXDD_MOUSE	0,05	0,70	1,42	1,08	1,65	-0,22	-4,63	1,59
P41216|ACSL1_MOUSE	0,05	0,70	1,43	1,09	1,65	-0,22	-4,64	1,59
Q61147|CERU_MOUSE	0,05	0,70	1,43	1,09	1,65	-0,21	-4,65	1,60
P29788|VTNC_MOUSE	0,05	0,70	1,43	1,09	1,65	-0,21	-4,66	1,60
Q9D1N9|RM21_MOUSE	0,05	0,70	1,43	1,10	1,65	-0,21	-4,67	1,60
Q9DCL9|PUR6_MOUSE	0,05	0,70	1,43	1,10	1,66	-0,21	-4,68	1,61
P60335|PCBP1_MOUSE	0,05	0,70	1,44	1,10	1,66	-0,21	-4,68	1,61
O70400|PDLI1_MOUSE	0,05	0,70	1,44	1,10	1,66	-0,21	-4,69	1,61
P51410|RL9_MOUSE	0,05	0,69	1,44	1,11	1,66	-0,21	-4,70	1,62
Q99L20|GSTT3_MOUSE	0,05	0,69	1,44	1,11	1,67	-0,21	-4,71	1,62

P59017|B2L13_MOUSE	0,05	0,69	1,44	1,11	1,67	-0,21	-4,72	1,62
P35762|CD81_MOUSE	0,05	0,69	1,44	1,11	1,67	-0,21	-4,72	1,62
Q8BM55|TM214_MOUSE	0,05	0,69	1,45	1,12	1,67	-0,21	-4,73	1,63
P00397|COX1_MOUSE	0,05	0,69	1,45	1,12	1,67	-0,21	-4,74	1,63
Q7TMF3|NDUAC_MOUSE	0,05	0,69	1,45	1,12	1,68	-0,21	-4,75	1,63
Q8K2M0|RM38_MOUSE	0,05	0,69	1,45	1,13	1,68	-0,21	-4,76	1,64
Q9ESB3|HRG_MOUSE	0,05	0,69	1,45	1,13	1,68	-0,21	-4,77	1,64
Q80WW9|DDRGK_MOUSE	0,05	0,69	1,46	1,13	1,68	-0,21	-4,77	1,64
P15535|B4GT1_MOUSE	0,05	0,69	1,46	1,13	1,68	-0,21	-4,78	1,65
P10518|HEM2_MOUSE	0,05	0,69	1,46	1,14	1,69	-0,21	-4,79	1,65
Q8R429|AT2A1_MOUSE	0,05	0,68	1,46	1,14	1,69	-0,21	-4,80	1,65
Q9CQC9|SAR1B_MOUSE	0,05	0,68	1,46	1,14	1,69	-0,21	-4,81	1,66
Q9WUB3|PYGM_MOUSE	0,05	0,68	1,47	1,15	1,69	-0,21	-4,81	1,66
Q571E4|GALNS_MOUSE	0,05	0,68	1,47	1,15	1,70	-0,21	-4,82	1,66
P48410|ABCD1_MOUSE	0,05	0,68	1,47	1,15	1,70	-0,21	-4,83	1,66
Q91X34|BAAT_MOUSE	0,05	0,68	1,47	1,15	1,70	-0,21	-4,84	1,67
Q8C767|PPR3B_MOUSE	0,05	0,68	1,47	1,16	1,70	-0,21	-4,85	1,67
Q3ULJ0|GPD1L_MOUSE	0,05	0,68	1,47	1,16	1,70	-0,21	-4,86	1,67
Q9D826|SOX_MOUSE	0,05	0,68	1,48	1,16	1,71	-0,21	-4,86	1,68
P00688|AMYP_MOUSE	0,05	0,68	1,48	1,17	1,71	-0,21	-4,87	1,68
Q9ET01|PYGL_MOUSE	0,05	0,68	1,48	1,17	1,71	-0,20	-4,88	1,68
P00687|AMY1_MOUSE	0,05	0,67	1,48	1,17	1,71	-0,20	-4,89	1,69
P32020|SCP2_MOUSE	0,05	0,67	1,48	1,17	1,72	-0,20	-4,90	1,69
Q99P30|NUDT7_MOUSE	0,05	0,67	1,49	1,18	1,72	-0,20	-4,90	1,69
Q9CRB3|HIUH_MOUSE	0,05	0,67	1,49	1,18	1,72	-0,20	-4,91	1,69
Q9DC50|OCTC_MOUSE	0,05	0,67	1,49	1,18	1,72	-0,20	-4,92	1,70
P13707|GPDA_MOUSE	0,05	0,67	1,49	1,19	1,72	-0,20	-4,93	1,70
P11930|NUD19_MOUSE	0,05	0,67	1,49	1,19	1,73	-0,20	-4,94	1,70
Q8BGG9|ACNT2_MOUSE	0,05	0,67	1,50	1,19	1,73	-0,20	-4,95	1,71
P24270|CATA_MOUSE	0,05	0,67	1,50	1,19	1,73	-0,20	-4,95	1,71
Q99LC9|PEX6_MOUSE	0,05	0,67	1,50	1,20	1,73	-0,20	-4,96	1,71

Q91XC9|PEX16_MOUSE	0,05	0,67	1,50	1,20	1,74	-0,20	-4,97	1,72
O35386|PAHX_MOUSE	0,05	0,67	1,50	1,20	1,74	-0,20	-4,98	1,72
Q9EPL9|ACOX3_MOUSE	0,05	0,66	1,51	1,21	1,74	-0,20	-4,99	1,72
Q9DBM2|ECHP_MOUSE	0,05	0,66	1,51	1,21	1,74	-0,20	-4,99	1,73
Q9WU19|HAOX1_MOUSE	0,05	0,66	1,51	1,21	1,74	-0,20	-5,00	1,73
P51660|DHB4_MOUSE	0,05	0,66	1,51	1,21	1,75	-0,20	-5,01	1,73
Q921H8|THIKA_MOUSE	0,05	0,66	1,51	1,22	1,75	-0,20	-5,02	1,73
Q9QXE0|HACL1_MOUSE	0,05	0,66	1,51	1,22	1,75	-0,20	-5,03	1,74
P34914|HYES_MOUSE	0,05	0,66	1,52	1,22	1,75	-0,20	-5,04	1,74
Q9QXY9|PEX3_MOUSE	0,05	0,66	1,52	1,23	1,75	-0,20	-5,04	1,74
Q9R0A0|PEX14_MOUSE	0,05	0,66	1,52	1,23	1,76	-0,20	-5,05	1,75
Q8VDG7|PAFA2_MOUSE	0,05	0,66	1,52	1,23	1,76	-0,20	-5,06	1,75
Q9R0H0|ACOX1_MOUSE	0,05	0,66	1,52	1,23	1,76	-0,20	-5,07	1,75
Q8VCH0|THIKB_MOUSE	0,05	0,66	1,53	1,24	1,76	-0,20	-5,08	1,76
Q9DCN1|NUD12_MOUSE	0,05	0,65	1,53	1,24	1,77	-0,20	-5,08	1,76
Q80XL6|ACD11_MOUSE	0,05	0,65	1,53	1,24	1,77	-0,20	-5,09	1,76
Q9DBK0|ACO12_MOUSE	0,05	0,65	1,53	1,25	1,77	-0,20	-5,10	1,77
Q2TPA8|HSDL2_MOUSE	0,05	0,65	1,53	1,25	1,77	-0,20	-5,11	1,77
Q99MZ7|PECR_MOUSE	0,05	0,65	1,54	1,25	1,77	-0,20	-5,12	1,77
Q5BL07|PEX1_MOUSE	0,05	0,65	1,54	1,25	1,78	-0,20	-5,13	1,77
O09174|AMACR_MOUSE	0,05	0,65	1,54	1,26	1,78	-0,19	-5,13	1,78
Q8BWN8|ACOT4_MOUSE	0,05	0,65	1,54	1,26	1,78	-0,19	-5,14	1,78
Q8R1M2|H2AJ_MOUSE	0,05	0,65	1,54	1,26	1,78	-0,19	-5,15	1,78
Q9CYV5|TM135_MOUSE	0,05	0,65	1,55	1,27	1,79	-0,19	-5,16	1,79
Q9QXD1|ACOX2_MOUSE	0,05	0,65	1,55	1,27	1,79	-0,19	-5,17	1,79
Q9DBA6|TYSD1_MOUSE	0,05	0,65	1,55	1,27	1,79	-0,19	-5,17	1,79
Q9WV68|DECR2_MOUSE	0,05	0,64	1,55	1,27	1,79	-0,19	-5,18	1,80
O35423|SPYA_MOUSE	0,05	0,64	1,55	1,28	1,79	-0,19	-5,19	1,80
O09012|PEX5_MOUSE	0,05	0,64	1,55	1,28	1,80	-0,19	-5,20	1,80
A2AKK5|ACNT1_MOUSE	0,05	0,64	1,56	1,28	1,80	-0,19	-5,21	1,80
Q99KR3|LACB2_MOUSE	0,05	0,64	1,56	1,29	1,80	-0,19	-5,22	1,81

Q9DBN5|LONP2_MOUSE	0,05	0,64	1,56	1,29	1,80	-0,19	-5,22	1,81
P50431|GLYC_MOUSE	0,05	0,64	1,56	1,29	1,80	-0,19	-5,23	1,81
P55096|ABCD3_MOUSE	0,05	0,64	1,56	1,29	1,81	-0,19	-5,24	1,82
O35678|MGLL_MOUSE	0,05	0,64	1,57	1,30	1,81	-0,19	-5,25	1,82
Q99LB2|DHRS4_MOUSE	0,05	0,64	1,57	1,30	1,81	-0,19	-5,26	1,82
P07146|TRY2_MOUSE	0,05	0,64	1,57	1,30	1,81	-0,19	-5,26	1,83
Q8C7E7|STBD1_MOUSE	0,05	0,64	1,57	1,31	1,82	-0,19	-5,27	1,83
Q9QYR7|ACOT3_MOUSE	0,05	0,64	1,57	1,31	1,82	-0,19	-5,28	1,83
O88844|IDHC_MOUSE	0,05	0,63	1,58	1,31	1,82	-0,19	-5,29	1,84
O70579|PM34_MOUSE	0,05	0,63	1,58	1,31	1,82	-0,19	-5,30	1,84
P42925|PXMP2_MOUSE	0,05	0,63	1,58	1,32	1,82	-0,19	-5,31	1,84
Q9DCM2|GSTK1_MOUSE	0,05	0,63	1,58	1,32	1,83	-0,19	-5,31	1,84
P05208|CEL2A_MOUSE	0,05	0,63	1,58	1,32	1,83	-0,19	-5,32	1,85
P98192|GNPAT_MOUSE	0,05	0,63	1,58	1,33	1,83	-0,19	-5,33	1,85
Q8BGC4|PTGR3_MOUSE	0,05	0,63	1,59	1,33	1,83	-0,19	-5,34	1,85
Q61285|ABCD2_MOUSE	0,05	0,63	1,59	1,33	1,84	-0,19	-5,35	1,86
P25688|URIC_MOUSE	0,05	0,63	1,59	1,33	1,84	-0,19	-5,35	1,86
Q6P6M5|PX11C_MOUSE	0,05	0,63	1,59	1,34	1,84	-0,19	-5,36	1,86
Q8CHK3|MBOA7_MOUSE	0,05	0,63	1,59	1,34	1,84	-0,19	-5,37	1,87
Q9D1G2|PMVK_MOUSE	0,05	0,63	1,60	1,34	1,84	-0,19	-5,38	1,87
Q9Z211|PX11A_MOUSE	0,05	0,63	1,60	1,34	1,85	-0,19	-5,39	1,87
Q61878|PRG2_MOUSE	0,05	0,62	1,60	1,35	1,85	-0,19	-5,40	1,87
Q9Z210|PX11B_MOUSE	0,05	0,62	1,60	1,35	1,85	-0,19	-5,40	1,88
P58137|ACOT8_MOUSE	0,05	0,62	1,60	1,35	1,85	-0,18	-5,41	1,88
Q8VCR7|ABHEB_MOUSE	0,05	0,62	1,61	1,36	1,86	-0,18	-5,42	1,88
P12815|PDCD6_MOUSE	0,05	0,62	1,61	1,36	1,86	-0,18	-5,43	1,89
Q99MD6|TRXR3_MOUSE	0,05	0,62	1,61	1,36	1,86	-0,18	-5,44	1,89
P14152|MDHC_MOUSE	0,05	0,62	1,61	1,36	1,86	-0,18	-5,44	1,89
Q8BGI5|PEX26_MOUSE	0,05	0,62	1,61	1,37	1,86	-0,18	-5,45	1,90
P15116|CADH2_MOUSE	0,05	0,62	1,62	1,37	1,87	-0,18	-5,46	1,90
P09405|NUCL_MOUSE	0,05	0,62	1,62	1,37	1,87	-0,18	-5,47	1,90

Q8VC48|PEX12_MOUSE	0,05	0,62	1,62	1,38	1,87	-0,18	-5,48	1,91
P49290|PERE_MOUSE	0,05	0,62	1,62	1,38	1,87	-0,18	-5,49	1,91
Q9CQ92|FIS1_MOUSE	0,05	0,62	1,62	1,38	1,87	-0,18	-5,49	1,91
Q9JJW0|PXMP4_MOUSE	0,05	0,62	1,62	1,38	1,88	-0,18	-5,50	1,91
Q8C0I1|ADAS_MOUSE	0,05	0,61	1,63	1,39	1,88	-0,18	-5,51	1,92
P11679|K2C8_MOUSE	0,05	0,61	1,63	1,39	1,88	-0,18	-5,52	1,92
Q6NXH9|K2C73_MOUSE	0,05	0,61	1,63	1,39	1,88	-0,18	-5,53	1,92
B1AUE5|PEX10_MOUSE	0,05	0,61	1,63	1,40	1,89	-0,18	-5,53	1,93
P53657|KPYR_MOUSE	0,05	0,61	1,63	1,40	1,89	-0,18	-5,54	1,93
Q8CI51|PDLI5_MOUSE	0,05	0,61	1,64	1,40	1,89	-0,18	-5,55	1,93
Q9Z2G9|HTAI2_MOUSE	0,05	0,61	1,64	1,40	1,89	-0,18	-5,56	1,94
P62702|RS4X_MOUSE	0,05	0,61	1,64	1,41	1,89	-0,18	-5,57	1,94
Q9WUR2|ECI2_MOUSE	0,05	0,61	1,64	1,41	1,90	-0,18	-5,58	1,94
O35381|AN32A_MOUSE	0,05	0,61	1,64	1,41	1,90	-0,18	-5,58	1,95
Q8BWP5|TTPA_MOUSE	0,05	0,61	1,65	1,42	1,90	-0,18	-5,59	1,95
Q9NYQ2|HAOX2_MOUSE	0,05	0,61	1,65	1,42	1,90	-0,18	-5,60	1,95
Q5XG73|ACBD5_MOUSE	0,05	0,61	1,65	1,42	1,91	-0,18	-5,61	1,95
Q8K1N1|PLPL8_MOUSE	0,05	0,61	1,65	1,42	1,91	-0,18	-5,62	1,96
P62137|PP1A_MOUSE	0,05	0,60	1,65	1,43	1,91	-0,18	-5,62	1,96
Q9CQD1|RAB5A_MOUSE	0,05	0,60	1,66	1,43	1,91	-0,18	-5,63	1,96
P97364|SPS2_MOUSE	0,05	0,60	1,66	1,43	1,91	-0,18	-5,64	1,97
Q9R0P3|ESTD_MOUSE	0,05	0,60	1,66	1,44	1,92	-0,18	-5,65	1,97
P06151|LDHA_MOUSE	0,05	0,60	1,66	1,44	1,92	-0,18	-5,66	1,97
O08917|FLOT1_MOUSE	0,05	0,60	1,66	1,44	1,92	-0,18	-5,67	1,98
P97425|ECP2_MOUSE	0,05	0,60	1,66	1,44	1,92	-0,18	-5,67	1,98
Q91V64|ISOC1_MOUSE	0,05	0,60	1,67	1,45	1,92	-0,18	-5,68	1,98
P47934|CACP_MOUSE	0,05	0,60	1,67	1,45	1,93	-0,18	-5,69	1,98
Q07076|ANXA7_MOUSE	0,05	0,60	1,67	1,45	1,93	-0,18	-5,70	1,99
Q99KB8|GLO2_MOUSE	0,05	0,60	1,67	1,46	1,93	-0,18	-5,71	1,99
Q8CC88|VWA8_MOUSE	0,05	0,60	1,67	1,46	1,93	-0,18	-5,71	1,99
Q8JZS0|LIN7A_MOUSE	0,05	0,60	1,68	1,46	1,94	-0,17	-5,72	2,00

Q8VBT2|SDHL_MOUSE	0,05	0,60	1,68	1,46	1,94	-0,17	-5,73	2,00
Q9CR35|CTRB1_MOUSE	0,05	0,60	1,68	1,47	1,94	-0,17	-5,74	2,00
Q61792|LASP1_MOUSE	0,05	0,59	1,68	1,47	1,94	-0,17	-5,75	2,01
Q8R1G2|CMBL_MOUSE	0,05	0,59	1,68	1,47	1,94	-0,17	-5,76	2,01
P09411|PGK1_MOUSE	0,05	0,59	1,69	1,48	1,95	-0,17	-5,76	2,01
Q8BI84|TGO1_MOUSE	0,05	0,59	1,69	1,48	1,95	-0,17	-5,77	2,02
Q99J47|DRS7B_MOUSE	0,05	0,59	1,69	1,48	1,95	-0,17	-5,78	2,02
Q9WUA5|EPM2A_MOUSE	0,05	0,59	1,69	1,48	1,95	-0,17	-5,79	2,02
Q9EST5|AN32B_MOUSE	0,05	0,59	1,69	1,49	1,96	-0,17	-5,80	2,02
Q64339|ISG15_MOUSE	0,05	0,59	1,69	1,49	1,96	-0,17	-5,80	2,03
Q9D0K1|PEX13_MOUSE	0,05	0,59	1,70	1,49	1,96	-0,17	-5,81	2,03
P63037|DNJA1_MOUSE	0,05	0,59	1,70	1,50	1,96	-0,17	-5,82	2,03
Q9CRD0|OCAD1_MOUSE	0,05	0,59	1,70	1,50	1,96	-0,17	-5,83	2,04
P47757|CAPZB_MOUSE	0,05	0,59	1,70	1,50	1,97	-0,17	-5,84	2,04
Q811U4|MFN1_MOUSE	0,05	0,59	1,70	1,50	1,97	-0,17	-5,84	2,04
Q9D5T0|ATAD1_MOUSE	0,05	0,59	1,71	1,51	1,97	-0,17	-5,85	2,05
Q3UZZ6|ST1D1_MOUSE	0,05	0,59	1,71	1,51	1,97	-0,17	-5,86	2,05
Q62093|SRSF2_MOUSE	0,05	0,58	1,71	1,51	1,98	-0,17	-5,87	2,05
P52840|ST1A1_MOUSE	0,05	0,58	1,71	1,52	1,98	-0,17	-5,88	2,05
Q922Z0|OXDD_MOUSE	0,05	0,58	1,71	1,52	1,98	-0,17	-5,89	2,06
P41216|ACSL1_MOUSE	0,05	0,58	1,72	1,52	1,98	-0,17	-5,89	2,06
Q61147|CERU_MOUSE	0,05	0,58	1,72	1,52	1,98	-0,17	-5,90	2,06
P29788|VTNC_MOUSE	0,05	0,58	1,72	1,53	1,99	-0,17	-5,91	2,07
Q9D1N9|RM21_MOUSE	0,05	0,58	1,72	1,53	1,99	-0,17	-5,92	2,07
Q9DCL9|PUR6_MOUSE	0,05	0,58	1,72	1,53	1,99	-0,17	-5,93	2,07
P60335|PCBP1_MOUSE	0,05	0,58	1,73	1,54	1,99	-0,17	-5,93	2,08
O70400|PDLI1_MOUSE	0,05	0,58	1,73	1,54	1,99	-0,17	-5,94	2,08
P51410|RL9_MOUSE	0,05	0,58	1,73	1,54	2,00	-0,17	-5,95	2,08
Q99L20|GSTT3_MOUSE	0,05	0,58	1,73	1,54	2,00	-0,17	-5,96	2,09
P59017|B2L13_MOUSE	0,05	0,58	1,73	1,55	2,00	-0,17	-5,97	2,09
P35762|CD81_MOUSE	0,05	0,58	1,73	1,55	2,00	-0,17	-5,98	2,09

Q8BM55|TM214_MOUSE	0,05	0,58	1,74	1,55	2,01	-0,17	-5,98	2,09
P00397|COX1_MOUSE	0,05	0,58	1,74	1,56	2,01	-0,17	-5,99	2,10
Q7TMF3|NDUAC_MOUSE	0,05	0,57	1,74	1,56	2,01	-0,17	-6,00	2,10
Q8K2M0|RM38_MOUSE	0,05	0,57	1,74	1,56	2,01	-0,17	-6,01	2,10
Q9ESB3|HRG_MOUSE	0,05	0,57	1,74	1,56	2,01	-0,17	-6,02	2,11
Q80WW9|DDRGK_MOUSE	0,05	0,57	1,75	1,57	2,02	-0,17	-6,02	2,11
P15535|B4GT1_MOUSE	0,05	0,57	1,75	1,57	2,02	-0,17	-6,03	2,11
P10518|HEM2_MOUSE	0,05	0,57	1,75	1,57	2,02	-0,17	-6,04	2,12
Q8R429|AT2A1_MOUSE	0,05	0,57	1,75	1,57	2,02	-0,17	-6,05	2,12
Q9CQC9|SAR1B_MOUSE	0,05	0,57	1,75	1,58	2,03	-0,17	-6,06	2,12
Q9WUB3|PYGM_MOUSE	0,05	0,57	1,76	1,58	2,03	-0,16	-6,07	2,13
Q571E4|GALNS_MOUSE	0,05	0,57	1,76	1,58	2,03	-0,16	-6,07	2,13
P48410|ABCD1_MOUSE	0,05	0,57	1,76	1,59	2,03	-0,16	-6,08	2,13
Q91X34|BAAT_MOUSE	0,05	0,57	1,76	1,59	2,03	-0,16	-6,09	2,13
Q8C767|PPR3B_MOUSE	0,05	0,57	1,76	1,59	2,04	-0,16	-6,10	2,14
Q3ULJ0|GPD1L_MOUSE	0,05	0,57	1,77	1,59	2,04	-0,16	-6,11	2,14
Q9D826|SOX_MOUSE	0,05	0,57	1,77	1,60	2,04	-0,16	-6,11	2,14
P00688|AMYP_MOUSE	0,05	0,57	1,77	1,60	2,04	-0,16	-6,12	2,15
Q9ET01|PYGL_MOUSE	0,05	0,56	1,77	1,60	2,04	-0,16	-6,13	2,15
P00687|AMY1_MOUSE	0,05	0,56	1,77	1,61	2,05	-0,16	-6,14	2,15
P32020|SCP2_MOUSE	0,05	0,56	1,77	1,61	2,05	-0,16	-6,15	2,16
Q99P30|NUDT7_MOUSE	0,05	0,56	1,78	1,61	2,05	-0,16	-6,16	2,16
Q9CRB3|HIUH_MOUSE	0,05	0,56	1,78	1,61	2,05	-0,16	-6,16	2,16
Q9DC50|OCTC_MOUSE	0,05	0,56	1,78	1,62	2,06	-0,16	-6,17	2,16
P13707|GPDA_MOUSE	0,05	0,56	1,78	1,62	2,06	-0,16	-6,18	2,17
P11930|NUD19_MOUSE	0,05	0,56	1,78	1,62	2,06	-0,16	-6,19	2,17
Q8BGG9|ACNT2_MOUSE	0,05	0,56	1,79	1,63	2,06	-0,16	-6,20	2,17
P24270|CATA_MOUSE	0,05	0,56	1,79	1,63	2,06	-0,16	-6,20	2,18
Q99LC9|PEX6_MOUSE	0,05	0,56	1,79	1,63	2,07	-0,16	-6,21	2,18
Q91XC9|PEX16_MOUSE	0,05	0,56	1,79	1,63	2,07	-0,16	-6,22	2,18
O35386|PAHX_MOUSE	0,05	0,56	1,79	1,64	2,07	-0,16	-6,23	2,19

Q9EPL9|ACOX3_MOUSE	0,05	0,56	1,80	1,64	2,07	-0,16	-6,24	2,19
Q9DBM2|ECHP_MOUSE	0,05	0,56	1,80	1,64	2,08	-0,16	-6,25	2,19
Q9WU19|HAOX1_MOUSE	0,05	0,56	1,80	1,65	2,08	-0,16	-6,25	2,20
P51660|DHB4_MOUSE	0,05	0,56	1,80	1,65	2,08	-0,16	-6,26	2,20
Q921H8|THIKA_MOUSE	0,05	0,55	1,80	1,65	2,08	-0,16	-6,27	2,20
Q9QXE0|HACL1_MOUSE	0,05	0,55	1,80	1,65	2,08	-0,16	-6,28	2,20
P34914|HYES_MOUSE	0,05	0,55	1,81	1,66	2,09	-0,16	-6,29	2,21
Q9QXY9|PEX3_MOUSE	0,05	0,55	1,81	1,66	2,09	-0,16	-6,29	2,21
Q9R0A0|PEX14_MOUSE	0,05	0,55	1,81	1,66	2,09	-0,16	-6,30	2,21
Q8VDG7|PAFA2_MOUSE	0,05	0,55	1,81	1,67	2,09	-0,16	-6,31	2,22
Q9R0H0|ACOX1_MOUSE	0,05	0,55	1,81	1,67	2,10	-0,16	-6,32	2,22
Q8VCH0|THIKB_MOUSE	0,05	0,55	1,82	1,67	2,10	-0,16	-6,33	2,22
Q9DCN1|NUD12_MOUSE	0,05	0,55	1,82	1,67	2,10	-0,16	-6,34	2,23
Q80XL6|ACD11_MOUSE	0,05	0,55	1,82	1,68	2,10	-0,16	-6,34	2,23
Q9DBK0|ACO12_MOUSE	0,05	0,55	1,82	1,68	2,10	-0,16	-6,35	2,23
Q2TPA8|HSDL2_MOUSE	0,05	0,55	1,82	1,68	2,11	-0,16	-6,36	2,23
Q99MZ7|PECR_MOUSE	0,05	0,55	1,83	1,69	2,11	-0,16	-6,37	2,24
Q5BL07|PEX1_MOUSE	0,05	0,55	1,83	1,69	2,11	-0,16	-6,38	2,24
O09174|AMACR_MOUSE	0,05	0,55	1,83	1,69	2,11	-0,16	-6,38	2,24
Q8BWN8|ACOT4_MOUSE	0,05	0,55	1,83	1,69	2,11	-0,16	-6,39	2,25
Q8R1M2|H2AJ_MOUSE	0,05	0,55	1,83	1,70	2,12	-0,16	-6,40	2,25
Q9CYV5|TM135_MOUSE	0,05	0,54	1,84	1,70	2,12	-0,16	-6,41	2,25
Q9QXD1|ACOX2_MOUSE	0,05	0,54	1,84	1,70	2,12	-0,16	-6,42	2,26
Q9DBA6|TYSD1_MOUSE	0,05	0,54	1,84	1,71	2,12	-0,16	-6,43	2,26
Q9WV68|DECR2_MOUSE	0,05	0,54	1,84	1,71	2,13	-0,16	-6,43	2,26
O35423|SPYA_MOUSE	0,05	0,54	1,84	1,71	2,13	-0,16	-6,44	2,27
O09012|PEX5_MOUSE	0,05	0,54	1,84	1,71	2,13	-0,16	-6,45	2,27
A2AKK5|ACNT1_MOUSE	0,05	0,54	1,85	1,72	2,13	-0,15	-6,46	2,27
Q99KR3|LACB2_MOUSE	0,05	0,54	1,85	1,72	2,13	-0,15	-6,47	2,27
Q9DBN5|LONP2_MOUSE	0,05	0,54	1,85	1,72	2,14	-0,15	-6,47	2,28
P50431|GLYC_MOUSE	0,05	0,54	1,85	1,73	2,14	-0,15	-6,48	2,28

P55096|ABCD3_MOUSE	0,05	0,54	1,85	1,73	2,14	-0,15	-6,49	2,28
O35678|MGLL_MOUSE	0,05	0,54	1,86	1,73	2,14	-0,15	-6,50	2,29
Q99LB2|DHRS4_MOUSE	0,05	0,54	1,86	1,73	2,15	-0,15	-6,51	2,29
P07146|TRY2_MOUSE	0,05	0,54	1,86	1,74	2,15	-0,15	-6,52	2,29
Q8C7E7|STBD1_MOUSE	0,05	0,54	1,86	1,74	2,15	-0,15	-6,52	2,30
Q9QYR7|ACOT3_MOUSE	0,05	0,54	1,86	1,74	2,15	-0,15	-6,53	2,30
O88844|IDHC_MOUSE	0,05	0,54	1,87	1,75	2,15	-0,15	-6,54	2,30
O70579|PM34_MOUSE	0,05	0,54	1,87	1,75	2,16	-0,15	-6,55	2,31
P42925|PXMP2_MOUSE	0,05	0,53	1,87	1,75	2,16	-0,15	-6,56	2,31
Q9DCM2|GSTK1_MOUSE	0,05	0,53	1,87	1,75	2,16	-0,15	-6,56	2,31
P05208|CEL2A_MOUSE	0,05	0,53	1,87	1,76	2,16	-0,15	-6,57	2,31
P98192|GNPAT_MOUSE	0,05	0,53	1,88	1,76	2,16	-0,15	-6,58	2,32
Q8BGC4|PTGR3_MOUSE	0,05	0,53	1,88	1,76	2,17	-0,15	-6,59	2,32
Q61285|ABCD2_MOUSE	0,05	0,53	1,88	1,77	2,17	-0,15	-6,60	2,32
P25688|URIC_MOUSE	0,05	0,53	1,88	1,77	2,17	-0,15	-6,61	2,33
Q6P6M5|PX11C_MOUSE	0,05	0,53	1,88	1,77	2,17	-0,15	-6,61	2,33
Q8CHK3|MBOA7_MOUSE	0,05	0,53	1,88	1,77	2,18	-0,15	-6,62	2,33
Q9D1G2|PMVK_MOUSE	0,05	0,53	1,89	1,78	2,18	-0,15	-6,63	2,34
Q9Z211|PX11A_MOUSE	0,05	0,53	1,89	1,78	2,18	-0,15	-6,64	2,34
Q61878|PRG2_MOUSE	0,05	0,53	1,89	1,78	2,18	-0,15	-6,65	2,34
Q9Z210|PX11B_MOUSE	0,05	0,53	1,89	1,79	2,18	-0,15	-6,65	2,34
P58137|ACOT8_MOUSE	0,05	0,53	1,89	1,79	2,19	-0,15	-6,66	2,35
Q8VCR7|ABHEB_MOUSE	0,05	0,53	1,90	1,79	2,19	-0,15	-6,67	2,35
P12815|PDCD6_MOUSE	0,05	0,53	1,90	1,79	2,19	-0,15	-6,68	2,35
Q99MD6|TRXR3_MOUSE	0,05	0,53	1,90	1,80	2,19	-0,15	-6,69	2,36
P14152|MDHC_MOUSE	0,05	0,53	1,90	1,80	2,20	-0,15	-6,70	2,36
Q8BGI5|PEX26_MOUSE	0,05	0,53	1,90	1,80	2,20	-0,15	-6,70	2,36
P15116|CADH2_MOUSE	0,05	0,52	1,91	1,80	2,20	-0,15	-6,71	2,37
P09405|NUCL_MOUSE	0,05	0,52	1,91	1,81	2,20	-0,15	-6,72	2,37
Q8VC48|PEX12_MOUSE	0,05	0,52	1,91	1,81	2,20	-0,15	-6,73	2,37
P49290|PERE_MOUSE	0,05	0,52	1,91	1,81	2,21	-0,15	-6,74	2,38

Q9CQ92|FIS1_MOUSE	0,05	0,52	1,91	1,82	2,21	-0,15	-6,74	2,38
Q9JJW0|PXMP4_MOUSE	0,05	0,52	1,91	1,82	2,21	-0,15	-6,75	2,38
Q8C0I1|ADAS_MOUSE	0,05	0,52	1,92	1,82	2,21	-0,15	-6,76	2,38
P11679|K2C8_MOUSE	0,05	0,52	1,92	1,82	2,22	-0,15	-6,77	2,39
Q6NXH9|K2C73_MOUSE	0,05	0,52	1,92	1,83	2,22	-0,15	-6,78	2,39
B1AUE5|PEX10_MOUSE	0,05	0,52	1,92	1,83	2,22	-0,15	-6,79	2,39
P53657|KPYR_MOUSE	0,05	0,52	1,92	1,83	2,22	-0,15	-6,79	2,40
Q8CI51|PDLI5_MOUSE	0,05	0,52	1,93	1,84	2,22	-0,15	-6,80	2,40
Q9Z2G9|HTAI2_MOUSE	0,05	0,52	1,93	1,84	2,23	-0,15	-6,81	2,40
P62702|RS4X_MOUSE	0,05	0,52	1,93	1,84	2,23	-0,15	-6,82	2,41
Q9WUR2|ECI2_MOUSE	0,05	0,52	1,93	1,84	2,23	-0,15	-6,83	2,41
O35381|AN32A_MOUSE	0,05	0,52	1,93	1,85	2,23	-0,15	-6,83	2,41
Q8BWP5|TTPA_MOUSE	0,05	0,52	1,94	1,85	2,23	-0,15	-6,84	2,41
Q9NYQ2|HAOX2_MOUSE	0,05	0,52	1,94	1,85	2,24	-0,15	-6,85	2,42
Q5XG73|ACBD5_MOUSE	0,05	0,52	1,94	1,86	2,24	-0,15	-6,86	2,42
Q8K1N1|PLPL8_MOUSE	0,05	0,52	1,94	1,86	2,24	-0,15	-6,87	2,42
P62137|PP1A_MOUSE	0,05	0,51	1,94	1,86	2,24	-0,15	-6,88	2,43
Q9CQD1|RAB5A_MOUSE	0,05	0,51	1,95	1,86	2,25	-0,15	-6,88	2,43
P97364|SPS2_MOUSE	0,05	0,51	1,95	1,87	2,25	-0,15	-6,89	2,43
Q9R0P3|ESTD_MOUSE	0,05	0,51	1,95	1,87	2,25	-0,14	-6,90	2,44
P06151|LDHA_MOUSE	0,05	0,51	1,95	1,87	2,25	-0,14	-6,91	2,44
O08917|FLOT1_MOUSE	0,05	0,51	1,95	1,88	2,25	-0,14	-6,92	2,44
P97425|ECP2_MOUSE	0,05	0,51	1,95	1,88	2,26	-0,14	-6,92	2,45
Q91V64|ISOC1_MOUSE	0,05	0,51	1,96	1,88	2,26	-0,14	-6,93	2,45
P47934|CACP_MOUSE	0,05	0,51	1,96	1,88	2,26	-0,14	-6,94	2,45
Q07076|ANXA7_MOUSE	0,05	0,51	1,96	1,89	2,26	-0,14	-6,95	2,45
Q99KB8|GLO2_MOUSE	0,05	0,51	1,96	1,89	2,27	-0,14	-6,96	2,46
Q8CC88|VWA8_MOUSE	0,05	0,51	1,96	1,89	2,27	-0,14	-6,97	2,46
Q8JZS0|LIN7A_MOUSE	0,05	0,51	1,97	1,90	2,27	-0,14	-6,97	2,46
Q8VBT2|SDHL_MOUSE	0,05	0,51	1,97	1,90	2,27	-0,14	-6,98	2,47
Q9CR35|CTRB1_MOUSE	0,05	0,51	1,97	1,90	2,27	-0,14	-6,99	2,47

Q61792|LASP1_MOUSE	0,05	0,51	1,97	1,90	2,28	-0,14	-7,00	2,47
Q8R1G2|CMBL_MOUSE	0,05	0,51	1,97	1,91	2,28	-0,14	-7,01	2,48
P09411|PGK1_MOUSE	0,05	0,51	1,98	1,91	2,28	-0,14	-7,01	2,48
Q8BI84|TGO1_MOUSE	0,05	0,51	1,98	1,91	2,28	-0,14	-7,02	2,48
Q99J47|DRS7B_MOUSE	0,05	0,51	1,98	1,92	2,28	-0,14	-7,03	2,49
Q9WUA5|EPM2A_MOUSE	0,05	0,50	1,98	1,92	2,29	-0,14	-7,04	2,49
Q9EST5|AN32B_MOUSE	0,05	0,50	1,98	1,92	2,29	-0,14	-7,05	2,49
Q64339|ISG15_MOUSE	0,05	0,50	1,99	1,92	2,29	-0,14	-7,06	2,49
Q9D0K1|PEX13_MOUSE	0,05	0,50	1,99	1,93	2,29	-0,14	-7,06	2,50
P63037|DNJA1_MOUSE	0,05	0,50	1,99	1,93	2,30	-0,14	-7,07	2,50
Q9CRD0|OCAD1_MOUSE	0,05	0,50	1,99	1,93	2,30	-0,14	-7,08	2,50
P47757|CAPZB_MOUSE	0,05	0,50	1,99	1,94	2,30	-0,14	-7,09	2,51
Q811U4|MFN1_MOUSE	0,05	0,50	1,99	1,94	2,30	-0,14	-7,10	2,51
Q9D5T0|ATAD1_MOUSE	0,05	0,50	2,00	1,94	2,30	-0,14	-7,10	2,51
Q3UZZ6|ST1D1_MOUSE	0,05	0,50	2,00	1,94	2,31	-0,14	-7,11	2,52
Q62093|SRSF2_MOUSE	0,05	0,50	2,00	1,95	2,31	-0,14	-7,12	2,52
P52840|ST1A1_MOUSE	0,05	0,50	2,00	1,95	2,31	-0,14	-7,13	2,52
Q922Z0|OXDD_MOUSE	0,05	0,50	2,00	1,95	2,31	-0,14	-7,14	2,52
P41216|ACSL1_MOUSE	0,05	0,50	2,01	1,96	2,32	-0,14	-7,14	2,53
Q61147|CERU_MOUSE	0,05	0,50	2,01	1,96	2,32	-0,14	-7,15	2,53
P29788|VTNC_MOUSE	0,05	0,50	2,01	1,96	2,32	-0,14	-7,16	2,53
Q9D1N9|RM21_MOUSE	0,05	0,50	2,01	1,96	2,32	-0,14	-7,17	2,54

10 CURRICULUM VITAE

PERSONAL INFORMATION
Name: Öznur
Family name: Singin
Date of birth: July 21st, 1990
Nationality: Turkish

EDUCATION
Since 09/2018 Doctoral student at Medical Faculty Mannheim, Heidelberg University-Heidelberg, Germany

02/2015 – 07/2017 Master student at Bioengineering Department, Ege University, Izmir, Turkey, Master of Science in Bioengineering

09/2009 – 07/2014 Bachelor student at Ege University, Izmir, Turkey, Bachelor of Science in Bioengineering

10/2012 – 02/2013 ERASMUS Student at University of Technology And Life Sciences, Bydgoszcz, Poland

11 ACKNOWLEDGEMENT

The completion of this doctoral thesis owes a great deal to the invaluable support and contributions of my fellow colleagues at the Department of Neuroanatomy, Mannheim Center for Translational Neuroscience (MCTN), Medical Faculty Mannheim, Heidelberg University.

To begin, I want to convey my profound appreciation to my supervisor Prof. Dr. Christian Schultz for his professional support throughout my journey. I would also like to thank my mentor, PD Dr. Markus Islinger, for his unwavering support and continuous guidance during the course of my doctoral research. He always encouraged me through the stressful and critical time of my PhD journey. His wealth of knowledge, unwavering commitment to research excellence, and his willingness to provide constructive feedback have been invaluable. I am truly fortunate to have had such a dedicated mentor who not only imparted valuable academic insights but also fostered personal and professional growth.

I have a great deal of appreciation for the mentorship and invaluable knowledge shared by Dr. Nina Bonekamp. Her contributions were indispensable in conducting essential experiments that contributed significantly to the successful completion of this thesis.
I would like to extend my heartfelt appreciation to Dr. Sandra Kühl, Silke Vorwald, Dilek Daskin-Türker, Anja Uhl and Heribert Mohr, for their exceptional support and kindness during my daily laboratory activities over the past four years. I also thank to Viktor Costina and Oliver Drews for mouse liver proteomics data.

I want to express my gratitude to the Deutsche Forschungsgemeinschaft for their financial support of the mouse liver proteomics study and to the Deutsches Zentrum für Herz- und Kreislaufforschung for their funding of the pig heart proteomics study. I also want to acknowledge the invaluable assistance provided by my colleagues from the University of Exeter and University of Amsterdam, who played a crucial role in supporting the technical aspects of the mouse liver experiments. Furthermore, I am thankful for the contributions of Sven Thoms in the pig heart experiments and for Peter Kim's willingness to share their BioID experiment findings.

Last but not least, I wish to thank Käthe Neumann and Gerlinde Baumann for their personal assistance with employment-related documentation.

I'd like to seize this moment to express my gratitude to my husband who help with the machine learning bioinformatics approach, my two beloved cats, my family, and all my friends for their unwavering support and encouragement, which have been instrumental in guiding me through this significant journey in my life.